Javier Pablo Navarro

Development and optimization of 3D advanced functional magnetic nanostructures grown by focused electron beam induced deposition

Departamento

Física de la Materia Condensada

Director/es

De Teresa Nogueras, José María
Magén Domínguez, César

http://zaguan.unizar.es/collection/Tesis

Universidad Zaragoza
1542

Tesis Doctoral

DEVELOPMENT AND OPTIMIZATION OF 3D ADVANCED FUNCTIONAL MAGNETIC NANOSTRUCTURES GROWN BY FOCUSED ELECTRON BEAM INDUCED DEPOSITION

Autor

Javier Pablo Navarro

Director/es

De Teresa Nogueras, José María
Magén Domínguez, César

UNIVERSIDAD DE ZARAGOZA

Física de la Materia Condensada

2020

Departamento de Física de la Materia Condensada

Instituto de Nanociencia de Aragón (INA)

Instituto de Ciencia de Materiales de Aragón (ICMA)

Universidad de Zaragoza - Consejo Superior de Investigaciones Científicas (CSIC)

Doctoral Thesis

Development and optimization of 3D advanced functional magnetic nanostructures grown by focused electron beam induced deposition

_____

Javier Pablo Navarro

Zaragoza, August 2019

Thesis supervisors:

José María de Teresa Nogueras

César Magén Domínguez

Contents

Agradecimientos (Acknowledgements)

Quiero comenzar agradeciendo el papel fundamental de mis directores de tesis, José María de Teresa y César Magén, quienes me han dado la oportunidad de iniciarme en la carrera investigadora, guiándome y aconsejándome convenientemente durante esta etapa, y cuya confianza, motivación y ayuda han sido los pilares básicos para la consecución de este trabajo.

Por supuesto, quiero mostrar el reconocimiento más especial a mi familia, en particular a mis padres y a mi hermana, por su paciencia y apoyo incondicionales e infinitos durante el camino recorrido hasta llegar aquí, y durante el que vendrá.

Asimismo, quiero dar las gracias a todos los investigadores a los que he tenido la oportunidad de conocer en el INA durante estos casi 5 años, y de los que he procurado aprender lo máximo posible. Muchas gracias a Soraya Sangiao, por ser el ejemplo brillante de constancia, dedicación y esfuerzo, por enseñarme que todo trabajo tiene su recompensa; a Irene Lucas, por despertar mi vocación divulgadora y asentar la educadora; a Rosa Córdoba, por su perseverancia, empeño y afán en el trabajo; y a Luis Serrano, por facilitarme seguir el hilo de sus investigaciones. Igualmente, gracias a Pedro Algarabel, Luis Morellón, Clara Marquina y Ricardo Ibarra por su amabilidad y buena acogida; a David Serrate por su carácter divertido, llano y abierto, por mostrar que el verdadero talento no se encuentra sólo en una cancha de la NBA; a Pepa Martínez y Javier Sesé por su colaboración y rigor en el trabajo; a José Ángel Pardo, por su preocupación y diligencia administrativa; a Pavel, por su generosidad y profesionalidad; y a Álvaro, Roger, Raúl, Luc, Simon, Myriam, Jorge, Noelia y Alfonso por su compañerismo.

Por otro lado, me gustaría acordarme de los actuales becarios, y de los que algún día lo fueron durante mi etapa en el INA. Gracias a Pilar, por su amistad y sus ánimos, por

ser la compañera infatigable durante todo este tiempo; a Bea, por su aprecio y honestidad, por su compañía desde primera hora de la mañana; a Laura, por saber contagiar su alegría y entusiasmo; a Inés, por transmitir su paciencia y saber estar; a Alberto, por acogerme como uno más, por su carácter siempre agradable y dispuesto, y por su valiosa ayuda informática; a Ismael, por enseñarme que debatir sonriendo es un argumento más para convencer; a José, por hacer de los disparates una virtud; a Mari Carmen, por irradiar y compaginar tranquilidad y buen hacer; y a María, por cederme la mesa y el espacio donde se han elaborado la mayor parte de los párrafos de este documento. También a Leyre, por su sonrisa constante; a Adán, por demostrar su formalidad y responsabilidad; a Pablo, por fomentar la humildad y el compañerismo; a Amelia, por hacer agradable el compartir despacho, y también congreso al otro lado del charco; a Rubén, por promulgar su prudencia y solidaridad; a Mario, por amenizar las pausas de descanso; y a Luis T., Barri, Carlos, Alberto M., Ana Carolina y Rafa, por su buen humor.

De igual modo, también los técnicos merecen una mención especial por su contribución a este trabajo. En particular, muchas gracias a Laura, por enseñarme los entresijos del equipo del que ha nacido gran parte de este trabajo, por su ayuda inestimable y su constante disponibilidad; a Isabel, por su sonrisa permanente, su inagotable interés y su constante disposición; a Rodrigo, por su interminable paciencia y responsabilidad, por su capacidad didáctica, y por compartir afición por la canasta; y a Alfonso, por su carácter ingenioso, su esfuerzo titánico, y por ayudarme a dar los primeros pasos delante del microscopio. También, gracias a Teo, Rubén, Gala, Carlos C., Ana, José Luis y Marta, por su ayuda y eficacia; y a Guillermo, Carlos M., Marten y Laura C. por contribuir a crear buen ambiente en el trabajo y las comidas.

También querría agradecer a aquellas personas que se han involucrado en la planificación de las tareas docentes. En concreto, José Ignacio Arnaudas, Antonio Badía, Gerardo Goya, Fernando López-Tejeira y María Luisa Ramón, mostrando su interés y ayudándome en la gestión y el buen quehacer relativo a la colaboración docente.

Asimismo, quiero acordarme de los colaboradores externos, cuyo trabajo también ha complementado el hilo conductor de esta tesis. En particular, gracias a Amalio Fernández-Pacheco, Dédalo Sanz, Luis Alfredo Rodríguez, Agustina Asenjo, Miriam Jaafar, Eider Berganza, Francesc Pérez-Murano, Matteo Lorenzoni, Christophe Gatel, Etienne Snoeck, Ingrid-Marie Andersen y Olivier Fruchart.

I would also like to thank Dr. Harald Plank, Dr. Robert Winkler and Dr. Ferdinand Hofer for hosting me during 3 months at the FELMI-ZFE. It was a nice professional and personal experience, and I have very fond memories of my research stay in Graz. Thanks Jürgen, Judith, Robert K., Conny, David, Georg, Harald F., Daniel, Martina, Angi, Manfred, Lukas, Ruth, Steffi, Krisztina and Claudia for your generous hospitality and kindness. I really had a great time in Austria with all of you.

También quiero acordarme de todos los amigos del pueblo que se han interesado por mí y por este trabajo. En especial, muchas gracias a Jorge, Alberto, Alba y Arancha por su preocupación, curiosidad y ánimo.

No quiero olvidarme del personal de administración: Raúl, Mercedes, Mari Carmen, María Jesús G., Juan y María Jesús C., cuya tarea es parte fundamental para el buen funcionamiento del centro. Gracias también a Susana por su ayuda informática.

Finally, I would like to thank the jury members for the time spent reading this thesis.

Acronyms

ADF: Annular Dark Field
AFM: Atomic Force Microscopy
AMR: Anisotropy Magnetoresistance
ARAGON: ARchitectural Adjustment by Grid Overlay Nanotechnology
BCC: Body-Centered-Cubic
BF: Bright Field
BSE: Backscattered Electrons
CBED: Convergent Beam Electron Diffraction
CCD: Charge-Coupled Device
CEMES: Centre d'Élaboration de Matériaux et d'Etudes Structurales
CNRS: Centre National de la Recherche Scientifique
CSIC: Consejo Superior de Investigaciones Científicas
CVT: Chemical Vapor Transport
DF: Dark Field
DMI: Dzyaloshinskii-Moriya Interaction
EBL: Electron Beam Lithography
EDS: Energy-Dispersive X-ray Spectroscopy
EELS: Electron Energy Loss Spectroscopy
EFTEM: Energy Filtered Transmission Electron Microscopy
EH: Electron Holography
ETD: Everhart Thornley Detector
FCC: Face-Centered-Cubic
FEBID: Focused Electron Beam Induced Deposition
FELMI-ZFE: Institut für Elektronenmikroskopie und Nanoanalytik - Zentrum für
                   Elektronenmikroskopie
FFT: Fast Fourier Transform
FIB: Focused Ion Beam
FIBID: Focused Ion Beam Induced Deposition
FSE: Forward-Scattered Electrons
FWHM: Full Width at Half Maximum
GB: Grain Boundary
GIF: Gatan Imaging Filter
GIS: Gas Injector System
GMR: Giant Magnetoresistance
GPA: Geometrical Phase Analysis

HAADF:	High-Angle Annular Dark Field
HCP:	Hexagonal-Closest-Packed
HRTEM:	High Resolution Transmission Electron Microscopy
IBE:	Ion Beam Etching
ICE:	Ion-Conversion and Electron
ICMA:	Instituto de Ciencia de Materiales de Aragón
ICMM:	Instituto de Ciencia de Materiales de Madrid
ICT:	Information and Communications Technology
INA:	Instituto de Nanociencia de Aragón
IP:	In-Plane
LACBED:	Large Angle Convergent Beam Electron Diffraction
LMA:	Laboratorio de Microscopías Avanzadas
LMI:	Liquid Metal Ion
MEMS:	Micro-Electro-Mechanical Systems
MFM:	Magnetic Force Microscopy
MOKE:	Magneto-Optical Kerr Effect
MRAM:	Magnetoresistive Random-Access Memory
MTJ:	Magnetic Tunnel Junction
OOMMF:	Object Oriented MicroMagnetic Framework
OOP:	Out-Of-Plane
PEEM:	PhotoEmission Electron Microscopy
ReRAM:	Resistive Random-Access Memory
SAED:	Selective Area Electron Diffraction
SE:	Secondary Electrons
SEM:	Scanning Electron Microscopy
S-FEG:	Schottky Field Emission Gun
SQUID:	Superconducting Quantum Interference Device
STEM:	Scanning Transmission Electron Microscopy
STO:	Strontium Titanium Oxide
TEM:	Transmission Electron Microscopy
TLD:	Through Lens Detector
TMR:	Tunnel Magnetoresistance
UV:	Ultraviolet
VLS:	Vapor-Liquid-Solid
VS:	Vapor-Solid
XMCD:	X-ray Magnetic Circular Dichroism
YBCO:	Yttrium Barium Copper Oxide

Abstract

Magnetic nanostructured materials attract particularly keen interest because of their possibilities to be implemented in future spintronic devices [1]. Specifically, ferromagnetic nanowires and nanotubes are potential candidates for fast and low-power domain wall conduit used for storing and handling information. In this regard, one of the most versatile and promising techniques for the fabrication of these nanostructures is Focused Electron Beam Induced Deposition (FEBID) [2]. As has been customary for more than 35 years, mainly two-dimensional (2D) deposits have been fabricated by this method. However, to meet the new market requirements for the development of more energy-efficient devices, advanced three-dimensional (3D) magnetic nano-objects emerge as extraordinarily promising structures for applications in magnetic data storage, logic and sensing.

This document includes different approaches for the tuning of dimensional, compositional and magnetic properties of 3D ferromagnetic nanowires. In this context, the new ARchitectural Adjustment by Grid Overlay Nanotechnology (ARAGON) Chip represents a step forward in the fabrication of tailored functional nanowires by FEBID on insulating substrates, which had been unattainable due to the impossible charge dissipation. This consists of an electrically-biased patterned metal structure which allows the growth and the *in situ* modulation of the nanowire geometry.

Although many efforts have been carried out to improve the properties of 2D deposits [3], scarce investigations have been performed in 3D nanostructures. In this light, the nanofabrication of 3D Co and Fe nanowires by FEBID and the subsequent *ex situ* and *in situ* post-growth annealing treatments have been explored for the first time [4][5]. High Resolution Transmission Electron Microscopy (HRTEM) imaging, Electron Energy Loss Spectroscopy (EELS) in Scanning Transmission Electron Microscopy (STEM) mode and Electron Holography (EH) have been used to monitor the structural,

chemical and magnetic alterations at each annealing temperature. The metallic composition increases with the temperature up to ~95% at., a recrystallization of the standard nanocrystalline as-deposited structure into large monocrystals, whose size is comparable to the nanowire diameter, is produced and the average net magnetic induction increases dramatically to values very close to the bulk one. This achievement opens new paths for the fabrication of either individual or arrays of 3D nanowires with high purity and crystallinity based on other materials, obtaining nanostructures which could be used for future applications.

On the other hand, the combination of more than one material by FEBID can give rise to new functionalities. On this basis, nanoscale heterostructured materials in the form of 3D core-shell nanowires have been developed [6]. This new approach has been applied to synthesize standing nanowires with ferromagnetic cores of Co or Fe coated with a protective Pt-C shell. This architecture aims at minimizing the degradation of magnetic properties caused by the natural surface oxidation of the core to a non-ferromagnetic material. This is a key issue in such thin ferromagnetic objects with a high surface-to-volume ratio. The structure and chemistry of the nanowires have been characterized in Pt-C-coated and uncoated nanostructures, revealing that the surface oxidation is suppressed from the magnetic cores and confined to the Pt-C layer, while keeping the cylindrical shape. The magnetic characterization has demonstrated that the average magnetization of the coated cores is strengthened up to 30% in the thinnest nanowires (~40-nm-thick cores) with respect to the unprotected ones.

Based on the method developed to grow 3D core-shell nanostructures by this fabrication technology, the growth and characterization of 3D ferromagnetic Co nanotubes have been performed. The heterostructured materials are composed by a 3D Pt-C nanowire acting as a core, and a Co coating forming the shell and the nanotube architecture. TEM experiments on a cross section have shown cores thinner than 100 nm and shells down to ~11 nm in thickness. The magnetic characterization performed by EH

and Magneto-Optical Kerr Effect (MOKE) magnetometry demonstrates their ferromagnetic behaviour, and micromagnetic simulations were carried out to understand the domain wall dynamics. These results prove that these nanostructures provide great functionality with potential application in the performance of magnetic devices.

In the past, a direct use of FEBID was the growth of magnetic tips of width around 50 nm with potential application in Magnetic Force Microscopy (MFM) [7]. In order to show that FEBID tips are superior than standard MFM tips and can lead to the next-generation of commercial MFM tips, dedicated experiments for the growth of vertical Co and Fe nanowires have been carried out. Here, the optimization of the MFM tips grown by FEBID and a comparison of their behaviour to that of standard MFM tips have been assessed. The tips have been tested in MFM experiments, in ambient conditions as well as in liquid environment, behaving appropriately in terms of mechanical stability, resolution and sensitivity [8]. Indeed, it has been demonstrated that Fe tips with 34 nm in diameter and a 7 nm-wide sharp end can be fabricated to achieve very high resolution as well as relatively low sample-tip magnetic interaction to minimize the influence of the magnetic tip on the magnetic state of small structures such as skyrmions. The Fe content is found to decrease as the tip end is approached, which influences the magnetization value and the magnetic stray fields generated around the tip end. This is the first step towards the research on quantitative MFM measurements.

Finally, taking advantage of the versatility of the FEBID technique, 3D Pt-C-coated Co nanowires with a shape-controlled structure have also been fabricated. This architecture consists of forming bends along the height (pinning sites), where domain walls can be located and obtained at remanence after saturating the magnetization with an applied magnetic field in the appropriate direction [9]. Therefore, the growth of complex architectures by FEBID opens new prospects for the development of novel magnetic devices.

References

[1]   A. Fernández-Pacheco, L. Serrano-Ramón, J. M. Michalik, M. R. Ibarra, J. M. De Teresa, L. O'Brien, D. Petit, J. Lee and R. P. Cowburn, "Three dimensional magnetic nanowires grown by focused electron-beam induced deposition", *Sci. Rep.* **3**, 1492 (2013).

[2]   J. Pablo-Navarro, D. Sanz-Hernández, C. Magén, A. Fernández-Pacheco and J. M. De Teresa, "Tuning shape, composition and magnetization of 3D cobalt nanowires grown by focused electron beam induced deposition (FEBID)", *J. Phys. D: Appl. Phys.* **50**, 18LT01 (2017).

[3]   M. V. Puydinger dos Santos, M. F. Velo, R. D. Domingos, Y. Zhang, X. Maeder, C. Guerra-Nuñez, J. P. Best, F. Béron, K. R. Pirota, S. Moshkalev, J. A. Diniz and I. Utke, "Annealing-Based Electrical Tuning of Cobalt-Carbon Deposits Grown by Focused Electron-Beam-Induced Deposition", *ACS Appl. Mater. Interfaces* **8**, 32496 (2016).

[4]   J. Pablo-Navarro, C. Magén and J. M. De Teresa, "Purified and Crystalline Three-Dimensional Electron-Beam-Induced Deposits: The Successful Case of Cobalt for High-Performance Magnetic Nanowires", *ACS Appl. Nano Mater.* **1**, 38 (2018).

[5]   J. Pablo-Navarro, R. Winkler, G. Haberfehlner, C. Magén, H. Plank and J. M. De Teresa, "*In situ* real time annealing of ultrathin vertical Fe nanowires grown by focused electron beam induced deposition", *Acta Materialia* **174**, 379 (2019).

[6]   J. Pablo-Navarro, C. Magén and J. M. De Teresa, "Three-dimensional core-shell ferromagnetic nanowires grown by focused electron beam induced deposition", *Nanotechnology* **27**, 285302 (2016).

[7]   M. Gavagnin, H. D. Wanzenboeck, S. Wachter, M. M. Shawrav, A. Persson, K. Gunnarsson, P. Svedlindh, M. Stöger-Pollach and E. Bertagnolli, "Free-Standing Magnetic Nanopillars for 3D Nanomagnet Logic", *ACS Appl. Mater. Interfaces* **6**, 20254 (2014).

[8]   M. Jaafar, J. M. De Teresa, A. Asenjo, J. Pablo-Navarro, P. Ares, C. Magén and J. Gómez-Herrero, "System for an Atomic Force Microscope". Spanish *OEPM P201731292* (2017) and International patent *PCT/ES2018/070709* (2018).

[9]   A. Wartelle, J. Pablo-Navarro, M. Staňo, S. Bochmann, S. Pairis, M. Rioult, C. Thirion, R. Belkhou, J. M. De Teresa, C. Magén and O. Fruchart, "Transmission XMCD-PEEM imaging of an engineered vertical FEBID cobalt nanowire with a domain wall", *Nanotechnology* **29**, 045704 (2018).

Resumen

Los materiales magnéticos nanoestructurados atraen un interés particular debido a la posibilidad de ser implementados en futuros dispositivos espintrónicos [1]. Específicamente, los nanohilos y nanotubos ferromagnéticos son candidatos potenciales para ser utilizados como vehículos excelentes para las paredes de dominio, usadas para almacenamiento y procesamiento de información. En este sentido, una de las técnicas más versátiles y prometedoras para la fabricación de estas nanoestructuras es la deposición inducida por haz de electrones focalizado (FEBID) [2]. Como viene siendo habitual desde hace más de 35 años, mediante esta técnica se han fabricado fundamentalmente depósitos en dos dimensiones (2D). Sin embargo, para dar respuesta a las exigencias del mercado actual con relación al desarrollo de dispositivos más eficientes energéticamente, los nano-objetos magnéticos avanzados en tres dimensiones (3D) se erigen como estructuras sumamente prometedoras para aplicaciones en almacenamiento, detección y lógica magnéticos.

Esta tesis incluye diferentes estrategias para controlar las propiedades dimensionales, composicionales y magnéticas de nanohilos 3D ferromagnéticos. En este contexto, un nuevo método cimentado en un chip nanotecnológico basado en una cuadrícula superpuesta para modificaciones estructurales (ARAGON) representa un paso adelante en la fabricación de nanohilos funcionales diseñados por FEBID sobre sustratos aislantes, lo cual había sido inalcanzable debido a la imposibilidad de la disipación de carga eléctrica durante el crecimiento. Esta estrategia consiste en una estructura metálica sometida a una diferencia de potencial que permite la fabricación y la modulación *in situ* de la geometría del nanohilo.

A pesar de que se han llevado a cabo muchos esfuerzos para mejorar las propiedades de los depósitos 2D [3], escasas investigaciones se han realizado con relación a las nanoestructuras 3D. Desde este punto de vista, se ha explorado por primera vez la

nanofabricación de nanohilos 3D de Co y Fe crecidos por FEBID y los posteriores tratamientos térmicos *ex situ* e *in situ* [4][5]. Para monitorizar los cambios estructurales, químicos y magnéticos en cada temperatura, se ha utilizado microscopía electrónica de transmisión de alta resolución (HRTEM), espectroscopía por pérdida de energía de los electrones (EELS) usando el modo de microscopía electrónica de transmisión por barrido (STEM), y holografía electrónica (EH). En particular, la composición metálica incrementa con la temperatura hasta ~95% at., se produce la recristalización de la estructura nanocristalina inicial en grandes monocristales cuyo tamaño es comparable al diámetro del nanohilo, y la inducción magnética media neta aumenta significativamente hasta valores muy próximos al del material masivo. Estos resultados abren nuevos caminos hacia la fabricación de nanohilos 3D individuales o en serie, con gran pureza y cristalinidad, basados en otro tipo de materiales, obteniendo nanoestructuras que podrían ser utilizadas para futuras aplicaciones.

Por otro lado, la combinación de más de un material por FEBID puede dar lugar a nuevas funcionalidades. Por ello, se han desarrollado materiales heteroestructurados en forma de nanohilos 3D con un núcleo y un recubrimiento [6]. Esta nueva estrategia ha sido aplicada para sintetizar nanohilos verticales con núcleos ferromagnéticos de Co o Fe recubiertos de una capa protectora de Pt-C. Esta arquitectura tiene como objetivo minimizar la degradación de las propiedades magnéticas debido a la oxidación superficial natural del núcleo, convirtiendo esta capa externa en un material no ferromagnético. Esto es una cuestión clave en objetos ferromagnéticos estrechos con un cociente superficie/volumen alto. Las propiedades estructurales y químicas de los nanohilos han sido caracterizadas en nanoestructuras sin recubrir y recubiertas con Pt-C, mostrando que la oxidación superficial se suprime de los núcleos magnéticos y es confinada en la capa de Pt-C, al mismo tiempo que se conserva su forma cilíndrica. La caracterización magnética ha demostrado que la inducción magnética media de los nanohilos recubiertos

aumenta hasta un 30% en el caso de los nanohilos más estrechos (diámetros de ~40 nm) con respecto a los núcleos sin recubrir.

Basándonos en este método para el crecimiento de nanoestructuras 3D con un núcleo y un recubrimiento mediante esta tecnología de fabricación, se ha llevado a cabo la síntesis y caracterización de nanotubos ferromagnéticos 3D de Co. En este caso, la heteroestructura está compuesto por un nanohilo 3D de Pt-C actuando como núcleo, y un revestimiento de Co formando el recubrimiento y la arquitectura del nanotubo. Los experimentos de TEM sobre una sección transversal muy delgada han mostrado núcleos con diámetros menores de 100 nm y recubrimientos que se reducen hasta ~11 nm de espesor. La caracterización magnética realizada mediante EH y magnetometría de efecto Kerr magneto-óptico (MOKE) demuestra su comportamiento ferromagnético. Asimismo, se han llevado a cabo simulaciones micromagnéticas para comprender la dinámica de las paredes de dominio. Estos resultados prueban que estas nanoestructuras ofrecen gran funcionalidad con potenciales aplicaciones en dispositivos magnéticos.

En el pasado, un uso directo de la técnica FEBID consistía en el crecimiento de puntas magnéticas con diámetros de alrededor de 50 nm con posibles aplicaciones en microscopía de fuerza magnética (MFM) [7]. Para demostrar que las puntas crecidas por FEBID son superiores a las puntas MFM estándar, y que pueden dar lugar a la siguiente generación de puntas MFM comerciales, se han realizado experimentos destinados al crecimiento de nanohilos verticales de Co y Fe. Se ha evaluado la optimización de las puntas MFM crecidas por FEBID y se ha realizado una comparación de su comportamiento con respecto a las puntas MFM estándar. Las puntas han sido analizadas en experimentos MFM, tanto en condiciones ambientales como en entorno líquido, comportándose apropiadamente en términos de estabilidad mecánica, resolución y sensibilidad [8]. Se ha demostrado que las puntas de Fe de 34 nm de diámetro con un diámetro final de 7 nm en el extremo pueden ser fabricadas para conseguir tanto alta resolución como una interacción magnética muestra-punta relativamente baja que

minimice la influencia de la punta magnética sobre el estado magnético de estructuras pequeñas tales como skyrmiones. Además, se ha detectado que el contenido de Fe decrece cuando la distancia a la punta se reduce, lo cual tiene efectos sobre los valores de la inducción magnética y los campos de fuga generados en las proximidades de la punta. Este es el primer paso hacia la investigación destinada a medidas de MFM cuantitativo.

Finalmente, aprovechando la versatilidad de la técnica FEBID, también se han fabricado nanohilos 3D de Co recubiertos con Pt-C con una morfología distinta a la de un pilar. Esta arquitectura consiste en formar curvaturas a lo largo de la longitud del nanohilo (sitios de anclaje), donde las paredes de dominio pueden estar localizadas, obteniéndose después de saturar la magnetización con un campo magnético aplicado en la dirección apropiada [9]. Por lo tanto, el crecimiento de arquitecturas 3D complejas por FEBID abre nuevas perspectivas para el desarrollo de novedosos dispositivos magnéticos.

Referencias

[1]   A. Fernández-Pacheco, L. Serrano-Ramón, J. M. Michalik, M. R. Ibarra, J. M. De Teresa, L. O'Brien, D. Petit, J. Lee and R. P. Cowburn, "Three dimensional magnetic nanowires grown by focused electron-beam induced deposition", *Sci. Rep.* **3**, 1492 (2013).

[2]   J. Pablo-Navarro, D. Sanz-Hernández, C. Magén, A. Fernández-Pacheco and J. M. De Teresa, "Tuning shape, composition and magnetization of 3D cobalt nanowires grown by focused electron beam induced deposition (FEBID)", *J. Phys. D: Appl. Phys.* **50**, 18LT01 (2017).

[3]   M. V. Puydinger dos Santos, M. F. Velo, R. D. Domingos, Y. Zhang, X. Maeder, C. Guerra-Nuñez, J. P. Best, F. Béron, K. R. Pirota, S. Moshkalev, J. A. Diniz and I. Utke, "Annealing-Based Electrical Tuning of Cobalt-Carbon Deposits Grown by Focused Electron-Beam-Induced Deposition", *ACS Appl. Mater. Interfaces* **8**, 32496 (2016).

[4]   J. Pablo-Navarro, C. Magén and J. M. De Teresa, "Purified and Crystalline Three-

Dimensional Electron-Beam-Induced Deposits: The Successful Case of Cobalt for High-Performance Magnetic Nanowires", *ACS Appl. Nano Mater.* **1**, 38 (2018).

[5]   J. Pablo-Navarro, R. Winkler, G. Haberfehlner, C. Magén, H. Plank and J. M. De Teresa, "*In situ* real time annealing of ultrathin vertical Fe nanowires grown by focused electron beam induced deposition", *Acta Materialia* **174**, 379 (2019).

[6]   J. Pablo-Navarro, C. Magén and J. M. De Teresa, "Three-dimensional core-shell ferromagnetic nanowires grown by focused electron beam induced deposition", *Nanotechnology* **27**, 285302 (2016).

[7]   M. Gavagnin, H. D. Wanzenboeck, S. Wachter, M. M. Shawrav, A. Persson, K. Gunnarsson, P. Svedlindh, M. Stöger-Pollach and E. Bertagnolli, "Free-Standing Magnetic Nanopillars for 3D Nanomagnet Logic", *ACS Appl. Mater. Interfaces* **6**, 20254 (2014).

[8]   M. Jaafar, J. M. De Teresa, A. Asenjo, J. Pablo-Navarro, P. Ares, C. Magén and J. Gómez-Herrero, "System for an Atomic Force Microscope". Spanish *OEPM P201731292* (2017) and International patent *PCT/ES2018/070709* (2018).

[9]   A. Wartelle, J. Pablo-Navarro, M. Staňo, S. Bochmann, S. Pairis, M. Rioult, C. Thirion, R. Belkhou, J. M. De Teresa, C. Magén and O. Fruchart, "Transmission XMCD-PEEM imaging of an engineered vertical FEBID cobalt nanowire with a domain wall", *Nanotechnology* **29**, 045704 (2018).

Chapter 1: Introduction

The first chapter is devoted to presenting the fundamentals and wide variety of applications of magnetic nanowires in Nanotechnology, and the opportunities opened for Focused Electron Beam Induced Deposition (FEBID) in this field. Special attention is paid to overview the state-of-the-art of the current technologies for the growth of such nano-objects. In this regard, FEBID technique emerges as a complementary technique to the existing fabrication methods for its versatility and high lateral resolution.

1.1 Nanotechnology

Nanoscience and Nanotechnology are multidisciplinary interconnected areas devoted to the synthesis, study and technological application of materials with at least one dimension between 1 and 100 nm in size. This expanded field of study covers many different areas such as physics, chemistry, materials science, engineering, biology or medicine, which converge in a constant movement forward towards the understanding of the physical phenomena at the nanoscale.

The keystone lies in the radically distinct properties between the macroscopic and nanoscopic scale materials. The dimensional reduction makes the systems to behave in a different way, often exhibiting new or unexpected properties. Thus, the study of nanostructures allows finding new functionalities and opens up the opportunity to develop novel applications.

This new field was heralded by R. Feynman on 29th December 1959, at the Annual Meeting of the American Physical Society in the California Institute of Technology. In his lecture entitled "*There's plenty of room at the bottom*", a wide range of applications was suggested to emerge in the following years, considering the miniaturization as the way forward [1]. Since then, research at the nanoscale has made an outstanding progress, confirming the encouraging predictions, and providing new applications. Some of these applications have occurred in Nanoelectronics and Information and Communications Technology (ICT) with advanced memory, logic and sensing devices, in the field of Energy with the development of efficient solar cells and high performance batteries, and in Medicine and Biotechnology with the use of magnetic nanoparticles as contrast agents for cancer treatments. The broad social impact of all these achievements, probably unprecedented since the Second Industrial Revolution, represents an undisputed global transformation which is bound to continue in future decades.
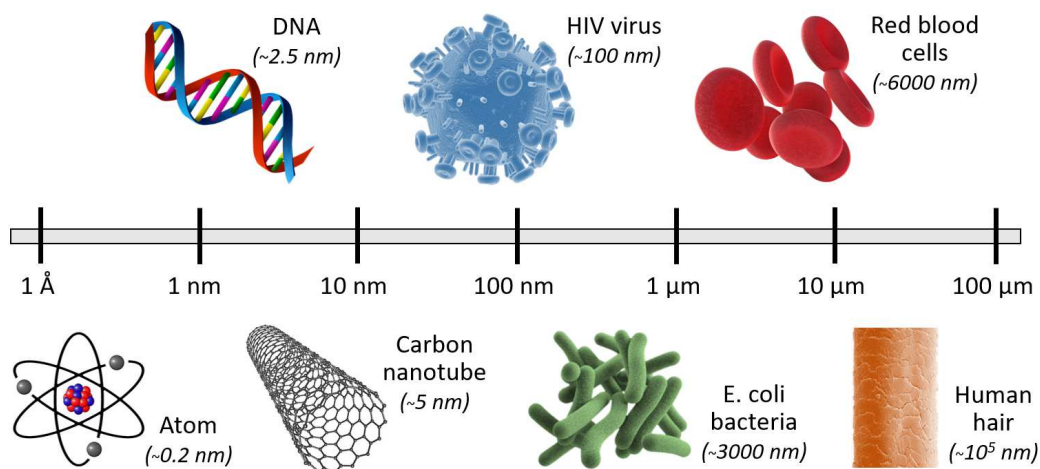
Figure 1.1. Illustration for the comparison of different elements with the nanometric scale.

Over the course of the recent history, the production and exploration of different types of nanomaterials (metallic, magnetic, insulating, superconducting, semiconductor, etc.) and their combinations have been the key focus for part of the scientific community. Specially, increased attention has been given to the basic science research with the hope of gaining greater understanding of the effects arisen at the nanometric scale and exploiting these new phenomena for numerous technological applications.

Among the great number of nano-objects which can be investigated, nanowires are one of the most interesting nanostructures due to their fundamental properties and potential applications. This includes semiconductor nanowires with outstanding electronic and optoelectronic properties due to the quantum confinement effect [2], metallic nanowires with prominent conductive and plasmonic performance and reliability [3], superconducting nanowires with ultrafast electron relaxation times and high operating temperatures ideal for photon detectors [4], carbon nanowires with promising electronic applications [5] or magnetic nanowires with the possibility of developing two dimensional (2D) and three-dimensional (3D) architectures (e.g., modulated in diameter, segmented with different compositions, etc.) and designing high-density devices [6].

In particular, magnetic nanowires deserve special attention. Several studies have been devoted to exploring and analysing their extraordinary properties: high anisotropy [7], diverse magnetization configurations [8], coercivity tuning and magnetization switching mechanisms, the presence of different types of domain walls (e.g. transverse-vortex walls [9], Bloch-point walls [10][11], etc.) and transformations between them [12], the influence of the domain wall width [13], the control of pinning sites [14], or the domain wall nucleation and propagation processes in the framework of the magnetization dynamics [15][16][17]. All these characteristics give the magnetic nanowires a strong potential for developing systems such as domain wall-based devices, with the capacity to move the domain walls under magnetic fields or spin-polarized currents.

With the aim of highlighting the importance of this type of nanostructure, especially the case of magnetic nanowires, the next sections will be devoted to presenting some of their specific applications.

1.2 Nanoelectronics

The capability to merge specific fields of nanoscience engenders new and exciting research areas. For instance, the crossover with the study of electron properties gives rise to nanoelectronics [18], where the electronic control is investigated with the goal of presenting nanodevices with improved properties. The prime example is the research on transistors, which has been successful in stimulating strong interest in the industry because of its promising prospects. Their great contributions have left a mark in the electronic systems based on chips, which are still under constant upgrades and refinements [19][20].

The size of the transistors determines the chip performance in terms of speed and efficiency. In this way, the smaller the transistor, the higher the density in a single chip and the better the computational performance. There have been continuous and successful efforts on downscaling to improve the information processing and memory devices.

Indeed, this gradual miniaturization was suggested by G. Moore in 1965, who proposed that the number of transistors per unit area would double every year as it had happened at that time [20]. Although this statement was not totally accurate, the Moore's law pointed in the right direction since the number of transistors which could set on a chip have been doubled roughly every two years. In the transistor manufacturing, the gate length has been progressively reduced according to the International Roadmap for Devices and Systems. Currently, the 5-nm-node technology has arrived on the market of the semiconductor industry following the predicted trend for 2019, and shorter transistor lengths are estimated for the coming years. However, the size of this technology is reaching the scale limits for the fabrication of circuit electronic components and new difficulties arise and need to be addressed, such as the heat dissipation —related to the energy efficiency and the durability of the chips— produced by a higher transistor packing density, and the quantum instability challenge when approaching the tunnelling regime.
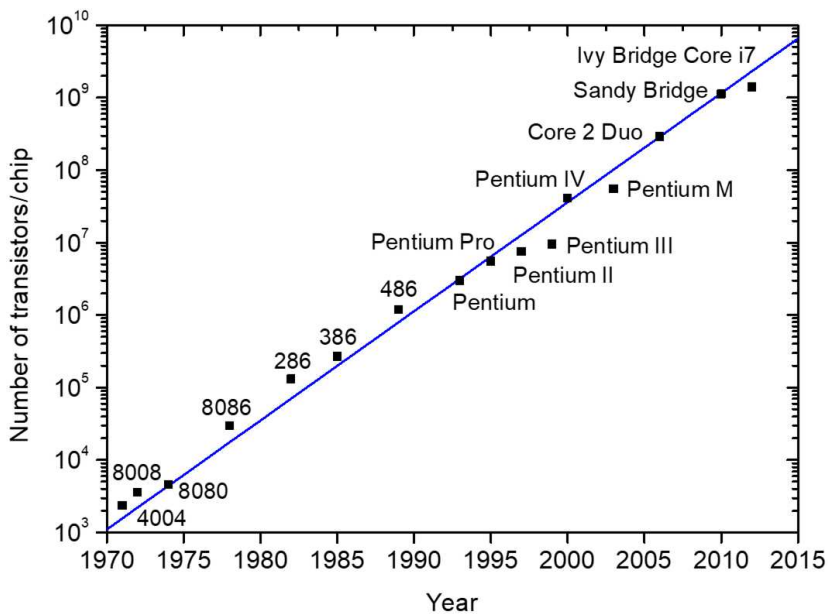
Figure 1.2. Number of transistors per chip in Intel microprocessors as a function of time.

In overcome these impending limitations, the miniaturization engineering, which has been leading the enhancement of the chips performance to the present, must be driven by new strategies and paradigms [21]. One of the possibilities is the "More Moore" approach, based on better system designs using the same electronic components. The second one, founded on the incorporation of new functionalities and the expansion to 3D architectures of current semiconductor technology, is called the "More than Moore" strategy. In this case, non-digital and non-electronic data (optical, mechanical, thermal, etc.) are combined with digital information in a single device, without the need of following the traditional scale reduction pace of the digital components. As a result, these strategic plans could bring about positive advances in nanoelectronics and lead to the development of a broad diversity of applications [22].

1.2.1 Non-volatile resistive memory

One of the best examples in line with the arguments set out previously is the non-volatile resistive memory. Within the sphere of nanoelectronics, it should be highlighted that the current flash memory technology is encountering downscaling restrictions, so research on the density and performance increase of the non-volatile memories stands as an urgent challenge to work in [23][24].

One possible alternative is the resistive random access memory (ReRAM), taking advantage of a high-speed resistive switching mechanism in metal/insulator/metal structures [25]. This system is characterized by ultra-small conducting filaments (~1-10 nm in diameter), which appear in the oxide insulating layer due to the electrical breakdown phenomenon when an electric field above a certain threshold is applied between the two metal electrodes. Thus, these filaments are responsible for modifying the transport properties of the capacitor at the nanoscale [26]. Since the work reported on NiO nanowires in 2008 [27], several experiments have been performed in order to improve the resistive switching behaviour by increasing the endurance and stability [28]

or reducing the operating voltage of the device [29]. In addition, novel approaches have been reported for the integration of these nanowires into memory devices such as the crossbar array methodology including metal-oxide core-shell nanowire heterostructures [30].

An impressive application of these nanowires stems from the possibility of fabricating flexible electronic circuits, which can be portable and wearable. As a result, the oxide nanowires are promising candidates to be incorporated in electronic devices for tracking human health parameters where the data could be stored [31].
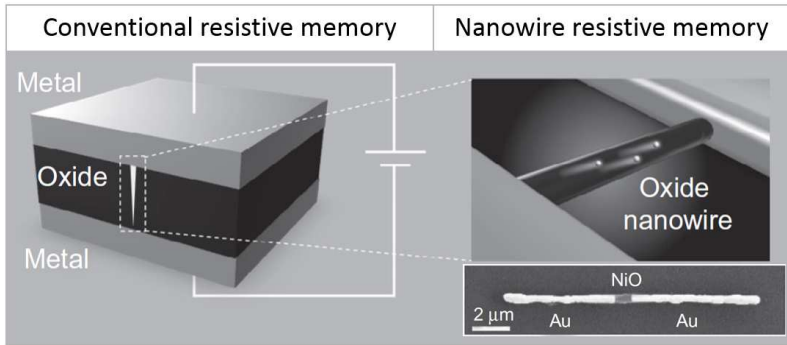
Figure 1.3. Schematic image of a conventional resistive memory and a nanowire one based on a metal-oxide-metal heterostructure. A Scanning Electron Microscopy (SEM) image of a Au-NiO-Au nanowire is shown to illustrate the real system [32].

1.3 Spintronics

The manipulation of the electron spin as well as the electron charge in solid state systems is the fundamental basis of spintronics. In order to unlock and take full advantage of this potential, the understanding of the interplay between the spin and its environment becomes crucial [33].

Encompassing the knowledge originated from the combination between the spin-dependent transport phenomena and electronics, several applications have been developed [34]. In particular, the use of ferromagnetic materials, where the electrical resistance depends on the electron current spin polarization, have given rise to remarkable

milestones. The first great example is the concept of magnetoresistive read head magnetic recording in 1971, based on the anisotropy magnetoresistance (AMR) [35], and its commercialization some years later [36]. Additionally, the discovery of the tunnel magnetoresistance (TMR) in 1975 brought an unprecedented evolution, establishing the basis of the non-volatile magnetoresistive random-access memory (MRAM) [37]. However, the finding of the giant magnetoresistance (GMR) in 1988 by A. Fert and P. Grünberg is considered as the main achievement in this field. This accomplishment deserves a special mention because it catapulted spintronics and the production of novel read heads for hard disks drives by IBM since 1997. The GMR effect has turned into a practical and real nanoscale device for widespread applications [38][39].

These breakthroughs stimulated new perspectives on the interplay between electron transport and magnetic properties, prompting the investigation of novel effects emanating from the spin-charge currents interaction, including switching mechanisms of the magnetic moments [40], such as the spin transfer torque phenomenon. Specifically, magnetic nanowires are ideal scaffolds where many of these phenomena can take place.

1.3.1 Magnetic domain walls

Magnetic domain walls can be defined as nano-objects which separate regions of different magnetization orientation, minimizing the magnetostatic energy. The balance between this energy, the magnetic anisotropy and the exchange energy determines their formation and nature. The study of these nanoscale transition areas as a tool to compute binary information in integrated magnetic circuits is a major step. Domain wall conduit can be achieved by the application of external magnetic fields or currents [41][42], and the control of this process in magnetic nanostructures, such as nanowires, attracts particularly keen interest because of their possible application in storage [43], memory [44] and logic devices [45]. Especially, the high domain wall velocities present in circular magnetic nanowires, the potential suppression of the Walker breakdown phenomenon or

the emergence of new types of domain walls such as curling states or Bloch points are characteristics which make them special architectures.

The capability to move magnetic domain walls in magnetic tracks, e.g. nanowires, particularly by spin transfer torque using spin-polarized electrical currents, opens new outlooks considering the storage track memory as the promising candidate [46]. In this case, the information storage unit (the bit) is the domain wall, rather than the magnetic domain itself in the conventional hard disks. The fast processing time of the semiconductor integrated circuits (CMOS) is conserved with no mechanical movement of the components. In addition, the configuration of the domain wall sequence can be very versatile, presenting 2D straight, bent or loop shapes. The ultimate geometry would be 3D magnetic tracks, as introduced by S. S. P. Parkin in 2008, which would definitely boost the storage areal density to compete with existing technologies [44].

1.3.2 Racetrack memory concept

The concept of the racetrack memory, represented in Figure 1.4, is composed by a magnetic track with a sequence of domain walls and two heads devoted to writing and reading data. The write head can use different strategies to generate a domain wall, such as an Oersted line, or the magnetic tunnel junction (MTJ) architecture as the read head does [47]. In this case, an insulating barrier separates two ferromagnetic layers whose magnetization is fixed in one layer and changeable in the other one [48]. This enables two different magnetic configurations (parallel or antiparallel) with different tunnel resistance, building the logic configuration. In practice, a spin-polarized current induces the domain wall motion along the magnetic structure (shifting), the write head switches the magnetization locally, nucleating domain walls (writing) which get pinned (storing) and the read head detects the magnetization direction (reading).
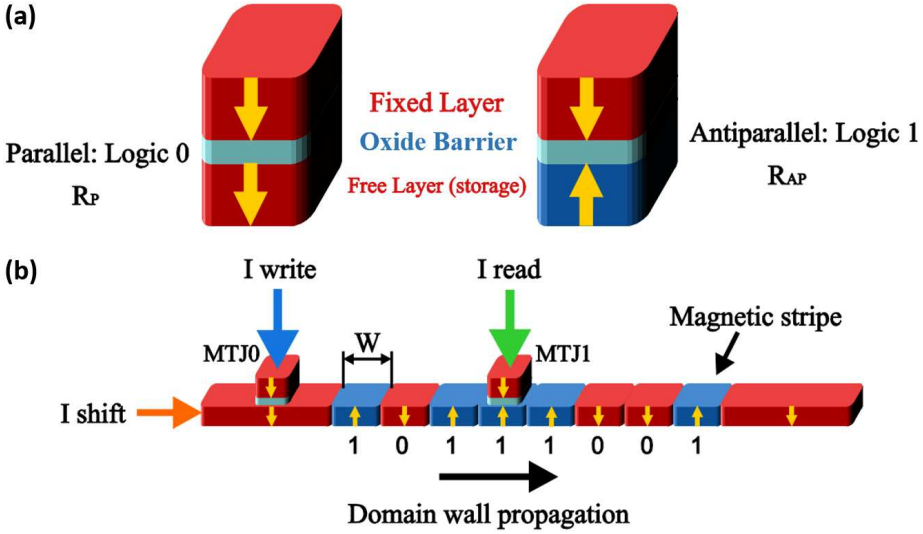
Figure 1.4. (a) Composition of the magnetic tunnel junction with the two possible configurations used in the write and read heads. (b) Schematic diagram of a racetrack memory concept [47].

The domain wall displacement is typically driven by spin-transfer-torque as a result of the spin-polarized currents injected into the ferromagnet. In the last decade, wall velocities up to 150 m/s using current densities above 100 MA/cm^2 have been reached by a lateral current injection [49]. The speed was enhanced by introducing a metallic layer with strong spin-orbit coupling under the ferromagnetic track, but keeping the high current densities [50]. Recently, in order to look for low-power-consumption devices, displacement at 500 m/s under 6 MA/cm^2 have been proven by the vertical injection of spin currents [51]. This evidences that continuous improvements are still promoting the refinement of devices within the ICT field.

1.4 Further applications of magnetic nanowires

The non-volatile resistive memory and the racetrack memory previously presented are two special examples that show the usefulness of nanowires in nanoelectronics and spintronics. Despite its straightforward geometry, this structure with high aspect and

surface-to-volume ratios has clear potential for a wide range of applications in diverse fields and, particularly in Nanomagnetism [52][53], magnetic nanowires exhibit exciting properties to be implemented in magnetic devices.

Hereafter, the discussion will be focused on 3D magnetic nanowires since this specific architecture constitutes the central topic of this thesis. In this section, a general overview of their applications as building block for functional devices is given [32].

1.4.1 Spincaloritronics

The driving of the magnetic moment through spin-polarized currents has been extensively studied in magnetic nanostructures such as wires containing domain walls [54] or vertical multi-layered nanowires [55]. Going one step further, the interaction between spin currents and heat currents can also be investigated, a new research area coined "Spincaloritronics" emerging in recent years. Thermoelectric and thermomagnetic phenomena are delved into the coupling of electron and heat currents [56], demonstrating that the polarization of the spin can be governed not only by electric fields but also by temperature gradients and vice versa. Since the magnetic state of a system can be modified thermally, efforts have been devoted to looking for magnetic devices within the spincaloritronic scope. The thermal manipulation and the interaction between heat and spin currents can lead to different applications such as heat sensors, thermometers, waste heat recyclers, power generators, coolers, etc.

1.4.2 High frequency devices

The propagation of electromagnetic waves and spin waves in confined geometries such as magnetic nanowires can give rise to novel microwave devices working up to the THz frequency range. The interaction between an incident electromagnetic wave and a magnetic nanostructure leads to new propagation mechanisms and diffraction phenomena. Specifically, complex architectures such as multi-layered nanowires and

nanotubes are still unexploited in this field. Therefore, a large variety of potential applications could arise in the following years in ICT or biomedical goals [57].

1.4.3 Biomedical applications

Magnetic nanowires have a great functionality in applications related to medicine, e.g., drug delivery or magnetic hyperthermia [58][59]. The morphology of these nano-objects makes them the ideal substitutes to magnetic nanoparticles. In particular, the adjustment of their magnetic anisotropy and coercive fields by modifying the diameter, length and composition, together with the tuning of the magnetocrystalline anisotropy, plays a crucial role in the control of their magnetic properties and behaviour by the application of relatively low external magnetic fields —on the order of 1 T— at a distance.

Firstly, the intrinsic magnetic features of these nanostructures allow using them as hybrid magneto-optical systems. Nanowires composed by sections with different nature along the length can be either magnetically or optically responsive to different stimuli, being a great choice to be key components in sensing devices [60].

Also, the cell trapping and separation procedures are benefitted from magnetic nanowires with high magnetic induction and aspect ratio, reducing the required magnetic fields to be used in comparison with other architectures [61]. The selectivity in the manipulation of cells in culture media has been improved as the nanowire length is correlated with the cell diameter. In this case, the anisotropic shape of the magnetic nanowires provides better output than the magnetically isotropic nanoparticles.

Regarding disease treatments, the biofunctionalization of magnetic nanowires allows avoiding the damages induced by the traditional cancer therapies. The greater specificity of magnetic hyperthermia enables the death of malignant cells by locating the functionalized nanowires on the tumour and inducing heat by alternating magnetic fields in the range of kHz. In comparison with nanoparticles, Fe nanowires reduce the time

required in the treatments due to their shape and better magnetic performance behaviour [62].

Magnetic nanowires can also be used as magnetic nanoactuators on different biological systems. In particular, Co nanowires were used to apply very accurately controlled forces to living cells through magnetic field-induced torque [63], observing mechanical stress responses which can be very efficient in cell treatments.

1.4.4 Magnetic Force Microscopy tips

The high aspect ratio, coercivity and small lateral resolution of magnetic nanowires make them perfect candidates for working as Magnetic Force Microscopy (MFM) tips. Among the several methods used for the fabrication of these nanowires on top of the standard Atomic Force Microscopy (AFM) probes [64][65], Focused Electron Beam Induced Deposition emerges as one of the most promising techniques due to the precise control of the deposition position and tilt angle with respect to the target sample [66]. Further details of this topic will be heavily discussed in Chapter 6.
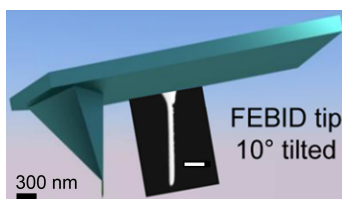
Figure 1.5. Diagram of a 3D Fe nanowire grown by FEBID onto an AFM probe. The inset shows an SEM image of the structure used for MFM measurements [66].

1.4.5 Magnetoplasmonics

Plasmons are collective excitations of the conduction electrons of a metal induced by incoming electromagnetic radiation. The magnetic behaviour of certain materials allows controlling the plasmonic properties of the structures by the application of external magnetic fields. This leads to the development of active magnetoplasmonic devices with applications from telecommunications to biosensing [67].

However, the magnetoplasmonic studies are generally limited to nanoparticles and films, with scarce investigations on ferromagnetic nanowires [68]. Specifically, their combination with plasmonic materials such as Au or Pt could give rise to multifunctional objects for this unexplored field. This research line has a long road ahead with promising applications in optical biochemical sensing devices or nanophotonics [69].

1.5 Design and fabrication of magnetic nanowires

In order to ensure proper operation of the applications presented previously, advanced fabrication techniques are required. In this section, diverse approaches for the crucial nanofabrication mainstay of magnetic nanostructures will be tackled. Different bottom-up and top-down approximations devoted to building magnetic nanowires, particularly in 3D, will be reviewed for a better understanding of their advantages [70].

1.5.1 Electrochemical synthesis

The electrochemical deposition, commonly used in research and industry, is a bottom-up technology which consists of an electrolytic process where, applying a current or voltage, the metallic ions of an electrolyte are reduced, creating a solid deposit on the cathode electrode. Regarding nanowires growth, the concept entails the deposition of the material inside the pores or channels of a membrane, leading to structures with the desired architecture. Although the template method can be employed in combination with other techniques, the electrochemical deposition constitutes a commonly used approach to fill the porous membranes with magnetic materials. Depending on the type of bias applied to the electrolyte, as mention below, different electrodeposition techniques can be explored.

On the one hand, it is worth mentioning the *potentiostatic electrodeposition*, based on a preservation of the potential in the working electrode with respect to the reference one. This type of deposition refers to one of the most common techniques for growing Fe, Co and Ni nanowires and alloys between them [71][72]. On the other hand, the *galvanostatic electrodeposition* relies on the application of a constant current density and

has been used for the fabrication of magnetic alloy nanowires and multi-layered architectures [73][74]. In comparison with the potentiostatic process, it is a more precise method in terms of the growth rate, implying a better control of the volume of deposited material by governing the deposition time.

Additionally, *pulse electrodeposition*, rooted in the combination of potentiostatic and galvanostatic pulses followed by an intermediate recovering step, could give rise to core-shell $Fe@FeO_x$ or $Ni@NiO$ nanowires obtained after an oxidation process once the nanostructures are out of the template [75]. Besides, as shown in Figure 1.6, multisegmented FeCo/Cu nanowires have been fabricated electrochemically by pulse electrodeposition alternating the voltage between -1.8 and -0.7 V for the FeCo and Cu segments, respectively. Moreover, modifying the pulse times, the length of each segment can be tuned [58].

The limitation to use conductive substrates for most of the electrodeposition methods can be overcome by using the *alternating current electrodeposition*. This strategy allows guaranteeing that the typical passivation oxide layer on top of the substrates will not be charged or polarized. In this way, metallic and semiconductor structures have been commonly fabricated with a direct contact to the substrate [76].

Among the huge number of variables which should be contemplated for a successful growth, e.g., bath pH, temperature or electrolyte composition, it should also be pointed out a correct level of wettability in the pore wall to favour the infiltration of the precursor inside the channel, or the control of the shrinkage array during the solidification of the material. This means that the widely used template-assisted method must be employed under optimized conditions, typically using ordered nanoporous anodic Al_2O_3 templates [77][78]. To obtain the desired nanostructure geometry, the dimensions of the template (pore diameter and length, and the distance between the pores) must be tuned. All these parameters will determine not only the morphology and structural features, but also the magnetic properties of the nanowires.
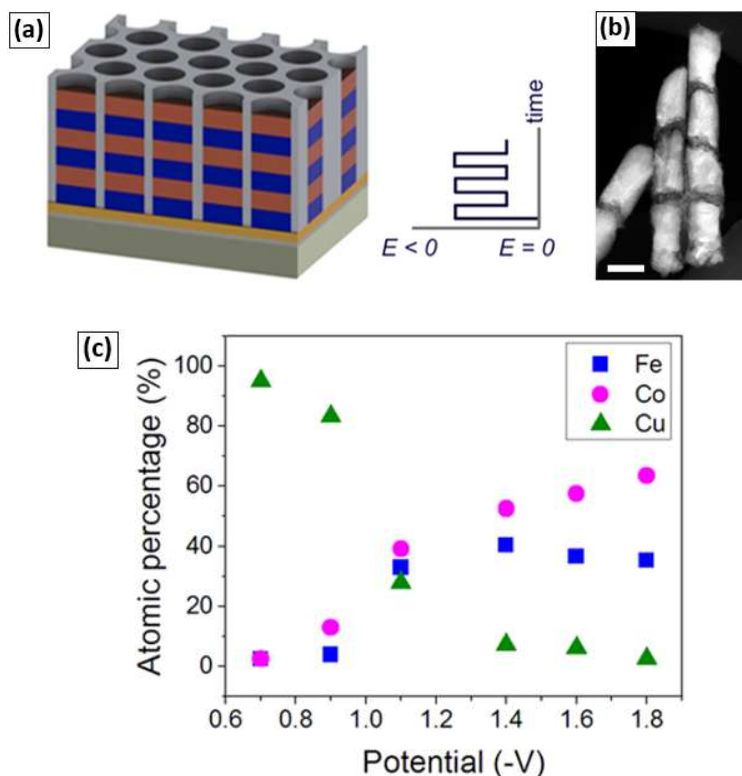
Figure 1.6. (a) Schematic diagram of the fabrication of multisegmented FeCo/Cu nanowires in an anodized aluminum oxide template by alternating the voltage potential to obtain FeCo- and Cu-rich sections. (b) Scanning Transmission Electron Microscopy (STEM) image where the FeCo (dark) and Cu (bright) segments are identified. Undefined scale bar is 100 nm. (c) Relative composition obtained by modifying the voltage potential [58].
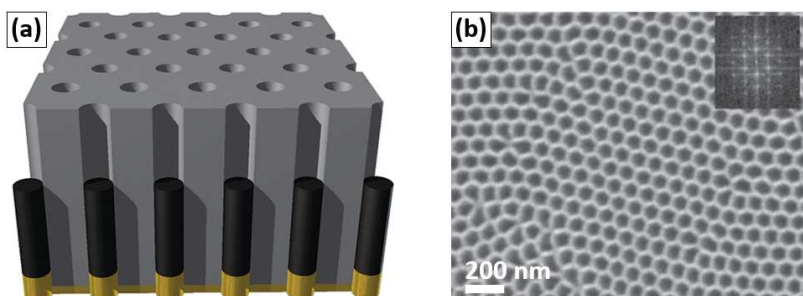
Figure 1.7. (a) Diagram of (Fe, Co)-Pd nanowires (in black) using an Al_2O_3 template (in grey) and Au nanocontacts (in yellow). (b) Top view SEM image of the array with the inset showing the Fast Fourier Transform (FFT) proving the hexagonal packing structure [71].

Figure 1.8 illustrates the influence of the fabrication method in the magnetic properties of Co nanowires, where the acidity of the electrolytic bath is varied, giving rise to different magnetic performance. Besides, it has been proved that the control of the pH allows an accurate adjustment of the crystallographic orientation and phase structure in Co nanowires [79].

The diameter modulation represents an interesting parameter to tune the morphology of the magnetic nanowires with important application in computing operation and thermoelectric energy conversion [80]. Firstly, the diameter of the porous can be controlled by the intrinsic oscillations of the channels during the growth of the template. This has been observed in galvanostatic anodizations when the voltage varies in a narrow range of values or in certain potentiostatic hard anodization processes [81][82].

The modulation can also take place with ultra-high anodization voltages resulting in a tube-shaped architecture [83]. The modulating features can be obtained by either the variation of the anodization parameters in the same process [84], or with alternate anodization parameters in consecutive steps. Although this latter method is an effective strategy, extremely accurate anodization parameters are needed to keep the periodic order of double-section channels [85][86]. The relevance of the pore diameter in the magnetic behaviour is exemplified in Figure 1.9 for Fe nanowires with different sections.
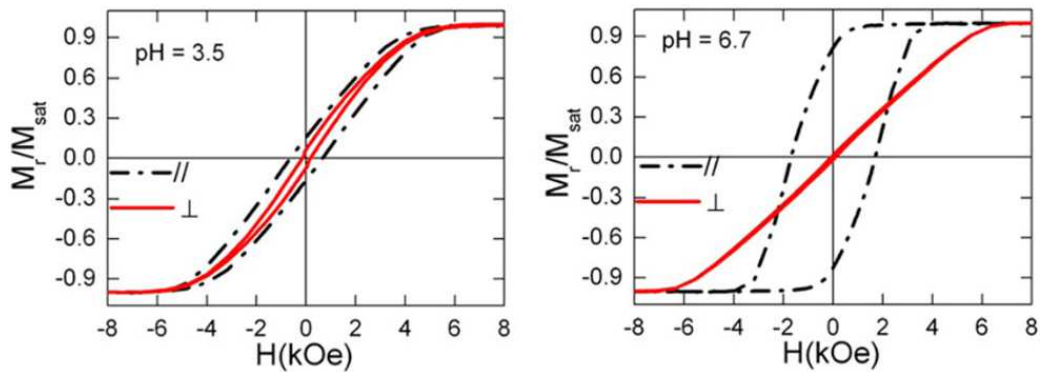
Figure 1.8. Reduced remanence as a function of the applied magnetic field parallel and perpendicular to the Co nanowires long axis for different pH solution values [87].
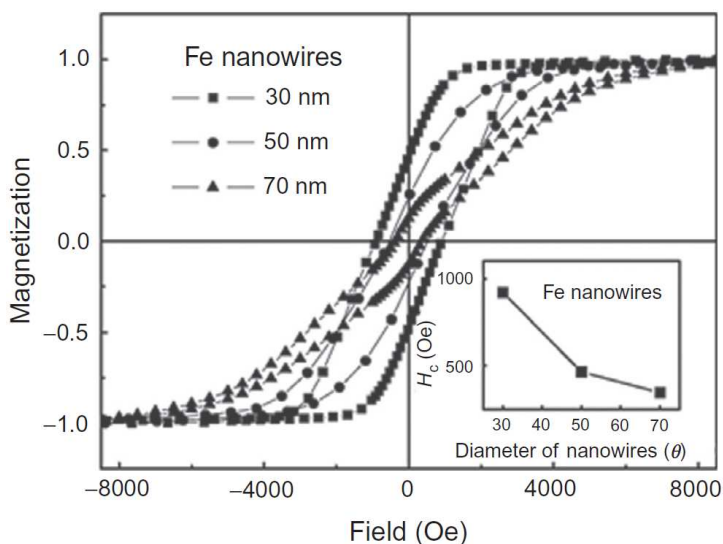
Figure 1.9. (a) Longitudinal hysteresis loops for Fe nanowires with a pore diameter of 30 nm (square dot), 50 nm (circle dot) and 70 nm (triangle dot). The coercive field as a function of the nanowire diameter is plotted in the inset [88].

Given all previously stated, it can be claimed that the use of electrodeposition techniques allows building homogeneous and heterogeneous compositional- and diameter-modulated nanowires, bringing a great versatility in terms of fabrication of magnetic nanowires with outstanding potential application.

1.5.2 Sol-gel technique

The sol-gel method is based on a dispersion of solid nanoparticles in a liquid medium, which subsequently forms a rigid array of micrometre or nanometre size [89]. Firstly, the colloidal nanoparticles are mixed in the solution until enough interconnected bonds are present to favour their cooperative behaviour, i.e., acting as a sol. The sol is casted into a template producing the precipitation of the colloidal particles, assembling a solid network with liquid in the interstices, giving rise to the gel. Then, the gel body is strengthened, and the liquid is eliminated from the system. Finally, the sample is heated to high temperatures to induce crystal growth.

This technique has been used for the growth of oxide magnetic structures such as $BiFeO_3$ nanowires with excellent multiferroic behaviour [90]. Also, the fabrication of $CoFe_2O_4$ [91] and $FeTiO_3$ nanowires [92] have been reported, in addition to Ni, Fe and CoFe nanotubes prepared after hydrogen reduction process [93]. Additionally, the combination of the sol-gel method and other electrodeposition approaches can result in many different designs such as the core-shell architecture. These composite magnetic nanostructures present physical phenomena which can be very attracting for multiple devices, especially those based on magnetoelectric effects [94].

1.5.3 Vapor-liquid-solid and vapor-solid processes

Two of the most common methods to grow heterostructured materials are the vapor-liquid-solid (VLS) and vapor-solid (VL) approaches [95][96]. Despite these techniques are normally associated with the fabrication of semiconductor materials, they also constitute a pillar in the fabrication of magnetic nanowires.

The VLS approach involves the presence of metallic nanoparticles distributed on a substrate, acting as catalysts for the growth of 3D nanowires. As illustrated in Figure 1.10, thermal treatment induces the semiconductor precursor gas to be adsorbed continuously in the metal nanoparticle until the metal-semiconductor liquid alloy is supersaturated. This leads to the nucleation of the solid semiconductor in the region close to the substrate, eventually producing the nanowire axial growth due to a continuous supply of precursor material in vapor phase. When the structure arises below the liquid nanoparticle, its surface can also adsorb the vapor precursor and grow in the radial direction in a VS process.

Based on this strategy, both axial and radial magnetic heterostructures can be fabricated with potential applications in spintronic devices. In the axial case, ferromagnetic Ni-Si alloys can be created in the contacting metal-semiconductor region when Ni atoms migrate into Si nanowires under thermal treatment [97].
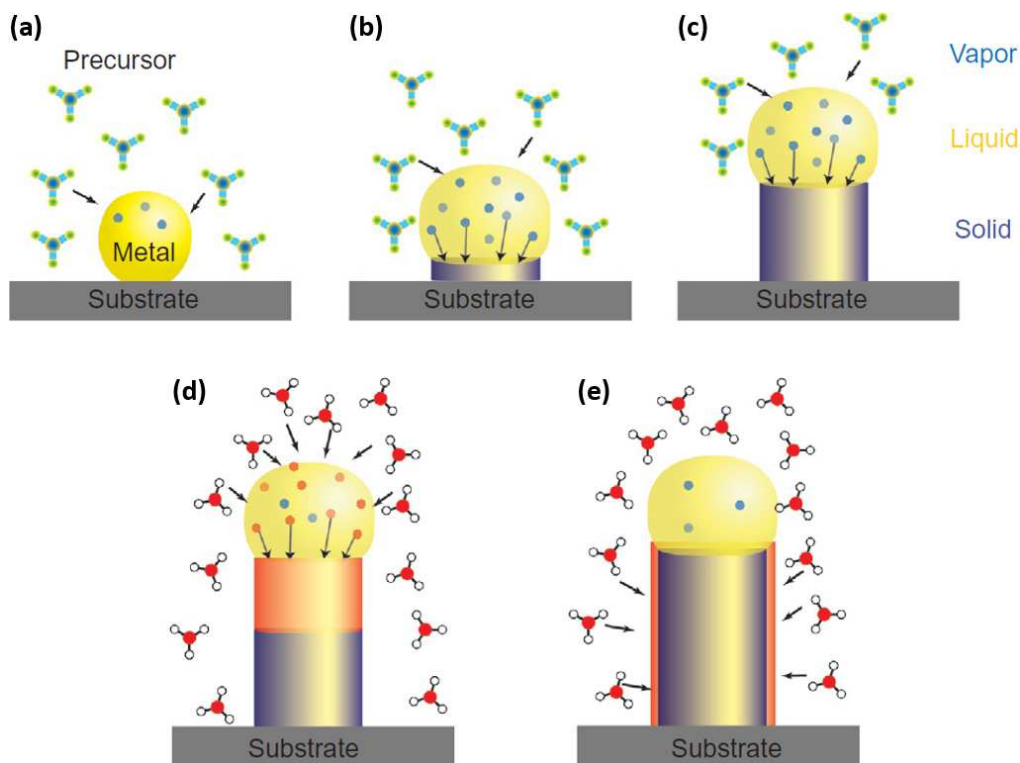
Figure 1.10. Schematic diagram showing the (a-c) VLS process. (d) Axial heterostructure grown by VLS process and (e) radial heterostructure via the VS processes [32].

Also, the production of segmented nanowires of Mn_5Ge_3/Ge has been achieved [98]. In the radial case, core-shell GaAs@GaMnAs nanowires have been synthesized in combination with molecular beam epitaxy, presenting ferromagnetic semiconductor shells [99]. Likewise, core-shell GaAs@Fe_3Si nanowires have also been fabricated to form magnetic nanorods [100].

1.5.4 Chemical vapor transport method

The epitaxial growth of single-crystalline nanowires can be performed by heterogeneous reactions where a solid source is heated to be transformed into the gaseous phase and subsequently deposited when the equilibrium with the substrate energy is

reached [101]. This is the basis of the chemical vapor transport (CVT) method which allows the fabrication of ferromagnetic Ni, Co and Fe nanowires by using metal halide precursors.

In the case of the Ni, vertical nanowires were grown for the first time in the last decade on amorphous $SiO_2//Si$ substrate using $NiCl_2 \cdot 6H_2O$ as the metal source [102]. Furthermore, mixed $CoCl_2$ and $NiCl_2$ precursors have been utilized to grow Ni-Co alloy nanowires epitaxially grown on *c*-cut sapphire substrates [103]. Vertical ferromagnetic $Fe_{1.3}Ge$ nanowires were fabricated on graphene [104], see Figure 1.11, being this system particularly appropriate for electronic and spintronic applications due to its great affinity with semiconductor technology [105].

Another possible strategy consists in the conversion of non-magnetic nanowires into magnetic nanowires through an annealing method applied after the CVT approach. For instance, a transformation via thermal diffusion can be adopted to fabricate ferromagnetic Fe_3Si nanowires from paramagnetic FeSi ones, retaining the epitaxial orientation of the original structure [106].
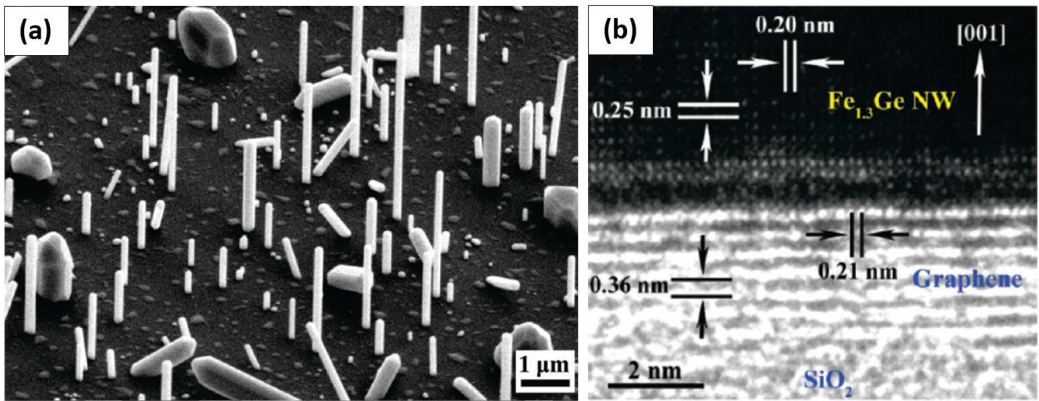
Figure 1.11. (a) SEM image of 3D ferromagnetic $Fe_{1.3}Ge$ nanowires grown on 2.7-nm-thick graphene substrate. (b) High Resolution Transmission Electron Microscopy (HRTEM) image of the interface between the nanowire and the substrate, showing the epitaxial growth [104].

1.5.5 Quenching and drawing technique

The fabrication of amorphous glass-coated micro- and nanowires has been carried out following the common quenching and drawing method, also called glass-coated melt spinning [107]. This rapid solidification technique is used for the fabrication of structures with diameters ranging from tens of nanometres to millimetres, tailoring the lateral dimension by adjusting the temperature of the precursor alloy and the cooling process [108]. After optimization, the growth of $Co_{68.15}Fe_{4.35}Si_{12.5}B_{15}$ and $Fe_{77.5}Si_{7.5}B_{15}$ nanowires with metallic core diameters between 90 and 180 nm were prepared for the first time in 2011 [109].

This technique presents some advantages with respect to other lithography and electrodeposition strategies. It is not only a cheap and straightforward method, with no limitation in terms of the nanowire length, but also allows tuning the composition, magnetization, magnetic anisotropy, switching magnetic field, domain wall motion, etc. All these possibilities should be considered to develop future logic and sensing devices.

1.5.6 Focused Electron Beam Induced Deposition

Studies on fundamental properties and technological applications of magnetic nanowires require a reproducible fabrication technique which provides single and isolated objects in targeted positions. These specifications can be fulfilled by Focused Electron Beam Induced Deposition (FEBID) technique, which plays a crucial role in the design and fabrication of many types of architectures allowing great versatility in shape, composition and magnetic features [110][111][112]. Since the nanostructures presented in this thesis have been fabricated by this technology, brief remarks will be done in this subsection and comprehensive explanations will be address throughout the manuscript.

The method, introduced for the first time by S. Matsui in 1984 [113], consists of a precursor gas decomposition by an electron beam, eventually producing a solid material only in the areas where the electron beam scans. This single-step nanolithography process

does not require the use of masks, resists or lift-off procedures. It is, however, influenced by a great number of parameters such as the electron beam voltage and current, precursor gas flux, etc. which need to be controlled and optimized.

Compositional, electrical and magnetic properties have been widely investigated in 2D Co and Fe nanowires [114][115][116][117], putting forward applications such as the ones based on direct nanomagnet logic devices to compute binary information or nanosensors [116][118]. The next natural step was to move into 3D deposits, where larger versatility in terms of shape can be obtained. In addition, the specific fabrication of 3D nanowires results in higher areal density and novel domain wall configurations. This has led to the FEBID design of magnetomechanical nanoactuators [119] or MFM tips [120], and could give rise to the construction of the 3D racetrack memory. However, scarce investigations have been performed along this line and challenges still remain for this out-of-plane (OOP) architectures [121]. With this motivation in mind, this thesis is devoted to the in-depth study of the growth and characterization of 3D ferromagnetic nanowires grown by FEBID.
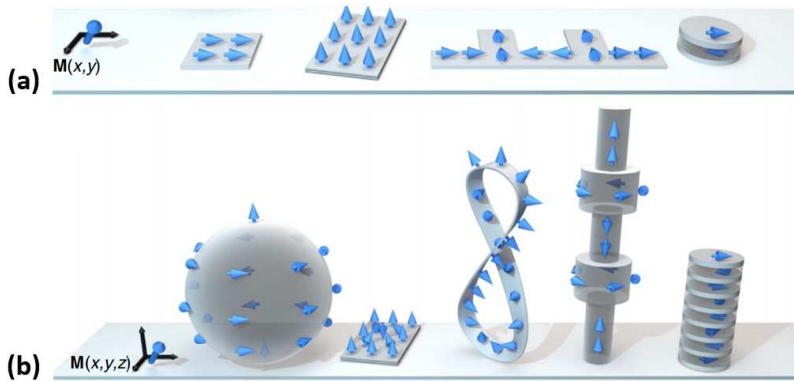
Figure 1.12. Schematic diagram of some (a) 2D and (b) 3D geometries examples and their magnetic configurations [70].

1.6 Outline of the thesis

This thesis is focused on investigating the multitude of aspects related to the development of 3D magnetic nanowires by FEBID and their characterization through advanced techniques. It includes the exploration of the fabrication conditions and growth modes (Chapter 3), the post-growth optimization of their physical properties (Chapter 4), the formation of new architectures and heterostructures (Chapter 5), and applications (Chapter 6).

Hitherto, in Chapter 1 the brief historical overview about the current and future applications of magnetic nanowires and the different methods used to fabricate these promising nano-objects have been described. This general perspective has been aimed to serve as a starting point to arouse curiosity into the reader, present a general framework of this manuscript and introduce some of the concepts which will be discuss hereafter.

In Chapter 2, descriptions of the fundamental experimental techniques employed for the growth and characterization of 3D nanowires are given. Special emphasis will be placed on FEBID nanofabrication technology, and in compositional and magnetic characterization by Transmission Electron Microscopy (TEM) techniques.

Chapter 3 is devoted to explaining how tuning the shape, composition and magnetization of these vertical nano-objects is possible due to the great versatility of FEBID and its combination with other strategies. Particular mention should be given to the new ARchitectural Adjustment by Grid Overlay Nanotechnology (ARAGON) Chip, allowing the fabrication of FEBID nanostructures on insulating substrates —which had been impossible until now—, and presenting an additional degree of freedom to modulate dimensional parameters of the nanostructures.

Chapter 4 discusses different approaches for the improvement and optimization of structural, compositional and ferromagnetic properties of the nanowires. Specifically, *in situ* and *ex situ* post-growth annealing treatments have been explored to enhance the crystallinity, metallic content and magnetic induction of the nanostructures.

In Chapter 5, the implementation of the core-shell architecture for the growth 3D FEBID Co@Pt and Fe@Pt nanowires is developed. This aims at minimizing the degradation of the ferromagnetic properties of the core caused by its natural surface oxidation to a non-ferromagnetic material. Additionally, this strategy was used to fabricate ferromagnetic Pt@Co nanotubes and investigating their magnetic behaviour.

Chapter 6 explores some possible applications of 3D ferromagnetic nanostructures grown by FEBID. Special attention will be paid to optimization of straight vertical nanowires for MFM measurements in different environments, and to the design of more complex 3D architectures based on hook-shaped nanowires aimed for domain wall conduit devices.

Finally, Chapter 7 gives a comprehensive overview of the key results of the thesis, summarize the main conclusions and discusses some future perspectives for 3D FEBID growth in the field of Nanomagnetism.

References

[1]   R. P. Feynman, "There's Plenty of Room at Bottom", *Engineering and Science*, 22 (1960).

[2]   W. Lu and C. M. Lieber, "Semiconductor nanowires", *J. Phys. D: Appl. Phys.* **39**, R387 (2006).

[3]   J. Jiu and K. Suganuma, "Metallic Nanowires and Their Applications", *IEEE CMPT* **6**, 1733 (2016).

[4]   R. Arpaia, M. Ejrnaes, L. Parlato, F. Tafuri, R. Cristiano, D. Golubev, Roman Sobolewski, T. Bauch, F. Lombardi and G. P. Pepe, "High-temperature superconducting nanowires for photon detection", *Physica C* **509**, 16 (2015).

[5]   S. Chaudhury and S. K. Sinha, "Carbon Nanotube and Nanowires for Future Semiconductor Devices Applications", *Nanoelectronics: Devices, Circuits and Systems*, Edited by B. K. Kaushik (2018).

[6]   M. Staňo and O. Fruchart, "Magnetic Nanowires and Nanotubes", *Handbook of Magnetic Materials*, Edited by E. Brück (2018).

[7]   V. Schuler, J. Milano, A. Coati, A. Vlad, M. Sauvage-Simkin, Y. Garreau, D. Demaille, S. Hidki, A. Novikova, E. Fonda, Y. Zheng and F. Vidal, "Growth and

magnetic properties of vertically aligned epitaxial CoNi nanowires in (Sr, Ba) TiO$_3$ with diameters in the 1.8-6nm range", *Nanotechnology* **27**, 495601 (2016).

[8] K. L. Metlov and K. Y. Guslienko, "Stability of magnetic vortex in soft magnetic nano-sized circular cylinder", *J. Magn. Magn. Mater.* **242-245**, 1015 (2002).

[9] S. Jamet, N. Rougemaille, J. C. Toussaint and O. Fruchart, "Head-to-head domain walls in one-dimensional nanostructures: an extended phase diagram ranging from strips to cylindrical wires", *Magnetic Nano- and Microwires: Design, Synthesis, Properties and Applications*, Edited by M. Vázquez (2015).

[10] N. Biziere, C. Gatel, R. Lassalle-Balier, M. C. Clochard, J. E. Wegrowe and E. Snoeck, "Imaging the Fine Structure of a Magnetic Domain Wall in a Ni Nanocylinder", *Nano Lett.* **13**, 2053 (2013).

[11] S. Da Col, S. Jamet, N. Rougemaille, A. Locatelli, T. O. Mentes, B. Santos Burgos, R. Afid, M. Darques, L. Cagnon, J. C. Toussaint and O. Fruchart, "Observation of Bloch-point domain walls in cylindrical magnetic nanowires", *Phys. Rev. B* **89**, 180405(R) (2014).

[12] A. Wartelle, B. Trapp, M. Staňo, C. Thirion, S. Bochmann, J. Bachmann, M. Foerster, L. Aballe, T. O. Menteş, A. Locatelli, A. Sala, L. Cagnon, J.-C. Toussaint and O. Fruchart, "Bloch-point-mediated topological transformations of magnetic domain walls in cylindrical nanowires", *Phys. Rev. B* **99**, 024433 (2019).

[13] J. Escrig, J. Bachmann, J. Jing, M. Daub, D. Altbir and K. Nielsch, "Crossover between two different magnetization reversal modes in arrays of iron oxide nanotubes", *Phys. Rev. B* **77**, 214421 (2008).

[14] Y. P. Ivanov, A. Chuvilin, S. Lopatin and J. Kosel, "Modulated Magnetic Nanowires for Controlling Domain Wall Motion: Toward 3D Magnetic Memories", *ACS Nano* **10**, 5326 (2016).

[15] A. Ghaddar, F. Gloaguen, J. Gieraltowski and C. Tannous, "Magnetic crossover effect in Nickel nanowire arrays", *Physica B* **406**, 2046 (2011).

[16] S. Bochmann, D. Döhler, B. Trapp, M. Staňo, O. Fruchart and J. Bachmann, "Preparation and physical properties of soft magnetic nickel-cobalt three-segmented nanowires", *J. Appl. Phys.* **124**, 163907 (2018).

[17] A. Thiaville and Y. Nakatani, "Domain-Wall Dynamics in Nanowires and Nanostrips", *Spin Dynamics in Confined Magnetic Structures III*, Edited by B. Hillebrands, A. Thiaville (2006).

[18] W. Lu and C. M. Lieber, "Nanoelectronics from the bottom up", *Nat. Mater.* **6**, 841 (2007).

[19] N. Spaldin, "Magnetic Materials. Fundamentals and Device Applications",

Cambridge University Press (2003).

[20] G. E. Moore, "Cramming more components onto integrated circuits", *Electronics* **38**, (1965).

[21] R. Chau, B. Doyle, S. Datta, J. Kavalieros and K. Zhang, "Integrated nanoelectronics for the future" *Nat. Mater.* **6**, 810 (2007).

[22] European Nanoelectronics Initiative Advisory, "Strategic Research Agenda", Second Edition (2007).

[23] S. H. Park, Y. Kim, W. Kim, J. Y. Seo and B.-G. Park, "Vertical-Channel STacked ARray (VCSTAR) for 3D NAND flash memory", *Solid-State Electronics* **78**, 34 (2012).

[24] G. I. Meijer, "Who Wins the Nonvolatile Memory Race?," *Science* **319**, 1625 (2008).

[25] J. J. Yang, D. B. Strukov and D. R. Stewart, "Memristive devices for computing", *Nat. Nanotechnol.* **8**, 13 (2013).

[26] Y. Yang, P. Gao, S. Gaba, T. Chang, X. Pan and W. Lu, "Observation of conducting filament growth in nanoscale resistive memories", *Nat. Commun.* **3**, 732 (2012).

[27] S. I. Kim, J. H. Lee, Y. W. Chang, S. S. Hwank and K.-H. Yoo, "Reversible resistive switching behaviors in NiO nanowires", *Appl. Phys. Lett.* **93**, 033503 (2008).

[28] K. Oka, T. Yanagida, K. Nagashima, T. Kawai, J.-S- Kim and B. H. Park, "Resistive-Switching Memory Effects of NiO Nanowire/Metal Junctions", *JACS* **132**, 6634 (2010).

[29] E. D. Herderick, K. M. Reddy, R. N. Sample, T. I. Draskovic and N. P. Padture, "Bipolar resistive switching in individual Au-NiO-Au segmented nanowires", *Appl. Phys. Lett.* **95**, 203505 (2009).

[30] C. Cagli, F. Nardi, B. Harteneck, Z. Tan, Y. Zhang and D. Ielmini, "Resistive-Switching Crossbar Memory Based on Ni-NiO Core-Shell Nanowires", *Small* **7**, 2899 (2011).

[31] D. Son, J. Lee, S. Qiao, R. Ghaffari, J. Kim, J. E. Lee, C. Song, S. J. Kim, D. J. Lee, S. W. Jun, S. Yang, M. Park, J. Shin, K. Do, M. Lee, K. Kang, C. S. Hwang, N. Lu, T. Hyeon and D.-H. Kim, "Multifunctional wearable devices for diagnosis and therapy of movement disorders", *Nat. Nanotechnol.* **9**, 397 (2014).

[32] M. Vázquez, "Magnetic Nano- and Microwires. Design, Synthesis, Properties and Applications", *Elsevier* (2015).

[33] I. Žutić, J. Fabian and S. Das Sarma, "Spintronics Fundamentals: and applications", *Rev. Mod. Phys.* **76**, 323 (2004).

[34]   S. D. Bader and S. S. P. Parkin, "Spintronics", *Annu. Rev. Condens. Matter Phys.* **1**, 71 (2010).

[35]   W. Thompson, "On the Electro-dynamic Qualities of Metals:-Effects of Magnetization on the Electric Conductivity of Nickel and of Iron", *Proc. R. Soc. Lond.* **8**, 546 (1857).

[36]   R. P. Hunt, "A Magnetoresistive Readout Transducer", *IEEE Trans. Magn.* **MAG-7**, 150 (1971).

[37]   M. Julliere, "Tunneling Between Ferromagnetic Films", *Phys. Lett.* **54A**, 225 (1975).

[38]   M. N. Baibich, J. M. Broto, A. Fert, F. Nguyen Van Dau and F. Petroff, "Giant Magnetoresistance of (001)Fe/(001)Cr Magnetic Superlattices", *Phys. Rev. Lett.* **61**, 2472 (1988).

[39]   S. M. Thompson, "The discovery, development and future of GMR: The Nobel Prize 2007", *J. Phys. D: Appl. Phys.* **41**, 093001 (2008).

[40]   A. Hönemann, C. Herschbach, D. V. Fedorov, M. Gradhand and I. Mertig, "Spin and charge currents induced by the spin Hall and anomalous Hall effects upon crossing ferromagnetic/nonmagnetic interfaces," *Phys. Rev. B* 99, 024420 (2019).

[41]   A. Fernández-Pacheco, J. M. De Teresa, R. Córdoba, M. R. Ibarra and D. Petit, "Domain wall conduit behavior in cobalt nanowires grown by focused electron beam induced deposition", *Appl. Phys. Lett.* **94**, 192509 (2009).

[42]   D. C. Ralph and M. D. Stiles, "Spin transfer torques", *J. Magn. Magn. Mater.* **320**, 1190 (2008).

[43]   M. Weigand, B. Van Waeyenberge, A. Vansteenkiste, M. Curcic, V. Sackmann, H. Stoll, T. Tyliszczak, K. Kaznatcheev, D. Bertwistle, G. Woltersdorf, C. H. Back and Gisela Schütz, "Vortex Core Switching by Coherent Excitation with Single In-Plane Magnetic Field Pulses", *Phys. Rev. Lett.* **102**, 077201 (2009).

[44]   S. S. P. Parkin, M. Hayashi and L. Thomas, "Magnetic Domain-Wall Racetrack Memory", *Science* **320**, 190 (2008).

[45]   D. A Allwood, G. Xiong, C. C. Faulkner, D. Atkinson, D. Petit and R. P. Cowburn, "Magnetic Domain-Wall Logic", *Science* **309**, 1688 (2005).

[46]   A. Brataas, A. D. Kent and H. Ohno, "Current-induced torques in magnetic materials", *Nat. Mater.* **11**, 372 (2012).

[47]   W. S. Zhao, Y. Zhang, H.-P. Trinh, J.-O. Klein, C. Chappert, R. Mantovan, A. Lamperti, R. P. Cowburn, T. Trypiniotis, M. Klaui, J. Heinen, B. Ocker, D. Ravelosona, "Magnetic Domain-Wall Racetrack Memory for high density and fast data Storage", *2012 IEEE 11th Int. Conf. Solid-State Integr. Circuit Technol.* (2012).

[48]   W. Zhao, D. Ravelosona, J.-O. Klein and C. Chappert, "Domain Wall Shift Register-Based Reconfigurable Logic", *IEEE Trans. Magn.* **47**, 2966 (2011).

[49]   L. Heyne, J. Rhensius, D. Ilgaz, A. Bisig, U. Rüdiger, M. Kläui, L. Joly, F. Nolting, L. T. Heyderman, J. U. Thiele, F. Kronast, "Direct Determination of Large Spin-Torque Nonadiabaticity in Vortex Core Dynamics", *Phys. Rev. Lett.* **105**, 187203 (2010).

[50]   S. Emori, D. C. Bono and G. S. D. Beach, "Interfacial current-induced torques in Pt/Co/GdOx", *Appl. Phys. Lett.* **101**, 042405 (2012).

[51]   P. J. Metaxas, J. Sampaio, A. Chanthbouala, R. Matsumoto, A. Anane, A. Fert, K. A. Zvezdin, K. Yakushiji, H. Kubota, A. Fukushima, S. Yuasa, K. Nishimura, Y. Nagamine, H. Maehara, K. Tsunekawa, V. Cros and J. Grollier, "High domain wall velocities via spin transfer torque using vertical current injection", *Sci. Rep.* **3**, 1829 (2013).

[52]   M. Melzer, M. Kaltenbrunner, D. Makarov, D. Karnaushenko, D. Karnaushenko, T. Sekitani, T. Someya and O. G. Schmidt, "Imperceptible magnetoelectronics", *Nat. Commun.* **6**, 6080 (2015).

[53]   D. Makarov, M. Melzer, D. Karnaushenko and O. G. Schmidt, "Shapeable magnetoelectronics", *Appl. Phys. Rev.* **3**, 011101 (2016).

[54]   G. Tatara and H. Kohno, "Theory of Current-Driven Domain Wall Motion: Spin Transfer versus Momentum Transfer", *Phys. Rev. Lett.* **192**, 086601 (2004).

[55]   M. D. Stiles and A. Zangwill, "Anatomy of spin-transfer torque", *Phys. Rev. B* **66**, 014407 (2002).

[56]   G. E. W. Bauer, E. Saitoh and B. J. van Wees, "Spin caloritronics", *Nat. Mater.* 11, 391 (2012).

[57]   H. Yang, M. Zeng and R. Yu, "Magnetic properties of the Ni_xCo_{1-x}/Cu multilayer nanowires", *Materials Research Bulletin*, **57**, 249 (2014).

[58]   B. Özkale, N. Shamsudhin, G. Chatzipirpiridis, M. Hoop, F. Gramm, X. Chen, X. Martí, J. Sort, E. Pellicer and S. Pané, "Multisegmented FeCo/Cu Nanowires: Electrosynthesis, Characterization, and Magnetic Control of Biomolecule Desorption", *ACS Appl. Mater. Interfaces* **7**, 7389 (2015).

[59]   X.-F. Han, S. Shamaila and R. Sharif, "Ferromagnetic Nanowires and Nanotubes", *Electrodeposited Nanowires Their Applications*, Edited by N. Lupu (2010).

[60]   B. He, T. J. Morrow and C. D. Keating, "Nanowire sensors for multiplexed detection of biomolecules", *Curr. Opin. Chem. Biol.* **12**, 522 (2008).

[61]   A. Hultgren, M. Tanase, E. J. Felton, K. Bhadriraju, A. K. Salem, C. S. Chen and D. H. Reich, "Optimization of Yield in Magnetic Cell Separations Using Nickel

Nanowires of Different Lengths", *Biotechnol. Prog.* **21**, 509 (2005).

[62]   W.-S. Lin, H.-M. Lin, H.-H. Chen, Y.-K. Hwu and Y.-J- Chiou, "Shape Effects of Iron Nanowires on Hyperthermia Treatment", *Journal of Nanomaterials* **2013**, 237439 (2013).

[63]   N. J. Sniadecki, A. Anguelouch, M. T. Yang, C. M. Lamb, Z. Liu, S. B. Kirschner, Y. Liu, D. H. Reich and C. S. Chen, "Magnetic microposts as an approach to apply forces to living cells", *PNAS* **104**, 14553 (2007).

[64]   G. Yang, J. Tang, S. Kato, Q. Zhang, L. C. Qin, M. Woodson, J. Liu, J. W. Kim, P. T. Littlehei, C. Park and O. Zhou, "Magnetic nanowire based high resolution magnetic force microscope probes", *Appl. Phys. Lett.* **87**, 123507 (2005).

[65]   S. Alotaibi, J. Samba, S. Pokharel, Y. Lan, K. Uradu, A. Afolabi, I. Unlu, G. Basnet, K. Aslan, B. N. Flanders, A. Lisfi and B. Ozturk "Individually grown cobalt nanowires as magnetic force microscopy probes", *Appl. Phys. Lett.* **102**, 092401 (2018).

[66]   M. Gavagnin, H. D. Wanzenboeck, S. Wachter, M. M. Shawrav, A. Persson, K. Gunnarsson, P. Svedlindh, M. Stöger-Pollach and E. Bertagnolli, "Free-Standing Magnetic Nanopillars for 3D Nanomagnet Logic" *ACS Appl. Mater. Interfaces* **6**, 20254 (2014).

[67]   G. Armelles, A. Cebollada, A. García-Martín and M. Ujué González, "Magnetoplasmonics: Combining Magnetic and Plasmonic Functionalities", *Adv. Optical Mater.* **1**, 10 (2013).

[68]   J. B. González-Díaz, A. García-Martín, G. Amelles, D. Navas, M. Vázquez, K. Nielsch, R. B. Wehrspohn and U. Gösele, "Enhanced Magneto-Optics and Size Effects in Ferromagnetic Nanowire Arrays", *Adv. Mater.* **19**, 2643 (2007).

[69]   V. Bonanni, S. Bonetti, T. Pakizeh, Z. Pirzadeh, J. Chen, J. Nogués, P. Vavassori, R. Hillenbrand, J. Åkerman and A. Dmitriev, "Designer Magnetoplasmonics with Nickel Nanoferromagnets", *Nano. Lett.* **11**, 5333 (2011).

[70]   A. Fernández-Pacheco, R. Streubel, O. Fruchart, R. Hertel, P. Fischer and R. P. Cowburn, "Three-dimensional nanomagnetism", *Nat. Commun.* **8**, 15756 (2017).

[71]   V. Vega, J. García, W. O. Rosa, L. G. Vivas, V. M. Prida, B. Hernando, M. Vázquez, "Magnetic Properties of (Fe, Co)-Pd Nanowire Arrays", *J. Nanosci. Nanotechnol.* **12**, 7501 (2012).

[72]   X. Liu, X. Zhao, Z. Gao, Y. Zhu, J. Wang, Z. Dai and G. Wu, "Structure-controlled Synthesis and Magnetism of CoCu Nanowires", *Chem. Lett.* **42**, 1108 (2013).

[73]   V. Vega, W. O. Rosa, J. García, T. Sánchez, J. D. Santos, F. Berón, K. R. Pirota, V. M. Prida and B. Hernando, "Template-assisted CoPd nanowire arrays:

magnetic properties and FORC analysis", *J. Nanosci. Nanotechnol.* **12**, 4736 (2012).

[74] V. Weihnacht, L. Péter, J. Tóth, J. Pádár, Zs. Kerner, C. M. Schneider and I. Bakonyi, "Giant Magnetoresistance in Co-Cu/Cu Multilayers Prepared by Various Electrodeposition Control Modes", *J. Electrochem. Soc.* **150**, C507 (2003).

[75] J. H. Lee, J. H. Wu, J. S. Lee, K. S. Jeon, H. R. Kim, J. H. Lee, Y. D. Suh and Y. K. Kim, "Synthesis and Characterization of Fe - FeO$_x$ Core-Shell Nanowires", *IEEE Trans. Magn.* **44**, 3950 (2008).

[76] P. Wang, L. Gao, Z. Qiu, X. Song, L. Wang, S. Yang, R. Murakami, "A multistep ac electrodeposition method to prepare Co nanowires with high coercivity", *J. Appl. Phys.* **104**, 064304 (2008).

[77] M. Vázquez, K. Pirota, J. Torrejón, D. Navas and M. Hernández-Vélez, "Magnetic behaviour of densely packed hexagonal arrays of Ni nanowires: Influence of geometric characteristics", *J. Magn. Magn. Mater.* **294**, 174 (2005).

[78] J. Klammer, J. Bachmann, W. Töllner, D. Bourgault, L. Cagnon, and U. Gösele and K. Nielsch, "Electrochemical route to thermoelectric nanowires via organic electrolytes", *Phys. Status Solidi B* **247**, 1384 (2010).

[79] A. Cortés, R. Lavín, J. C. Denardin, R. E. Marotti, E. A. Dalchiele, P. Valdivia, H. Gómez, "Template Assisted Electrochemical Growth of Cobalt Nanowires : Influence of Deposition Conditions on Structural , Optical and Magnetic Properties", *J. Nanosci. Nanotechnol.* **11**, 3899 (2011).

[80] X. Zianni, "Diameter-modulated nanowires as candidates for high thermoelectric energy conversion efficiency", *Appl. Phys. Lett.* **97**, 233106 (2010).

[81] K. Schwirn, W. Lee, R. Hillebrand, M. Steinhart, K. Nielsch and U. Gösele, "Self-Ordered Anodic Aluminum Oxide Formed by H$_2$SO$_4$ Hard Anodization", *ACS Nano* **2**, 302 (2008).

[82] W. Lee, J.-C. Kim and U. Gösele, "Spontaneous Current Oscillations during Hard Anodization of Aluminum under Potentiostatic Conditions", *Adv. Funct. Mater.* **20**, 21 (2010).

[83] L. Yi, L. Zhiyuan, C. Shuoshuo, H. Xing and H. Xinhua, "Novel AAO films and hollow nanostructures fabricated by ultra-high voltage hard anodization", *Chem. Commun.* **46**, 309 (2010).

[84] W. Lee, K. Schwirn, M. Steinhart, E. Pippel, R. Scholz and U. Gösele, "Structural engineering of nanoporous anodic aluminium oxide by pulse anodization of aluminium", *Nat. Nanotechnol.* **3**, 234 (2008).

[85] W. Lee, R. Ji, U. Gösele and K. Nielsch, "Fast fabrication of long-range ordered

porous alumina membranes by hard anodization", *Nat. Mater.* **5**, 741 (2006).

[86]   K. Pitzschel, J. Bachmann, S. Martens, J. M. Montero-Moreno, J. Kimling, G. Meier, J. Escrig, K. Nielsch and D. Görlitz, "Magnetic reversal of cylindrical nickel nanowires with modulated diameters", *J. Appl. Phys.* **109**, 033907 (2011).

[87]   L. G. Vivas, J. Escrig, D. G. Trabada, G. A. Badini-Confalonieri and M. Vázquez, "Magnetic anisotropy in ordered textured Co nanowires", *Appl. Phys. Lett.* **100**, 252405 (2012).

[88]   X. F. Qin, C. H. Deng, Y. Liu, X. J. Meng, J. Q. Zhang, F. Wang and X. H. Xu, "Magnetization Reversal of High Aspect Ratio Iron Nanowires Grown by Electrodeposition", *IEEE Trans. Magn.* 48, 3136 (2012).

[89]   J. V. Masi and S. Masi, "Sol-Gel Magnetic Materials", *Proceedings: Electrical Insulation Conference and Electrical Manufacturing and Coil Winding Conference* (2002).

[90]   L. A. S. de Oliveira and R. Pirota, "Sol-gel route to prepare well-ordered nanowires with anodic aluminum oxide template", *J. Sol-Gel Sci. Technol.* **63**, 275 (2012).

[91]   G. Ji, S. Tang, B. Xu, B. Gu and Y. Du, "Synthesis of $CoFe_2O_4$ nanowire arrays by sol-gel template method", *Chem. Phys. Lett.* **379**, 484 (2003).

[92]   U. Khan, W. J. Li, N. Adeela, M. Irfan, K. Javed, C. H. Wan, S. Riaza and X. F. Han, "Magnetic response of hybrid ferromagnetic and antiferromagnetic core-shell nanostructures", *Nanoscale* **8**, 6064 (2016).

[93]   Z. Hua, S. Yang, H. Huang, L. Lv, M. Lu, B. Gu and Y. Du, "Metal nanotubes prepared by a sol-gel method followed by a hydrogen reduction", *Nanotechnology* **17**, 5106 (2006).

[94]   W. Eerenstein, N. D. Mathur and J. F. Scott, "Multiferroic and magnetoelectric materials", *Nature* **442**, 759 (2006).

[95]   R. S. Wagner and W. C. Ellis, "Vapor-liquid-solid mechanism of single crystal growth", *Appl. Phys. Lett.* **4**, 89 (1964).

[96]   L. J. Lauhon, M. S. Gudiksen and C. M. Lieber, "Semiconductor nanowire heterostructures", *Philos Trans A Math Phys Eng Sci.* **362**, 1247 (2004).

[97]   Y. Wu, J. Xiang, C. Yang, W. Lu and C. M. Lieber, "Single-crystal metallic nanowires and metal/semiconductor nanowire heterostructures", *Nature* **430**, 61 (2004).

[98]   J. Tang, C.-Y. Wang, L.-T. Chang, Y. Fan, T. Nie, M. Chan, W. Jiang, Y.-T. Chen, H.-J. Yang, H.-Y. Tuan, L.-J. Chen and K. L. Wang, "Electrical Spin Injection and Detection in Mn_5Ge_3/Ge/Mn_5Ge_3 Nanowire Transistors", *Nano Lett.* **13**, 4036 (2013).

[99]   A. Rudolph, M. Soda, M. Kiessling, T. Wojtowicz, D. Schuh, W. Wegscheider, J. Zweck, C. Back and E. Reiger, "Ferromagnetic GaAs/GaMnAs Core-Shell Nanowires Grown by Molecular Beam Epitaxy", *Nano Lett.* **9**, 3860 (2009).

[100] M. Hilse, J. Herfort, B. Jenichen, A. Trampert, M. Hanke, P. Schaaf, L. Geelhaar and H. Riechert, "GaAs−Fe₃Si Core−Shell Nanowires: Nanobar Magnets", *Nano Lett.* **13**, 6203 (2013).

[101] P. Schmidt, M. Binnewies, R. Glaum and M. Schmidt, "Chemical Vapor Transport Reactions-Methods, Materials, Modeling", *Advanced Topics on Crystals Growth*, Edited by S. O. Ferreira (2013).

[102] K. T. Chan, J. J. Kan, C. Doran, L. Ouyang, D. J. Smith and E. E. Fullerton, "Oriented Growth of Single-Crystal Ni Nanowires onto Amorphous SiO_2," *Nano. Lett.* **10**, 5070 (2010).

[103] N. Bagkar, K. Seo, H. Yoon, J. In, Y. Jo and B. Kim, "Vertically Aligned Single-Crystalline Ferromagnetic Ni3Co Nanowires", *Chem. Mater.* **22**, 1831 (2010).

[104] H. Yoon, T. Kang, J. M. Lee, S. Kim, K. Seo, J. Kim, W. I. Park and B. Kim, "Epitaxially Integrating Ferromagnetic $Fe_{1.3}Ge$ Nanowire Arrays on Few-Layer Graphene", *J. Phys. Chem. Lett.* **2**, 956 (2011).

[105] H. Yoon, A. T. Lee, E.-A. Choi, K. Seo, N. Bagkar, J. Cho, Y. Jo, K. J. Chang and B. Kim, "Structure-Induced Ferromagnetic Stabilization in Free-Standing Hexagonal $Fe_{1.3}Ge$ Nanowires", *J. Am. Chem. Soc.* **132**, 17447 (2010).

[106] K. Seo, N. Bagkar, S. Kim, J. In, H. Yoon, Y. Jo and B. Kim, "Diffusion-Driven Crystal Structure Transformation: Synthesis of Heusler Alloy Fe_3Si Nanowires", *Nano Lett.* **10**, 3643 (2010).

[107] H. Chiriac, S. Corodeanu, M. Lostun, G. Ababei and T.-A. Óvári, "Magnetic behavior of rapidly quenched submicron amorphous wires", *J. Appl. Phys.* **107**, 09A301 (2010).

[108] A. Chizhik, A. Zhukov and J. Gonzalez, "Magnetic properties of sub-micrometric Fe-rich wires", *Thin Solid Films* **543**, 130 (2013).

[109] H. Chiriac, S. Corodeanu, M. Lostun, G. Stoian, G. Ababei and T.-A. Óvári, "Rapidly solidified amorphous nanowires", *J. Appl. Phys.* **109**, 063902 (2011).

[110] I. Utke, P. Hoffmann and J. Melngailis, "Gas-assisted focused electron beam and ion beam processing and fabrication", *J. Vac. Sci. Technol. B* **26**, 1197 (2008).

[111] W. F. van Dorp and C. W. Hagen, "A critical literature review of focused electron beam induced deposition", *J. Appl. Phys.* **104**, 081301 (2008).

[112] I. Utke, S. Moshkale and P. Russell, "Nanofabrication Using Focused Ion and Electron Beams. Principles and Applications", *Oxford Univ. Press* (2012).

[113] S. Matsui and K. Mori, "New Selective Deposition Technology by Electron Beam

Induced Surface Reaction", *Jpn. J. Appl. Phys.* **23**, L706 (1984).

[114] A. Fernández-Pacheco, J. M. De Teresa, R. Córdoba and M. R. Ibarra, "Magnetotransport properties of high-quality cobalt nanowires grown by focused-electron-beam-induced deposition", *J. Phys. D: Appl. Phys.* **42**, 055005 (2009).

[115] L. A. Rodríguez, L. Deen, R. Córdoba, C. Magén, E. Snoeck, B. Koopmans and J. M. De Teresa, "Influence of the shape and surface oxidation in the magnetization reversal of thin iron nanowires grown by focused electron beam induced deposition", *Beilstein J. Nanotechnol.* 6, 1319 (2015).

[116] L. Serrano-Ramón, R. Córdoba, L. A. Rodríguez, C. Magén, E. Snoeck, C. Gatel, I. Serrano, M. R. Ibarra and José María De Teresa, "Ultrasmall Functional Ferromagnetic Nanostructures Grown by Focused Electron-Beam-Induced Deposition", *ACS Nano* **5**, 7781 (2011).

[117] M. Jaafar, L. Serrano-Ramón, A. Fernández-Pacheco, M. R. Ibarra, J. M. De Teresa and A. Asenjo, "Hysteresis loops of individual Co nanostripes measured by magnetic force microscopy", *Nanoscale Res. Lett.* **6**, 407 (2011).

[118] M. Gavagnin, H. D. Wanzenboeck, D. Belić and E. Bertagnolli, "Synthesis of Individually Tuned Nanomagnets for Nanomagnet Logic by Direct Write Focused Electron Beam Induced Deposition", *ACS Nano* **7**, 777 (2013).

[119] P. Vavassori, M. Pancaldi, M. J. Perez-Roldan, A. Chuvilin and A. Berger, "Remote Magnetomechanical Nanoactuation", *Small* **12**, 1013 (2016).

[120] L. M. Belova, O. Hellwig, E. Dobisz and E. Dan Dahlberg, "Rapid preparation of electron beam induced deposition Co magnetic force microscopy tips with 10 nm spatial resolution", *Rev. Sci. Instrum.* **83**, 093711 (2012).

[121] A. Fernández-Pacheco, L. Serrano-Ramón, J. M. Michalik, M. R. Ibarra, J. M. De Teresa, L. O'Brien, D. Petit, J. Lee and R. P. Cowburn, "Three dimensional magnetic nanowires grown by focused electron-beam induced deposition", *Sci. Rep.* **3**, 1492 (2013).

Chapter 2: Experimental techniques

In this chapter, the main experimental techniques used for the fabrication and characterization of the nanostructures studied within this thesis are described. Particularly, in-depth descriptions of Focused Electron Beam Induced Deposition technology and Transmission Electron Microscopy are presented. Special emphasis is also focused on annealing and magnetic characterization methods, with strong focus on the Off-Axis Electron Holography technique.

2.1 Micro- and nanolithography techniques

The possibility of fabricating micro- and nanostructures opens the path towards systems of nanometre-scale size with novel capabilities and better performance. In this respect, micro- and nanolithography techniques are common methods used to produce minute structures by transferring a specific pattern to a sample. These nanoscale architectures are fabricated following two radically different routes: the bottom-up and the top-down approaches. The bottom-up methods concerns designs based on self-assembly or self-organization processes, highlighting the electrochemical deposition or the block co-polymers technology with promising applications and great tunability of the size, shape and periodicity of microdomains [1]. The top-down strategies are basically rooted in the deposition of thin films onto which the motifs are patterned by lithography techniques [2][3]. Several different types of top-down nanometre scale patterning lithography techniques have been developed over the course of the history, including: focused ion beam lithography [4][5]; electron beam lithography (EBL) [6][7]; those based on photons such as near-field scanning optical lithography [8], laser lithography [9], interference or holographic lithography [10][11][12], extreme ultraviolet lithography [13], X-ray lithography [14] and zone plate array lithography [15]; nano-stamping techniques such as micro-contact printing [16][17], nano-imprint [18] and step and flash imprint lithography [19]; and others such as nanogrifting [20] or dip-pen lithography [21].

In addition to the techniques mentioned above, FEBID deserves a special note as it has allowed the growth of most of the nanostructures fabricated in this thesis. Therefore, it will be described in detail throughout this section.

2.1.1 Dual Beam SEM-FIB system

The Dual Beam equipment combines a Focused Electron Beam, Scanning Electron Microscope (SEM), and a Focused Ion Beam (FIB) [22]. The system consists of an

electron column oriented vertically and an ion column tilted 52 degrees with respect to the electron column. The columns are pointing towards the working chamber where the sample is mounted in the intersection point of both electron and ion beams (eucentric height). A piezoelectric platform or stage is used to move and oriented the sample.

The electron column contains an electron source in the upper part. It is designed for generating a stable electron emission, using typically a Schottky field emission gun (S-FEG) with a ZrO_2-coated tungsten tip. This involves a thermally assisted field emission working at ~1300 K, with a brightness of ~10^8 A/cm^2/sr and energy spread of ~0.7 eV, eventually reaching an optimum resolution of ~0.9 nm using a monochromator. The ion column includes a liquid metal ion (LMI) source where a coil heater around the metal reservoir nurtures a tungsten needle to produce the ion probe after applying a voltage to the extraction electrode. A value of ~10^8 V/m allows the electrons to tunnel through the potential barrier generating a positively charged ion. In our case, Ga^+ is used due to its low melting point (29.8 ℃), low vapour pressure ($<10^{-37}$ mbar at room temperature) and long life (~1500 hours), exhibiting ~10^6 A/cm^2/sr and 4 nm resolution at best. However, new helium and neon ion microscopes with much better resolution (~0.5 nm) are currently being developed and marketed [23].

The optical system of both columns is composed by electromagnetic lenses and a set of apertures devoted to controlling the primary beam parameters. Right after the electron/ion gun, the condenser system defines the main probe features (mostly beam current and probe size). Afterwards, the scan coils enable the beam deflection controlled by the scan unit and the objective lens allows focusing the beam in the plane of interest. The electron beam voltage can operate usually between ~20 V and ~30 kV whereas the ion beam voltage ranges from ~500 V to ~30 kV. In the case of the current, by selecting different aperture sizes the electron beam generally works between ~1 pA and ~25 nA and the ion beam between ~0.1 pA and ~65 nA.
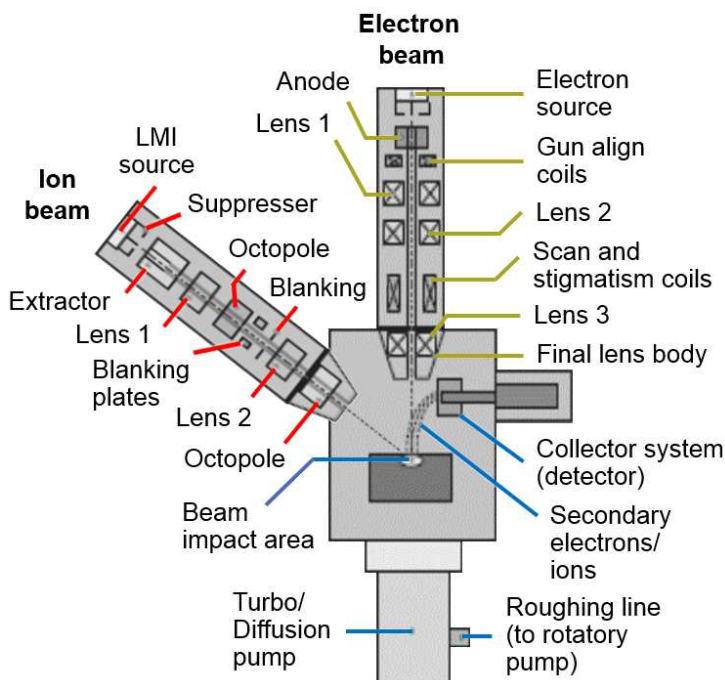
Figure 2.1. Schematic diagram of a Dual Beam SEM-FIB system.

The piezoelectric platform can be moved in the three spatial directions, rotated 360 degrees and tilted at any angle between -10 and 60 degrees. The vacuum system is comprised by four ion getter pumps working on the columns, and rotatory and turbomolecular pumps acting on the working chamber, reaching pressures below ~10^{-7} mbar in the columns (~10^{-10} mbar in the gun compartments) and around 1×10^{-6} mbar in the working chamber.

The image acquisition relies on the fundamental basis of a scanning microscope. The primary beam is scanned by the scan coils over a surface area of the sample following a desired pattern called raster, usually a square pattern defined by the scan unit. Normally, this scan entails a series of lines in the horizontal direction of a plane, slightly shifted by the scan coils from one another in the vertical direction using the scan generator. The interaction between the primary beam and the sample generates particles and radiation

which can be collected by the different detectors while the beam scans. After data processing, the final image is displayed in the computer screen. It is useful to place the specimen in the eucentric height, enabling simultaneous imaging using electrons and ions when tilting the stage.

The SEM column is generally devoted to imaging. The electron-sample interaction broadly generates secondary electrons (SE), backscattered electrons (BSE), characteristic X-rays, Auger electron and cathodoluminescence (visible light). In our case, SE and BSE are the most used particles for imaging operation. The SE are generated by the inelastic scattering of the primary beam with the valence electrons of the outer shells of the sample atoms. They are emitted with energies lower than ~50 eV, having mean free paths below 50 nm. Thus, since only the surface ones can escape and be detected, they are used to obtain images of topographic contrast. On the other hand, the BSE are generated by the quasi-elastic scattering of the primary beam with the nuclei of the atoms. Thus, the energy lost by these electrons is very little, being the momentum transfer large, allowing the electrons to be scattered at high angles and frequently backscattered. As BSE are high-energy electrons, they also come from the deeper regions of the sample and do not give accurate morphological information. However, they provide images with compositional contrast: the scattering cross section of the BSE increases with the atomic number, Z; therefore, the areas containing heavy elements are brighter than that of the lighter ones in the SEM images.
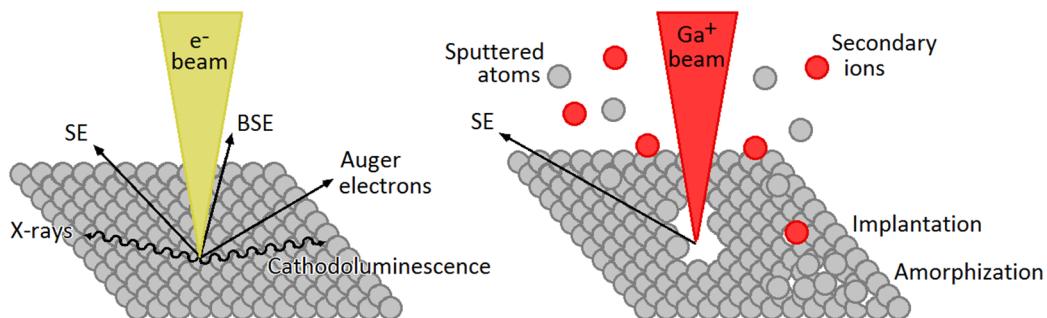
Figure 2.2. Basic diagram of the events caused by the beam-sample interaction.

In the case of FIB, the use is not limited to imaging. The ion-sample interaction generates SE, secondary ions and ion implantation, among others. When the kinetic energy of the ion beam exceeds the binding energy of the target material, the physical sputtering of the atoms occurs, thus the milling of the material surface. These events can also induce amorphization and volatilization of the irradiated region of the specimen [24].

The detectors installed in the system are usually the Everhart Thornley detector (ETD), the Through Lens detector (TLD) and the Ion-Conversion and Electron detector (ICE). The ETD is a scintillator photo-multiplier detector which collects SE, BSE and secondary ions. The TLD is mainly used for high resolution imaging and collects both SE and BSE. The ICE is a charged particle detector which collects secondary ions, SE and BSE. In our case, mainly ETD and TLD, and in lesser extent ICE, have been used to acquire images collecting SE. In addition, three working modes can be selected to tune the final performance: the field-free mode, the immersion mode and the Energy-Dispersive X-ray Spectroscopy (EDS) mode. The field-free mode generally assists navigation at low magnifications and can be used with ETD and ICE detectors. Moreover, an infrared charge-coupled device (CCD) camera allows the inner part of the working chamber to be observed and is used for spatial orientation of the sample. The immersion mode is used for ultra-high-resolution imaging, switching on the immersion lens (applying a magnetic field to collect more electrons) and normally collecting the SE with the TLD detector. Finally, the EDS mode is suitable for X-ray spectroscopy, reducing the power of the immersion lens and improving the X-ray signal. For this purpose, an EDS detector is mounted to collect X-ray photons coming from the sample.

Furthermore, the equipment is fitted with a gas injector system (GIS) formed by a set of injectors containing precursor material, which can be delivered locally on the surface substrate thanks to a stainless-steel needle and a very narrow nozzle. A heater regulates the temperature inside the GIS to the tenth of a degree, so an optimum value can be achieved, high enough to sublimate the precursor while preventing its thermal

decomposition inside the crucible. If a constant temperature is reached, a specific steady pressure is obtained. This implies that, if the vacuum in the working chamber is kept constant, the gas flux just depends on the saturated vapor pressure of the precursor and on the resistance due to the needle wall. The precursors used in this thesis and their operation temperatures are: dicobalt octacarbonyl, $Co_2(CO)_8$, at ~27 ºC; diiron nonacarbonyl, $Fe_2(CO)_9$, at ~28 ºC; trimethyl methylcyclopentadienyl platinum, $CH_3C_pPt(CH_3)_3$ at ~45 ºC; and tungsten hexacarbonyl, $W(CO)_6$, at ~55 ºC.

The system is also equipped with a nanomanipulator (Omniprobe®), used for precise sample mechanical operations in specific procedures such as lamella preparation. Finally, an anti-vibration system to minimize mechanical instabilities is placed in the ground.
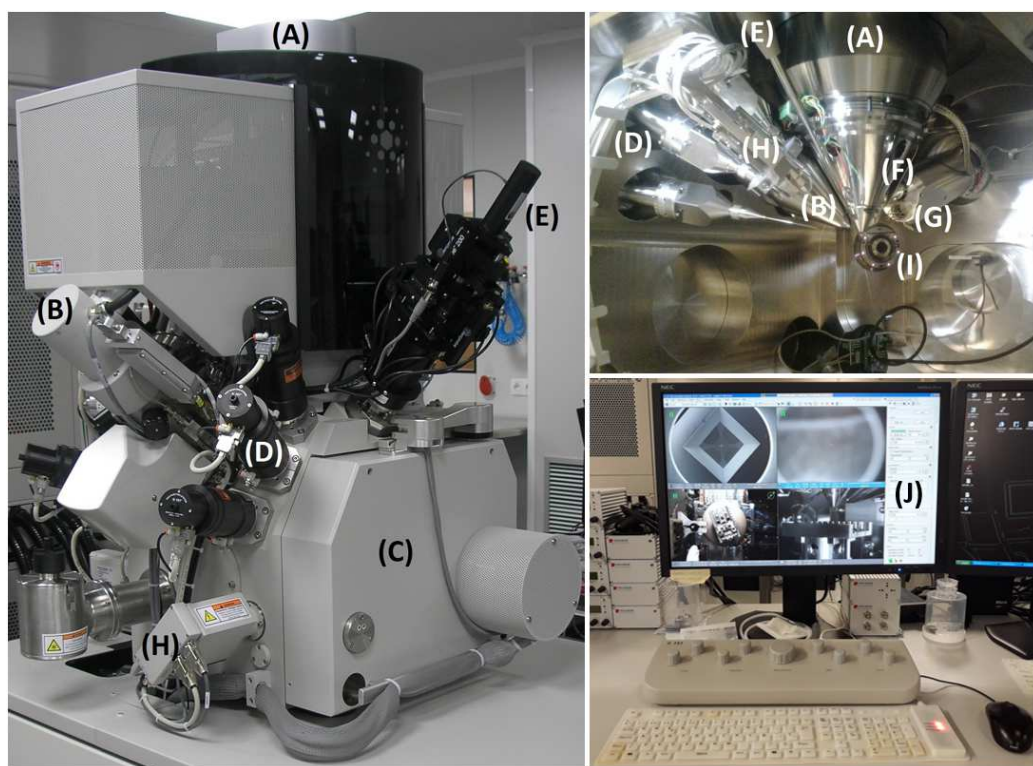
Figure 2.3. Image of the main components of a Dual Beam system: (A) SEM column, (B) FIB column, (C) process chamber, (D) gas injector system, (E) nanomanipulator, (F) TLD detector, (G) ETD detector, (H) ICE detector, (I) CCD camera and (J) software of the system.

Three commercial Dual Beam systems have been used: two FEI Helios NanoLab 600 and 650, installed in the Class 10000 clean room of the Laboratorio de Microscopías Avanzadas (LMA) located in the Instituto de Nanociencia de Aragón (INA) at the Universidad de Zaragoza, and the FEI Nova 200 NanoLab of the Institut für Elektronenmikroskopie und Nanoanalytik - Zentrum für Elektronenmikroskopie (FELMI-ZFE). Even though these instruments present some minor differences, the work is performed similarly in all of them.

2.1.1.1 Focused Electron Beam Induced Deposition

FEBID is a single-step nanolithography technique based on the delivery of precursor gas molecules close to the substrate, subsequently adsorbed on the surface, and eventually dissociated by a finely-focused electron beam producing a deposit of solid material [25][26][27][28].

Before the consolidation of FEBID, the potential of electron beam induced processing for patterning was hinted in the 1970s by the local deposition of contaminants in SEM [29]. When the SEM scans a region, a layer of a few nanometres starts to cover the scanned area. This phenomenon is produced by the decomposition of hydrocarbons present in the vacuum chamber as residual gases and adsorbed on the scanned surface. The technique was formally introduced in 1984 by S. Matsui [30][31], injecting different precursor gas molecules on purpose inside the vacuum chamber producing nanostructures with distinct functionalities. The last 30 years have witnessed the increasing interest of the scientific community and industry in the development of FEBID. Nowadays, this method is capable of nanometre-scale resolution for the growth of 2D [32] and 3D [33] structures. This unique capability of FEBID has been exploited in a broad range of applications, such as integrated circuit edit and mask repair [34], creation of electrical contacts [35], growth of magnetic nanowires [36], fabrication of plasmonic nanostructures [37], photodetection [38], gas sensing [39], etc.; thus becoming a key lithographic technique in Nanotechnology [40] and Materials Science [41].

Once the precursor gas molecules are injected locally near the substrate surface, some of them are dissociated by the electron beam. The non-volatile part of the gas is deposited whereas the volatile one is pumped out of the working chamber. The shape of the deposit is defined by the electron beam scan as well as the complex interactions between electron beam, substrate, precursor molecules and the growing structure [42][43]. For instance, the diffusion, adsorption and desorption phenomena of the molecules over the substrate or the probability of an electron to break the molecule bonds, mainly related to the electron energy, are crucial ingredients to understand the growth processes and determine how the fabrication process takes place.

The FEBID is also governed by many different parameters which must be controlled to obtain the desired nanostructures: the electron beam voltage, electron beam current, dwell time, refresh time, overlap, pitch, scan direction, pattern dimensions, precursor gas flux, etc. These variables will be discussed in Chapter 3, giving some details about their main functions and capabilities.
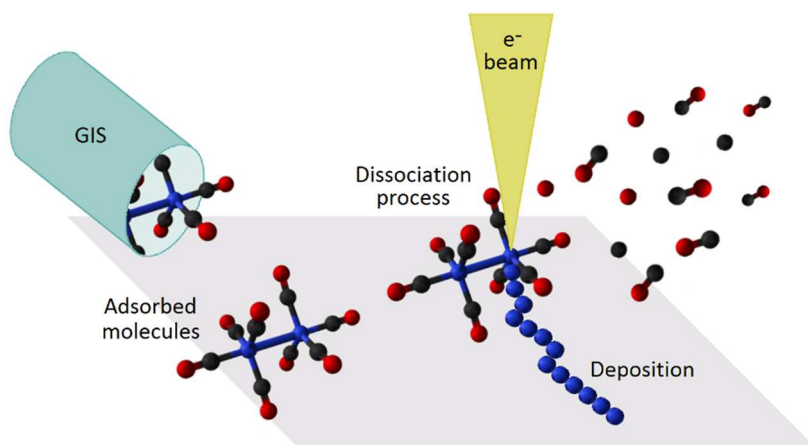
Figure 2.4. Diagram of the FEBID process using $Co_2(CO)_8$ as gas precursor.

2.1.2 Optical lithography

The optical lithography is based on the fabrication of microstructures by transferring a pattern into a wafer using masks and photosensitive materials which are subsequently developed with ultraviolet (UV) light. The process consists of several steps in sequence to obtain the final system.

In the basic process, a photosensitive chemical photoresist is spread all over the sample, already grown on top of the substrate, by spin coating. The photoresist is a viscous fluid usually composed by a polymer, a photosensitive component and a solvent. The polymer supplies the viscosity, adherence and resilience required for the ulterior chemical etching; the photosensitive component makes the photoresist sensitive to the UV radiation; and the solvent allows the polymer to be in solution and can be subsequently eliminated by soft-baking. Two different types of photoresists can be used, depending on its solubility upon UV irradiation: positive and negative photoresists. In a positive photoresist, the UV light breaks the polymer chains due to chemical reactions and the photosensitive complex increases its solubility, whereas the non-irradiated areas remain insoluble in the developer. The process is quite the contrary for a negative photoresist: it is soluble in the developer, while UV irradiation induces crosslinking of the polymer chains that reduces its solubility.

The desired pattern is transferred into the photoresist using a photomask, typically made of quartz with the motifs imprinted in chromium. Quartz is transparent to the UV light and the chromium absorbs this type of light. After the UV exposure, the resist becomes sensitized, the sample is immersed in the developing fluid and the soluble areas are removed. Then, dry or wet etching is performed to eliminate the film areas unprotected by the resist, and so the pattern is transferred to the sample. Finally, the remaining non-sensitized resist preserved on top of the remaining sample is removed by using acetone.

In the lift-off procedure, the growth of the film is carried out only after the motifs have been transferred onto a layer of resist on the substrate. Then, the sample is fabricated covering the substrate unprotected regions and resist areas, ensuring that the thickness of the resist is at least 50% higher than that of the sample. This guarantees that the underneath resist will be removed together with the sample deposited on top, keeping the areas where the sample is in direct contact with the substrate. If a positive mask is used, the sample pattern is supplementary to that of the mask and obtained without the etching step, in contrast to the basic optical lithography process.

The system used for optical lithography is the high-precision mask aligner SUSS MicroTec MA6 equipped with a Hg lamp exposure source, achieving a resolution down to ~2 µm. It is installed in the Class 100 clean room of the LMA-INA at the Universidad of Zaragoza. Besides, a spin coater and a hot plate SUSS MicroTec Delta 20T/200 are available in the same room to produce homogenous photoresist coatings under a speed up to 10^4 rpm and heat it up to 250 ºC.

Furthermore, thin film grown in the lift-off process is performed in an electron beam evaporator (E-beam PVD) Edwards 500 installed at the Class 10000 clean room. Thicknesses from 1 nm to 500 nm of metallic materials can be deposited with a resolution of 0.1 nm using a quartz balance for calibration. The base pressure is ~2×10^{-7} mbar, having four different targets to deposit material.

When dry etching is required, the removal of sample material is performed by physical processes using Ion Beam Etching (IBE). In this case, a beam of inert ions sputters the sample surface eliminating material in a uniform and homogeneous way. This has been carried out in the IBE SISTEC 600 equipment, fitted with argon gas, working at 2×10^{-7} mbar and equipped with a radiofrequency generator at 13.56 Hz and 600 W.
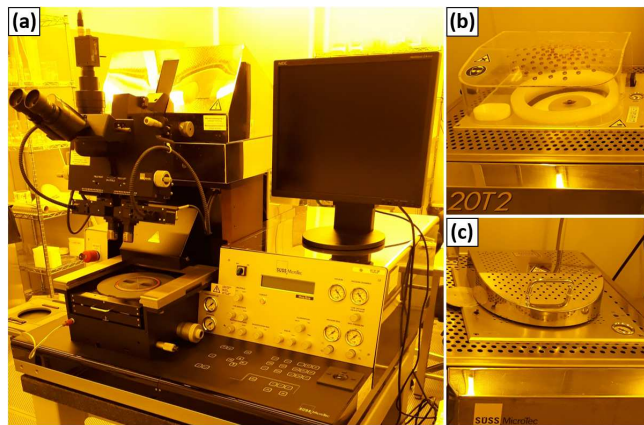
Figure 2.5. Images of (a) the mask aligner SUSS MicroTec MA6, and (b) the spin coater and (c) hot plate SUSS MicroTec Delta 20T/200 equipment for optical lithography.

Figure 2.6. Images of (a) the Ion Beam Etching and Milling SISTEC 600 and (b) the electron-beam evaporator (E-beam PVD) Edwards 500.

2.2 Transmission Electron Microscopy

TEM is a nanocharacterization technique based on the formation of an image with the electrons transmitted through a thin specimen irradiated with a high-energy electron beam, of typically 80-300 keV.

The spatial resolution of an optical system is limited by the radiation wavelength, λ. Even though residual aberrations introduced by the electron optics of the microscope, as

well as mechanical, electronic and thermal instabilities, degrades the resolution power, modern microscopes routinely provide atomic resolution, ~2 Å, and last-generation aberration corrected microscopes improve this value down to the sub-Å range [44].

When the primary electron-specimen interaction takes place, multiple events are originated, such as SE, BSE, characteristic X-rays, Auger electron, cathodoluminescence (visible light), inelastic scattering, elastic scattering, thermal diffuse scattering and Bremsstrahlung X-rays [45].

The microscope is divided in three main parts: the electron gun; the column, which includes the illumination system, the objective lens and the imaging system; and, the camera section. The electron source, located in the upper part of the machine, is composed by an emitter with an electrostatic lens (e.g., Wehnelt electrode in a thermionic gun or gun lens in a FEG). Then, the illumination system, placed in the column, starts to define the way the electrons will irradiate the specimen. It is composed by a set of condenser lenses (usually two or three) and condenser apertures devoted to defining the beam current, size and convergent angle.

The microscope can be configured to provide a broad beam illumination of the specimen, often known as TEM mode, or a convergent beam to form a small (sub-nm) probe. The latter is used in Scanning Transmission Electron Microscopy (STEM) mode, where this convergent probe is scanned over the specimen in a similar fashion as in SEM. To optimize and provide versatility to these types of illumination, a condenser mini lens located before the objective lens is strong excited (TEM mode) or weak excited (STEM mode).

Next to the region where the EDS detector are placed, the objective lens is devoted to forming the first image of the sample, thus being determinant for the ultimate resolution. It is disposed after the illumination system and is typically composed by two lenses called objective condenser lens and objective imaging lens, conforming the upper and lower polepieces, respectively. These twin lenses are symmetrically placed, and their

polepieces are separated by a space of ~6 mm where the specimen holder is inserted. The sample is fastened to a holder, allowing the displacement and tilting of the specimen around two independent axes in certain ranges. Some instruments are fitted with a Lorentz lens below the objective lens. This element is mandatory to form an image of the object if working in magnetic-field-free condition, the so-called Lorentz mode. As the objective lens applies a magnetic field of about 2 T around the specimen, it must be switched off to image the magnetization state of ferromagnetic specimens in remanence, and the Lorentz lens acts as an alternate objective lens inducing negligible field in the sample position.

The imaging system is situated in the lower part of the column. The diffraction pattern of the sample is formed in the back focal plane of the objective lens, a few millimetres below the specimen position. In this plane, the objective aperture can be inserted to select one or more diffracted beams. Depending on this choice, different imaging modes will be operating. In the case of a crystalline specimen, by choosing either only the direct beam or only one diffracted spot, Bright Field (BF) or Dark Field (DF) imaging is performed, respectively. These are often used to strengthen the image contrast or analyse the presence of crystalline defects. High Resolution Transmission Electron Microscopy (HRTEM) is performed when a larger aperture (or none) selects the direct beam and a set of diffracted beams symmetrically excited. As a result, in the objective lens' image plane, the interference pattern between these diffracted beams forms a HRTEM image, a representation of the crystalline lattice of the specimen.

In order to select the area of the specimen contributing to the diffraction pattern, the selected area diffraction aperture can be inserted in the first image plane of the objective lens. Being the object plane and the image plane optically conjugated, this real aperture —consisting of a metal slit with holes of different sizes— emulates the operation of a virtual aperture placed in the specimen plane. Some microscopes are fitted with an electrostatic Möllenstedt biprism installed in one of the holes of the selected area aperture

to perform Electron Holography (EH) experiments. It consists of a ~1 µm wire in diameter made of drawn glass fibre coated with a metal, usually gold or platinum. Please, refer to Off-Axis EH subsection for further details.

Finally, the imaging system is a set of lenses that project the image or the diffraction pattern onto a viewing screen or the recording device. Controlling the strength of an intermediate lens, the projector lens allows to screen either an image or the diffraction pattern of the specimen for viewing or recording. The projection meets a fluorescent screen or a computer-controlled CCD camera, both positioned below the imaging lenses. In STEM mode, some dedicated detectors can be used depending on the scattering angle of the electrons: high-angle annular dark field (HAADF), annular dark field (ADF) and BF detectors. In this case, the image formation is performed electronically, similarly to an SEM. Finally, it is after the imaging system where an electron energy loss spectrometer or energy filter is usually installed in analytical microscopes.

The electromagnetic lenses introduce aberrations, defined as defects in the image formation associated with a lack of correspondence between the points of an object and the points of its image. Similarly to light optics, the image formation with non-paraxial electrons induce aberrations such as astigmatism, coma, chromatic aberration, spherical aberration, etc. However, simultaneously the electromagnetic lenses included in the TEM are round-shaped and benefit from the Lorentz force not only to command the electron beam direction but also the aberration correction. For instance, the magnetic dipoles are used to deflect the electron beam; and, quadrupoles, hexapoles, octupoles and dodecapoles are utilized to right aberrations together with the apertures, which can exclude the aberrated electrons. As an example, the objective lens is designed to present small chromatic (~1 mm) and spherical (~1 mm) aberrations thanks to an extremely small focal length of ~1 mm. As a result, most of the aberrations can be corrected easily with the optical elements, except the spherical aberration which finally determines the spatial resolution in a conventional TEM, i.e., ~2 Å. To overcome this limitation, subsidiary

aberration correctors installed in the column (both for the objective lens in TEM mode and for the probe in STEM mode) are used to achieve a resolution below 1 Å. The so-called imaged-corrected microscopes set the corrector immediately after the objective lens for improving the resolution in TEM techniques, whereas in the probed-corrected microscopes is disposed just before the scan coils and the objective lens for enhancing the resolution in STEM techniques.

The vacuum system helps avoiding the collision and scattering of electrons with residual gas molecules, allowing the electrons to travel along the column and clearly interact with the specimen. It also keeps specimen surface clean enough during the experiments. For this aim, the machine is typically equipped with rotatory, oil-diffusion, turbomolecular and ion getter pumps, working together with a liquid N_2 trap, to achieve $\sim 2 \times 10^{-8}$ mbar in the gun, $\sim 4.5 \times 10^{-8}$ mbar in the column and $\sim 8.5 \times 10^{-7}$ mbar in the camera chamber. Besides, before inserting the sample inside the column, the standard procedure is to eliminate the possible surface contamination of both the sample and holder. For this, an external plasma cleaner system generates a reactive O_2/Ar plasma which remove the organic residues, especially carbon-hydrogen bonds.

Seven different transmission electron microscopes have been used: the commercial FEI Titan Cube 60-300, Titan Low Base 60-300, Tecnai F30 and Tecnai T20 installed at the INA in Zaragoza; the FEI Titan Cube G2 60-300 and Tecnai F20 at the FELMI-ZFE in Graz; and, the Hitachi I2TEM hosted by the Centre d'Élaboration de Matériaux et d'Etudes Structurales (CEMES) - Centre National de la Recherche Scientifique (CNRS) in Toulouse. The instrument used for each experiment along this thesis will be specified in due course.
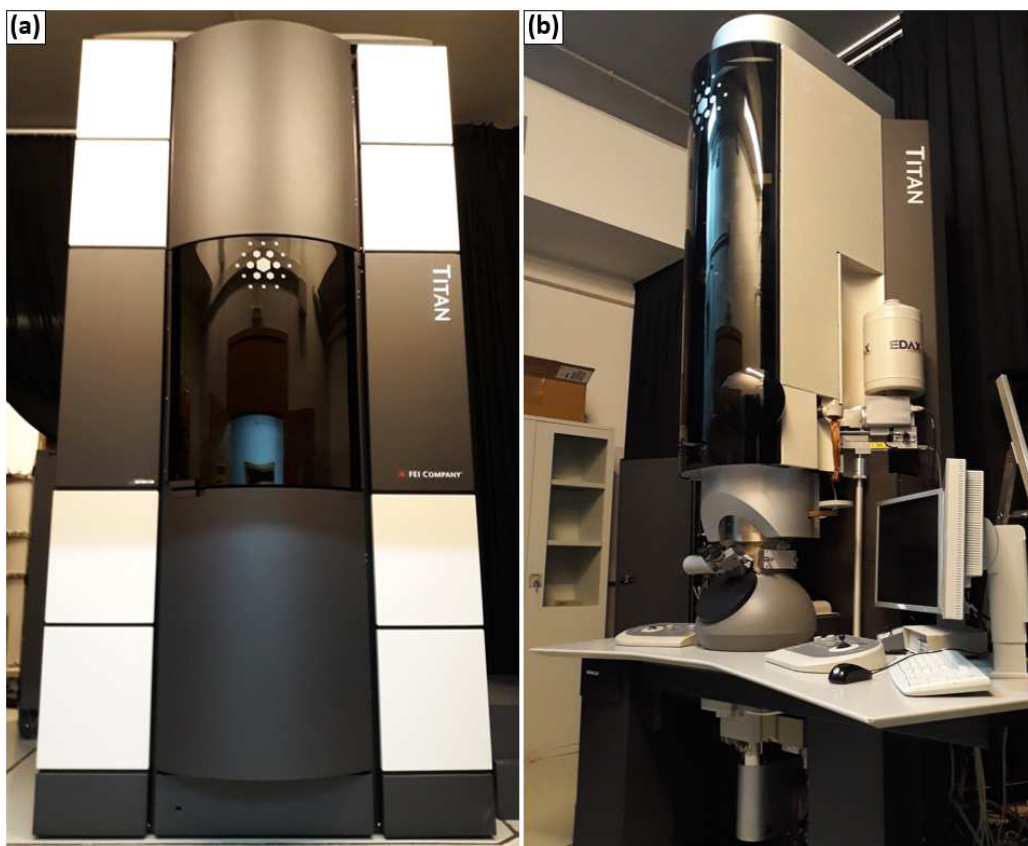
Figure 2.7. Images of (a) the FEI Titan Cube 60-300 and (b) Titan Low Base 60-300 TEM microscopes.

2.2.1 Transmission Electron Microscopy techniques

The numerous events produced by electron-matter interaction can be exploited in different ways to characterize materials, and dozens of imaging, diffraction and spectroscopic techniques have been developed over decades. Please, refer to textbooks for a general overview. Here, special focus is given to those techniques used in this thesis.

Regarding the imaging techniques, diffraction contrast (BF, DF and weak beam), phase contrast (HRTEM) and energy filter TEM and STEM imaging (BF-, DF- and HAADF-STEM) are most common. Concerning diffraction techniques, selective area electron diffraction (SAED), convergent beam electron diffraction (CBED), large angle

convergent beam electron diffraction (LACBED) and energy filtered electron diffraction are the most significant ones. In the case of analytical techniques, electron energy loss spectroscopy (EELS), EDS, spectrum imaging (STEM-EELS/EDS) and image spectrum (e.g., energy filtered TEM images) can be utilized for chemical characterization. Finally, other techniques can be applied to measure other specimen properties such as EH, Lorentz microscopy, *in situ* TEM, electron tomography, cryogenic TEM, environmental TEM, electron magnetic circular dichroism (electron energy-loss magnetic chiral dichroism), confocal TEM, time resolved TEM, etc.

Nonetheless, only 8 techniques have been used in this thesis: HRTEM, HAADF-STEM, DF-STEM, STEM-EELS, STEM-EDS, EH, *in situ* TEM and SAED. In brief, HRTEM is based on the imaging of the interference pattern of multiple elastic diffracted beams; in HAADF-STEM, high angle scattering electrons are collected with an intensity dependence on the average atomic number, forming a chemical contrast (*Z*-contrast) image; in DF-STEM, diffraction disks in the surroundings of the direct beam are collected giving rise to a diffraction contrast image; STEM-EELS is used for the chemical analysis by measuring the energy lost by the electrons which pass through the specimen; in STEM-EDS, the chemical composition can be measured by the collection of the generated X-ray photons; EH is used to characterize the magnetic state of the specimen; *in situ* TEM is devoted to performing experiments measuring the properties of a material on site; and, SAED, a technique appropriate for microstructural analysis.

2.2.1.1 Electron Energy Loss Spectroscopy

Spectroscopic techniques are based on the occurrence of inelastic scattering interaction of primary electrons with matter, which can be used to analyze the chemical and electronic properties of the specimen.

The EELS analysis technique can be used to obtain specimen compositional information benefiting from the electron energy lost in the electron beam-sample

interaction. More specifically, elastic electrons conserve their energy, whereas the inelastically scattered electrons carry different energies once they pass through the sample. In other words, the narrow energy range of the primary electron beam is dispersed in the transmitted electron beam.

In general, EELS shows its enormous potential in combination with STEM mode. In this case, the method supplies qualitative and quantitative analyses offering the possibility of chemical mapping down to atomic resolution, elemental quantification, fine structure analysis, etc. However, the signal intensity decreases quickly while increasing the energy loss, and this fact hampers the investigation of heavy atoms and limits the spectrum usefulness up to ~2-3 keV [46]. It is worth underscoring at this point that EDS is a perfect complementary technique to cover this shortcoming evidenced by EELS.

The scattering mechanisms can be classified in three main groups according to the spectrum energy ranges. The zero-loss spectrum region (approximately $E < 1$ eV) contains the elastic and quasielastic electrons. The zero-loss peak underlies the energy spread of the electron source, generally measured by the full width at half maximum (FWHM). The low loss region (approximately 1 eV $< E < 50$ eV) yields mainly electronic information coming from the inter- and intra-band transitions [47], surface and volume plasmon excitations [48] and Cherenkov radiation [49]. Finally, the high-loss region ($E > 50$ eV), also called core-loss region, essentially encloses details about core-shell electronic states, bonding and atomic distribution or crystal environment [50]. Therefore, it allows the chemical identification and quantification [51], which are the tools most commonly used in the characterization experiments performed throughout this thesis.

In an EELS spectrometer, the transmitted electrons, selected by an entrance aperture, travel through a magnetic prism, being deflected a certain angle depending on the lost energy by a magnetic field, and then a complex electron optical system projects the spectrum onto a CCD camera. In many cases the same spectrometer can also act as an energy filter to form energy filtered TEM (EFTEM) images, i.e., images formed by

electrons of a specific energy loss. As a result, a spectrum is formed by representing the intensity and the energy loss. Many parameters can be controlled such as the spectrometer energy resolution, entrance aperture, collection angle, objective aperture diameter, camera length, etc. Further details and specific values will be given during the next chapters as the experiments are presented.

Three different spectrometers have been used: a Tridiem 863 Gatan Energy Filter (GIF) installed in the FEI Tecnai F30 TEM; a Tridiem 866 ERS GIF in the FEI Titan Low Base 60-300; and a GIF Quantum in the FEI Titan Cube G2 60-300 [52].

2.2.1.2 Energy-Dispersive X-ray Spectroscopy

The EDS system is based on the analysis of X-ray photons coming from the sample. This process comes about when the electron beam excites an electron of the inner shell of the atom, generating a hole. Subsequently, electrons from a higher-energy shell occupies the created hole, producing X-rays in cascade with discrete, characteristic energies corresponding to the difference between energy levels of the atom [53].

Since the X-rays have specific energies which depends on the energy difference between two atomic levels and each chemical element has a unique atomic structure, EDS technique provides information about the chemical composition of the sample. In the EDS spectra, where the number of counts as a function of the energy is represented, each peak is associated with one electronic transition of a single element [54].

The EDS system is composed by the detector, the processing electronics and the computer. Firstly, the detector generates a charge pulse which is proportional to the photon energy, converting it to a voltage signal before amplifying it by means of a field-effect transistor. Then, the pulse is identified electronically, and a digital signal is stocked in the corresponding channel allocated for that specific energy displaying the spectrum.

In this thesis, three different EDS systems have been used at the INA: the APOLLO X detector associated with the EDAX software and mounted in the FEI Helios NanoLab

650; the EDAX 136-5 detector coupled with the Genesis RTEM software embedded in FEI's TIA software installed in the FEI Tecnai F30 TEM; and, the Oxford INCA 200 EDS setup from Oxford Instruments set in the FEI Helios NanoLab 600.

2.2.1.3 Off-Axis Electron Holography

Off-Axis EH is an interferometric technique which measures the amplitude and the phase shift of the electron wave transmitted through the specimen. This phase shift is directly related to the electromagnetic fields produced by the sample, which can be determined in a quantitative way.

The behaviour of a relativistic electron wave, $\psi(\vec{r})$, in an electromagnetic field is described by the Dirac equation:

$$\frac{1}{2m_e} = \left(-i\hbar\nabla + e\vec{A}\right)^2 \psi(\vec{r}) = e[U^* + \gamma V]\,\psi(\vec{r}) \tag{2.1}$$

where m_e is the rest mass of the electron, $\hbar$ the reduced Planck constant, e the electron charge, $\vec{A}$ the magnetic potential, V the electric potential, $\gamma = 1 + eU^*/m_e c^2$ the relativistic Lorentz factor and U^* the relativistic accelerating potential. The solution of the equation is the object wavefunction whose phase shift, $\varphi(x,y)$, is altered by the Aharonov-Bohn effect [55]. Particularly, the phase shift of an electron wave advancing along the z axis and passing through a magnetic specimen with neutral charge can be expressed mathematically as:

$$\varphi(x,y) = \frac{\pi\gamma}{\lambda U^*} \int V_{MIP}(x,y,z)\,dz - \frac{e}{\hbar} \iint B_\perp(x,y,z)\,dxdz \tag{2.2}$$

where λ is the electron relativistic wavelength, V_{MIP} the mean inner potential and $B_\perp$ the magnetic induction vector orthogonal to the unitary vectors along x and z axes [56].

At this point, it should be introduced the object electron wave, ψ_{obj}, defined as the transmitted electron wavefunction in the exit surface of the specimen. If a very thin

specimen is considered, the electrons are elastically scattered and the absorption effects can be neglected, giving rise to the following equation:

$$\psi_{obj}(\vec{r}) = a(\vec{r}) \exp[i\varphi(\vec{r})] \tag{2.3}$$

where a is the amplitude of the exit wavefunction and φ the phase shift induced by the electric and magnetic potentials of the specimen. Then, the objective lens forms a diffraction pattern and an image in the back focal plane and the image plane, respectively. In this process, the objective lens introduces aberrations to the object electron wave. Thus, the object electron wave in the back focal plane, ψ_{diff}, can be expressed as a function of the frequency $\vec{k}$:

$$\psi_{diff}(\vec{k}) = \psi_{obj}(\vec{k}) \, T(\vec{k}) \tag{2.4}$$

where $T(\vec{k})$ is the phase contrast transfer function, a mathematical expression of the modifications of the electron wave caused by the instrument (not by the specimen):

$$T(\vec{k}) = A(\vec{k}) \exp\left[-g(\vec{k})\right] \exp\left[i\chi(\vec{k})\right] \tag{2.5}$$

where $A(\vec{k})$ is the aperture-related frequency cutoff, $\exp\left[-g(\vec{k})\right]$ the damping introduced by microscope instabilities and $\chi(\vec{k})$ the phase shift introduced by the aberrations of the objective lens. In a first approximation, if low order aberrations (such as stigmatism, coma) are suppressed:

$$\chi(\vec{k}) = \frac{2\pi}{\lambda} \left[\frac{\Delta_z}{2} \lambda^2 k^2 + \frac{C_s}{4} \lambda^4 k^4 \right] \tag{2.6}$$

where Δ_z is the defocus and C_s is the spherical aberration coefficient. As a result, this phase shift is transferred to the image, ultimately establishing the bases of the phase contrast imaging. Nonetheless, since the image should be in focus, and the magnetic induction emerged from the specimen induces small angular deflections ($k \ll \lambda$), $\chi(\vec{k})$

can be neglected. In this case, the image electron wave, ψ_{imag}, and the intensity of the image, I, are:

$$\psi_{imag}(\vec{k}) = FT^{-1}\big[\psi_{obj}(\vec{k})\,T(\vec{k})\big] \cong a(\vec{r})\exp[i\varphi(\vec{r})] = \psi_{imag}(\vec{r}) \qquad (2.7)$$

$$I(\vec{r}) = \psi_{imag}(\vec{r})\,\psi^*_{imag}(\vec{r}) = |a(\vec{r})|^2 \qquad (2.8)$$

The image only contains information about amplitude variations (which are very small in thin specimens), and the phase information, dependant of the electric and magnetic fields, is lost. To overcome this issue, EH enables the retrieval of the amplitude and the phase of the electron wave separately [57][58].

Experimentally, EH is based on the interference between two different electron waves; a reference electron wave, ψ_{ref}, which propagates through the vacuum, ideally interacting with no electromagnetic field; and the object electron wave, ψ_{obj}, transmitted through the sample, which experiences a phase shift by interacting with any electromagnetic field inside and around the specimen. The overlapping and interference of ψ_{ref} and ψ_{obj} is originated by the deflection of the electrons when a voltage is applied to the electrostatic Möllenstedt biprism, generating the holographic fringes. The BF image of the specimen, overlapped with the fringe pattern, is the so-called electron hologram [59][60].

From the theoretical point of view, in EH ψ_{ref} and ψ_{obj} are considered plane waves:

$$\psi_{ref}(\vec{r}) = \exp\big[i2\pi\,\vec{k}\cdot\vec{r}\big] \qquad (2.9)$$

$$\psi_{obj}(\vec{r}) = a(\vec{r})\exp\big[i2\pi\,\vec{k}\cdot\vec{r} + i\varphi(\vec{r})\big] \qquad (2.10)$$

The two waves are deflected by the biprism $\alpha/2$ and $-\alpha/2$ angles along x axis, respectively.
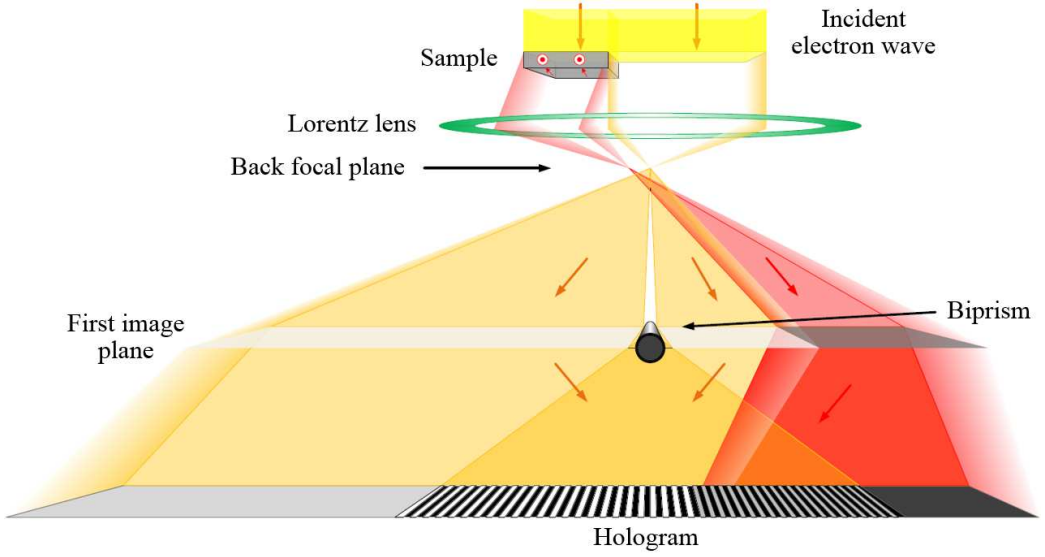
Figure 2.8. Basic scheme of the EH technique, reproduced from [61] with permission.

This leads to the ψ_{int} electron wave along x axis in the superimposing:

$$\psi_{int}(\vec{r}) = a(\vec{r}) \exp\left[-i\pi\frac{\alpha}{\lambda}x + i\varphi(\vec{r})\right] + \exp\left[i\pi\frac{\alpha}{\lambda}x\right] \tag{2.11}$$

whose intensity I is:

$$I(\vec{r}) = |\psi_{int}(\vec{r})|^2 = 1 + a^2(\vec{r}) + 2a(\vec{r})\cos\left[2\pi\frac{\alpha}{\lambda}x - \varphi(\vec{r})\right] \tag{2.12}$$

where $1 + a^2(\vec{r})$ contains the intensity of the BF image, and the sinusoidal term represents the interference fringes pattern of the hologram with its argument depending only on the phase of the object electron wave. The calculation of the Fourier Transform (FT) of the intensity leads to:

$$FT|I(\vec{r})| = \delta(u) + FT[a(\vec{r})] + FT[a(\vec{r})\exp[i\varphi(\vec{r})]] \otimes \delta\left(\vec{u} + \frac{\alpha}{\lambda}\hat{x}\right) +$$
$$+ FT[a(\vec{r})\exp[-i\varphi(\vec{r})]] \otimes \delta\left(\vec{u} - \frac{\alpha}{\lambda}\hat{x}\right) \tag{2.13}$$

where $\otimes$ indicates the convolution operation. In the reciprocal space, the hologram is formed by three different components: a central band and two sidebands. The first two terms of the right-hand side of the Equation 2.13 represent the central band and contains the BF image related to the elastic and inelastic scattered electrons with the amplitude of the object electron wave. These do not store any detail about the phase, so they have not further interest to obtain magnetic information. On the other hand, each sideband contains redundant information about the amplitude and phase separately; hence, data processing is only done with one of them. The inverse Fourier Transform (FT^{-1}) of a centred sideband allows the reconstruction of the object electron wave as the combination of an amplitude image and a phase image:

$$FT^{-1}\big[FT[a(\vec{r})\exp[i\varphi(\vec{r})]] \otimes \delta[\vec{u}]\big] = a(\vec{r})\exp[i\varphi(\vec{r})] = \psi_{obj}(\vec{r}) \qquad (2.14)$$

where:

$$\varphi(\vec{r}) = \arctan\left[\frac{\mathrm{Im}\big[\psi_{obj}(\vec{r})\big]}{\mathrm{Re}\big[\psi_{obj}(\vec{r})\big]}\right] \qquad (2.15)$$

$$a(\vec{r}) = \left[\big[\mathrm{Im}[\psi_{obj}(\vec{r})^{obj}]\big]^2 + \big[\mathrm{Re}[\psi_{obj}(\vec{r})^{obj}]\big]^2\right]^{1/2} \qquad (2.16)$$

So far, this process can be applied to any magnetic specimen. However, in order to continue with the process devoted to separating the electrostatic and magnetic contributions, it is illustrative to consider a specific example. Please, refer to Annex A where the data processing is applied for ferromagnetic nanowires.

Two different TEM microscopes have been used for the EH experiments: the commercial FEI Titan Cube 60-300 at the INA in Zaragoza and the Hitachi I2TEM at the CEMES-CNRS in Toulouse.

2.3 Annealing techniques

The fabrication of nanostructures by FEBID technique has some drawbacks which can be overcome by annealing experiments. The metallic purity, the crystallinity and the magnetization of the deposits is susceptible of being improved by this strategy.

Two different annealing setups have been used: a heating stage mounted inside the SEM Quanta FEG 250 installed at the INA in Zaragoza and a heating chip Wildfire S3 from DENSsolutions in the FEI Titan Cube G2 60-300 at the FELMI-ZFE in Graz.

The first one, devoted to *ex situ* experiments, is formed by a heating stage base which holds all the components [62]. It includes two disk-shaped insulating elements made of aluminous foam and a heater placed between the insulators consisting of a micro-furnace in which samples are heated from the sides, ensuring temperature uniformly distributed. It is also equipped with a thermocouple, ceramic connectors, a graphite crucible to mount the samples, two ceramics papers on top to reduce heat losses and protect the insulators from damage, a cover plate to fix the components and a heat shield to keep the temperature homogeneous in the sample. In addition, it is fitted with a chamber feed-through plate, a water chiller, a flow box, water hoses and a microprocessor-controller, devoted to providing the desired temperature in the heating stage. The sensor accuracy is ±1 ºC with an operation range from room temperature to ~1000 ºC with a maximum heating ramp of 50 ºC/min.

The second one is the TEM-heating system Wildfire S3 for *in situ* experiments. The specimen is placed in a heating chip which includes micro-electro-mechanical systems (MEMS) [63]. The substrate includes oval holes where the suspended nanostructures can be imaged. The chip is specially developed for having small drift (< 1 nm/min at 800 ºC), heating rates of 200 ºC/ms and image resolution of ~0.6 Å at 800 ºC. Then it is mounted into the heating stage using a lock and four pin connections to control the temperature.
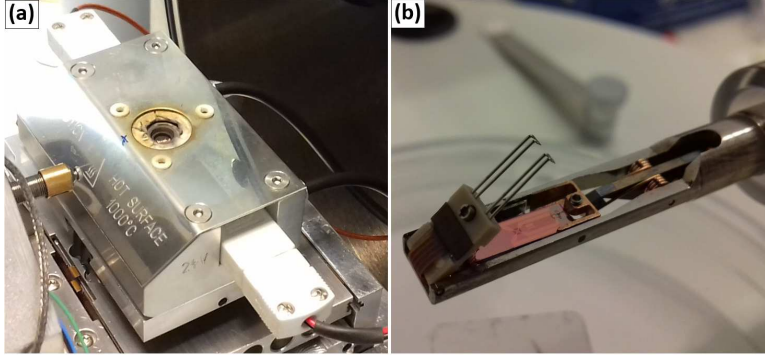
Figure 2.9. Images of (a) the heating stage mounted in the SEM Quanta FEG 250, and (b) the Wildfire S3 *in situ* TEM heating holder from DENSsolutions.

2.4 Further magnetic characterization techniques

In this section, three different experimental methods employed for the magnetic characterization of ferromagnetic nanostructures are described. The physical principles of Superconducting QUantum Interference Device (SQUID) magnetometry, Magneto-Optical Kerr Effect (MOKE) magnetometry and MFM will be sketched.

2.4.1 Superconducting Quantum Interference Device magnetometry

The SQUID is used for measuring changes in the magnetic field related to the magnetic flux quantization. It is considered one of the most sensitive magnetic flux detectors, achieving a field resolution of 10^{-17} T [64]. The principle which underpins the operation of a SQUID is the quantization of the magnetic flux [65][66]:

$$\Phi_0 = \frac{h}{2e} \cong 2.07 \times 10^{-15} \text{ T} \cdot m^2 \tag{2.17}$$

where Φ_0 is the magnetic flux quantum, h is the Planck constant and e the electron charge. The device is based on a superconducting loop interrupted by either one (RF-SQUID) or two parallel Josephson junctions (DC-SQUID) [67]. Explaining the basics in the last case, the bias current enters the loop and is divided into two paths where the

Josephson junctions are present by introducing a very thin insulating layer. A magnetic flux, Φ, threads the superconducting loop being an integer number multiple of the elementary magnetic flux quantum, Φ_0.

Two wavefunctions represent the two superconducting areas separated by the Josephson junctions with phases θ_1 and θ_2:

$$\psi_1 = |\psi|e^{i\theta_1} \tag{2.18}$$

$$\psi_2 = |\psi|e^{i\theta_2} \tag{2.19}$$

Both wavefunctions penetrate the thin insulating layer and overlap, thus Cooper pairs of electrons tunnel through the barrier with a current, I_s, which is proportional to the phase difference between the two superconducting parts at the insulating layer [68]:

$$I_s = I_c \sin(\theta_2 - \theta_1) \tag{2.20}$$

where I_c is the critical current. If a constant bias current is kept, the voltage across the junctions oscillates with the phase change. At the same time, the current flowing through the SQUID is modulated by the magnetic flux passing through the loop. Thus, measuring the voltage, the response to a change of flux can be detected.

The SQUID equipment used in this thesis was a home-made system developed by Dr. María José Martínez-Pérez from the Instituto de Ciencia de Materiales de Aragón (ICMA), Universidad de Zaragoza-Consejo Superior de Investigaciones Científicas (CSIC).

2.4.2 Magneto-Optical Kerr Effect magnetometry

Magnetization induces changes in the optical properties of the material. In particular, when polarized light is reflected a magnetic surface, its polarization and intensity are modified [69]. These changes of a polarized laser beam after reflecting from a magnetized

sample surface can be detected by MOKE magnetometry, eventually inferring the magnetization of the sample.

Firstly, the machine is typically composed by a 3D motion stage to place the sample. Also, a quadrupole electromagnet surrounds the sample and can apply magnetic fields in two orthogonal directions. The magnetic fields are measured by sensors installed into the coils while an electronic control loop adjusts the electron current in the coils in real time to provide the desired field strength. In addition, the optics head unit contains the laser optics allowing the beam to leave the head and come to a polarizer which selects the light polarization. Then, the beam is focused on the sample surface by a set of lenses which allows the laser to be incident either normal to the surface or at 45 degrees to the surface normal [70]. After the beam is reflected from the sample surface, it is collimated by a lens and passes through an analyser. Then, the intensity and polarization are evaluated.

The system shows the polarization rotation, also called Kerr signal, as a function of the applied magnetic field, obtaining the hysteresis loop. In general, this technique provides high sensitivity and fast measurement times, being considered an excellent method for experiments on magnetic nanostructures [71], microstructures [72] and thin films [73].

Two different MOKE systems have been used: few experiments were performed in the NanoMOKE®3 magneto-optical magnetometer installed in the ICMA, Universidad de Zaragoza-CSIC, and most work has been performed in the MOKE equipment settled in the Cavendish Laboratory at the University of Cambridge.

2.4.3 Magnetic Force Microscopy

The MFM technique is a non-contact mode of the scanning force microscopy based on the detection of magnetic tip-sample interactions at the nanoscale. The method lies in understanding and exploiting the long-range forces arising from the magnetic fields in order to investigate magnetic domain structures [74].

The system is basically composed by a magnetic probe and a scanning detection system. The probe is usually formed by a non-magnetic cantilever, typically silicon- or silicon nitride-based. Its tip, which has a radius of curvature on the order of nanometres, is coated by a magnetic material. The experimental set-up also includes a laser spot reflecting from the upper part of the cantilever into a photodetector (array of photodiodes) to measure the deflection of the cantilever while it is scanning the sample surface thanks to a piezoelectric scanner.

There are many forces involved in the tip-sample interaction: mechanical contact forces, capillary forces, van der Waals forces, electrostatic forces, magnetic forces, etc. The magnetic field gradient of the sample produces a force which typically becomes relevant between 20 nm and 100 nm, ensuring the magnetostatic coupling between the tip and the sample at this long range. As a result, one of the most widespread approaches is the retrace mode, where a first pass registers the topography, as occurs in AFM, and a second one repeats the line scan at a certain distance *z* above it. Using this strategy, it is possible to correlate the topographic and magnetic information. The MFM contrast is proportional to the magnetic pole density at the surface. Thus, samples with perpendicular or in-plane (IP) anisotropy can be studied, where the poles are located at the domains or at the domain walls, respectively. After signal processing, a magnetic image of the sample is obtained.

The sensitivity and spatial resolution, which can achieve values of ~10 nm under optimum conditions [75][76], determine the potential of the technique and are limited by different factors such as the tip-sample distance, the magnetized volume of the tip, the type of cantilever, the tip magnetic moment, etc.

Two different operation modes can be used to measure the tip-sample interaction: the static mode, where the magnetic force coming from the sample and acting on the tip is detected; and, the dynamic mode, where the force derivative is registered. Focusing on the dynamic MFM to illustrate the working mode, the cantilever is driven to work near

its resonant frequency by piezoelectric elements [77]. The presence of the gradient of the force, $\partial F_z/\partial z$, modifies the effective spring constant of the cantilever, K [78]:

$$K = K_0 + \frac{\partial F_z}{\partial z} \tag{2.21}$$

where K_0 is the spring constant of the free cantilever. If there is an attractive (repulsive) force between the sample and the tip, the cantilever effectively softens (stiffens), the resonant frequency decreases (increases) and the detection system measures a shift on the oscillation amplitude, phase or frequency. For instance, in the case of the frequency:

$$\frac{\Delta\omega}{\omega_0} \propto \frac{1}{2K} \frac{\partial F_z}{\partial z} \tag{2.22}$$

where $\Delta\omega$ is the frequency shift and ω_0 the frequency of the free cantilever. Thus, the scanning of the sample surface allows obtaining the image of the field gradients associated with the magnetic domains [79].

The MFM measurements have been performed using a scanning force microscope from Nanotec Electronica installed at the Instituto de Ciencia de Materiales de Madrid (ICMM), CSIC.

References

[1] W. A. Lopes and H. M. Jaeger, "Hierarchical self-assembly of metal nanostructures on diblock copolymer scaffolds", *Nature* **414**, 735 (2001).

[2] D. Bratton, D. Yang, J. Dai and C. K. Ober, "Review Recent progress in high resolution lithography", *Polym. Adv. Technol.* **17**, 94 (2006).

[3] C. Park, J. Yoon and E. L. Thomas, "Enabling nanotechnology with self assembled block copolymer patterns", *Polymer* **44**, 6725 (2003).

[4] C. M. Melliar-Smith, "Ion etching for pattern delineation", *J. Vac. Sci. Technol.* **13**, 1008 (1976).

[5] H. Morimoto, Y. Sasaki, K. Saitoh, Y. Watakabe and T. Kato, "Focused ion beam lithography and its application to submicron devices", *Microelectron. Eng.* **4**, 163 (1986).

[6]   S. Y. Chou, M. S. Wei, P. R. Krauss and P. B. Fischer, "Single-domain magnetic pillar array of 35 nm diameter and 65 Gbits/in.^{2} density for ultrahigh density quantum magnetic storage", *J. Appl. Phys.* **96**, 6673 (1974).

[7]   D. V. Nicolau, T. Taguchi, H. Taniguchi and S. Yoshikawa, "Negative and Positive Tone Protein Patterning on E-Beam/Deep-UV Resists", *Langmuir* **15**, 3845 (1999).

[8]   M. K. Herndon and R. T. Collins, "Near-field scanning optical nanolithography using amorphous silicon photoresists", *Appl. Phys. Lett.* **74**, 141 (1999).

[9]   J. Fischer and M. Wegener, "Three-dimensional optical laser lithography beyond the diffraction limit", *Laser Photonics Rev.* **7**, 22 (2013).

[10]   A. Lasagni, C. Holzapfel, T. Weirich and F. Mu, "Laser interference metallurgy : A new method for periodic surface microstructure design on multilayered metallic thin films", *Appl. Surf. Sci.* **253**, 8070 (2007).

[11]   M. Campbell, D. N. Sharp, M. T. Harrison, R. G. Denning and A. J. Turberfield, "Fabrication of photonic crystals for the visible spectrum by holographic lithography", *Nature* **404**, 53 (2000).

[12]   T. A. Savas, M. Farhoud, H. I. Smith, M. Hwang and C. A. Ross, "Properties of large-area nanomagnet arrays with 100 nm period made by interferometric lithography", *J. Appl. Phys.* **85**, 6160 (1999).

[13]   B. Wu and A. Kumar, "Extreme ultraviolet lithography: A review", *J. Vac. Sci. Technol. B* **25**, 1743 (2007).

[14]   C. Miramond, C. Fermon, F. Rousseaux, D. Decanini and F. Carcenac, "Permalloy cylindrical submicron size dot arrays", *J. Magn. Magn. Matter* **165**, 500 (1997).

[15]   I. J. Djomehri, T. A. Savas and H. I. Smith, "Zone-plate-array lithography in the deep ultraviolet", *J. Vac. Sci. Technol. B* **16**, 3426 (1998).

[16]   J. L. Wilbur, A. Kumar, H. A. Biebuyck, E. Kim and G. M. Whitesides, "Microcontact printing of self-assembled monolayers: applications in microfabrication", *Nanotechnology* **7**, 452 (1996).

[17]   A. Cerf, C. Thibault, M. Geneviève and C. Vieu, "Ordered arrays of single DNA molecules by a combination of capillary assembly , molecular combing and soft-lithography", *Microelectron. Eng.* **86**, 1419 (2009).

[18]   S. Y. Chou, P. R. Krauss and P. J. Renstrom, "Nanoimprint lithography", *J. Vac. Sci. Technol. B* **14**, 4129 (1996).

[19]   T. Bailey, B. J. Choi, M. Colburn, M. Meissl, S. Shaya, J. G. Ekerdt, S. V Sreenivasan and C. G. Willson, "Step and flash imprint lithography: Template surface treatment and defect analysis", *J. Vac. Sci. Technol. B* **18**, 3572 (2000).

[20] K. Wadu-Mesthrige, S. Xu, N. A. Amro and G. Liu, "Fabrication and Imaging of Nanometer-Sized Protein Patterns", *Langmuir* **15**, 8580 (1999).

[21] R. D. Piner, J. Zhu, F. Xu, S. Hong and C. A. Mirkin, ""Dip-pen" Nanolithography", *Science* **283**, 661 (1999).

[22] FEI Company, "Helios NanoLab 450/450 S/450 ML/650/600i User Operation Manual", (2012).

[23] N. Klingner, R. Heller, G. Hlawacek, J. von Borany, J. Notte, J. Huang and S. Facsko, "Nanometer scale elemental analysis in the helium ion microscope using time of flight spectrometry", *Ultramicroscopy* **162**, 91 (2016).

[24] T. Fujii, K. Iwasaki, M. Munekane, T. Takeuchi, M. Hasuda, T. Asahata, M. Kiyohara, T. Kogure, Y. Kijima and T. Kaito, "A nanofactory by focused ion beam", *J. Micromech. Microeng.* **15**, S286 (2005).

[25] S. J. Randolph, J. D. Fowlkes and P. D. Rack, "Focused, Nanoscale Electron-Beam-Induced Deposition and Etching," *Crit. Rev. Solid State Mater. Sci.* **31**, 55 (2006).

[26] W. F. Van Dorp and C. W. Hagen, "A critical literature review of focused electron beam induced deposition", *J. Appl. Phys.* **104**, 081301 (2008).

[27] I. Utke, P. Hoffmann and J. Melngailis, "Gas-Assisted Focused Electron Beam and Ion Beam Processing and Fabrication", *J. Vac. Sci. Technol. B* **26**, 1197 (2008).

[28] M. Huth, F. Porrati, C. Schwalb, M. Winhold, R. Sachser, M. Dukic, J. Adams and G. Fantner, "Focused electron beam induced deposition: A perspective", *Beilstein J. Nanotechnol.* **3**, 597 (2012).

[29] A. N. Broers, W. W. Molzen, J. J. Cuomo and N. D. Wittels, "Electron-beam fabrication of 80-Å metal structures", *Appl. Phys. Lett.* **29**, 596 (1976).

[30] S. Matsui and K. Mori, "New Selective Deposition Technology by Electron Beam Induced Surface Reaction", *Jpn. J. Appl. Phys.* **23**, L706 (1984).

[31] S. Matsui and K. Mori, "New selective deposition technology by electron-beam induced surface reaction", *J. Vac. Sci. Technol. B* **4**, 299 (1986).

[32] L. van Kouwen, A. Botman and C. W. Hagen, "Focused electron-beam-induced deposition of 3 nm dots in a scanning electron microscope" *Nano Lett.* **9**, 2149 (2009).

[33] J. D. Fowlkes, R. Winkler, B. B. Lewis, M. G. Stanford, H. Plank and P. D. Rack, "Simulation-Guided 3D Nanomanufacturing via Focused Electron Beam Induced Deposition", *ACS Nano* **10**, 6163 (2016).

[34] T. Bret, T. Hofmann and K. Edinger, "Industrial perspective on focused electron beam-induced processes", *Appl. Phys. A* **117**, 1607 (2014).

[35]   S. Sangiao, S. Martín, A. González-Orive, C. Magén, P. J. Low, J. M. De Teresa and P. Cea, "All-Carbon Electrode Molecular Electronic Devices Based on Langmuir-Blodgett Monolayers", *Small* **13**, 1603207 (2017).

[36]   I. Utke, P. Hoffmann, R. Berger, and L. Scandella, "High-resolution magnetic Co supertips grown by a focused electron beam", *Appl. Phys. Lett.* **80**, 4792 (2002).

[37]   R. Winkler, F.-P. Schmidt, U. Haselmann, J. D. Fowlkes, B. B. Lewis, G. Kothleitner, P. D. Rack and H. Plank, "Direct-Write 3D Nanoprinting of Plasmonic Structures", *ACS Appl. Mater Interfaces* **9**, 8233 (2017).

[38]   K. Makise, K. Mitsuishi, M. Shimojo and K. Furuya, "A nanosized photodetector fabricated by electron-beam-induced deposition", *Nanotechnology* **20**, 425305 (2009).

[39]   F. Kolb, K. Schmoltner, M. Huth, A. Hohenau, J. Krenn, A. Klug, E. J. W. List and H. Plank, "Variable tunneling barriers in FEBID based PtC metal-matrix nanocomposites as a transducing element for humidity sensing", *Nanotechnology* **24**, 305501 (2013).

[40]   L. Hirt, A. Reiser, R. Spolenak and T. Zambelli, "Additive Manufacturing of Metal Structures at the Micrometer Scale", *Adv. Mater.* **29**, 1604211 (2017).

[41]   M. Huth, F. Porrati and O. V. Dobrovolskiy, "Focused electron beam induced deposition meets materials science", *Microelectron. Eng.* **185-186**, 9 (2018).

[42]   H. Plank, D. A. Smith, T. Haber, P. D. Rack and F. Hofer, "Fundamental Proximity Effects in Focused Electron Beam Induced Deposition", *ACS Nano* **6**, 286 (2012).

[43]   R. Winkler, A. Szkudlarek, J. D. Fowlkes, P. D. Rack, I. Utke and H. Plank, "Toward Ultraflat Surface Morphologies During Focused Electron Beam Induced Nanosynthesis: Disruption Origins and Compensation", *ACS Appl. Mater. Interfaces* **7**, 3289 (2015).

[44]   P. Hawkes and J. C. H. Spence, "Science of Microscopy", *Springer* (2007).

[45]   D. B. Williams and C. B. Carter, "Transmission Electron Microscopy. A textbook for materials science", *Springer* (2009).

[46]   I. Maclaren, K. J. Annand, C. Black and A. J. Craven, "EELS at very high energy losses", *Microscopy* **67**, 78 (2018).

[47]   Y. Sato and M. Terauchi, "High-Energy Resolution Electron Energy-Loss Spectroscopy Study of Interband Transitions Characteristic to Single-Walled Carbon Nanotubes", *Microsc. Microanal.* **20**, 807 (2014).

[48]   C. Colliex, M. Kociak and O. Stéphan, "Electron Energy Loss Spectroscopy imaging of surface plasmons at the nanometer scale", *Ultramicroscopy* **162**, A1 (2016).

[49]   N. Zabala, A. Rivacoba, F. J. García de Abajo and A. Pattantyus, "Cherenkov radiation effects in EELS for nanoporous alumina membranes", *Surf. Sci.* **532-535**, 461 (2003).

[50]   J. A. Mundy, Q. Mao, C. M. Brooks, D. G. Schlom and D. A. Muller, "Atomic-resolution chemical imaging of oxygen local bonding environments by electron energy loss spectroscopy", *Appl. Phys. Lett.* **101**, 042907 (2012).

[51]   L. Lajaunie, F. Boucher, R. Dessapt and P. Moreau, "Quantitative use of electron energy-loss spectroscopy Mo-M$_{2,3}$ edges for the study of molybdenum oxides", *Ultramicroscopy* **149**, 1 (2015).

[52]   A. Gubbens, M. Barfels, C. Trevor, R. Twesten, P. Mooney, P. Thomas, N. Menon, B. Kraus, C. Mao and B. McGinn, "The GIF Quantum, a next generation post-column imaging energy filter", *Ultramicroscopy* **110**, 962 (2010).

[53]   C. E. Lyman, D. E. Newbury, J. I. Goldstein, D. B. Williams, A. D. Romig Jr., J. Armstrong, P. Echlin, C. Fiori, D. C. Joy, E. Lifshin and K.-R. Peters, "Scanning Electron Microscopy, X-Ray Microanalysis, and Analytical Electron Microscopy. A Laboratory Workbook", *Springer* (1990).

[54]   J. R. Michael, "Energy-Dispersive X-ray Spectrometry in Ultra-high Vacuum Environments", *X-Ray Spectrometry in Electron Beam Instruments*, Edited by D.B. Williams, J. I. Goldstein and D. E. Newbury, *Springer* (1995).

[55]   Y. Aharonov and D. Bohm, "Significance of electromagnetic potentials in the quantum theory", *Phys. Rev.* **115**, 485 (1959).

[56]   H. Lichte and M. Lehmann, "Electron holography-basics and applications", *Rep. Prog. Phys.* **71**, 016102 (2008).

[57]   E. Snoeck, R. E. Dunin-Borkowski, F. Dumestre, P. Renaud, C. Amiens, B. Chaudret and P. Zurcher, "Quantitative magnetization measurements on nanometer ferromagnetic cobalt wires using electron holography", *Appl. Phys. Lett.* **82**, 88 (2003).

[58]   L. Marín, L. A. Rodríguez, C. Magén, E. Snoeck, R. Arras, I. Lucas, L. Morellón, P. A. Algarabel, J. M. De Teresa and M. R. Ibarra, "Observation of the Strain Induced Magnetic Phase Segregation in Manganite Thin Films", *Nano Lett.* **15**, 492 (2015).

[59]   H. Lichte, "Parameters for high-resolution electron holography", *Ultramicroscopy* **51**, 15 (1993).

[60]   A. Tonomura, "Electron-holographic interference microscopy", *Adv. Phys.* **41**, 59 (1992).

[61]   C. Magén, L. A. Rodríguez, L.-E. Serrano-Ramón, C. Gatel, E. Snoeck and J. M. De Teresa, "In situ Lorentz microscopy and electron holography magnetization

studies of ferromagnetic focused electron beam induced nanodeposits", *Magnetic Characterization Techniques for Nanomaterials*, Edited by C. S. S. R. Kumar, *Springer* (2017).

[62] FEI Company, "The Quanta FEG 250/450/650 User Operation Manual", (2010).

[63] T. P. Almeida, D. McGrouther, Y. Pivak, H. H. Perez Garza, R. Temple, J. Massey, C. H. Marrows and S. McVitie, "Preparation of high-quality planar FeRh thin films for in situ TEM investigations", *J. Phys.: Conf. Ser.* **903**, 012022 (2017).

[64] R. L. Fagaly, "Superconducting quantum interference device instruments and applications", *Rev. Sci. Instrum.* **77**, 101101 (2006).

[65] B. S. Deaver and W. M. Fairbank, "Experimental evidence for quantized flux in superconducting cylinders", *Phys. Rev. Lett.* **7**, 43 (1961).

[66] R. Doll and M. Näbauer, "Experimental proof of magnetic flux quantization in a superconducting ring", *Phys. Rev. Lett.* **7**, 51 (1961).

[67] B. D. Josephson, "Possible new effects in superconductive tunneling", *Phys. Lett.* **1**, 251 (1962).

[68] R. P. Feynman, R. B. Leighton and M. L. Sands, "The Feynman lectures on physics", *Addison-Wesley Pub. Co.* (1963).

[69] Z. Q. Qiu and S. D. Bader, "Surface magneto-optic Kerr effect (SMOKE)", *J. Magn. Magn. Mater.* **200**, 664 (1999).

[70] Durham Magneto Optics Ltd, "NanoMOKE®3 User Manual", (2012).

[71] S. Pathak and M. Sharma, "Magneto-optical Kerr effect measurements on highly ordered nanomagnet arrays", *J. Appl. Phys.* **111**, 07E331 (2012).

[72] Y. Jingfan, R. Pérez del Real, G. Infante and M. Vázquez, "Local magnetization profile and geometry magnetization effects in microwires as determined by magneto-optical Kerr effect", *J. Appl. Phys.* **113**, 043904 (2013).

[73] A. Berger, S. Knappmann and H. P. Oepen, "Magneto-optical Kerr effect study of ac susceptibilities in ultrathin cobalt films", *J. Appl. Phys.* **75**, 5598 (1994).

[74] U. Hartmann, "Magnetic force microscopy", *Adv. Mater.* **2**, 550 (1990).

[75] L. M. Belova, O. Hellwig, E. Dobisz and E. Dan Dahlberg, "Rapid preparation of electron beam induced deposition Co magnetic force microscopy tips with 10 nm spatial resolution", *Rev. Sci. Instrum.* **83**, 093711 (2012).

[76] M. R. Koblischka, U. Hartmann and T. Sulzbach, "Improving the lateral resolution of the MFM technique to the 10 nm range", *J. Magn. Magn. Mater.* **272-276**, 2138 (2004).

[77] G. Binnig, C. F. Quate and C. Gerber, "Atomic Force Microscope", *Phys. Rev. Lett.* **56**, 930 (1986).

[78] D. Rugar and P. Hansma, "Atomic Force Microscopy", *Physics Today* **43**, 23 (1990).

[79] O. Kazakova, R. Puttock, C. Barton, H. Corte-León, M. Jaafar, V. Neu and A. Asenjo, "Frontiers of magnetic force microscopy", *J. Appl. Phys.* **125**, 060901 (2019).

Chapter 3: Tuning the growth of 3D nanowires by FEBID

This chapter covers the capability of Focused Electron Beam Induced Deposition to tailor shape, composition and magnetization of 3D nanowires. Particularly, a comprehensive study about the complex mechanisms which govern the growth process and strategies undertaken to tailor their physical properties are tackled. Further, a special section about electrically-biased metal structure patterned on insulators is addressed, which allows fabricating nanostructures on insulating substrates and tuning the lateral dimension of 3D nano-objects by electric biasing.

3.1 Principles of FEBID

FEBID relies on the decomposition of the precursor gas molecules delivered close to the substrate by a finely-focused electron beam, producing a deposit [1][2][3][4]. The shape of the deposit is determined by the electron beam scan as well as complex interactions between the electron beam, substrate, precursor gas molecules and the growing structure [5][6]. Understanding the influence of the FEBID parameters is a key point to develop proper approaches for the fabrication of nanostructures with optimum properties. Simultaneously, it is important to understand the mechanisms governing the deposition to provide a complete view of this technique.

The concurrent control of the various parameters that play a role in the growth process of nanostructures by FEBID is a daunting task [1]. The energy of the primary electrons, which is directly related to beam acceleration voltage, and the electron beam current, defined as the electron flow reaching the sample surface, are two of the most important variables. However, one should also point out other parameters related to the electron beam scan such as the dwell time, which identifies the lapse for which the electron beam is held still on a particular point; the refresh time, which is the period of time between the start of two consecutive loops and allows precursor gas replenishment during the time where the beam is paused in between the loops; the pitch, which is the distance between two neighbouring dwell points; and, the scan direction, associated with the movement of the beam within the pattern. In addition, the number of loops, pattern dimensions and geometry are included. Finally, parameters related to the environmental conditions such as the base pressure, the type of gas precursor and flux, the position of the GIS nozzle, the type of substrate, the temperature or the residence time of the precursor molecules are also decisive variables for the fabrication of nano-objects.

With the goal of learning how these parameters affect the growth operation and handle them, the dissociation process caused by the electron beam deserves special attention. Among the many distinct electron-molecule interaction processes [7], the

elastic scattering, vibrational and electronic excitation, dissociative electron attachment, neutral and bipolar dissociation, and dissociative ionization can be mentioned. In light of this situation, it may be thought that the beam-molecule interaction is too complex to have a thorough knowledge and comprehension of the mechanism at molecular scale. In fact, few experimental [8] and theoretical studies [9] in this regard are reported in literature. However, unsophisticated simulations of the fabrication process by continuum models and approaches of growth geometries by Monte Carlo method have been already considered to clarify the intricacies of the FEBID growth process [10].

To shed light on this topic, the single precursor species continuum model of FEBID should be contemplated. This model considers a weak precursor-substrate interaction and neglects the interplay between the adsorbed precursor gas molecules. Firstly, Langmuir adsorption where the surface coverage is described as a function of the precursor adsorbate density, n, is assumed. Secondly, an average residence time, τ, of the precursor gas molecules on the substrate surface is taken into account. Thirdly, the surface diffusion phenomenon of the precursor gas molecules is also considered. Finally, the dissociation induced by the electron beam is modelled by a depletion of n proportional to the dissociation cross-section, σ_d, and the electron flux distribution per unit time and area, f. Thus, the radially symmetric rate equation is written as follows [11]:

$$
\frac{\partial n(r,t)}{\partial t} = sJ\left[1 - \frac{n(r,t)}{n_{ML}}\right] - \frac{n(r,t)}{\tau} + D\left[\frac{\partial^2 n(r,t)}{\partial r^2} + \frac{1}{r}\frac{\partial n(r,t)}{\partial r}\right] -
$$
$$
- \sigma_d f(r)n(r,t) \tag{3.1}
$$

where the adsorption, desorption, diffusion and dissociation terms can be sequentially identified in the right-hand side of the equation. In the adsorption term, s is the sticking coefficient, J the precursor flux, n_{ML} the complete area density which corresponds to that of a monolayer, and $1 - n/n_{ML}$ the fraction of surface sites available for adsorption. The desorption term defines the adsorbate density per τ period before desorption. The

diffusion term denotes the spreading of the precursor gas molecules on the surface and is proportional to the diffusion constant, D. Finally, the dissociation term indicates the reduction of n assuming an energy-integrated σ_d and a radially symmetric f with the Gaussian shape:

$$f(r) = \frac{I/e}{2\pi a^2} \exp\left(-\frac{r^2}{2a^2}\right) \tag{3.2}$$

where I is the electron beam current, e the electron charge, a the standard deviation and r the radial parameter.

Additionally, the local deposition growth rate $\mathcal{R}$ can be defined as:

$$\mathcal{R}(r) = \frac{V\sigma_d f(r)}{t_D} \int_0^{t_D} n(r,t)\, dt \tag{3.3}$$

where V is the non-volatile deposited product arisen from a precursor gas molecule and t_D the dwell time. Neglecting the diffusion term —which can be a good approach for a wide range of D and t_D values [1]—, the analytical solution of Equation 3.3 can be obtained:

$$\mathcal{R} = V\sigma_d f \left[sJ\left(\frac{1}{k_r} - \frac{1}{k_d}\right)\frac{1 - \exp(-k_d t_D)}{k_d t_D} + \frac{sJ}{k_d} \right] \tag{3.4}$$

where k_d is the depletion rate and k_r the replenishment rate:

$$k_d = \frac{sJ}{n_{ML}} + \frac{1}{\tau} + \sigma_d f \tag{3.5}$$

$$k_r = \frac{sJ}{n_{ML}} + \frac{1}{\tau} \tag{3.6}$$

A rough interpretation of the growth rate can be obtained as a function of t_D. On the one hand, for relatively small t_D, —typically on the order of nanoseconds —, $\mathcal{R}$ increases

as a function of f. This depositing scenario is the *electron-limited regime* because the growth is restricted by inability of the electron beam to decompose all precursor molecules. On the other hand, in the case of large t_D, the dissociation rate exceeds the gas precursor replenishment rate, giving rise to the *precursor-limited regime*. The balance between the availability of precursor molecules on the growth area and the electron beam current is very important because it will determine whether the growth occurs in the *precursor-limited regime* or the *electron-limited regime*, which will affect not only the growth rate but also the composition of the nanowire [12]. Furthermore, when thermal heating of the growing deposit occurs, as previously found in FEBID [13][14][15][16][17], the decomposition of the precursor gas molecules will be more efficient if temperatures close to the thermal decomposition of the precursor are reached. These concepts are of utmost importance for determining the appropriate conditions, i.e., the ideal value of each parameter, to ensure an efficient decomposition process.

The general notion of the theory presented here can be applied for the fabrication of any type of structure and offers a starting point to begin working. However, although this brings a global overview, given the multitude of nanostructures shapes and materials, the optimization process of the specific variables is essential to find out the best results.

3.2 Tailoring the fundamental properties of 3D cobalt nanowires

Many types of materials raise great interest for their study at the nanoscale. For instance, thin-film layers and multilayers based on magnetic materials have nowadays various applications in the fields of data storage and sensing, one example of this being the hard disks [18][19]. Even so, individual magnetic nano-objects are also being investigated and engage huge attention due to their great potential in applications such as sensors [20], memories [21] and logics [22]. In this case, most of the approaches for their fabrication rely on standard lithography procedures, most adequate for patterning 2D structures onto magnetic thin films and multilayers. However, there is an increasing

interest on the fabrication of 3D magnetic nanostructures. In this regard, FEBID is one of the techniques that allow addressing the growth of such 3D structures [23][24][25][26][27], particularly those based on magnetic materials [28][29][30][31] [32][33][34][35][36][37].

The use of precursor gas molecules containing magnetic elements such as Co, Fe and Ni permits the growth of magnetic deposits [28][38][39][40][41][42][43][44]. A large development has been made towards the growth of magnetic deposits with high metal content, high magnetization, high resolution and complex shapes, as recently reviewed [45][46]. Such development has been focused on the optimization of thin in-plane magnetic layers, whereas limited work has been done in the case of 3D magnetic deposits. However, there are many promising applications of 3D magnetic deposits in scanning probe techniques, such as MFM [34] and Ferromagnetic Resonance Force Microscopy [47], racetrack-type magnetic memories [31], Hall sensors [48][49], nanomagnetic logic circuits [34][50], superconducting vortex lattice pinning [51], remote magneto-mechanical actuation [37], etc. 3D fabrication implies the understanding of specific growth phenomena which do not happen in the case of 2D deposits, and as a result new interpretation emerges from the nanofabrication process.

Previous work on the growth of 3D nanowires by FEBID has shown the relevance of several parameters that should be taken into account. For example, the use of sub-nA electron beam currents produced by field-emission guns is mandatory for the growth of narrow nanowires (<100 nm in diameter) [31][52]. Moreover, thermal effects can be of tremendous importance in 3D nanostructures given that precursor replenishment in the area of growth occurs at a lower rate compared to in-plane deposits because the diffusion mechanism of precursor gas molecules from the substrate will be weakened as the deposit grows in height. When growing a 3D nanowire, the substrate surface close to the growth point is small and the number of precursor gas molecules adsorbed to be decomposed is lower than in 2D deposits. In addition, since heat dissipation is difficult, the temperature

increases in the growth point and can give rise to interesting effects such as growth regime transitions, discussed in the next subsections.

In this context, the impact of the most relevant growth parameters on the specific properties of 3D ferromagnetic nanostructures and their final performance will be explored in this section. The focus is put on the characterization of the obtained nanowire's diameter, composition and magnetization, with the aim of growing narrow nanowires (<100 nm in diameter), with high Co content (>80% at.) and magnetization approaching the bulk value.

3.2.1 Experimental details

The nanowires were fabricated in the commercial Helios Nanolab 600 and 650 Dual Beam equipment using $Co_2(CO)_8$ as a gas precursor. The substrates were TEM Cu grids. Co deposits were grown with low electron beam currents (≤100 pA). The voltage was fixed to 5 kV given that preliminary experiments did not lead to significant changes in the composition from 5 kV to 30 kV. The nanowires were grown in spot mode, where the electron beam is continuously irradiating a single point. A base chamber pressure of ~1×10^{-6} mbar was achieved before the injection of the precursor, with the GIS needle position at ~50 μm in x, y and z directions. The precursor gas flux was tuned via a manual valve, which permits to vary the chamber pressure up to ~4×10^{-5} mbar. Even though the precursor gas flux cannot be measured directly, given its linear relationship with the chamber pressure increase during gas injection, ΔP, and the precursor gas flux, J, stated as $J \propto \Delta P$ [53], monitorization of the chamber pressure during growth allows to establish relative correlations with the physical properties of the 3D nanowires.

Some of the EDS experiments were performed in the Helios Nanolab 650 Dual Beam, using an excitation electron beam voltage of 5 kV and beam current of 800 pA. Other EDS experiments were carried out in an FEI Tecnai F30 TEM operated at 300 kV. EELS experiments were performed in the FEI Tecnai F30 TEM and in a probe-corrected

Titan Low Base 60-300 TEM, both operated at 300 kV. The second one is equipped with a high brightness S-FEG and a CETCOR corrector for the condenser system to provide sub-Å probe size. The experiments were acquired with a 50 mrad convergence semi-angle and EELS spectra with an energy dispersion of 0.8 eV and energy resolution around 1.5 eV.

Off-Axis EH was carried out in an image-corrected FEI Titan Cube 60-300 TEM operated at 300 kV and equipped with an S-FEG and a CETCOR corrector for the objective lens and a motorized electrostatic biprism. The experiments were performed in Lorentz mode, where the objective lens is switched off and the Lorentz lens operates as the image-forming lens. The image corrector was aligned to minimize the aberrations of the Lorentz lens, providing a spatial resolution of 1-2 nm. The excitation of the biprism was varied between 180 and 220 V, depending on the actual diameter of the nanowires, to produce holograms with a fringe contrast range of 20-25%. The acquisition time of the holograms was set to 5 s. The magnetic induction was calculated using the Equation A.3.

3.2.2 Linear and radial growth regimes

The interplay of the precursor gas flux and the electron beam for the fabrication of out-of-plane ferromagnetic Co nanowires grown by FEBID is investigated. In particular, the results reveal a set of growth parameters which produce a change in the diameter during the growth of a single nanowire. This is a consequence of the subtle balance between the factors governing the growth of 3D nanowires, as discussed hereafter.

Let us focus on the first SEM image of a 3D Co nanowire presented in this thesis, shown in Figure 3.1(a). As it can be observed, a narrow nanowire with a diameter of 62 nm and length of 1.60 µm (aspect ratio of 25, defined as the quotient between the length and the diameter) is obtained with a beam current of 86 pA and ΔP of 7.3×10^{-6} mbar.
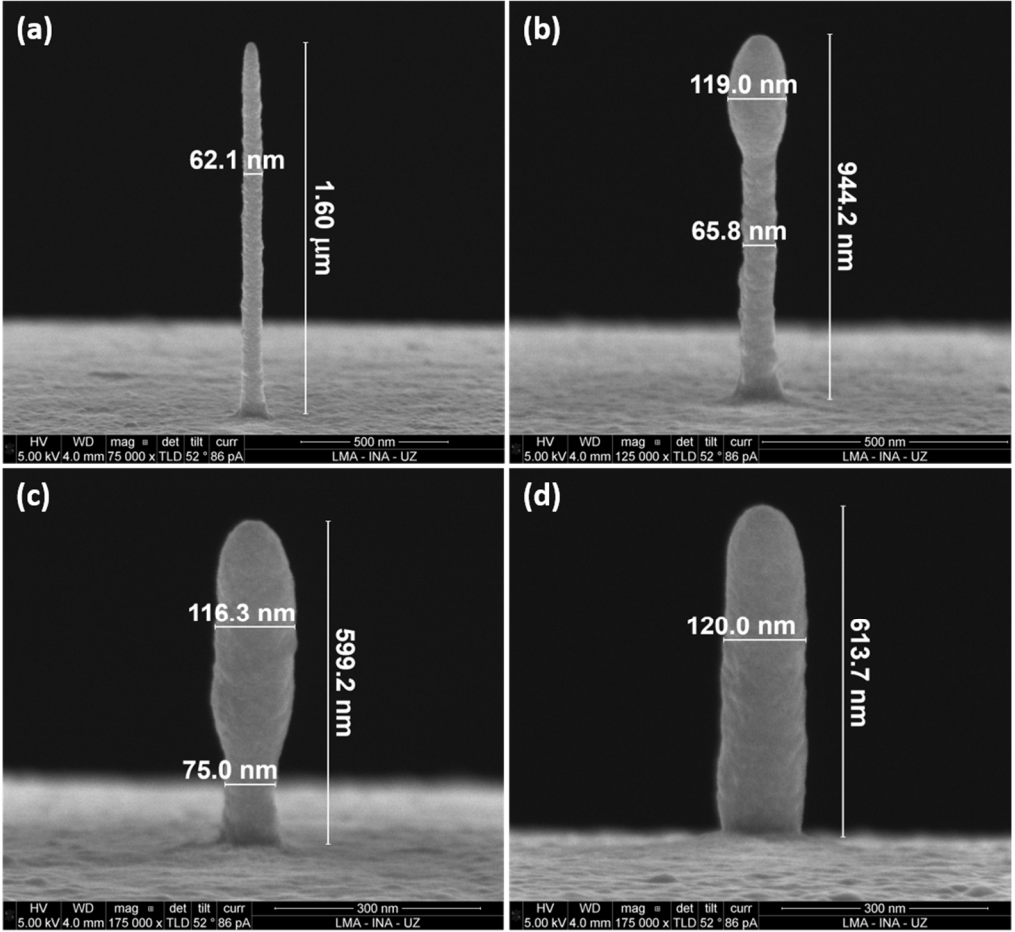
Figure 3.1. SEM images of Co nanowires grown at 86 pA and ΔP of (a) 7.3×10^{-6} mbar, (b) 6.4×10^{-6} mbar, (c) 5.9×10^{-6} mbar and (d) 5.1×10^{-6} mbar. The transition from linear to radial regime with decreasing precursor flux is noticed.

A decrease in ΔP to 6.4×10^{-6} mbar provokes a change in the growth mode at the height of 650 nm, resulting in a nanowire with a small diameter in the first segment (66 nm) and a larger diameter in the second one (119 nm), as shown in Figure 3.1(b). A further decrease in ΔP to 5.9×10^{-6} mbar induces the appearance of the larger diameter closer to the substrate, at the height of 160 nm, as illustrated in Figure 3.1(c). If an even lower ΔP is used, 5.1×10^{-6} mbar, the nanowire grows from the beginning with the larger

diameter (120 nm), as shown in Figure 3.1(d). From now on, the growth mode with smaller diameter is referred as *linear regime* whereas the growth mode with larger diameter is referred as *radial regime*. It is experimentally observed that if the growth current is increased, the radial-to-linear crossover occurs at higher precursor gas flux.

Although a theoretical quantitative model to explain this change in the growth mode is beyond the scope of this study, a qualitative interpretation of the phenomenon can be addressed here. Fundamentally, thermal and diffusion effects are expected to play a crucial role in the observed phenomenon. Thus, a reduced thermal dissipation at long wire lengths sparks off an increased temperature at the tip of the nanowire, which will lead to an increased thermal desorption of the precursor gas molecules [54]. Additionally, a reduced number of molecules will be able to diffuse from the substrate as the nanowire grows.

Similarly to the case of in-plane deposits, the height growth rate of the nanowires increases with the working pressure, as shown in Figure 3.2, which is indicative of growth in the precursor-limited regime [12]. As a result, the height growth rate is higher in the linear regime than in the radial one. Moreover, a change in the growth-rate slope is observed at the crossover between the linear and radial regimes, highlighted with two visual dashed guide lines. It should be stressed that the average height growth rate is well defined for nanowires with pure linear or radial regimes but, in the case of nanowires with transition between both growth modes, this value will depend on the relative contribution of both segments to the total height. The height growth rate was determined from data in Table 3.1 considering the total height of the nanowire and the deposition time, defined as the time spent to grow. Also, the volume growth rate as a function of the working pressure was calculated, increasing linearly in the linear growth mode.
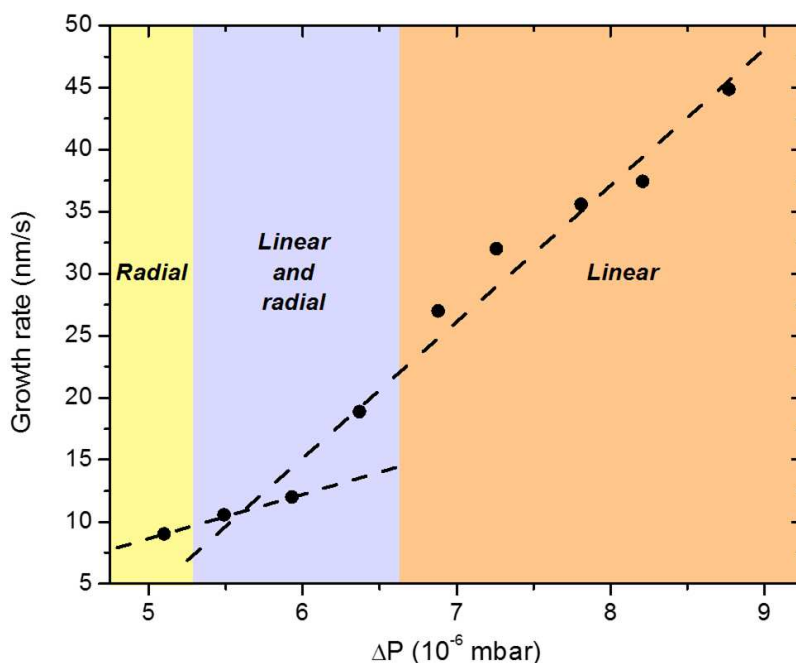
Figure 3.2. Growth rate of nanowires grown at 86 pA as a function of ΔP. A change in slope is noticed at the crossover from radial to linear regimes. In the combined *linear and radial regime*, the nanowire presents two dashed segments: one with the features of the linear growth mode and other one with the features associated with the radial growth mode.

ΔP (10^{-6} mbar)	Deposition time (s)	Height (μm)	Growth rate (nm/s)
8.8	37	1.66	44.9
8.2	43	1.61	37.4
7.8	43	1.53	35.6
7.3	50	1.60	32.0
6.9	50	1.35	27.0
6.4	50	0.944	18.9
5.9	50	0.599	12.0
5.5	62	0.655	10.6
5.1	68	0.614	9.0

Table 3.1. Data of the nanowires represented in Figure 3.2: ΔP during growth, deposition time, height and growth rate.

3.2.3 Composition as a function of the growth regime

The impact of the growth mode (linear or radial) on the composition is discussed here. Figure 3.3 illustrates the composition as a function of the position along the length of a nanowire with the combined linear and radial regimes.

The deposition by FEBID always contains contaminants from the precursor gas molecules which do not contribute to the magnetic signal. In this case, whereas Co composition brings about high functionality regarding its magnetic nature, C and O components degrade the ferromagnetic properties of the Co nanowires. In the nanowires with double growth mode, such as the one presented in Figure 3.3, the metallic composition increases from ~75% at. in the linear regime up to ~90% at. in the radial regime. At the same time, C and O relative compositions decrease from the linear to the radial segments for the benefit of the metallic content.
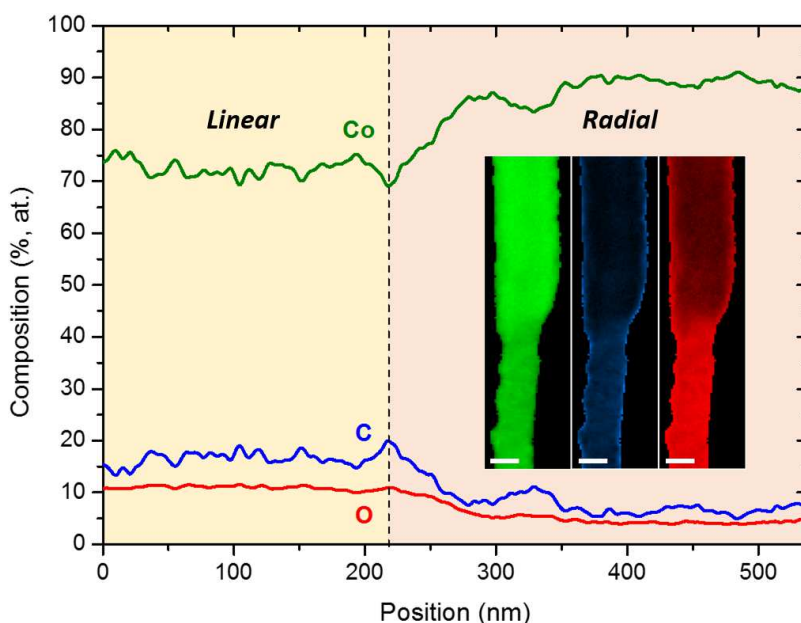
Figure 3.3. Relative composition as a function of the position along the length of a nanowire obtained by EELS. The dashed line represents the spontaneous transition in the growth regime. The inset depicts the STEM-EELS chemical maps showing the spatial distribution of Co, C and O in green, blue and red, respectively. Undefined scale bars are 50 nm in all images.

Consequently, this reveals that the decomposition efficiency is better in the radial regime, obtaining a significantly higher Co content, but being detrimental to the lateral resolution. Therefore, a trade-off between two parameters must be reached. Simultaneously, these results open a new research line which consists on understanding how the composition can be changed depending on the diameter, i.e., relying upon the growth mode or regime.

This somehow indicates that the composition of the deposits is strongly affected by the precursor gas flux, which at the same time controls the growth mode. To support this hypothesis, a dedicated experiment was performed to determine the composition of nanowires with single and double growth modes. As shown in Figure 3.4, the composition as a function of ΔP is plotted.
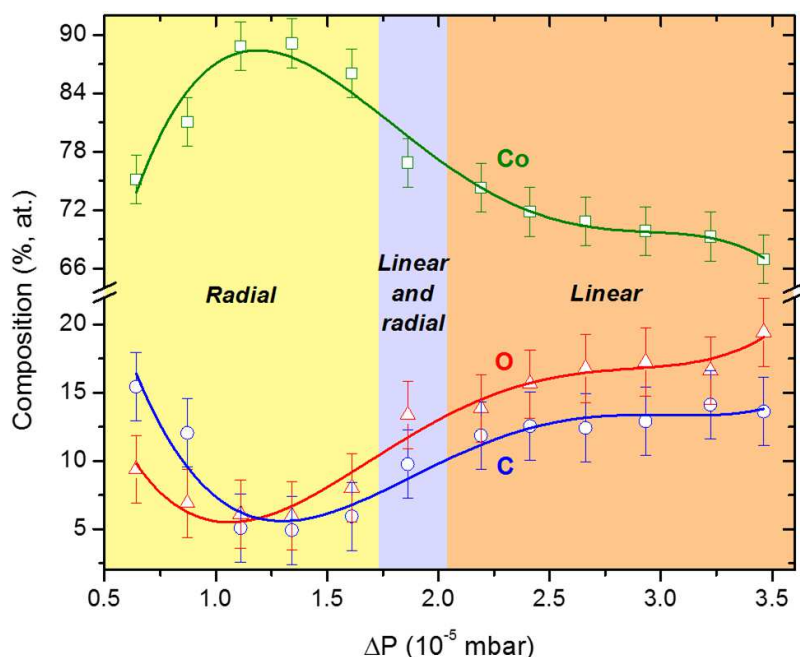
Figure 3.4. Relative composition of nanowires grown at 100 pA as a function of ΔP obtained by EDS. The composition of the sample belonging to the "linear and radial" regime has been determined at the base of the nanowire, which corresponds to the linear regime.

Although specific experiments and/or simulations could shed more light on the origin of this change in composition, from general arguments it can be stated that at lower precursor gas flux the Co content diminishes due to decomposition of residual contaminant species in the working chamber, mainly C and O. Also, the behaviour of the Co content as a function of ΔP resembles that observed in in-plane deposits [49]: an optimum precursor flux window (1×10^{-5} mbar $< \Delta P < 1.5 \times 10^{-5}$ mbar) exists, where the Co content is relatively high. On the other hand, at higher precursor gas flux the Co content is reduced because incompletely decomposed precursor gas molecules are incorporated to the deposit. The number of precursor gas molecules is so high that the electron beam cannot properly dissociate the gas. The different origin of the decreased Co content at low and high precursor flux can be also noted in the C/O ratio, which is smaller than 1 at high precursor gas flux and larger than 1 at low precursor gas flux. From Figure 3.4, under this growth conditions, it is clear that optimum Co content (>85% at.) can be only achieved in the radial regime, where the diameter is at least ~120 nm.

The inefficient decomposition phenomenon has also been found in the experiment represented in Figure 3.5. To evidence clearly this effect, STEM-EELS chemical maps and profiles were acquired in a nanowire grown in the radial regime under the appropriate conditions to induce the phenomenon. As illustrated, a Co content decrease is exhibited in the core centre. This entails a relative C composition increase in that area, so the uniform composition disappears completely. It could be thought that the central part of the nanowire is so thick that EELS signals are not quantified properly due to multiple scattering [55]. However, the decrease of intensity in the core region observed in the HAADF-STEM image of the cross section, shown in the rounded inset of Figure 3.5, can only be explained by a reduction of the average atomic number in this region, thus a reduction of the Co content.
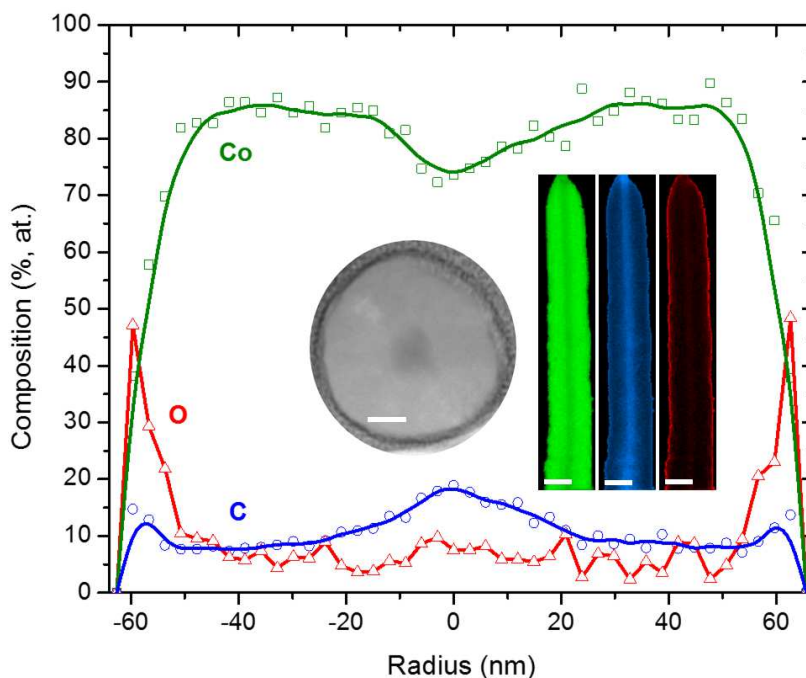
Figure 3.5. Relative composition profiles as a function of the radius of the nanowire determined by STEM-EELS. The inset depicts the HAADF-STEM image of a cross-section in grey scale, and the chemical maps showing the spatial distribution of Co, C and O in green, blue and red, respectively. Undefined scale bars are 25 nm in the STEM image and 100 nm in the STEM-EELS maps.

This is in good agreement with previous studies suggestions, where the Co signal decrease could be induced by a lack of precursor gas molecules due to a temperature increase, caused by the constant impact of the primary electrons [56][57]. A higher temperature leads to a decrease in τ and the precursor desorbs faster. By this, the material deposited in the centre of the nanowire are residual components, basically C atoms with a slight contribution of O ones. On the contrary, the volume around the core centre mainly grows thanks to SE emission, and it contains a higher metallic content due to its lower temperature. This is reminiscent of the basics related to a recent publication for the

growth of vertical hollow nanowires by He$^+$ Focused Ion Beam Induced Deposition (FIBID) [58].

Since the decomposition of the precursor gas molecules is closely linked to the electron beam properties, the electron beam current appears to be a critical growth factor. As a first approximation, let us focus the attention on nanowires with just one single growth mode. As previously mentioned, a low electron beam current is a pre-requisite for the growth of small-diameter nanowires. This is typically produced by using small apertures which limit the electron beam size for the fabrication process and, in this case, because of the inherent $Co_2(CO)_8$ properties. For example, the results obtained for the $Fe_2(CO)_9$ precursor gas are completely different, where the metallic composition is constant for all the available electron beam currents. In this scenario, it is important to assess the evolution of all the compositional elements in the resulting 3D Co-FEBID nanostructures as a function of the electron beam current. Figure 3.6 shows Co, C and O contents evaluated as a function of the electron beam current. An increase of the electron beam current provokes an increment of the metallic composition. This fact reinforces the idea that a compromise in the electron beam current regarding the lateral dimensions and the metallic composition must be made.
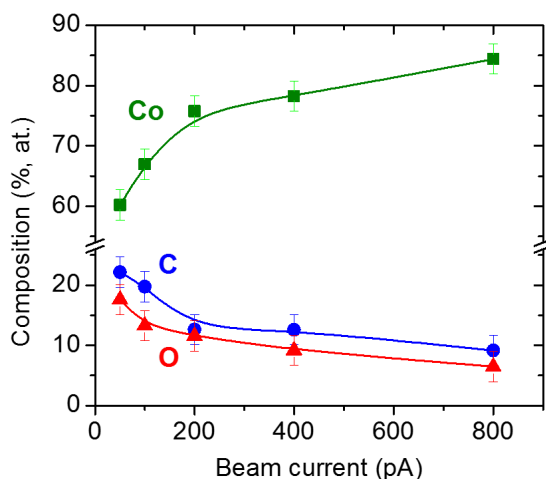
Figure 3.6. Relative composition as a function of the electron beam current for Co nanowires.

In this line, dedicated experiments have been carried out using the best growth conditions to obtain the highest possible metallic content at each particular value of the nanowire diameter. The results are summarized in Figure 3.7, where the Co content is represented as a function of the diameter for optimum growth conditions. The specific growth parameters of each nanowire are displayed in Table 3.2.

Figure 3.7 indicates that a high Co content (>85% at.) can be achieved in nanowires with diameter larger than ~120 nm, which correspond to the radial regime. However, the Co content in the nanowires with linear regime, whose diameter is smaller than ~80 nm, starts from ~75% at. for diameters of ~80 nm and diminishes quickly as the diameter is reduced. For instance, for diameters of ~60 nm the Co content is only ~45% at. Given that the nanowires present typical oxidized shells of around 5 nm [52][59], the measured average Co content will be lower as the wire diameter decreases. This means that in the core of the nanowire the Co content is expected to be higher than the average value, this effect being more significant for the narrowest nanowires.
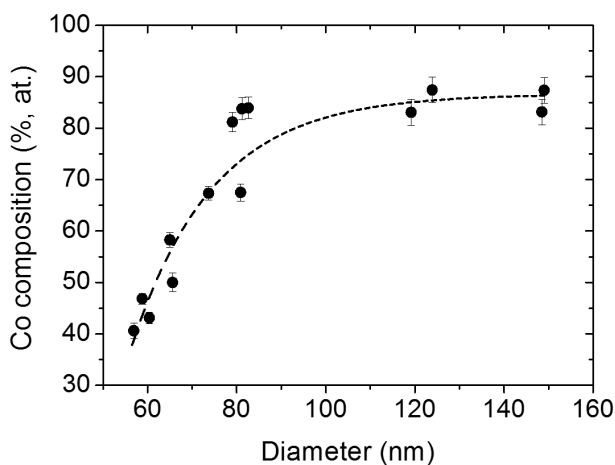
Figure 3.7. Co composition as a function of the nanowire diameter for optimized growth conditions at each particular value of the diameter.

Diameter (nm)	Co composition (%, at.)	Technique	Growth current (pA)	ΔP (10⁻⁶ mbar)
56.9	40.6	EDS	50	2.8
58.8	46.9	EDS	25	10.3
60.4	43.1	EDS	50	10.2
65.0	58.3	EDS	100	10.5
65.6	50.0	EDS	100	9.3
73.7	67.3	EDS	100	8.1
79.1	81.2	EDS	50	6.9
80.9	67.5	EDS	100	8.1
81.2	83.8	EDS	100	8.4
82.6	84.0	EDS	50	7.8
119.2	83.1	EELS	50	2.8
123.9	87.4	EDS	50	5.2
148.5	83.2	EDS	100	6.9
149.0	87.4	EELS	100	6.1

Table 3.2. Data associated with the information represented in Figure 3.7: diameter, Co content and technique used to obtain it, electron beam current and ΔP during growth. A typical error of ~2% at. in composition is considered assuming uniform distribution.

3.2.4 Magnetic induction as a function of the diameter

In order to correlate the Co content of the nanowires with their magnetization, EH experiments have been carried out. Three nanowires which contain different metallic compositions and growth modes have been analysed to obtain quantitative values of the magnetic induction.

By using Equation A.3, the average magnetic induction inside the nanowire along its long axis, denoted simply as B hereafter, can be calculated. In Figure 3.8, the results corresponding to three nanowires, representative of the three different regimes found, are shown.
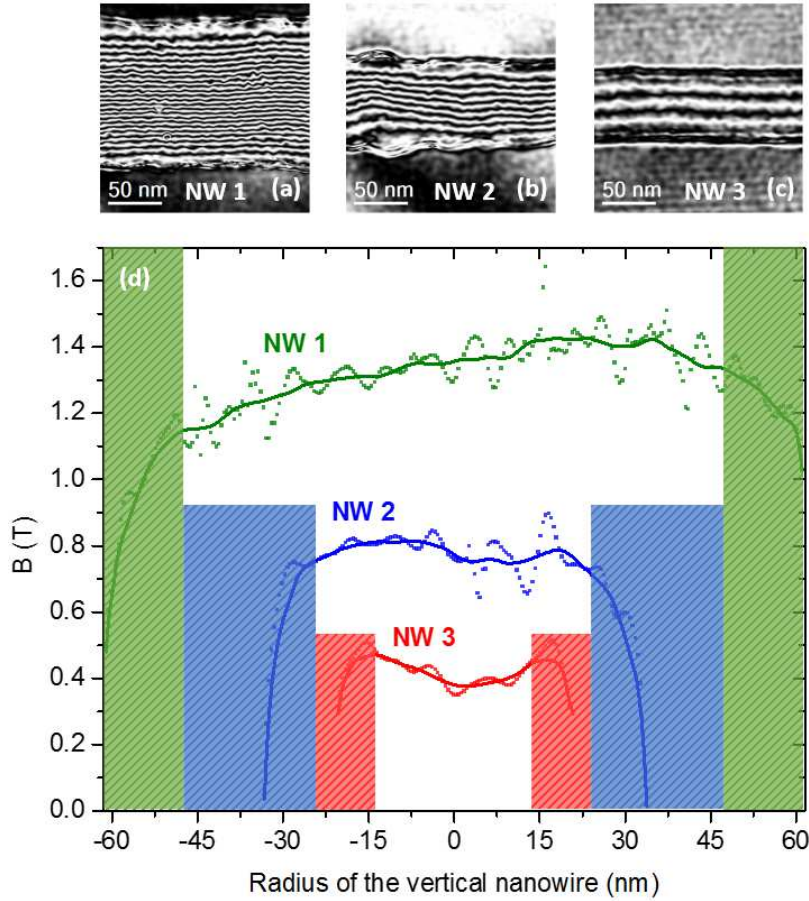
Figure 3.8. (a) Magnetic induction flux lines of nanowires with Co content of (a) 87.4% at. (NW1), (b) 67.5% at. (NW2), and (c) 40.6% at. (NW3), all obtained from the magnetic phase image after normalizing by the maximum thickness and performing the cosine of 700 times the magnetic phase shift image. (d) Transversal profiles of B of NW1, NW2 and NW3.

The values obtained for B close to the nanowires' surfaces are not reliable due to the uncertainties in the sample thickness at those positions and edge effects at the oxidized nanowire surface. For this reason, the values of B obtained at the edges of the nanowires are masked with a semi-transparent band, whereas only the values obtained in the central part of the nanowires are trustworthy. The nanowire with the largest diameter, 123.9 nm, corresponding to the radial regime, presents a B (~1.33 T) not far from the bulk value,

1.76 T. This high value of the magnetization correlates well with the high Co content in the nanowire, 87.4% at. A second nanowire, corresponding to the intermediate linear and radial regime, has been analysed at the base, in the section grown under linear regime. It presents a B of 0.78 T, around 50% of the bulk magnetization of Co. This reduction is expected given the reduced Co content (67.5% at.) in this nanowire. A third nanowire, corresponding to the linear regime, presents a lower B (~0.41 T), which can be expected given its even lower Co content (40.6% at.).

3.2.5 Discussion of the results

It can be argued that FEBID growth of functional magnetic nanostructures requires exhaustive control of a high number of growth parameters. Their precise tuning can be crucial in particular cases, such as the growth of 3D Co nanowires discussed in this section. In the process of growth optimization, a number of interesting phenomena that should be taken into account for their practical application have been encountered.

The first important finding regards the existence of two growth modes with different physical properties, denoted linear and radial regimes due to certain similarities with reported growth of 3D Fe nanowires [13]. In the radial regime, the nanowires feature diameters >120 nm with very high Co contents (>85% at.), showing a high magnetization not far from the bulk value (1.76 T). In the linear regime, the diameters are typically lower than 80 nm with the Co content strongly diminishing for decreasing diameter. For instance, B is around 1/2 of the bulk value for nanowires with ~80 nm in diameter and ~75% at. Co, reducing B down to 1/4 of the bulk value for nanowires with ~60 nm in diameter and ~45% at. Co. It cannot be discarded that the nanowires of low Co content have areas with inhomogeneous composition, with the richer Co regions contributing more to the magnetization of the nanowire. Interestingly, inside the same nanowire, a transition between both growth modes can be observed in a certain range of growth parameters. This effect seems to indicate that thermal desorption and diffusion effects

during the growth may play a key role. The capacity to dissipate the heat originated by the electron beam is reduced as the nanowire grows in height, being the tip growing progressively further away from the substrate. At a certain height, there is an overheating which could result in a change of the growth mode. Recent results, published after our work had finished, highlight this effect and provide a quantitative description [17]. The existence of such single nanowires with two diameters seems useful for studies of magnetic-domain-wall propagation, given the tendency of domain walls to get pinned at the location of the transition between both diameters [60].

The correlation found between the diameter of the nanowire and its composition is important given the relationship observed between the Co content and the magnetization of the nanowire. If a nanowire with B close to the bulk value is required, the best option is to grow a nanowire with diameter of at least 120 nm. However, in many practical situations, narrow nanowires (<100 nm) are requested, in which case a maximum Co content of ~80% at. can be achieved. In such situation, B is observed to decrease with respect to the bulk value. There are many potential applications of these nanowires such as magnetic functionalization of cantilevers [61][28][34][62][30], 3D logic structures [34][50], cylindrical conduits for domain-wall propagation [31], etc. where lateral resolution is more important than the absolute value of the magnetization. In those cases, the type of nanowires grown here in the linear regime meet the required physical properties. Just as a particular example, the Fe magnetic rods used in the past by Franken et al. had B of 0.13 T and were able to pin domain walls in a domain-wall conduit [33].

3.3 Electrically-biased patterned metal structure

In spite of what has been presented in the previous section, FEBID still presents some limitations with respect to the precise control of the dimensions of nano-objects as well as its use on insulating substrates. To overcome these limitations, in this section a novel approach based on the use of electrically-biased metal structures patterned on the

surface of the substrate is explored, called the *ARAGON-Chip* (acronym derived from ARchitectural Adjustment by Grid Overlay Nanotechnology-Chip) [63]. Hereafter, this refers to any type of insulating substrate top-covered with a periodically patterned metal layer.

3.3.1 Introduction

One of the prominent properties searched by any lithography technique is the capability to be used on an arbitrary substrate. In the case of lithography techniques based on charged particles, such as EBL and FIB lithography, a limiting factor is the difficulty of working on insulating substrates [64][65]. The building of electric fields in the vicinity of an insulating substrate (due to charging effects) produces unwanted beam deflections that ruin the resolution or even impede their practical application [66][67][68]. In the case of EBL, the problem can be circumvented by working under critical-energy conditions [69], using variable-pressure EBL [70], or including additional steps in the process, like the evaporation of a metal layer on top of the resist that is subsequently etched away [71]. In the case of FIB, it has been found that using electron irradiation simultaneously is helpful towards charge minimization [72].

FEBID is another charged-particle nanolithography technique suffering from the same problem when applied on insulating substrates. In general, FEBID applications are developed using substrates allowing the charge dissipation and the avoidance of detrimental electric potentials in the proximity of the substrate surface. In fact, it has recently shown that the use of an insulating substrate (such as polycarbonate) hampers the growth of high-resolution nanostructures by FEBID unless pads for charge dissipation exist on the substrate, close to the area of growth [73].

In this thesis, the strategy followed to overcome the charging problem of FEBID consists on the use of patterned metal structures fabricated by optical lithography, which could also be produced by any other lithography technique. Moreover, if the patterned

metal structure on an insulating substrate is electrically biased, tunable electric fields can be created on the substrate surface, producing a tremendous impact on the trajectories of the primary electrons and the generated SE. Hereafter, it will be shown that this new degree of freedom in FEBID is useful to tune the dimensions of 3D nanostructures grown by this technique. A previous proof-of-concept work has shown that an electric field produced by a continuous metallic substrate can modify the dimensions of FEBID deposits grown on its surface [74]. Also, local electric fields have been previously used to tailor the growth of nanowires using techniques such as VLS processes [75], resulting in a flexible method to tune their dimensions. However, in this case the interest is focused on patterned metal structures with micrometric holes, which allows the local application of tunable high electric fields inside the holes.

Finally, electron beam defocus will be used as a new tool to modulate the diameter and length of 3D nanowires. Although the dimension broadening effect of beam defocus has already been reported in FEBID [76], *in situ* control of this parameter to obtain 3D structures with tailored varying diameters represents a new avenue in the use of FEBID for the growth of functional magnetic, superconducting or photonic materials.

3.3.2 Experimental details

Patterned metal structures were fabricated on SiO_2, MgO and quartz substrates by optical lithography. Firstly, the electron-beam-evaporator equipment was used to deposit two consecutive metallic layers: a Cr layer with ~10 nm in thickness to improve the adherence and a Cu layer of ~500 nm. The chamber base pressure was 4×10^{-7} mbar, increasing up to 1×10^{-6} mbar in the Cr deposition, using a current of 20 mA for 105 seconds. The pressure for the Cu deposition was 1.5×10^{-6} mbar at 25 mA for 18 minutes. After that, a standard lithography procedure was followed using a positive resist and a mask with a periodic array of holes, so the metallic film was perforated with circular holes with a diameter of ~4 μm, as shown in Figure 3.9.

In order to apply local electric fields inside the holes, a cable connects an external voltage source to the sample holder through a chamber feedthrough. A microwire is bonded between the sample holder and the Cu perforated layer. The source allows applying DC voltages from -200 V to +200 V.

The 3D Pt-C and W-C nanowires were fabricated in the commercial Helios Nanolab 650 Dual Beam equipment using $(CH_3)_3Pt(CpCH_3)$ [77] and $W(CO)_6$ [78] as gas precursors, respectively. The GIS needles position were at ~50 µm in x, y and z directions, and the chamber growth pressure was 1×10^{-5} mbar (base pressure of 2×10^{-6} mbar). On the one hand, the deposits specifically devoted to the ARAGON-Chip experiments were fabricated selecting an electron beam voltage of 30 kV and an electron beam current of 25 pA. The growth pattern was the usual single circle scanned by the electron beam for 211 seconds and 60 seconds in the case of Pt-C nanowires, and for 175 seconds in the case of W-C ones. On the other hand, the W-C deposits used for beam defocus experiments and grown using the immersion imaging mode were fabricated with an electron beam voltage of 5 kV, and electron beam currents of 11 pA and 25 pA with deposition times of 90 seconds and 120 seconds.
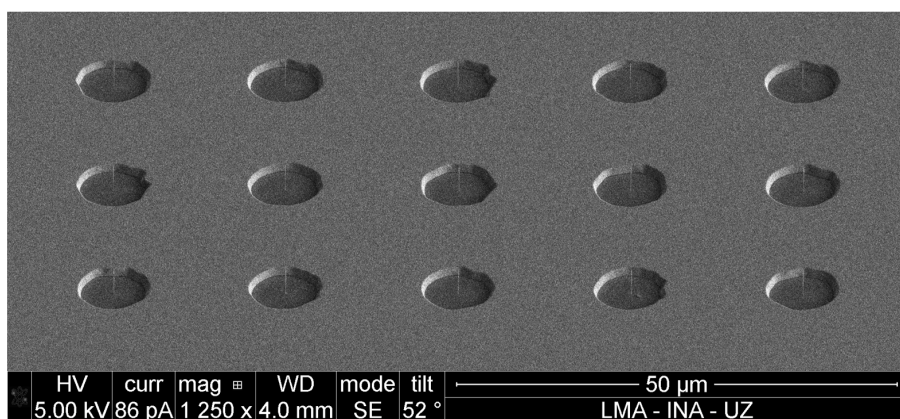
Figure 3.9. SEM image illustrating a general view of the ARAGON-Chip, where an area with 15 open circles was used for the fabrication of 3D nanowires.

3.3.3 Growth on insulating substrates

FEBID experiments have been performed using various insulating substrates in order to verify that the observed behaviour is general for non-conductive systems and cannot be attributed to one particular type of substrate. As expected, bare insulating MgO and quartz substrates did not allow the growth of Pt-C or W-C vertical nanowires, due to the presence of large and uncontrolled electric fields on the substrate surface that affect dramatically the trajectory of the incoming electron beam and the SE generated at the substrate. Moreover, in the case of growth of vertical nanowires by FEBID, charging effects are expected to be very important because the electron irradiation point is fixed, and most of the charges accumulate in the substrate, below and in the proximity of the nanowire standing point. As shown in Figure 3.10, it was found that no nanowire could be grown on MgO and quartz substrates, in contrast to the use of a 285-nm-thick amorphous SiO_2 layer on Si substrate, where charge dissipation is possible via the underlying conductive Si.

Our strategy to avoid charging effects during the growth of vertical nanowires by FEBID is sketched in Figure 3.11, based on the ARAGON-Chip concept, where an electrically-biased Cu thin layer is patterned with a periodic array of holes on top of an insulating substrates.
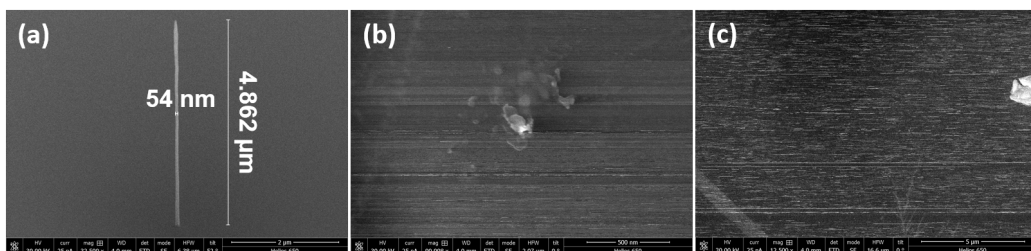
Figure 3.10. SEM images of a 3D Pt-FEBID nanowire and their corresponding attempts grown on the insulating (a) amorphous SiO_2, (b) MgO and (c) quartz substrates. These deposits were fabricated in 211 seconds.
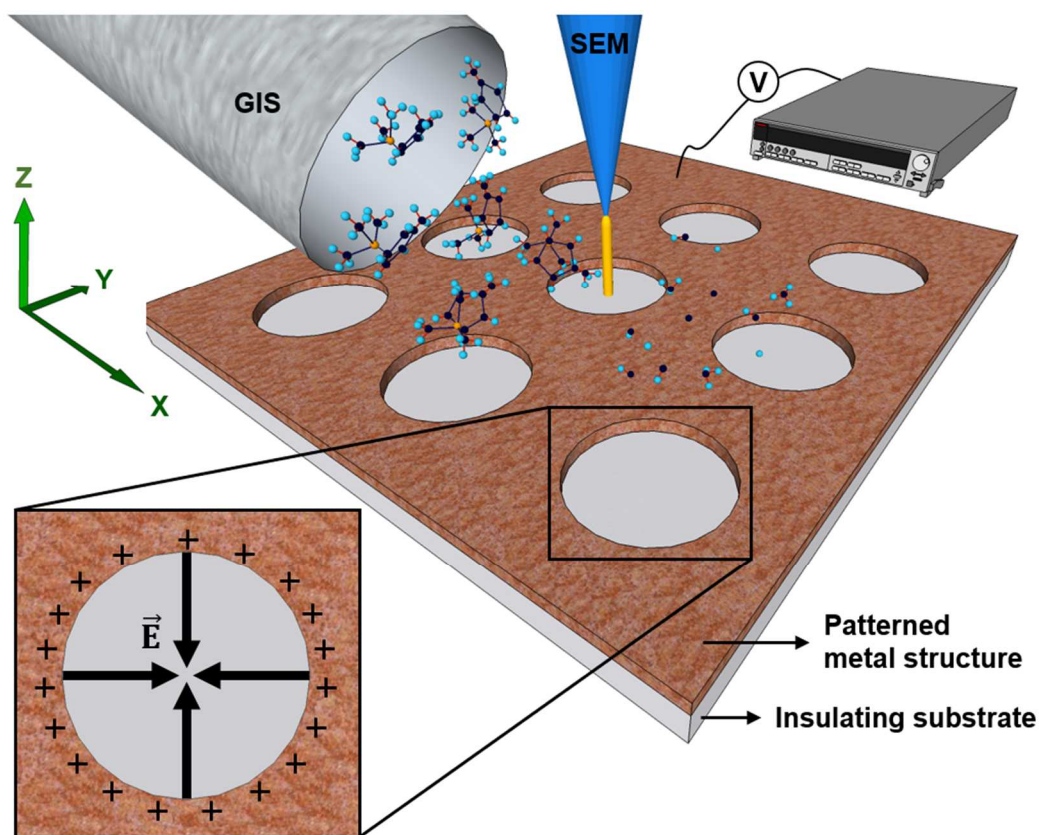
Figure 3.11. Sketch illustrating the FEBID process carried out on an insulating substrate with an electrically-biased patterned metal structure (ARAGON-Chip) in order to grow 3D nanostructures and tune their dimensions by application of local electric fields.

This approach has been found to be efficient to evacuate the charge produced during the nanowire growth, as particularly shown in Figure 3.12. In this figure, it can be noted that there is no difference between performing the growth on the Cu layer itself and on an insulating MgO substrate, in the centre of a hole perforated on the Cu layer. In both cases, a Pt-C nanowire grows with a diameter of 70 nm and similar length. This means that charging effects are suppressed.
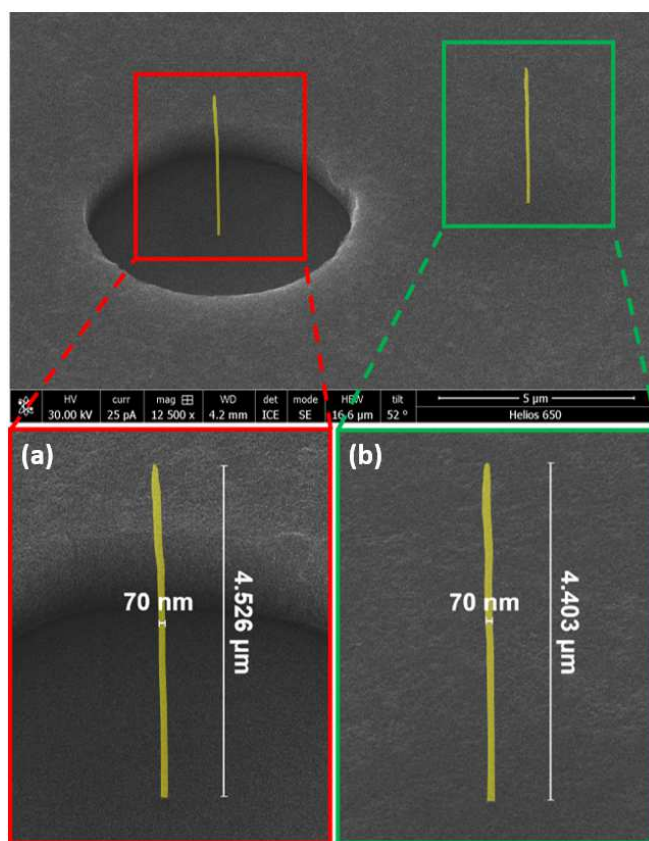
Figure 3.12. SEM images of artificially coloured Pt-C nanowires grown in 211 seconds on (a) an insulating MgO substrate at the centre of a ~4-μm-diameter hole of the perforated Cu layer and (b) onto the Cu layer.

3.3.4 Electric field numerical calculations

In addition to the capability of growing nanostructures onto insulating substrates by using the ARAGON-Chip, Figure 3.11 illustrates the possibility of getting benefit from an additional degree of freedom: the application of an electric potential to the perforated Cu layer. For that, an external voltage source is used to provide a voltage difference between the Cu layer and the electrical ground of the system, which coincides with that of the sample holder. Consequently, large variations in the local electric fields are produced inside and around the holes, as shown in Figure 3.13. In order to quantitatively

describe this effect, the total electric field produced in the vicinity of a circular hole can be determined using the superposition principle. The total electric field is calculated as the field induced by a disk of the same size as the circular hole deducted from the field of an infinite sheet (without the hole), considering that both disk and sheet carry the same surface charge density, σ, generated through the application of an electric potential. The radial field, E_{r_disk}, and the axial field, E_{z_disk}, can be calculated as a function of the distance from the symmetry axis of an uniformly-charged circular disk of radius R using the following expressions [79]:

$$E_{r\_disk} = \frac{\sigma}{2\pi\varepsilon_0} \left[\frac{\delta}{\beta} \left(K(k) - E(k) \right) - \frac{2}{\delta} K(k) \right] \qquad (3.10)$$

$$E_{z\_disk} = \frac{\sigma}{2\varepsilon_0} [a' + b'\beta^2 + c'\beta^4 + d'\beta^6] \qquad (3.11)$$

where ε_0 is the vacuum permittivity, $K(k)$ and $E(k)$ are complete elliptic integrals of the first and second kind, respectively, with $k = 2\sqrt{\beta}/\delta$, and:

$$\delta^2 = 1 + \alpha^2 + \beta^2 + 2\beta \qquad (3.12)$$

with $\alpha = z/R$ and $\beta = r/R$, and:

$$a' = 1 - \frac{\alpha}{(1 + \alpha^2)^{1/2}} \qquad (3.13)$$

$$b' = -\frac{3}{4} \frac{\alpha}{(1 + \alpha^2)^{5/2}} \qquad (3.14)$$

$$c' = -\frac{15}{64} \frac{3\alpha - 4\alpha^3}{(1 + \alpha^2)^{9/2}} \qquad (3.15)$$

$$d' = -\frac{45}{2304} \frac{35\alpha - 140\alpha^3 + 56\alpha^5}{(1 + \alpha^2)^{13/2}} \qquad (3.16)$$

Figure 3.13 shows the numerical calculations of the electric field in the vicinity of a circular hole with R of ~2 μm in two different sections of the patterned metal structure.
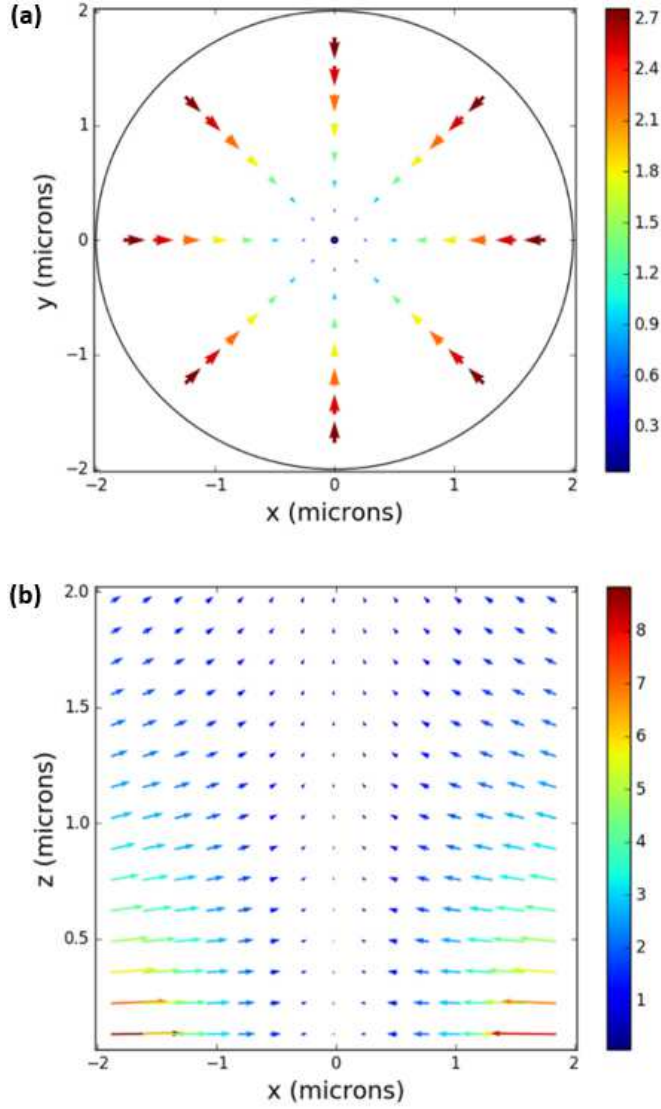
Figure 3.13. Vector maps of the numerical calculations of the electric field in the vicinity of a circular hole with R of ~2 µm, in two different sections of the patterned metal structure, produced by the application of a negative voltage to the chip: (a) electric field in the hole plane, xy plane in Figure 3.11, at a distance of 1 µm in the z direction from the substrate and (b) electric field in the plane perpendicular to the hole, xz plane in Figure 3.11, containing the vertical symmetry axis of the hole. Electric field values are expressed in units of $\sigma/(2\varepsilon_0)$.

The vector map of the electric field in the xy plane of Figure 3.11 is displayed in Figure 3.13(a), which illustrates that the application of a negative (positive) DC voltage in such structure produces large and highly directional electric fields pointing towards (or from) the centre of the hole. In the centre of the hole, the electric field vanishes. The total electric field in the plane perpendicular to the hole, xz plane in Figure 3.11, corresponds to the vector map shown in Figure 3.13(b). The electric field is very small along the symmetry axis of the circular hole and grows rapidly as the distance from this axis increases.

The electric field numerical calculations and vector maps representations were performed by Dr. Soraya Sangiao.

3.3.5 Dimensional modulation as a function of the applied voltage

It has been observed that the growth of the nanowires under different voltage values applied to the ARAGON-Chip, whilst keeping the other growth conditions constant, affects dramatically the dimensions of the nanowires. In these experiments, Pt-C and W-C nanowires are grown at the centre of the holes with amorphous SiO_2 substrate under different voltages in the range of -200 V to +200 V.

On the one hand, as shown in Figure 3.14(a), the nanowire diameter is found to change from a large value around 100 nm under -200 V to a minimum value of 50 nm at -25 V, and then increasing up to 90 nm under +200 V. This figure illustrates the tuning of the value of the nanowire diameter by a factor of 2 by application of the created local electric fields. On the other hand, the aspect ratio of the nanowire is also represented in Figure 3.14(a). It shows a maximum value at around -25 V, in good correspondence with the minimum value of the diameter at such voltage, and indicates that the aspect ratio increases by a factor of 4 working under such voltage in comparison to -200 V. SEM images of Pt-C nanowires grown respectively under -100 V, -35 V and +100 V are shown in Figure 3.14(b-d). At -100 V the diameter at a height of 1 μm is 73 nm, whereas it

decreases to 50 nm under -35 V and increases again to 83 nm under +100 V. Moreover, the nanowire length is, respectively to those voltages, 2.6 µm (-100 V), 2.9 µm (-35 V) and 2.2 µm (+100 V), corresponding to linear growth rates of 43.3 nm/s, 48.3 nm/s and 36.7 nm/s, respectively. Thus, the results are conclusive with respect to an optimized nanowire growth in terms of resolution under negative voltages around -25 V.
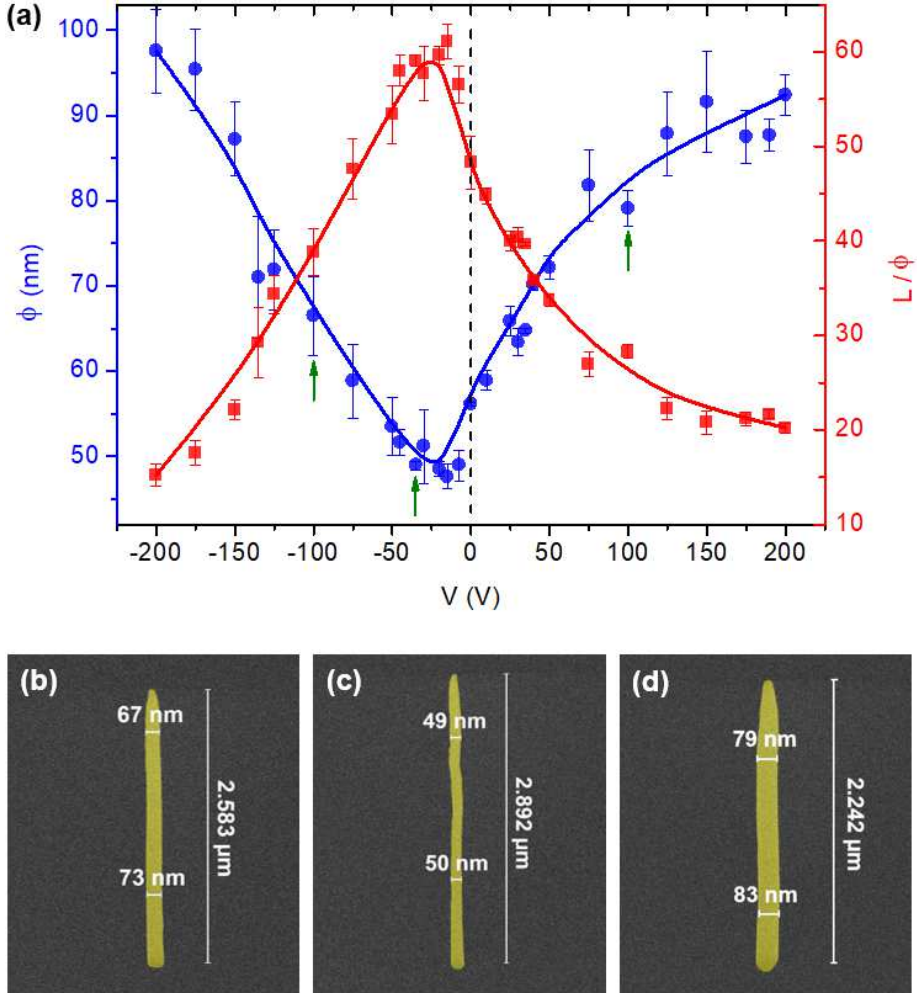
Figure 3.14. Dimensional modulation of Pt-C nanowires grown for 60 seconds on amorphous SiO_2 substrate: (a) dependence of the diameter and the aspect ratio with the voltage applied to the ARAGON-Chip. SEM artificially coloured images of selected nanowires grown under (b) -100 V, (c) -35 V and (d) +100 V, matching the points marked with green arrows in (a).

Similar experiments have been carried out to investigate the influence of local electric fields on the dimensions of W-C nanowires using the ARAGON-Chip on the same amorphous SiO_2 substrate. As shown in Figure 3.15, the minimum nanowire diameter (~65 nm) occurs in the -25 V to -50 V range and the aspect ratio is maximized in the same voltage range. In this case, the degree of tunability of the diameter and the aspect ratio compared to the Pt-C case is lower but substantial (factors of 1.3 and 1.7, respectively).

In view of the set of results obtained for Pt-C and W-C nanowires, spatially-dependent electric fields can be established as a new degree of freedom to tune the dimensions of nanowires grown by the FEBID technique using this novel approach. The origin of the effect will be discussed hereafter in the light of the physical phenomena involved in the FEBID growth and the electric field distribution in the ARAGON-Chip.
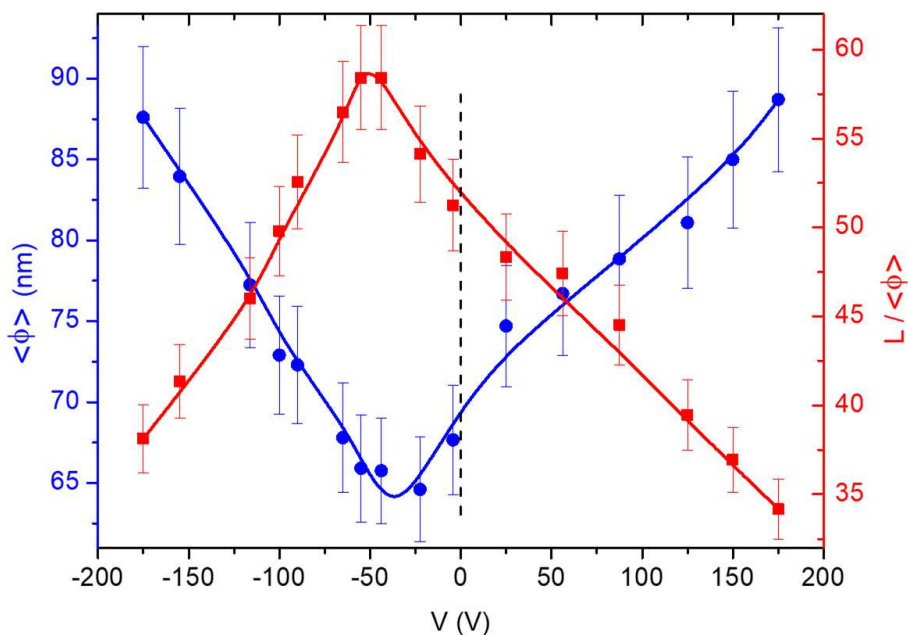
Figure 3.15. Dimensional modulation of W-C nanowires grown on amorphous SiO_2 substrate illustrating the dependence of their diameter and aspect ratio with the voltage applied to the ARAGON-Chip.

3.3.6 Qualitative discussion of the electric field action

Regarding the physical phenomena involved in the growth of vertical structures by FEBID, Fowlkes et al. noted that the most significant contribution to the dissociation of the precursor gas molecules arises from the primary beam electrons and their generated secondary electrons (SE-I), with lower relevance from BSE and their generated secondary electrons (SE-II) [80]. Later, Smith et al. stressed the important role played by forward-scattered electrons (FSE) in the growth of 3D nanowires as well as the dependence of the effect with the primary beam energy and the resulting growth regime [81]. Moreover, Arnold et al. showed that SE-II are responsible for the halo deposit around the main deposit in 2D structures, affecting the final deposit resolution [82]. A similar study by Schmied et al. in the case of 3D deposits has shown various competing effects, with significant broadening of the deposit width under intermediate or low electron beam energy [83]. The FEBID process is thus complex and depends on many parameters, but in general the precursor dissociation process is determined by high-energy electrons (mainly arising from primary beam electrons and FSE) as well as by low-energy electrons (mainly SE-I and SE-II). Therefore, our experimental finding of a considerable effect of local electric fields on the dimensions of FEBID deposits should be correlated with the effect produced by such electric fields on the trajectories of these electrons responsible for the precursor gas molecules dissociation.

In consideration of the previously reported results, a qualitative explanation of the observed effect can be provided. From the electrostatic point of view, the electric field distribution generated at the perforated Cu film is in fact acting as a small (de)focusing lens. The electrostatic lenses can be found in electron and ion microscopes [84], and other devices based on charged particles [85]. In the ARAGON-Chip, as the primary electron beam approaches the perforated charged film, it suffers a deviation towards the optical axis (under negative voltage) or off the optical axis (under positive voltage), as sketched in Figure 3.16. In both cases, this effectively leads to an electron beam defocus.
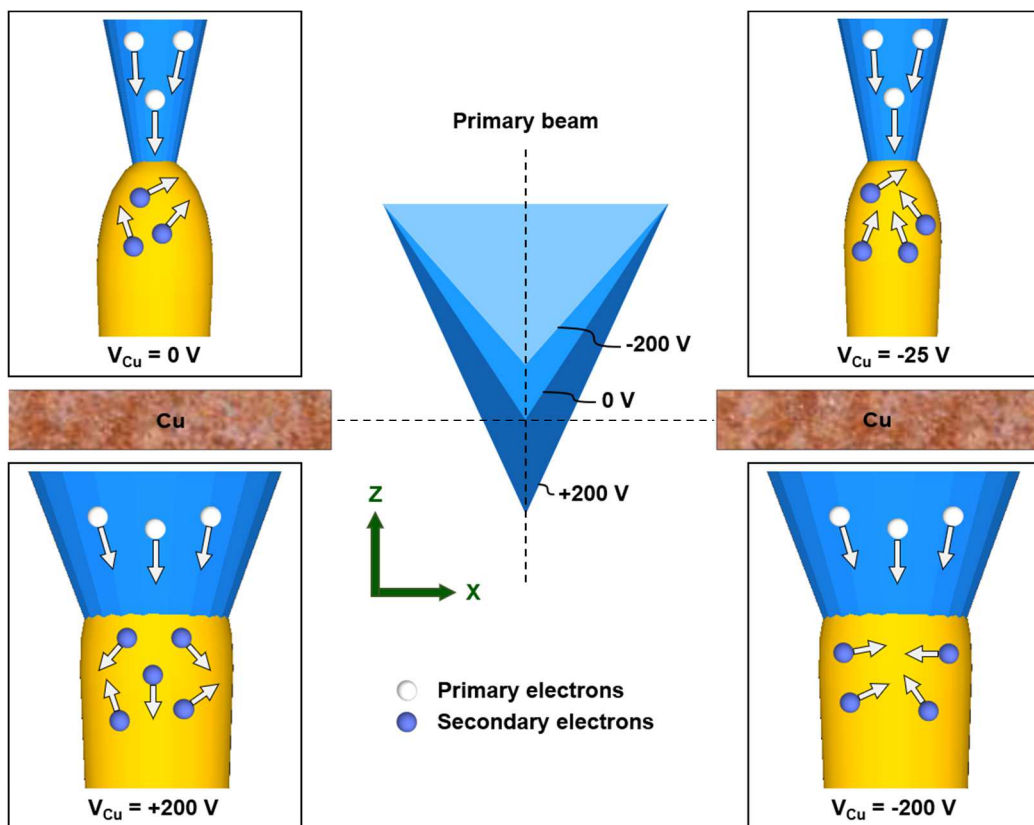
Figure 3.16. Sketch illustrating the relevant phenomena involved in the growth of 3D nanowires by FEBID when an external positive or negative voltage is applied to the ARAGON-Chip. On the one hand, the primary beam becomes slightly defocused, giving rise to the diameter broadening. On the other hand, the SE are strongly attracted to ($V_{Cu} < 0$) or repelled from ($V_{Cu} > 0$) the optical axis, contributing to the nanowire narrowing or broadening, respectively.

As reported by Plank et al. [76], the effect of defocusing the primary electron beam triggers an increase of the nanowire diameter. On the other hand, the high electric field will strongly modify the trajectory of the SE produced in the substrate and the growing structure, which is also crucial for the FEBID growth.

Due to the low energy of SE-I and SE-II (<50 eV) [86], they will undergo strong attraction to or repulsion from the optical axis for negative or positive voltage,

respectively. In fact, similar voltage values in the range of a few tens or hundreds of volts are actually used in electron microscopes to optimize the imaging contrast by SE, where biasing voltage can be applied to the sample itself [87][88] or to the electron detector [89][90]. As a result, combining the growth by FEBID and the ARAGON-Chip strategy, the use of a negative voltage will push SE-I and SE-II to the hole centre contributing to decrease the nanowire diameter, whereas the use of a positive voltage makes SE-I and SE-II to be pulled out from the hole central axis leading to a diameter enlargement.

Summarizing, when a negative voltage is applied to the perforated Cu film, two effects will compete: nanowire narrowing due to the effect of the electric field on the SE-I and SE-II, and nanowire broadening due to the defocusing effect of the electric field on the primary beam electrons. This agrees with the experimental results shown in Figure 3.14 and Figure 3.15. Starting from 0 V, the nanowire diameter first decreases down to an applied voltage of around -25 V, then increasing the thickness as the voltage is reduced to -200 V. As the sketch in Figure 3.16 also illustrates, this is the expected evolution given the rapid focusing of the SE towards the hole central axis at low voltages and the smoother increase of the primary beam diameter with the voltage. Finally, at positive voltage, the diameter is always increasing with voltage given that both effects contribute to the nanowire broadening.

3.3.7 Dimensional modulation as a function of the beam defocus

In order to verify the hypothesis described above, additional experiments were performed where the electron beam focus conditions were controllably changed before and during the nanowire growth. For that, the focus height, z, was varied with respect to the optimum focus condition, $(z = 0)$, to investigate the corresponding changes in the nanowire diameter and height with the defocus, Δz.

The first experiments consisted of growing Pt-C nanowires for different z values fixed during the whole nanowire growth. From the optimum focus condition, both

overfocus ($z < 0$) and underfocus ($z > 0$) conditions were considered. In the first case the beam is focused below the hole xy plane, whereas in the second one the beam is focused above it. The obtained results for the values of the diameter and aspect ratio as a function of z are represented in Figure 3.17. In order to check that the broadening effect is independent of the voltage applied to the ARAGON-Chip, the experiments were performed at -25 V and -200 V, represented in Figure 3.17(a) and 3.17(b), respectively. The z value has been swept a maximum of 40 µm, leading to enormous differences in the nanowire diameter and aspect ratio. These variations reach a factor of 3 for the diameter and a factor of 12 for the aspect ratio with Δz of ~20 µm.

On the one hand, these results highlight the importance of a good primary beam focus in order to achieve the highest resolution in the growth of 3D nanostructures. In order to show the differences which appear in the SEM images when the z value varies, an example is shown in Figure 3.18. It can be appreciated the defocusing effect of a Δz of ~20 µm in comparison with the optimum focus position for imaging acquisition. On the other hand, the results interestingly show an additional ingredient to play with during the growth of 3D nanostructures by FEBID. To exploit this additional parameter, the z value was varied during the growth of single nanowires in order to create continuous nanostructures with modulated diameter. First, as shown in Figure 3.19(a), a Pt-C nanowire with large diameter (146 nm) starts to grow due to the primary beam defocus (Δz of 20 µm). At 72 seconds, by bringing z into the optimal position with a quick (~1 second) change in the z position, a narrow section (64 nm in diameter) starts to grow. After 72 seconds, the z position is modified 20 µm, producing a primary beam defocus and the corresponding increase of the diameter to 119 nm. After another 72 seconds in these conditions, the growth is finished, obtaining a diameter-modulated nanowire with wide-narrow-wide sections. A second diameter-modulated nanowire has been grown following a similar strategy but with narrow-wide-narrow sections, as shown in 3.19(b).
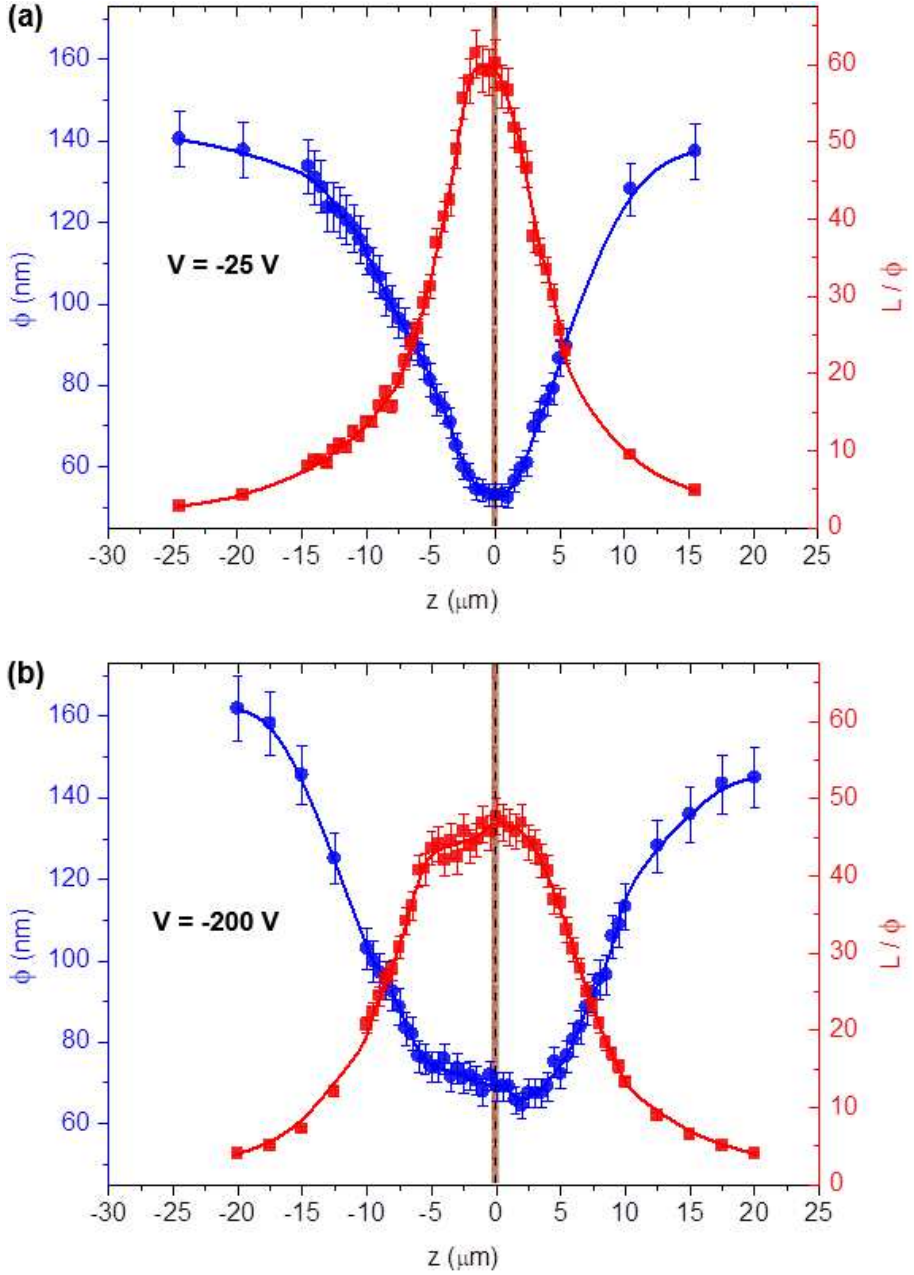
Figure 3.17. Dimensional modulation of Pt-C nanowires grown for 60 seconds on amorphous SiO$_2$ substrate: dependence of the diameter at half nanowire's height and aspect ratio as a function of the primary beam focus height. The external voltage applied to the ARAGON-Chip was (a) -25 V and (b) -200 V.

131
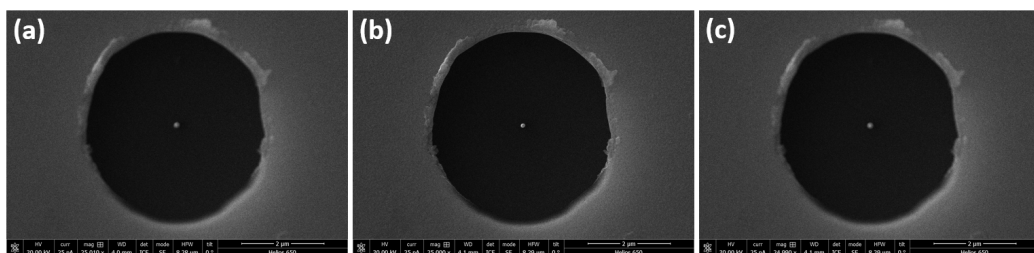
Figure 3.18. SEM top view images of a ~4-µm-diameter hole with a 3D Pt-FEBID nanowire grown on the amorphous SiO_2 substrate, with the electron beam focused (a) 20 µm above the height of the Cu surface, (b) at the height of the Cu surface and (c) 20 µm under the height of the Cu surface. In all cases there is no voltage applied to the ARAGON-Chip.
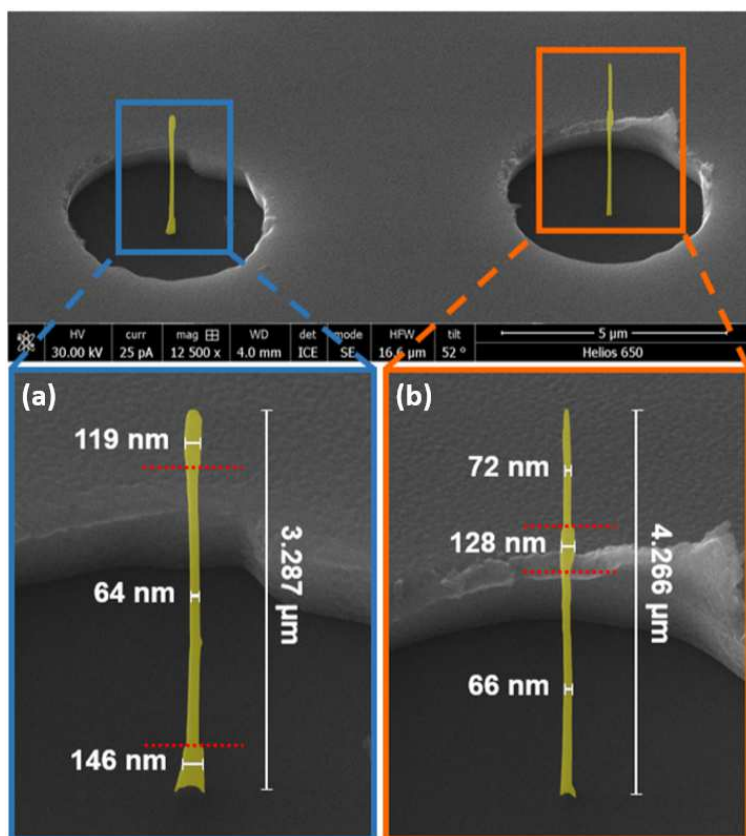
Figure 3.19. Diameter-modulated Pt-C artificially coloured nanowires grown on SiO_2 substrate by means of the *in situ* variation of the primary electron beam focus condition. Each thin and thick diameter region was fabricated for 72 seconds.

It is interesting to mention that, despite every section in the nanowires of Figure 3.19 has been grown for 72 seconds, their respective length is different. This is expected for sections with dissimilar diameter, where it would be expected the conservation of the volume growth rate instead of the linear growth rate. However, this length difference also occurs for sections with the same diameter, as it can be clearly observed in Figure 3.19(b) for the narrow sections. In this case, the top narrow section is shorter than the bottom one, which can be explained by the diminishment of the growth rate with an increasing distance to the substrate caused by precursor gas diffusion effects [91].

It has been checked that the nanowire diameter increases as z moves away from its optimum position. In the light of this finding, inducing a Δz keeping the substrate still has the same effect as moving the substrate in the vertical axis when keeping z constant. However, mechanical movements of the stage make this latter approach less refined, thus the diameter changes have been always obtained introducing a Δz. So far, for a single nanowire grown under a constant z, slight changes in diameter along the length were detected. Nevertheless, additional experiments were carried out growing W-C nanowires and inducing diameter changes keeping the same z value and substrate position during the whole growth. For this purpose, a further step towards dimensional modulation of 3D nanowires can be taken by using the immersion imaging mode during growth.

In this mode, a magnetic field is applied to collect a higher number of electrons than in standard field-free mode, obtaining ultra-high-resolution images. As shown in Figure 3.20, this mode will be used for the fabrication of nanowires. The nanostructures were grown at different positions of a still sloping substrate under the same focus condition, where just the substrate height changes for each case. The red dotted line indicates the constant z value used for the growth of the nanowires. Figure 3.20(a) illustrates the nanowire with the optimum focus height at the growth starting point. A smooth continuous beam defocus Δz is introduced *per se* during the growth of the nanostructure, increasing the diameter from 39 nm to 52 nm as the focus is gradually driven away.
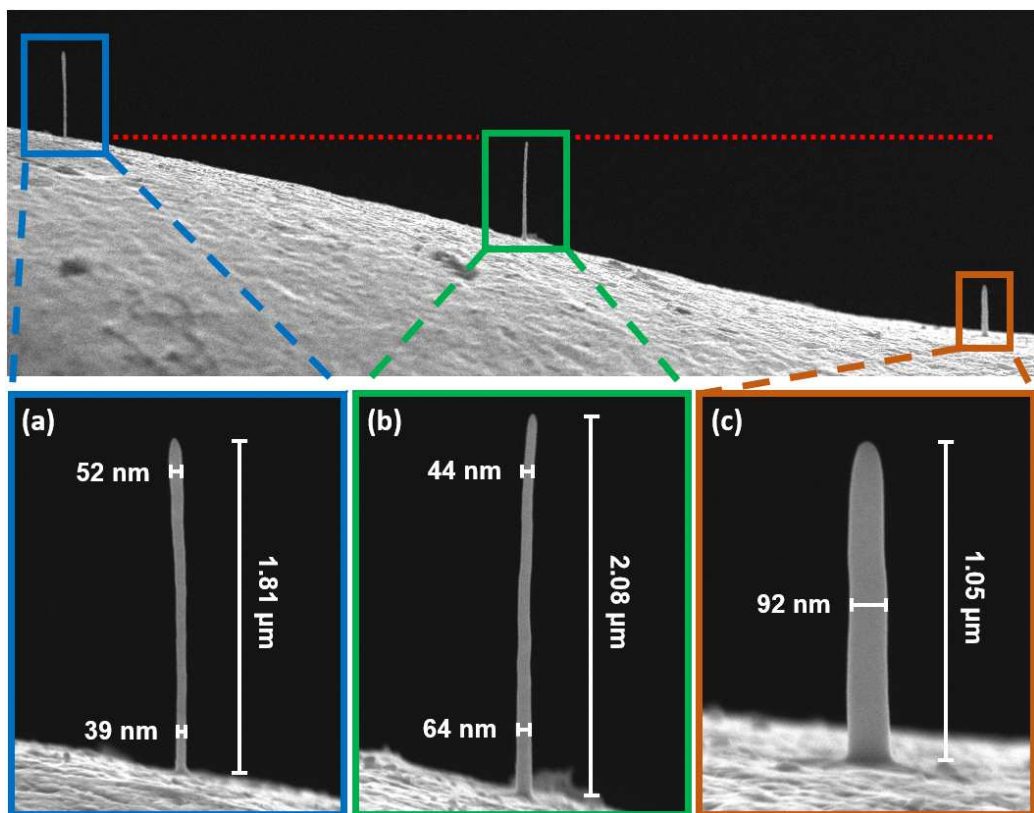
Figure 3.20. SEM images of W-C nanowires grown at 11 pA for 120 seconds on a TEM Cu grid by means of the immersion mode, keeping the same *z* value (at the indicated red dotted line) and varying the substrate height.

In comparison with the field-free mode, the immersion mode produces a more convergent beam, revealing a higher focus capacity (spatial resolution) and a shorter depth of field which leads to a stronger change in the nanowire diameter. This explains the narrow diameters obtained at the optimum focus condition and its rapid broadening few nanometres away. In the case of growth using the field-free mode, this effect is not appreciable and cannot be used to modulate naturally the diameter in a single nanowire. This result simulates the electron beam cone in the immersion mode, which is very noticeable near the optimum focus condition. As shown in Figure 3.20(b), if a nanowire

starts to grow from a different substrate height (~2.2 µm below the optimum focus), similar effects are provoked. In this case, the diameter is reduced from 64 nm down to 44 nm as the focus is progressively approaching its optimum position. Finally, Figure 3.20(c) illustrates a nanowire grown far away from this situation, where negligible changes in its expected larger diameter are identified.

After optimizing *z* to near the optimum focus position as well as possible, a diameter of ~29 nm has been achieved, as shown in Figure 3.21(a). This value improves the resolution reached using the field-free mode, although a significant diameter increase in the first few nanometres off the optimum focus condition is produced. In order to solve this problem, the diameter change induced naturally by the immersion mode can be compensated by introducing the appropriate Δ*z*, which must be gradually changed as the nanostructure grows upward. An example is displayed in Figure 3.21(b).
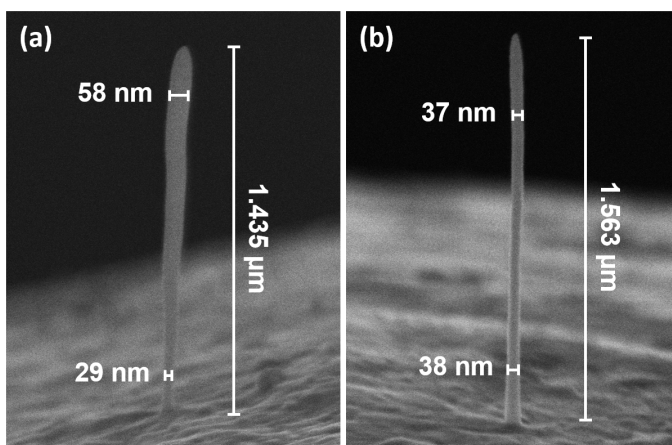
Figure 3.21. SEM images of W-C nanowires grown at 25 pA on a TEM Cu grid by means of the immersion mode and fabricated (a) in 90 seconds, and (b) in 120 seconds simultaneously compensating Δ*z* during the nanowire growth.

3.4 Conclusions

In the first part of this chapter, it has been demonstrated that control of the growth parameters in FEBID, especially the electron beam current and the precursor flux, allows tuning the diameter, composition and magnetization of 3D Co nanowires. Firstly, the application of this nanolithography technique for the fabrication of these nanostructures with simultaneous high metallic content (~80 % at.), small diameter (<100 nm) and high magnetization has been achieved by optimization of the growth parameters. Secondly, the existence of two growth regimes, i.e., radial and linear, have been unveiled, with a sharp transition between them for certain experimental conditions. In the radial regime, the nanowire diameter is at least ~120 nm and the Co content is >85% at. In the linear regime, the diameter is smaller than 80 nm and the Co content is, at best, ~75% at. The Co nanowires obtained by the described growth routes provides functional nanostructures for applications in spintronics, and magnetic sensing and actuation at the nanoscale.

In the second part, the use of an electrically-biased patterned metal structure fabricated on the surface of insulating substrates was introduced. This novel concept, coined ARAGON-Chip, serves to grow nano-objects by FEBID on insulating substrates thanks to charge dissipation, and provides additional tuning of their dimensions by the application of spatially-dependent electric fields. The application of a moderate voltage (up to 200 V) can dramatically change the dimensions of the growing 3D nanowires by acting as an electrostatic lens on the primary electron beam and the generated SE. Two competing effects arising from the generated electric fields were identified: a slight change in the primary beam focus point and a strong deflection on the SE. These findings are exploited to modulate *in situ* the diameter of 3D Pt-C and W-C FEBID nanowires. Changing the primary electron beam focus, diameters as small as 50 nm can be easily modulated by a factor of 2. The tuning of the diameter by this method has been compared to that performed by using the immersion imaging mode during the growth processes.

References

[1] M. Huth, F. Porrati, C. Schwalb, M. Winhold, R. Sachser, M. Dukic, J. Adams and G. Fantner, "Focused electron beam induced deposition: A perspective", *Beilstein J. Nanotechnol.* **3**, 597 (2012).

[2] S. J. Randolph, J. D. Fowlkes and P. D. Rack, "Focused, Nanoscale Electron-Beam-Induced Deposition and Etching", *Crit. Rev. Solid State Mater. Sci.* **31**, 55 (2006).

[3] W. F. Van Dorp and C. W. Hagen, "A critical literature review of focused electron beam induced deposition", *J. Appl. Phys.* **104**, 081301 (2008).

[4] I. Utke, P. Hoffmann and J. Melngailis, "Gas-Assisted Focused Electron Beam and Ion Beam Processing and Fabrication", *J. Vac. Sci. Technol. B* **26**, 1197 (2008).

[5] H. Plank, D. A. Smith, T. Haber, P. D. Rack and F. Hofer, "Fundamental Proximity Effects in Focused Electron Beam Induced Deposition", *ACS Nano* **6**, 286 (2012).

[6] R. Winkler, A. Szkudlarek, J. D. Fowlkes, P. D. Rack, I. Utke and H. Plank, "Toward Ultraflat Surface Morphologies During Focused Electron Beam Induced Nanosynthesis: Disruption Origins and Compensation", *ACS Appl. Mater. Interfaces* **7**, 3289 (2015).

[7] I. Utke, S. Moshkale and P. Russell, "Nanofabrication Using Focused Ion and Electron Beams. Principles and Applications", *Oxford Univ. Press* (2012).

[8] J. D. Wnuk, S. G. Rosenberg, J. M. Gorham, W. F. Van Dorp, C. W. Hagen and D. H. Fairbrother, "Electron beam deposition for nanofabrication : Insights from surface science", *Surf. Sci.* **605**, 257 (2011).

[9] K. Muthukumar, I. Opahle, J. Shen, H. O. Jeschke and R. Valentí, "Interaction of $W(CO)_6$ with SiO_2 surfaces: A density functional study", *Phys. Rev. B* **84**, 205442 (2011).

[10] J. D. Fowlkes and P. D. Rack, "Fundamental Electron-Precursor-Solid Interactions Derived from Time-Dependent Electron-Beam-Induced Deposition Simulations and Experiments", *ACS Nano* **4**, 1619 (2010).

[11] V. Friedli and I. Utke, "Optimized molecule supply from nozzle-based gas injection systems for focused electron- and ion-beam induced deposition and etching: simulation and experiment", *J. Phys. D: Appl. Phys.* **42**, 125305 (2009).

[12] S. Wachter, M. Gavagnin, H. D. Wanzenboeck, M. M. Shawrav, D. Belić and E. Bertagnolli, "Nitrogen as a carrier gas for regime control in focused electron beam induced deposition", *Nanofabrication* **1**, 16 (2014).

[13] G. Hochleitner, H. D. Wanzenboeck and E. Bertagnolli, "Electron beam induced deposition of iron nanostructures", *J. Vac. Sci. Technol. B* **26**, 939 (2008).

[14] R. Córdoba, J. Sesé, J. M. De Teresa and M. R. Ibarra, "High-purity cobalt nanostructures grown by focused-electron-beam-induced deposition at low current", *Microelectron. Eng.* **87**, 1550 (2010).

[15] L. M. Belova, E. D. Dahlberg, A. Riazanova, J. J. L. Mulders, C. Christophersen and J. Eckert, "Rapid electron beam assisted patterning of pure cobalt at elevated temperatures via seeded growth", *Nanotechnology* **22**, 145305 (2011).

[16] W. F. Van Dorp, T. W. Hansen, J. B. Wagner and J. T. M. De Hosson, "The role of electron-stimulated desorption in focused electron beam induced deposition", *Beilstein J. Nanotechnol.* **4**, 474 (2013).

[17] E. Mutunga, R. Winkler, J. Sattelkow, P. D. Rack, H. Plank and J. D. Fowlkes, "Impact of Electron-Beam Heating during 3D Nanoprinting", ACS Nano **13**, 5198 (2019).

[18] U. Hartmann, "Magnetic multilayers and giant magnetoresistance. Fundamentals and industrial applications", *Springer* (2000).

[19] A. Fert, "Nobel Lecture: Origin, development, and future of spintronics", *Rev. Mod. Phys.* **80**, 1517 (2008).

[20] A. Candini, G. C. Gazzadi, A. Di Bona, M. Affronte, D. Ercolani, G. Biasiol and L. Sorba, "Hall nano-probes fabricated by focused ion beam", *Nanotechnology* **17**, 2105 (2006).

[21] C. Chappert, A. Fert and F. N. Van Dau, "The emergence of spin electronics in data storage", *Nat. Mater.* **6**, 813 (2007).

[22] M. T. Niemier, G. H. Bernstein, G. Csaba, A. Dingler, X. S. Hu, S. Kurtz, S. Liu, J. Nahas, W. Porod, M. Siddiq and E. Varga, "Nanomagnet logic: progress toward system-level integration", *J. Phys.: Condens. Matter* **23**, 493202 (2011).

[23] M. Castagné, M. Benfedda, S. Lahimer, P. Falgayrettes and J. P. Fillard, "Near field optical behaviour of C supertips", *Ultramicroscopy* **76**, 187 (1999).

[24] G. C. Gazzadi, S. Frabboni and C. Menozzi, "Suspended nanostructures grown by electron beam-induced deposition of Pt and TEOS precursors", *Nanotechnology* **18**, 445709 (2007).

[25] P. Bøggild, T. M. Hansen, C. Tanasa and F. Grey, "Fabrication and actuation of customized nanotweezers with a 25 nm gap", *Nanotechnology* **12**, 331 (2001).

[26] K. Höflich, R. Bin Yang, A. Berger, G. Leuchs and S. Christiansen, "The Direct Writing of Plasmonic Gold Nanostructures by Electron-Beam-Induced Deposition", *Adv. Mater.* **23**, 2657 (2011).

[27] J. D. Fowlkes, R. Winkler, B. B. Lewis, M. G. Stanford, H. Plank and P. D. Rack,

"Simulation-Guided 3D Nanomanufacturing via Focused Electron Beam Induced Deposition", *ACS Nano* **10**, 6163 (2016).

[28]   I. Utke, P. Hoffmann, R. Berger and L. Scandella, "High-resolution magnetic Co supertips grown by a focused electron beam", *Appl. Phys. Lett.* **80**, 4792 (2002).

[29]   M. Takeguchi, M. Shimojo, R. Che and K. Furuya, "Fabrication of a nano-magnet on a piezo-driven tip in a TEM sample holder", *J. Mater. Sci.* **41**, 2627 (2006).

[30]   L. M. Belova, O. Hellwig, E. Dobisz and E. Dan Dahlberg, "Rapid preparation of electron beam induced deposition Co magnetic force microscopy tips with 10 nm spatial resolution", *Rev. Sci. Instrum.* **83**, 093711 (2012).

[31]   A. Fernández-Pacheco, L. Serrano-Ramón, J. M. Michalik, M. R. Ibarra, J. M. De Teresa, L. O'Brien, D. Petit, J. Lee and R. P. Cowburn, "Three dimensional magnetic nanowires grown by focused electron-beam induced deposition", *Sci. Rep.* **3**, 1492 (2013).

[32]   H. Lavenant, V. Naletov, O. Klein, G. De Loubens, L. Casado and J. M. De Teresa, "Mechanical magnetometry of Cobalt nanospheres deposited by focused electron beam at the tip of ultra-soft cantilevers", *Nanofabrication* **1**, 65 (2014).

[33]   J. H. Franken, M. A. J. Van Der Heijden, T. H. Ellis, R. Lavrijsen, C. Daniels, D. Mcgrouther, H. J. M. Swagten and B. Koopmans, "Beam-Induced Fe Nanopillars as Tunable Domain-Wall Pinning Sites", *Adv. Funct. Mater.* **24**, 3508 (2014).

[34]   M. Gavagnin, H. D. Wanzenboeck, S. Wachter, M. M. Shawrav, A. Persson, K. Gunnarsson, P. Svedlindh, M. Stöger-Pollach and E. Bertagnolli, "Free-Standing Magnetic Nanopillars for 3D Nanomagnet Logic" *ACS Appl. Mater. Interfaces* **6**, 20254 (2014).

[35]   G. C. Gazzadi and S. Frabboni, "Structural transitions in electron beam deposited Co-carbonyl suspended nanowires at high electrical current densities", *Beilstein J. Nanotechnol.* **6**, 1298 (2015).

[36]   M. J. Perez-Roldan, F. Tatti, P. Vavassori, A. Berger and A. Chuvilin, "Segregation of materials in double precursor electron-beam-induced-deposition: a route to functional magnetic nanostructures", *Nanotechnology* **26**, 375302 (2015).

[37]   P. Vavassori, M. Pancaldi, M. J. Perez-Roldan, A. Chuvilin, and A. Berger, "Remote Magnetomechanical Nanoactuation", *Small* **12**, 1013 (2016).

[38]   A. Fernández-Pacheco, J. M. De Teresa, R. Córdoba and M. R. Ibarra, "Magnetotransport properties of high-quality cobalt nanowires grown by focused-electron-beam-induced-deposition", *J. Phys. D: Appl. Phys.* **42**, 055005 (2009).

[39]   M. Takeguchi, M. Shimojo and K. Furuya, "Fabrication of magnetic nanostructures using electron beam induced chemical vapour deposition",

Nanotechnology **16**, 1321 (2005).

[40]   R. Lavrijsen, R. Córdoba, F. J. Schoenaker, T. H. Ellis, B. Barcones, J. T. Kohlhepp, H. J. M. Swagten, B. Koopmans, J. M. De Teresa, C. Magén, M. R. Ibarra, P. Trompenaars and J. J. L. Mulders, "Fe:O:C grown by focused-electron-beam-induced deposition: magnetic and electric properties", *Nanotechnology* **22**, 025302 (2011).

[41]   A. Perentes, G. Sinicco, G. Boero, B. Dwir and P. Hoffmann, "Focused electron beam induced deposition of nickel", *J. Vac. Sci. Technol. B* **25**, 2228 (2007).

[42]   R. Córdoba, B. Barcones, E. Roelfsema, M. A. Verheijen, J. J. L. Mulders, P. H. F. Trompenaars and B. Koopmans, "Functional nickel-based deposits synthesized by focused beam induced processing", *Nanotechnology* **27**, 065303 (2016).

[43]   E. Nikulina, O. Idigoras, J. M. Porro, P. Vavassori, A. Chuvilin and A. Berger, "Origin and control of magnetic exchange coupling in between focused electron beam deposited cobalt nanostructures", *Appl. Phys. Lett.* **103**, 123112 (2013).

[44]   M. Gavagnin, H. D. Wanzenboeck, D. Belic, M. M. Shawrav, A. Persson, K. Gunnarsson, P. Svedlindh and E. Bertagnolli, "Magnetic force microscopy study of shape engineered FEBID iron nanostructures", *Phys. Status Solidi A* **211**, 368 (2014).

[45]   J. M. De Teresa and A. Fernández-Pacheco, "Present and future applications of magnetic nanostructures grown by FEBID", *Appl. Phys. A* **117**, 1645 (2014).

[46]   J. M. De Teresa, A. Fernández-Pacheco, R. Córdoba, L. Serrano-Ramón, S. Sangiao and M. R. Ibarra, "Review of magnetic nanostructures grown by focused electron beam induced deposition (FEBID)", *J. Phys. D: Appl. Phys.* **49**, 243003 (2016).

[47]   F. Guo, L. M. Belova and R. D. McMichael, "Spectroscopy and imaging of edge modes in permalloy nanodisks", *Phys. Rev. Lett.* **110**, 017601 (2013).

[48]   M. Gabureac, L. Bernau, I. Utke, and G. Boero, "Granular Co-C nano-Hall sensors by focused-beam-induced deposition", *Nanotechnology* **21**, 115503 (2010).

[49]   L. Serrano-Ramón, R. Córdoba, L. A. Rodríguez, C. Magén, E. Snoeck, C. Gatel, I. Serrano, M. R. Ibarra and J. M. De Teresa, "Ultrasmall functional ferromagnetic nanostructures grown by focused electron-beam-induced deposition", *ACS Nano* **5**, 7781 (2011).

[50]   N. Sharma, R. A. van Mourik, Y. Yin, B. Koopmans and S. S. P. Parkin, "Focused-electron-beam-induced-deposited cobalt nanopillars for nanomagnetic logic", *Nanotechnology* **27**, 165301 (2016).

[51]   O. V. Dobrovolskiy, E. Begun, M. Huth, V. A. Shklovskij and M. I. Tsindlekht,

"Vortex lattice matching effects in a washboard pinning potential induced by Co nanostripe arrays", *Physica C* **471**, 449 (2011).

[52]   J. Pablo-Navarro, C. Magén and J. M. de Teresa, "Three-dimensional core-shell ferromagnetic nanowires grown by focused electron beam induced deposition", *Nanotechnology* **27**, 285302 (2016).

[53]   I. Serrano-Esparza, R. Córdoba, J. J. L. Mulders, M. R. Ibarra and J. M. De Teresa, "Precursor competition in focused-ion-beam-induced co-deposition from $W(CO)_6$ and $C_{10}H_8$", *Sci. Lett.* **4**, 127 (2015).

[54]   A. Szkudlarek, M. Gabureac and I. Utke, "Determination of the Surface Diffusion Coefficient and the Residence Time of Adsorbates via Local Focused Electron Beam Induced Chemical Vapour Deposition", *J. Nanosci. Nanotechnol.* **11**, 8074 (2011).

[55]   R. F. Egerton, "Electron Energy-Loss Spectroscopy in the Electron Microscope", *Springer* (2011).

[56]   A. Fernández-Pacheco, J. M. De Teresa, A. Szkudlarek, R. Córdoba, M. R. Ibarra, D. Petit, L. O'Brien, H. T. Zeng, E. R. Lewis, D. E. Read and R. P. Cowburn, "Magnetization reversal in individual cobalt micro- and nanowires grown by focused-electron-beam-induced-deposition", *Nanotechnology* **20**, 475704 (2009).

[57]   F. J. Schoenaker, R. Córdoba, R. Fernández-Pacheco, C. Magén, O. Stéphan, C. Zuriaga-Monroy, M. R. Ibarra and J. M. De Teresa, "Focused electron beam induced etching of titanium with XeF_2", *Nanotechnology* **22**, 265304 (2011).

[58]   R. Córdoba, A. Ibarra, D. Mailly and J. M. De Teresa, "Vertical Growth of Superconducting Crystalline Hollow Nanowires by He^+ Focused Ion Beam Induced Deposition", *Nano Lett.* 18, 1379 (2018).

[59]   S. Sangiao, C. Magén, D. Mofakhami, G. De Loubens and J. M. De Teresa, "Magnetic properties of optimized cobalt nanospheres grown by focused electron beam induced deposition (FEBID) on cantilever tips", *Beilstein J. Nanotechnol.* **8**, 2106 (2017).

[60]   E. Berganza, C. Bran, M. Jaafar, M. Vázquez and A. Asenjo, "Domain wall pinning in FeCoCu bamboo-like nanowires", *Sci. Rep.* **6**, 29702 (2016).

[61]   Y. M. Lau, P. C. Chee, J. T. L. Thong, and V. Ng, "Properties and applications of cobalt-based material produced by electron-beam-induced deposition", *J. Vac. Sci. Technol. A* **20**, 1295 (2002).

[62]   G. Tosolini, J. M. Michalik, R. Córdoba, J. M. de Teresa, F. Pérez-Murano and J. Bausells, "Magnetic properties of cobalt microwires measured by piezoresistive cantilever magnetometry", *Nanofabrication* **1**, 80 (2014).

[63]   J. Pablo-Navarro, Soraya Sangiao, C. Magén and J. M. De Teresa, "Diameter

modulation of 3D nanostructures in focused electron beam induced deposition using local electric fields and beam defocus", *Nanotechnology* (2019).

[64] K. M. Satyalakshmi, A. Olkhovets, M. G. Metzler, C. K. Harnett, D. M. Tanenbaum and H. G. Craighead, "Charge induced pattern distortion in low energy electron beam lithography", *J. Vac. Sci. Technol. B* **18**, 3122 (2000).

[65] L. D. Menard and J. M. Ramsey, "Fabrication of sub-5 nm nanochannels in insulating substrates using focused ion beam milling", *Nano Lett.* **11**, 512 (2011).

[66] J. Cazaux, "Some considerations on the electric field induced in insulators by electron bombardment", *J. Appl. Phys.* **59**, 1418 (1986).

[67] M. Toth, W. R. Knowles and B. L. Thiel, "Secondary electron imaging of nonconductors with nanometer resolution", *Appl. Phys. Lett.* **88**, 023105 (2006).

[68] W.-Q. Li, K. Mu, and R.-H. Xia, "Self-consistent charging in dielectric films under defocused electron beam irradiation", *Micron* **42**, 443 (2011).

[69] J. Joo, B. Y. Chow and J. M. Jacobson, "Nanoscale patterning on insulating substrates by critical energy electron beam lithography", *Nano Lett.* **6**, 2021 (2006).

[70] B. D. Myers and V. P. Dravid, "Variable pressure electron beam lithography (VP-eBL): A new tool for direct patterning of nanometer-scale features on substrates with low electrical conductivity", *Nano Lett.* **6**, 963 (2006).

[71] D. R. S. Cumming, I. I. Khandaker, S. Thoms and B. G. Casey, "Efficient diffractive optics made by single-step electron beam lithography in solid PMMA", *J. Vac. Sci. Technol. B* **15**, 2859 (1997).

[72] D. J. Stokes, T. Vystavel and F. Morrissey, "Focused ion beam (FIB) milling of electrically insulating specimens using simultaneous primary electron and ion beam irradiation", *J. Phys. D: Appl. Phys.* **40**, 874 (2007).

[73] P. Peinado, S. Sangiao and J. M. De Teresa, "Focused Electron and Ion Beam Induced Deposition on Flexible and Transparent Polycarbonate Substrates", *ACS Nano* **9**, 6139 (2015).

[74] Y. R. Choi, P. D. Rack, B. Frost and D. C. Joy, "Effect of electron beam-induced deposition and etching under bias", *Scanning* **29**, 171 (2007).

[75] F. Panciera, M. M. Norton, S. B. Alam, S. Hofmann, K. Mølhave and F. M. Ross, "Controlling nanowire growth through electric field-induced deformation of the catalyst droplet", *Nat. Commun.* **7**, 12271 (2016).

[76] H. Plank, C. Gspan, M. Dienstleder, G. Kothleitner and F. Hofer, "The influence of beam defocus on volume growth rates for electron beam induced platinum deposition", *Nanotechnology* **19**, 485302 (2008).

[77] J. M. De Teresa, R. Córdoba, A. Fernández-Pacheco, O. Montero, P. Strichovanec

and M. R. Ibarra, "Origin of the Difference in the Resistivity of As-Grown Focused-Ion- and Focused-Electron-Beam-Induced Pt Nanodeposits", *J. Nanomater.* **2009**, 936863 (2009).

[78]   M. Huth, D. Klingenberger, C. Grimm, F. Porrati and R. Sachser, "Conductance regimes of W-based granular metals prepared by electron beam induced deposition", *New J. Phys.* **11**, 033032 (2009).

[79]   K. A. G. Rao, N. Nadasen and V. M. Naik, "Theoretical and numerical analysis of non-conventional systems for generating static electric fields: A monograph", *Strategic Book Publishing* (2013).

[80]   J. D. Fowlkes, S. J. Randolph and P. D. Rack, "Growth and Simulation of High-Aspect Ratio Nanopillars by Primary and Secondary Electron-Induced Deposition", *J. Vac. Sci. Technol. B* **23**, 2825 (2005).

[81]   D. A. Smith, J. D. Fowlkes and P. D. Rack, "A nanoscale three-dimensional Monte Carlo simulation of electron-beam-induced deposition with gas dynamics", *Nanotechnology* **18**, 265308 (2007).

[82]   G. Arnold, R. Timilsina, J. Fowlkes, A. Orthacker, G. Kothleitner, P. D. Rack and H. Plank, "Fundamental resolution limits during electron-induced direct-write synthesis", *ACS Appl. Mater. Interfaces* **6**, 7380 (2014).

[83]   R. Schmied, J. D. Fowlkes, R. Winkler, P. D. Rack and H. Plank, "Fundamental edge broadening effects during focused electron beam induced nanosynthesis", *Beilstein J. Nanotechnol.* **6**, 462 (2015).

[84]   J. Orloff and L. W. Swanson, "An asymmetric electrostatic lens for field-emission microprobe applications", *J. Appl. Phys.* **50**, 2494 (1979).

[85]   A. T. J. B. Eppink and D. H. Parker, "Velocity map imaging of ions and electrons using electrostatic lenses: Application in photoelectron and photofragment ion imaging of molecular oxygen", *Rev. Sci. Instrum.* **68**, 3477 (1997).

[86]   Y. Lin and D. C. Joy, "A new examination of secondary electron yield data", *Surf. Interface Anal.* **37**, 895 (2005).

[87]   M. Futamoto, M. Hanbücken, C. J. Harland, G. W. Jones and J. A. Venables, "Visualization of submonolayer and surface topography by biassed secondary electron imaging: Application to Ag layers on Si and W surfaces", *Surf. Sci.* **150**, 430 (1985).

[88]   C. A. Walsh, "Effect of specimen bias on secondary electron images in the STEM", *Ultramicroscopy* **45**, 85 (1992).

[89]   T. E. Everhart and R. F. M. Thornley, "Wide-band detector for micro-microampere low-energy electron currents", *J. Sci. Instrum.* **37**, 246 (1960).

[90]   B. L. Thiel, M. Toth, R. P. M. Schroemges, J. J. Scholtz, G. Van Veen and W. R.

Knowles, "Two-stage gas amplifier for ultrahigh resolution low vacuum scanning electron microscopy", *Rev. Sci. Instrum.* **77**, 033705 (2006).

[91]   J. Pablo-Navarro, D. Sanz-Hernández, C. Magén, A. Fernández-Pacheco and J. M. De Teresa, "Tuning shape, composition and magnetization of 3D cobalt nanowires grown by focused electron beam induced deposition (FEBID)", *J. Phys. D: Appl. Phys.* **50**, 18LT01 (2017).

Chapter 4: Towards properties improvement by thermal annealing

In this chapter, thermal annealing strategies are followed to overcome the Focused Electron Beam Induced Deposition deficiencies in terms of purity and crystallinity. Different *ex situ* and *in situ* post-growth treatments were performed in 3D Co and Fe nanowires to increase the metallic composition, induce a crystallization of the pseudo-amorphous as-grown structures and enhance the net magnetic induction values. Dedicated *in situ* TEM experiments were carried out to monitor in real time changes in the nanowires properties as a function of temperature and time, shedding light on the nanoscale processes involved during the annealing procedure.

4.1 Introduction

The FEBID fabrication process implies the electron-beam-induced decomposition of a metal-organic precursor gas adsorbed on the growth surface, fundamentally driven by the SE emitted by the substrate or the nascent deposit material [1]. One of the main issues of this synthetic technique is the existence of chemical impurities due to incompletely dissociated precursor gas molecules incorporated into the deposit. In addition, the structures also contain different levels of contaminants originating from the dissociation of residual gases in the working chamber [2]. Despite this, as described in Chapter 3, purity can be improved by precise control of primary electron beam parameters, chamber base pressure, precursor gas flux, etc. [3], which in some cases enables the fabrication of deposits of high metallic content [4][5][6][7][8]. However, in many cases the as-grown metallic content often remains moderate [9]. Thus, the lack of purity and the poor crystallinity will in general be limiting factors for capitalizing the full potential of FEBID.

To face this limitation, diverse approaches have been followed to increase the purity of FEBID deposits, as reviewed by Botman et al. in 2009 [2], and further explored since. This includes *in situ* [10][11] and *ex situ* [12][13][14] post-annealing treatments at high vacuum and under controlled reactive gas atmospheres [15][16], use of substrates at high temperatures during growth [17][18], electron beam irradiation of the deposits [19][20], laser-assisted heating during deposition [21][22], post-growth Joule heating upon injection of high electric currents [23], supersonic jet delivery of precursor gas [24], use of carbon-free precursor gases [25], and combinations of all these methods [16][26][27][28][29]. For example, astounding success has been achieved in growing virtually-pure Pt deposits by post-growth electron irradiation in O atmosphere [15], or functional Au plasmonic nanostructures by electron beam irradiation in water vapor atmosphere [30]. However, such widely-used strategies have been generally applied to 2D deposits, whereas purification of 3D objects have been scarcely attempted [31]. The

latter presents specific problems: for instance, the architecture stability can be compromised due to the high-volume shrinkage occurring in low metal content deposits, eventually leading to a substantial modification of the object shape or even the collapse of the 3D structures [32].

In our case, a special emphasis should be given to magnetic materials grown by FEBID. Specifically, Co- [33], Fe- [34] and Ni-based [35] precursor gases have been used, in which low metallic content results in degraded magnetic properties. As a result, the functionality of FEBID-grown magnetic devices may be compromised. Nevertheless, under optimum growth conditions, Co and Fe deposits are amongst the FEBID materials with highest metallic content levels (~95% at.) [5][36][37][38]. In both cases, as-grown high purity 2D deposits have been achieved with limited lateral resolution and small crystalline size. In the case of 3D magnetic deposits, the dispersion of composition values found in the literature is high, given the strong dependence of the growth mode to small changes in the numerous growth parameters [37][39]. Nonetheless, 3D nanostructures with a high aspect ratio, such as vertical nanowires, evidence a drastic reduction of the metallic content for decreasing diameter. Moreover, the natural oxidation of the surface upon air exposure (typically 5-nm-thick) becomes critical as the surface-to-volume ratio significantly increases and impairs the ferromagnetic properties of the nanostructures due to the formation of non-ferromagnetic species [40][41]. It is particularly important to emphasize that the purity and crystallinity will have great impact in the electrical transport [10] and magnetic properties (saturation magnetization, magnetocrystalline anisotropy, coercive field, etc.) [39][42], both key for the potential application of FEBID magnetic deposits. For all these reasons, purification of 3D FEBID magnetic objects is an exciting challenge and different methods have been explored over the years.

The first attempts to purify Fe deposits were carried out by Shimojo et al. through *ex situ* thermal annealing and electron beam irradiation in ultra-high vacuum, demonstrating the formation of highly-magnetic α-Fe deposits, in some cases coexisting

with Fe carbides [13]. The same group subjected 3D nanostructures to post annealing up to 600 ºC, achieving Fe contents near 60% at. [43]. Studies on FEBID Co include the work by Belova et al., who analyzed C-seeded micrometric deposits grown on substrates at 70 ºC, on the verge of the thermal decomposition of the precursor gas, which presented a metal content >95% at. Co [44]. Begun et al. explored the catalytic activity of Co in a H_2 reactive atmosphere upon electron beam irradiation, observing the formation of metallic Co only in a 20-nm-thick surface region of the deposit [45]. The effect of intense electric current on the properties of suspended Co nanowires has also been reported to induce purification from 80% to 89% at. Co and crystallization into large face-centered-cubic (*fcc*) crystals caused by local Joule heating and electromigration [23]. Recently, post-growth annealing in high vacuum of thin Co stripes increased its composition from 67% to 84% at. Co, with a conductivity of metallic behavior and three orders of magnitude higher than that of the as-grown material [10].

Such previous work has provided hints on how to improve the purity and crystallinity of magnetic deposits grown by FEBID. This chapter will summarize the high-vacuum thermal annealing procedures followed in this thesis to obtain purified and crystalline 3D Co magnetic nanowires from FEBID deposits, maintaining the original shape. In the case of 3D Fe-FEBID nanostructures, the evolution of the morphology and compositional distribution was monitored in real time [31][46]. Such successful post-processing methods may facilitate the development of future applications based on 3D magnetic nanostructures.

4.2 Annealing process on 3D cobalt nanowires

In this section, the attention is drawn to the synthesis of pure and fully-crystalline 3D Co nanowires. The aim is to increase the crystallinity and metallic content under *ex situ* annealing, simultaneously improving the saturation magnetization value. Moreover, another key objective is to minimize the volume shrinkage, ensuring good mechanical

stability of the 3D objects. Thanks to the purification processes, the attention of as-grown FEBID magnetic nanostructures can be focused on tailoring the lateral dimensions and increasing architectural accuracy to produce individual or arrays of customized 3D nanostructures. These can be later *ex situ* annealed to obtain devices of pure material with optimum magnetic response for the numerous applications foreseen, i.e., magnetic data storage and logic systems, Hall-effect nanosensing, catalytic growth of nanostructures, cantilever functionalization or magnetic nanoactuators [38].

4.2.1 Experimental details

The nanostructures were grown in the commercial Helios Nanolab 650 Dual Beam system using $Co_2(CO)_8$ as precursor gas. After the optimization of the parameters, the deposits were fabricated selecting an electron beam voltage of 5 kV, an electron beam current of 100 pA and a chamber growth pressure of 2.6×10^{-6} mbar (base pressure of 1.3×10^{-6} mbar). Two different batches were grown under the same main conditions: batch 1 for structural, chemical and magnetic characterization, and batch 2 for nanoSQUID magnetometry. In batch 1, the growth pattern was a single point scanned in spot mode by the electron beam for 45 seconds in standard TEM Cu grids [31][39], whereas in batch 2 the growth was performed for 40-60 seconds onto a 500-nm-thick Si_3N_4 membrane covered by 10 nm of Al avoiding charging effects for the nanowire which was not annealed and in thinned (few µm-thick) TEM Cu grids for the nanowires devoted to annealing [47].

The *ex situ* post-growth annealing in high vacuum took place in an SEM Quanta FEG 250 system. The SEM chamber was initially evacuated until the base pressure decreased below 4×10^{-6} mbar. A heating ramp of 50 ºC/min was programmed, corresponding to the maximum allowed by the equipment, until the target annealing temperature for each sample was reached. Then the samples were annealed at 150 ºC, 300 ºC, 450 ºC and 600 ºC for 100 minutes. The use of metallic grids is paramount to

guarantee good thermalization of the nanowires during the post-processing. The base pressure increased during the early stages of the annealing process due to degassing of the SEM components near heating stage before falling back gradually to the base pressure until the experiment is finished. After annealing, the heater was switch off and the specimen cooled down spontaneously to room temperature still in high vacuum.

HRTEM imaging was performed in the Titan Cube 60-300 at the LMA operated at 300 kV. SAED was carried out in the Tecnai T20 at 200 kV using a 10 µm aperture. STEM and EELS experiments were carried out in the Titan Low Base 60-300 system at 300 kV. The STEM-EELS experiments were performed with a 25 mrad convergence semi-angle, an energy dispersion of 0.5 eV/pixel with a resolution of 1.5 eV, a GIF aperture of 2.5 mm, a camera length of 10 mm, a pixel time of 15 ms and an estimated electron beam current of 270 pA. EDS semi-quantitative experiments were carried out in the Helios Nanolab 650 Dual Beam system after the natural oxidation of the nanowires and before the annealing process, using an electron beam voltage of 5 kV, an electron beam current of 800 pA, and a base pressure of 1.43×10^{-6} mbar.

Off-Axis EH experiments were performed at 300 kV in the Titan Cube 60-300. The biprism was excited between 150 and 170 V to create the overlapping area ranging from 400 nm to 500 nm in width, with a fringe contrast ranging from 20% to 25%. The hologram acquisition time was 5 seconds. Central regions of the nanowires were analysed, far from the tip where the magnetic induction may not be homogeneously along the nanowire long axis. The magnetic induction was calculated using the Equation A.3.

For the nanoSQUID magnetic characterization, the nanowires could be directly grown on the surface of the nanoSQUID sensor and in close vicinity to the nanoloop to guarantee large magnetic coupling between the nanostructure and the nanoloop. However, the nanowire would form an angle with respect to the nanoSQUID plane and with the applied magnetic field, *H*, hindering the interpretation of the measurements. Moreover, the yttrium barium copper oxide (YBCO) nanoSQUID can under no

circumstances be subjected to the annealing process. For these two reasons, nanowires were grown and annealed on a separate substrate and later transferred to the nanoSQUID, for which a special process has been developed. In fact, two different approaches were used for the reference as-deposited nanowire and the ones intended for annealing, respectively. The transfer processes for the as-deposited nanowire and for the annealed ones is summarized in Figure 4.1 and Figure 4.2, respectively.

Figure 4.1. Transfer of the as-deposited Co nanowire. Artificially coloured SEM images with the nanowire in yellow and indicated by a yellow arrow, the nanomanipulator in blue and the Pt-FIBID deposit in green.
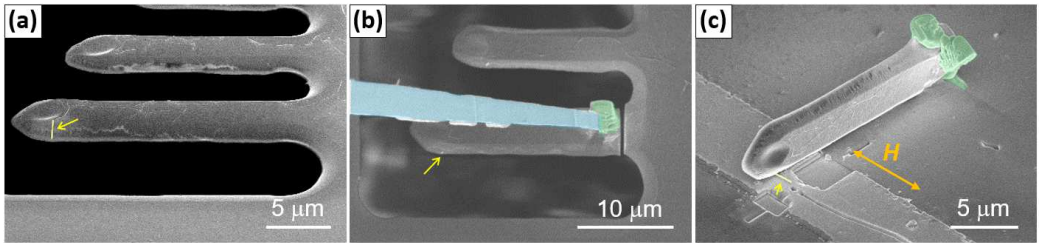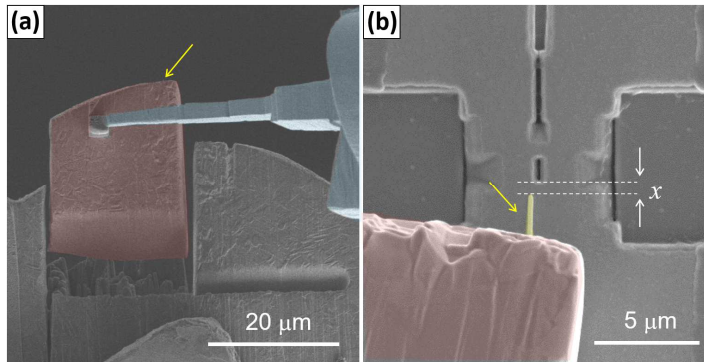

Figure 4.2. Transfer of an annealed Co nanowire. Artificially coloured SEM images with the nanowire in yellow and indicated by a yellow arrow, the nanomanipulator in blue and the Cu lamella in red. The distance x in (b) denotes the gap between the nanowire tip and the nanoloop edge.

As shown in Figure 4.1(a), the nanowire is grown vertically on an Al-coated Si_3N_4 palette, before manually rotating it by 90 degrees, so that the nanowire lies horizontally. After the attachment of the nanomanipulator to the palette by Pt-FIBID using $(CH_3)_3Pt(CpCH_3)$ precursor gas, the palette is released by FIB-cutting, as illustrated in Figure 4.1(b). As seen in Figure 4.1(c), the palette is transferred to the nanoSQUID, ensuring that the nanowire long axis is parallel to the substrate plane and perpendicular to the grain boundary (GB) plane, i.e., along H direction, with the tip as close as possible to the nanoloop. Finally, the palette is attached to the substrate by Pt-FIBID and the nanomanipulator is released. In the case of annealed nanowires, the procedure is similar, but using metallic palettes to guarantee proper annealing. For this reason, Cu grids, previously thinned and partially cut into microscopic lamellae were used as carriers to facilitate the subsequent transfer steps, as shown in Figure 4.2.

NanoSQUIDs are made of an 80-nm-thick YBCO film epitaxially grown on a $SrTiO_3$ (STO) bicrystal substrate, with a misorientation of 24 degrees, and covered by 70 nm of Au. The STO GB is naturally transferred to the YBCO film, behaving as a Josephson junction. The fabrication of submicron junctions from GBs in cuprates is a difficult task due to O out-diffusion from the junction and the ensuing degradation. This is overcome by FIB-milling producing an amorphous YBCO and STO redeposit covering the junction edges and preventing O out-diffusion. The central loop is also patterned by FIB intersecting the GB, as shown in Figure 4.3. Using commercial readout electronics, the devices are current-biased and operate in flux locked loop mode thanks to the patterning of a ~180-nm-wide constriction which allows coupling the net flux, Φ, to the nanoloop.

Each nanoSQUID is mounted, in proper thermal contact, to a sapphire plate installed in a variable temperature insert. This plate is located on a rotator for aligning the nanoSQUID, so that no Φ is coupled both to the nanoloop and to the Josephson junctions.
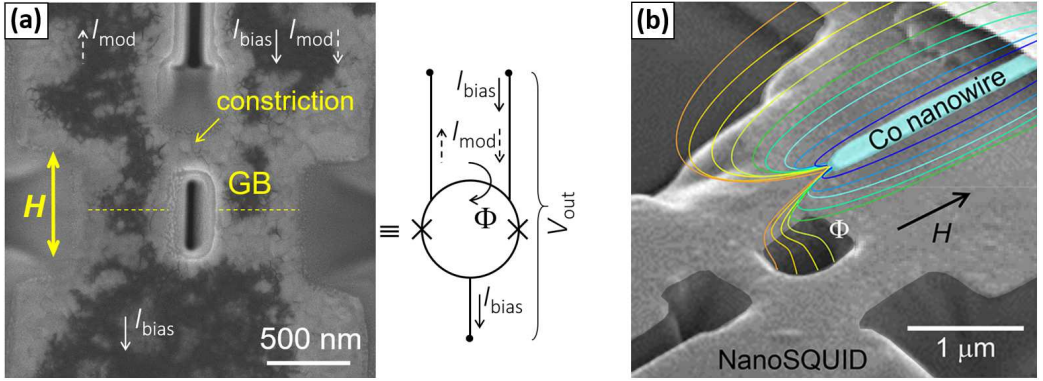
Figure 4.3. NanoSQUID, (a) equivalent electric circuit scheme and (b) flux, Φ, representation. The H direction, and the GB and constriction positions are highlighted. A current, I_{mod}, flowing through the constriction couples Φ to the nanoloop, serving to modulate the nanoSQUID response. The biasing current, I_{bias}, and the output voltage, V_{out}, are also indicated.

Magnetization measurements are performed by sweeping H at 8.3 mT/s and measuring the output voltage, V_{out}, as the nanowire is driven through magnetization reversal. The V_{out} is converted into units of Φ threading the nanoloop:

$$\Phi_{exp} = \frac{V_{out}M}{R_f} \tag{4.1}$$

where Φ_{exp} is the total flux signal coupled to the nanoSQUID from the nanowire, M the mutual inductance between the nanoloop and the constriction ($\sim\Phi_0/mA$), and R_f the feedback resistance of the readout electronics with a typical value of 3.3 kΩ. The reproducibility in the nanoSQUID fabrication has been checked and approved after growing and annealing two different nanowires under the same conditions, placing them on two different sensors and obtaining the congruent results.

The nanoSQUID magnetometry experiments were performed by Dr. María José Martínez-Pérez.

4.2.2 Structural and chemical changes as a function of the annealing temperature

The fabrication of 3D Co nanowires by FEBID of batch 1 was performed with the optimal growth parameters to obtain small diameters (~90 nm) with high aspect ratio (>15) and moderately high metallic purity [39]. EDS chemical analysis performed at half height of nanowires showed $(65 \pm 3)\%$ at. Co, $(23 \pm 3)\%$ at. C and $(11 \pm 1)\%$ at. O. Given these conditions, a net magnetic induction of ~0.80 T is obtained.

Five sets of specimens have been grown on five TEM Cu grids, labelled from A1 to E1. As summarized in Table 4.1, the post-growth annealing was carried at different temperatures: 150 ºC, 300 ºC, 450 ºC and 600 ºC, keeping grid A1 as the reference as-deposited sample. All the nanowires were exposed to air before and after the annealing procedure, suffering surface oxidation.

As illustrated in Figure 4.4 and Figure 4.5, HRTEM imaging and EELS chemical mapping in STEM mode have been used to track the structural and chemical evolution of the nanowires upon increasing annealing temperature. First, as shown in Figure 4.4(a), the as-deposited nanowires display the expected nanocrystalline microstructure, with no texture. The Fast Fourier Transform (FFT) of the image reveals a diffuse diffraction ring. Also, the presence of a ~5-nm-thick layer of Co_xO_y covering the whole nanostructure can be detected in the HRTEM image, as a brighter, lower density thin layer at the surface [48].

Sample	Annealing temperature (ºC)	Start pressure (10^{-6} mbar)	Final pressure (10^{-6} mbar)
A1	-	-	-
B1	150	2.3	3.6
C1	300	2.5	3.4
D1	450	3.2	4.5
E1	600	4.0	7.4

Table 4.1. Annealing conditions of each Co nanowire studied on batch 1.
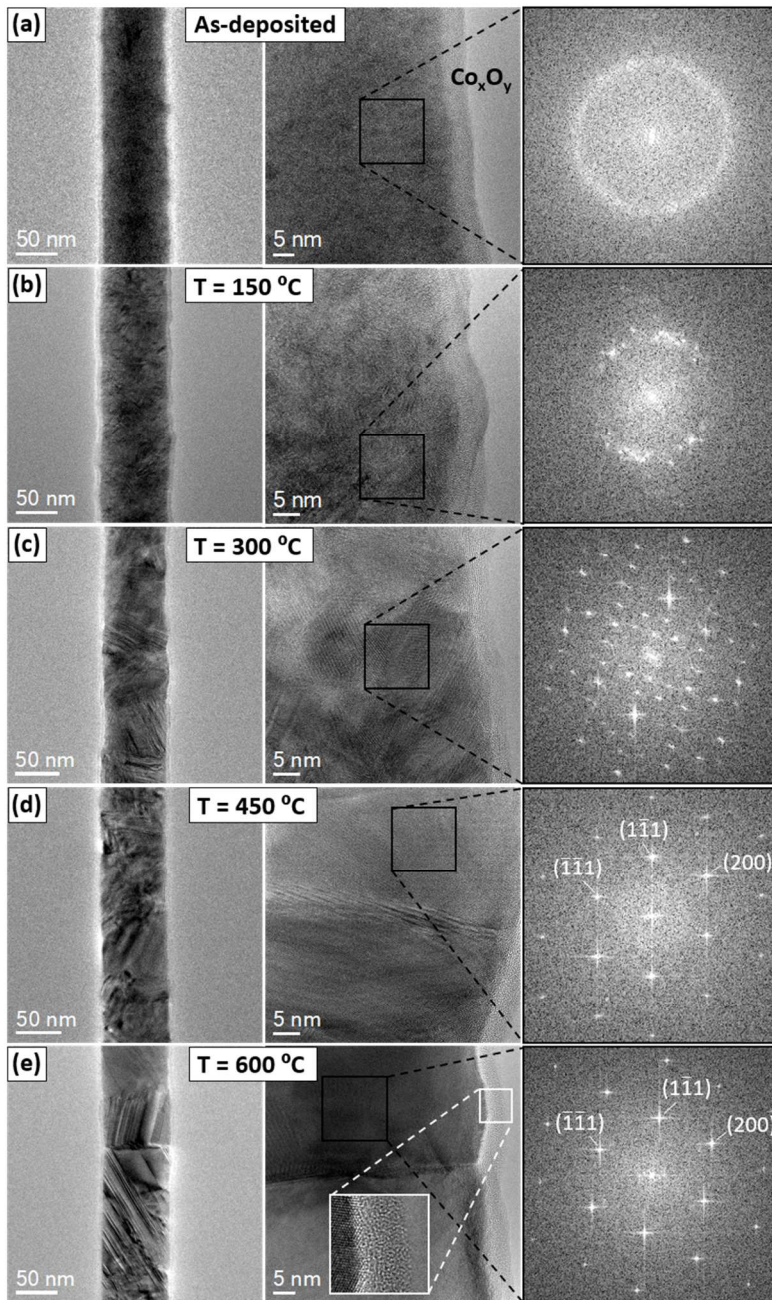
Figure 4.4. TEM (left column) and HRTEM (central column) images of (a) an as-deposited Co nanowire and the ones annealed at (b) 150 ℃, (c) 300 ℃, (d) 450 ℃ and (e) 600 ℃. Each sample is accompanied by the corresponding FFT of a 12 x 12 nm^2 area of the image (right column). Indexed FFT images correspond to *fcc* (011) crystals.
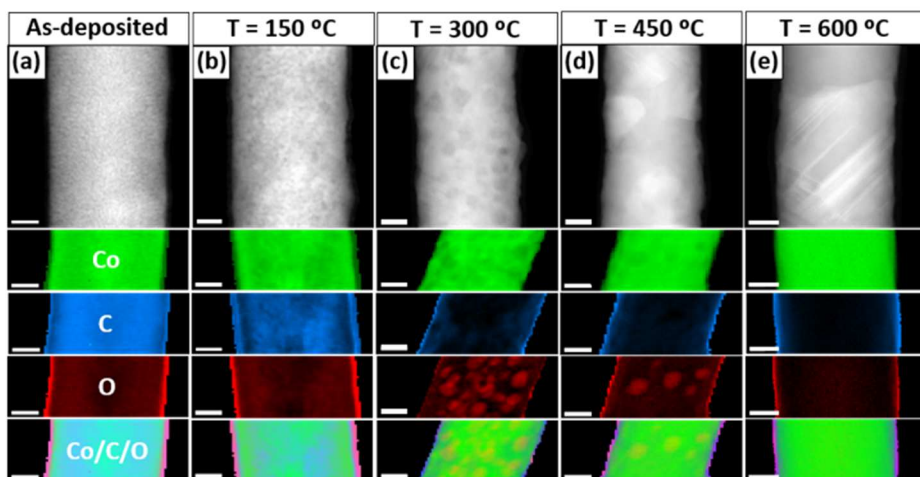
Figure 4.5. HAADF-STEM images (first row) and STEM-EELS chemical maps of (a) an as-deposited Co nanowire and the ones annealed at (b) 150 ºC, (c) 300 ºC, (d) 450 ºC and (e) 600 ºC. The chemical maps show the spatial distribution of Co, C and O, in green, blue and red, respectively. The lowest panels represent the relative compositions of Co, C and O in the same images. Scale bars are 20 nm in all images.

This finding is confirmed in Figure 4.5(a) where the EELS chemical map depicts an O-rich layer of comparable size surrounding the nanowire. Interestingly, the relative composition of O inside the nanowires is not perfectly homogeneous, gradually increasing from the core towards the surface. As shall be seen later, the non-ferromagnetic behaviour of the surface oxidation layer causes an overall deterioration of the ferromagnetic properties [48]. The crystallinity increases as the annealing temperature rises. Grain size is hard to quantify accurately due to the density and superposition of the crystals, but it can be roughly estimated by inspecting the HRTEM images and the features of the FFT. At 150 ºC some individual spots can also be identified together with the diffuse diffraction ring, denoting the presence of grains of larger size with sufficient crystalline coherence to produce clear Bragg diffraction spots. Also, the diffusion of contaminants has already begun, as the O distribution turns out to be more inhomogeneous. At 300 ºC diffuse scattering has disappeared in the FFT and large Co grains have grown to reach diameters around 10-15 nm. Well-defined O-rich regions

have clearly segregated all over a higher purity Co matrix, which correspond to Co oxide nanoparticles with a typical size of around 10 nm. Among the most common Co oxides, CoO is stable up to 900 °C in air and ambient temperatures, while it tends to transform into Co_3O_4 around 600-700 °C [49], much above the annealing temperatures discussed here. Thus, it is plausible that the observed oxide particles are CoO. Nanowires annealed at 450 °C present abundant regions where the FFT evidences a single crystalline pattern. This indicates that, in these areas, the grain size is large enough to not overlap with other crystals. When they do, mostly in the boundaries between two large crystals, Moiré fringes may appear in the STEM and HRTEM images. In turn, the grain size is becoming comparable to the diameter of the nanowire. This causes the drastic diminution of the number of O-rich grains with respect to annealing at 300 °C. Finally, the annealing at 600 °C gives rise to a nanowire composed by a succession of large single-crystals as wide as the nanowire itself. Remarkably, a GB spanning the whole nanowire width and separating two large crystals is observed in Figure 4.4(e). Chemical maps in Figure 4.5(e) evidence that O has practically disappeared inside the nanowires, whilst the natural oxidation still remains at the surface.

The nanowires microstructure as a function of the annealing temperature was further investigated acquiring SAED patterns (Figure 4.6) and HRTEM images of representative grains of both hexagonal-closest-packed (*hcp*) and *fcc* structures (Figure 4.7).
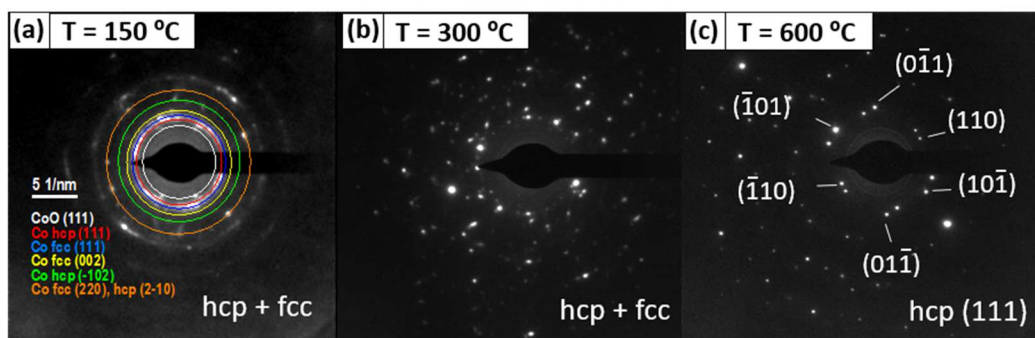
Figure 4.6. SAED patterns of Co nanowires annealed at (a) 150 °C, (b) 300 °C and (c) 600 °C.
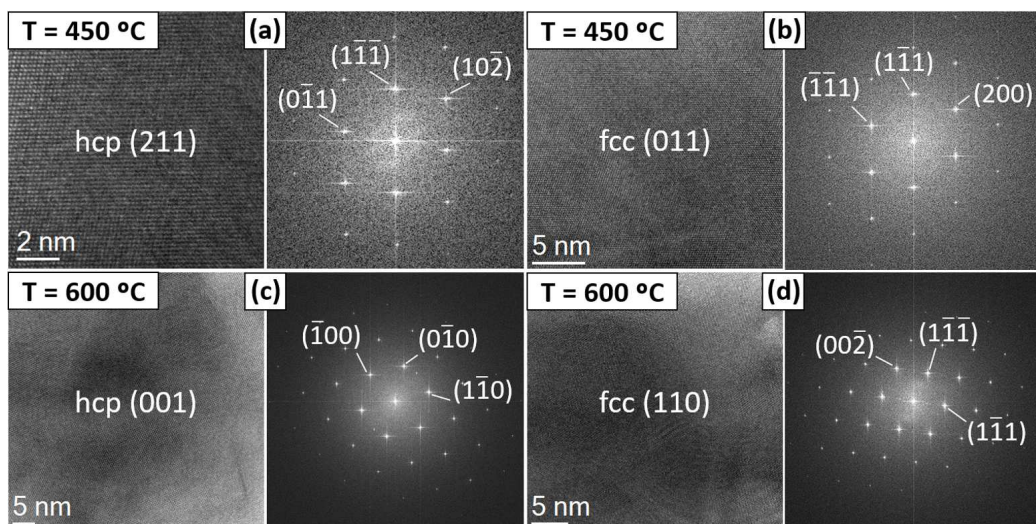
Figure 4.7. HRTEM images and their corresponding FFT of *hcp* and *fcc* Co grains of nanowires annealed at (a,b) 450 ℃ and (c,d) 600 ℃.

In the SAED experiments, at 150 ℃ diffraction spots corresponding to Co *fcc*, Co *hcp* and CoO have been found. At 300 ℃ the diffraction pattern is not polycrystalline anymore, resulting in crystals with *fcc* and *hcp* structure. Finally, at 600 ℃ the diffraction pattern is almost single crystalline. In this particular case, two *hcp* crystals near (111) zone axis have been recorded. In the HRTEM experiments, individual large Co grains with *fcc* or *hcp* crystal structure can be identified at 450 ℃ and 600 ℃.

A quantitative analysis of the composition as a function of the annealing temperature is shown in Figure 4.8. The overall Co composition of the nanowires, obtained from the integration of the spectral images shown in Figure 4.5, are plotted in Figure 4.8(a). The average metallic content increases from ~71% at. Co of as-deposited nanowires up to ~90% at. Co after annealing at 600 ℃. Both C and O content decrease showing different dependences: while the O diminishes from ~16% at. O (as-grown) to ~3% at. O (600 ℃-annealed), C content decreases more slowly from ~13% to ~7% at. C. This means that whereas O virtually disappears from the structure (except the possible oxidation of the surface), about 50% of the original C contamination remains after annealing at the

maximum temperature. Figure 4.8 (b) shows the radial dependence of the Co composition as a function of the annealing temperature. The metallic content increases from $(72 \pm 2)\%$ at. Co in the as-deposited sample up to $(93 \pm 2)\%$ at. Co at 450 ºC and above, with the detection of some local Co variations at intermediate temperatures related to the presence of the oxide grains. This evidences that, except for the outer surface of the nanowire, where natural oxidation and accumulation of non-volatile contaminants migrate, the inner part of the nanowire is virtually pure after annealing.
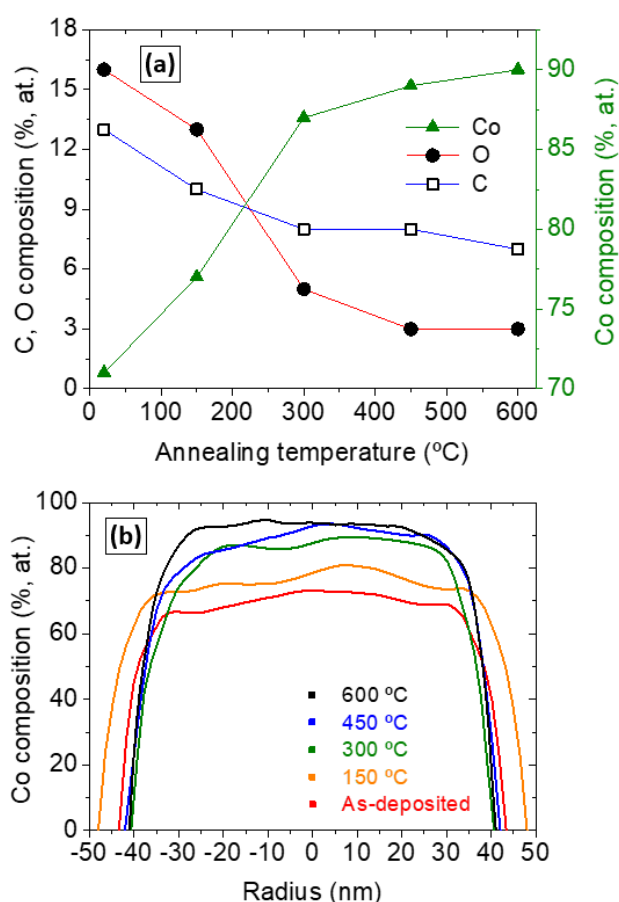
Figure 4.8. (a) Overall composition of the Co nanowires as a function of the annealing temperature extracted from the integration of Co, O and C signals of the STEM-EELS spectrum images in Figure 4.5. (b) Profiles of the Co composition of the nanowires as a function of the radial position for different annealing temperatures.

Interestingly, the composition of the non-ferromagnetic surface also changes with the annealing temperature, as shown in Figure 4.9.
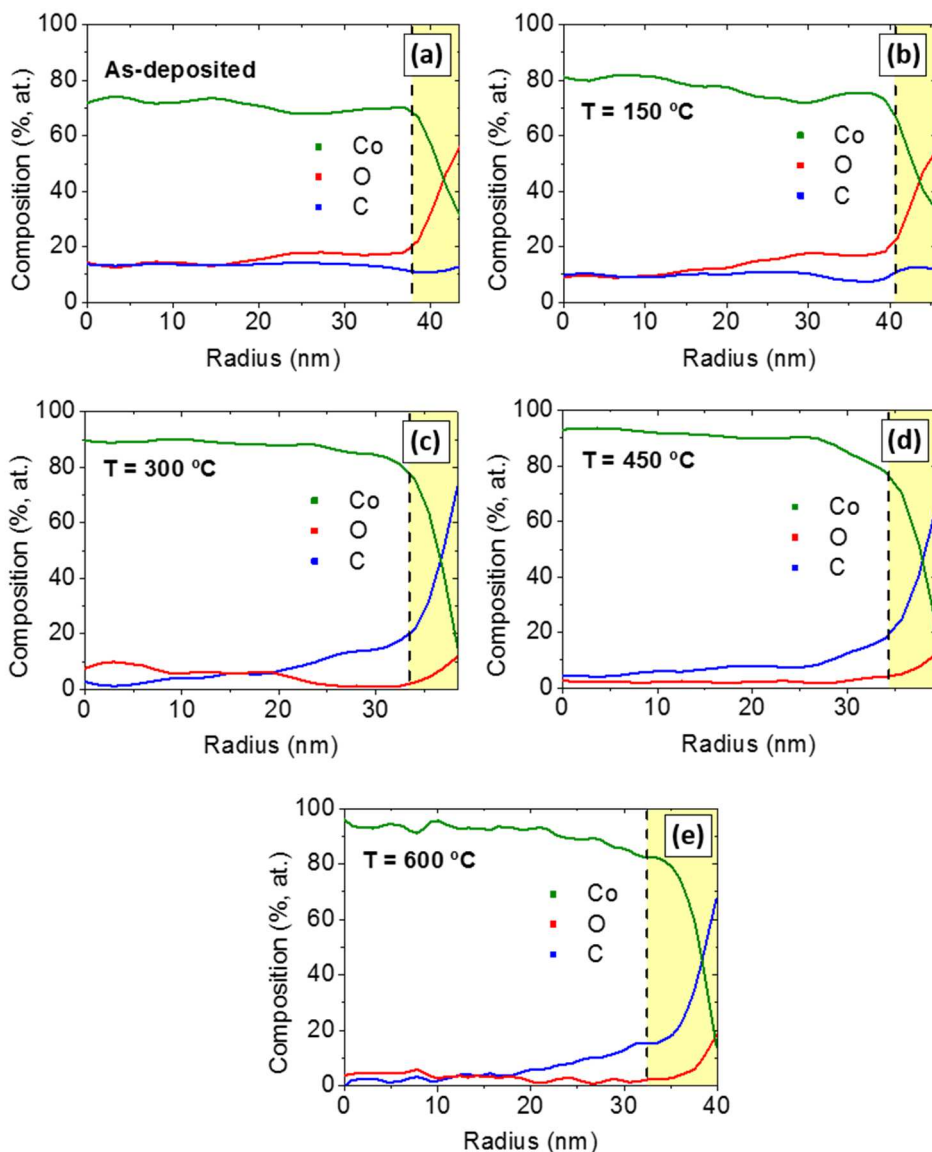
Figure 4.9. STEM-EELS profiles of the Co (in green), O (in red) and C (in blue) relative compositions as a function of the radius of (a) an as-deposited nanowire and the ones annealed at (b) 150 °C, (c) 300 °C, (d) 450 °C and (e) 600 °C. Yellow bands and dashed lines are guides to the eye showing the shells of the nanostructures.

For the as-deposited and 150 ºC-annealed nanowires the O/C ratio is over 1. However, for those nanowires annealed at 300 ºC or higher temperatures, the O/C ratio is reversed, particularly in the surface where the C content increases dramatically up to 60-70% at.

The spatially-resolved quantification of the chemical composition of the annealed nanowires shown in Figure 4.8 and Figure 4.9 gives some clues about the annealing process. Puydinger et al. reported that the expected mechanism for purification of Co-FEBID deposits is the thermal activation of precursor residues in the form of CO or CO_2 [10]. Upon thermal annealing, these volatile species migrate to the surface and evaporate, which accounts for a practically total loss of O except for the inevitable surface oxidation. The remaining C is non-volatile and accumulates in the surface at high annealing temperatures, in agreement with the observation of partially graphitized C at the surface even after annealing at 600 ºC, as shown in Figure 4.4(e). In these conditions the nanowires are apparently more resistant to oxidation, as the surface O content after annealing is much diminished with respect to as-deposited nanowires. Indeed, the formation of a ~5-10 nm carbonaceous layer may act as a protective coating from oxidation.

A key aspect of this annealing process for technological applications is preserving the original architecture of the nanostructure. As illustrated in Figure 4.10, the diameter and length of the Co nanowires are virtually the same before and after the annealing treatment, even at the highest annealing temperature. As no significant reduction of the volume occurs, the shape of the as-deposited nanostructure is conserved, enabling the application of this method to more complex geometries.
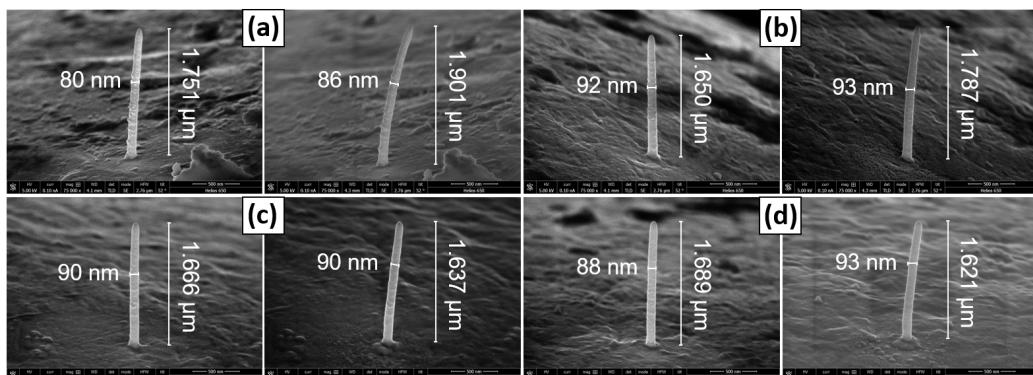
Figure 4.10. SEM images of Co nanowires annealed at (a) 150 ºC, (b) 300 ºC, (c) 450 ºC and (d) 600 ºC before (left) and after (right) the annealing treatment.

4.2.3 Magnetic induction dependence with annealing temperature

The drastic increase of Co content upon annealing must have a direct impact on the magnetization of the nanowire. The remanent net magnetic induction along the nanowire long axis, B, averaged across the thickness of the sample along the electrons trajectory, has been estimated by EH. As shown in Figure 4.11, the purification of the Co nanowires upon thermal annealing also strengthens B.

The B value sharply increases in the first stage of annealing, from (0.80 ± 0.04) T in the as-deposited sample up to (1.09 ± 0.08) T at 150 ºC, (1.20 ± 0.13) T at 300 ºC and (1.32 ± 0.06) T at 450 ºC, tending to stabilize at this point up to 600 ºC, with (1.36 ± 0.02) T. This enhancement of B as a function of the annealing temperature replicates the rise on metallic content, both increasing gradually until they tend to saturate around 450 ºC. It is worth noting that the presence of large *hcp* and *fcc* crystals, which implies the appearance of significant magnetocrystalline anisotropy [50], does not affect the remanent orientation of B. This is evidenced by the perfectly axial orientation of the flux lines all along the nanowires. Therefore, the strong magnetic shape anisotropy of high aspect ratio Co nanowires still dominates.
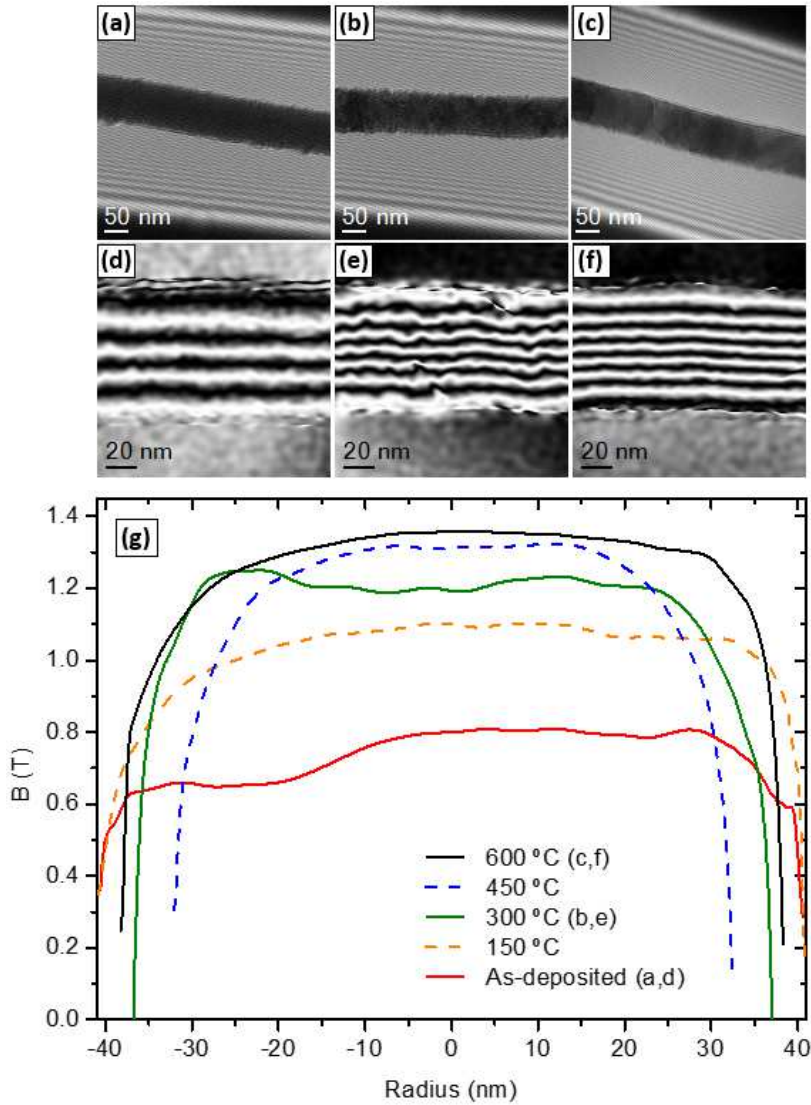
Figure 4.11. Electron holograms and *B* flux representations of (a,d) as-deposited Co nanowires and the ones annealed at (b,e) 300 ℃ and (c,f) 600 ℃. The *B* flux images are obtained by normalizing the φ_{MAG} ones to the diameter (maximum thickness) and calculating the cosine of 350 times the normalized φ_{MAG}. (g) Profile of the thickness-averaged axial component of *B* calculated as a function of the annealing temperature.

Despite the chemical quantification and the novel microstructure obtained after high-temperature annealing indicates that the inner part of the nanowires is essentially

pure Co, the estimated B of 1.36 T is still far from the bulk value (1.76 T). One reason for this discrepancy is the fact that C migration towards the nanowire surface plus the possible oxidation of the outer part of the nanowire make that the effective magnetic thickness is less than the nominal one. Therefore, the structural model would be that of a pure Co nanowire covered at the surface by a 5-10 nm-thick non-magnetic shell, composed of diffused residual C contaminants and naturally-oxidized Co formed upon exposure to air. If the shell thickness is neglected from the calculation just taking into account the core diameter, B increases up to 1.61 T, much nearer the bulk Co values already found in 2D deposits [8]. In fact, a similar correction on the chemical composition would bring the metallic content of the inner part of the nanowire closer to 100% at. Co. The estimated B values, corrected by the thickness of the non-magnetic shell, have been plotted in comparison with the overall Co content as a function of the annealing temperature in Figure 4.12. The correlation between these magnitudes is clear, i.e., both increase gradually up to 300 ºC, then tend to saturation at 450 ºC.
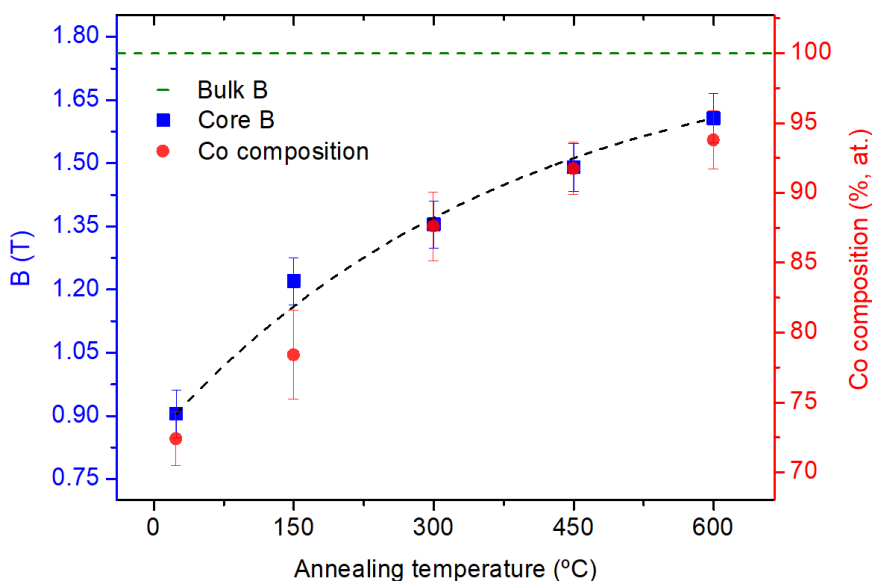
Figure 4.12. Average B and Co composition as a function of the annealing temperature considering the experimental data extracted from the central 20 nm of each nanowire.

The successful application of *ex situ* post-growth purification procedure to FEBID Co opens a new scenario in which, instead of maximizing metallic content during deposition, the optimization of growth conditions can be focused on other key parameters such as lateral size, geometric complexity or growth rate [29][51], which are key for the implementation of 3D FEBID deposits as racetrack memories, magnetic sensors or actuators. Nonetheless, the application of this procedure to other FEBID materials should be analyzed carefully, and further progress in the fabrication of as-grown deposits with higher metallic content would be required before applying the method described here. For instance, in the Co case, 65% at. Co is enough to guarantee the architectural stability of the initial design. However, in the example of low-purity Pt-FEBID using the standard precursor $(CH_3)_3Pt(CpCH_3)$, containing only 18% at. of Pt [52], it is likely that a similar process causes a large volume reduction [52]. In this chapter, the initial purity issue of 3D Fe-FEBID nanowires will be analysed in section 4.3.

4.2.4 Magnetic characterization by nanoSQUID magnetometry

The growth and annealing of 3D Co nanowires by FEBID of batch 2 were carried out with the same growth conditions as batch 1. Five samples labelled from A2 to E2 have been fabricated. The most relevant physical parameters of the nanowires and the magnitudes determined from the nanoSQUID experiments are listed in Table 4.2.

Sample	T_{ann} (ºC)	Diameter (nm)	Length (µm)	V_{mag} (10^6 nm³)	Height (nm)	μ_{NW} ($10^9 \, \mu_B$)	Purity (a.u.)
A2	-	71	1.8	7.13	379	1.1	0.75
B2	150	63	2.3	7.17	1050	1.0	0.84
C2	300	73	2.2	9.21	1055	1.4	0.96
D2	450	77	1.9	8.85	980	1.5	1.06
E2	600	76	2.1	9.53	483	1.8	1.06

Table 4.2. Nanowires experimental data: annealing temperature (T_{ann}), the diameter excluding the non-magnetic external layer (~5 nm); length; magnetic volume, V_{mag}; height of the nanowire tip with respect to the SQUID surface; total magnetic moment, μ_{NW}; and Co purity.

Firstly, Figure 4.13 shows representative hysteresis loops measured at 15 K for each nanowire by nanoSQUID magnetometry. The square shape of the loops indicates the quasi single-domain state of the nanowires, as expected due to their large aspect ratio, with *H* applied along the nanowire easy axis. In the classical Stoner-Wohlfarth model [53], the magnetization reversal of a single-domain particle takes place coherently, i.e., all magnetic moments reverse in unison. However, in this case, magnetic moments will tilt around the easy axis of the nanowire in a vortex-like configuration, which saves some magnetostatic energy at the cost of exchange energy, according to the curling model [54]. This accepted mechanism for magnetization reversal in nanowires will be used as a starting point to analyse the obtained experimental results.
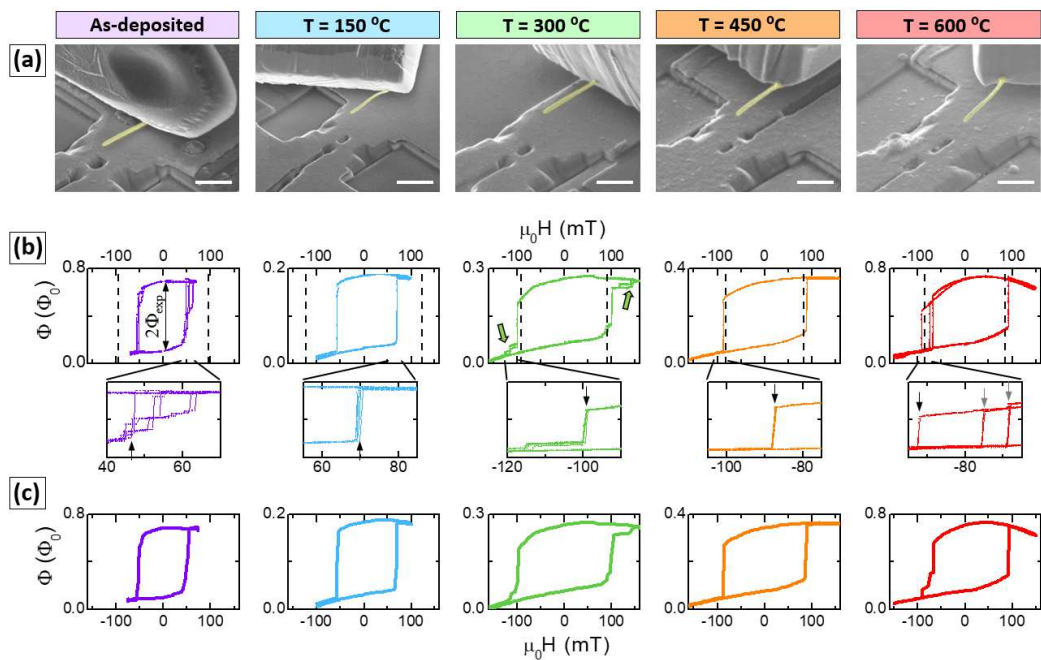
Figure 4.13. (a) NanoSQUIDs SEM images with Co nanowires in yellow. Scale bars are 1 μm. (b) Hysteresis loops at 15 K with dashed lines corresponding to the theoretical nucleation fields resulting from the curling model. An enlarged view of the magnetization reversal region is plotted. Black arrows indicate the nucleation fields, grey arrows highlight distinct switching events (600 ℃) and green thick arrows indicate minor steps after the main switching event (300 ℃). (c) Mean hysteresis loops obtained after averaging over 30-50 curves.

Under these circumstances and assuming a negligible contribution of the magnetocrystalline anisotropy due to the standard polycrystalline nature of the nanowires, the nucleation magnetic field is given by Equation 4.2:

$$H_n^{cur} = \kappa B \left(\frac{\lambda_{ex}}{R} \right)^2 \tag{4.2}$$

where $\kappa = 3.39$ for an infinite cylinder, R the radius of the nanowire and λ_{ex} the exchange length defined as:

$$\lambda_{ex} = \left[\frac{2A}{\mu_0 B^2} \right]^{1/2} \tag{4.3}$$

where A is the exchange stiffness, B is the saturation magnetic induction, and μ_0 the magnetic permeability constant.

If the Co purity, p, can be determined in the range ($0 < p < 1$), it can be estimated that:

$$B = pB_{bulk} = p \cdot 1.4 \times 10^6 \text{ A/m} \tag{4.4}$$

$$A = pA_{bulk} = p \cdot 2.5 \times 10^{-11} \text{ J/m} \tag{4.5}$$

for pure crystalline Co.

Finally, by combining Equations 4.2 and 4.3, H_n^{cur} can be calculated as:

$$H_n^{cur} = \frac{2\kappa}{\mu_0 R^2} \tag{4.6}$$

As a result, the insertion of the R values extracted from data on Table 4.2 yields the dashed lines plotted in Figure 4.13(b).

In the case of the as-deposited and 150 ºC-annealed nanowires, the curling model overestimates by far the experimentally measured nucleation fields. This happens because magnetization reversal in real nanowires is more likely to undergo a nucleation

167

and propagation process, which is energetically favourable and occurs at fields lower than H_n^{cur}. In this scenario, a small reversed region is first nucleated by curling together with the corresponding domain wall [55]. Subsequently, the domain wall moves rapidly ─in a timescale in the ns-ps range─ through the nanowire until the magnetization reversal is completed. In the case of 300 ºC-, 450 ºC- and 600 ºC-annealed nanowires, the estimated H_n^{cur} values are strikingly close to the experimental coercive fields.

Aside from the possible curling model interpretations, in the light of the experimental results obtained, it can be stated that the coercivity increases with the annealing temperature from the 40-50 mT range for the as-deposited and 150 ºC-annealed nanowires up to ~100 mT for the nanowires annealed at the highest temperatures. This is consistent with the remarkable increase of the grain size up 300 ºC.

As shown in the bottom panels of Figure 4.13(b), an in-depth inspection reveals that the switching takes place in several steps for the as-deposited nanowire, implying a nucleation-propagation process for the magnetization reversal. Starting from the quasi-single domain saturated state at large positive (negative) H, the first step observed in the hysteresis curve when decreasing (increasing) H stems from the nucleation of a domain wall. This defines the experimental nucleation fields, H_n^+ and H_n^-, for increasing and decreasing H, respectively. The presence of steps evidences that the as-deposited nanowire is not fully homogeneous, containing structural defects, impurities or a certain degree of surface roughness acting as pinning defects in the domain wall movement.

However, magnetization reversal of the rest of the nanowires occurs in extremely well-defined single switching events. This entails that these nanowires have fewer (or a different type of) defects compared to the as-deposited one. For instance, in the case of the 300 ºC-annealed nanowire, an additional minor step is always observed at large positive and negative H after the main switching event; and, in the case of the 600 ºC-annealed nanowire and only for decreasing H, three clearly separated switching events can be distinguished, apparently revealing different reversal paths undertaken

stochastically. Despite the keen interest on individual hysteresis loops, Figure 4.13(c) illustrates the hysteresis loops resulting after averaging over 30-50 curves in order to mimic the results obtained when measuring many identical nanowires.

Differences between the nanowires become even more evident when performing measurements at variable temperature, from 1.4 K to 80 K. Figure 4.14 displays the temperature dependence of $\langle H_n \rangle$, where $\langle H_n \rangle = (\langle H_n^+ \rangle - \langle H_n^- \rangle)/2$, with $\langle H_n^\pm \rangle$ being the mean value of $H_n^\pm$ after averaging over 30-50 curves. In the case of the as-deposited nanowire, $\langle H_n \rangle$ values decrease with increasing temperature. In the case of the 150 °C-annealed nanowire, $\langle H_n \rangle$ exhibits three regimes: it increases first with increasing temperature up to T < 30 K; and then decreases for T > 30 K showing a large step at T = 60 K. A similar step can also be observed for the 300 °C-annealed nanowire. Finally, in the case of 450 °C- and 600 °C-annealed nanowires, $\langle H_n \rangle$ decreases for increasing temperature, observing a clear flattening at temperatures below ~20 K. Since the $\langle H_n \rangle$ decrease with increasing the temperature is connected to a thermally activated process for magnetization reversal, other interpretation is required for the results obtained at intermediate annealing temperatures.
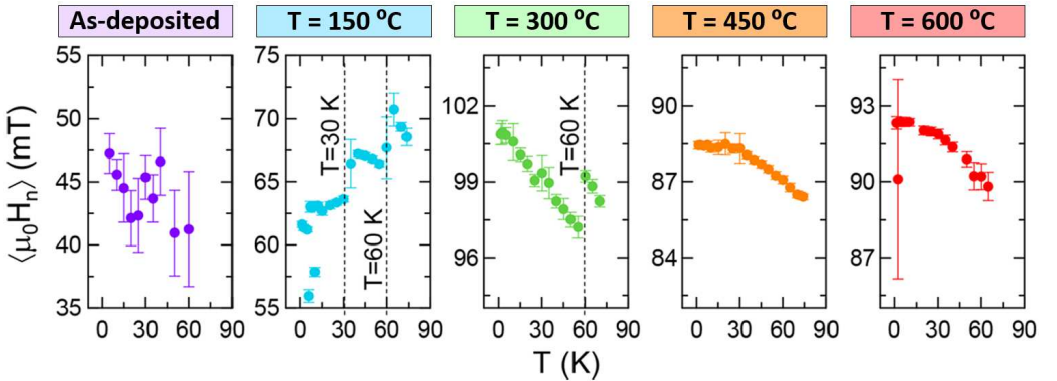
Figure 4.14. Temperature dependence of $\langle H_n \rangle$. Dashed lines indicate relevant temperature ranges discussed in the text. Noticing that the vertical axis covers 20 mT in the case of as-deposited and 150 °C-annealed nanowires, and just 10 mT in the rest.

In general, it could even be argued that the remarkable differences can be attributable to structural changes which lead to different nucleation mechanisms for the reversed domain [56]. In the case of the as-deposited nanowire, the large scattering suggests that multiple and almost equivalent paths to reverse the magnetization might be found. This can be supported by the presence of pinned Co atoms or antiferromagnetic species such as CoO or Co_3O_4. The interaction between Co nanocrystals and pinned Co atoms or antiferromagnetic regions leads to spin frustration, which typically exhibits a non-reproducible spin glass-like behaviour. In turn, the effective reversal path varies fairly from one hysteresis measurement to the other, leading to a quite broad $H_n^{\pm}$ distribution.

In the case of the nanowire annealed at 150 ℃, the slight shift of the hysteresis loops toward positive H values at 15 K according to Figure 4.13(b), and the $\langle H_n \rangle$ increase with increasing temperature at T < 30 K observed in Figure 4.14, unveils an exchange biased behaviour [57]. This can be explained by the presence of Co_3O_4, which is antiferromagnetic below ~35 K, exhibiting a Néel temperature, T_N, typically in the 30 < T_N < 40 K range [58], eventually producing the positive loops shift at $T < T_N$ [59]. The CoO has a T_N close to room temperature, so no influence should be assigned in this case. Finally, the effect disappears at $T > 35$ K, where $\langle H_n \rangle$ decreases with increasing temperature. In addition to that, a small negative H-shift is observed at $T > 60$ K for both 150 ℃- and 300 ℃-annealed nanowires, which indeed corresponds to the annealing temperatures when O-rich regions nucleate in the nanowire core, inducing the observed exchange bias phenomenon.

In order to understand the internal structure of the nanowires, some micromagnetic simulations were performed at 0 K to assess the experimental $\langle H_n \rangle$ values obtained at the lowest temperature, 1.4 K. Firstly, as shown in Figure 4.15, the numerically calculated $\langle H_n \rangle R^2$ values neglecting any contribution of the magnetocrystalline anisotropy, K_u, follow an approximately flat horizontal curve. The experimental points associated with the as-deposited and 150 ℃-annealed nanowires lie below the calculated data points,

whereas the values obtained for the 300 ℃-, 450 ℃-, and 600 ℃-annealed nanowires are much larger than the simulated ones.

On the one hand, the defects in the real as-deposited and 150 ℃-annealed nanowires act as localized nucleation points for reversed domains, decreasing the effective energy barriers for magnetization reversal and thus $\langle H_n \rangle$. In order to emulate these effects, as Figure 4.15 illustrates, numerical simulations were carried out assuming randomly distributed pinning centres with fixed magnetization and neglecting K_u contribution. As expected, the numerically calculated $\langle H_n \rangle R^2$ values are reduced in comparison with those obtained in the absence of pinning centres, where the switching mechanism is energetically less favourable. In this new situation, the experimental data are in good agreement with the simulation results. On the other hand, the high crystallinity obtained in the 300 ℃-, 450 ℃- and 600 ℃-annealed nanowires suggests that K_u must be considered in these cases. For this purpose, as shown in Figure 4.15, numerical simulations were implemented assuming a net uniaxial anisotropy constant, $K_u = \beta K_u^{bulk}$, where $K_u^{bulk} = 5.2 \times 10^5$ J/m³ is that of bulk crystalline Co. By setting $\beta = 0.09$, a good level of correspondence is revealed between the experimental data and the simulated ones. Consequently, this confirms that this behaviour is originated from the crystallization of larger and larger pure Co crystals as annealing temperature increases.
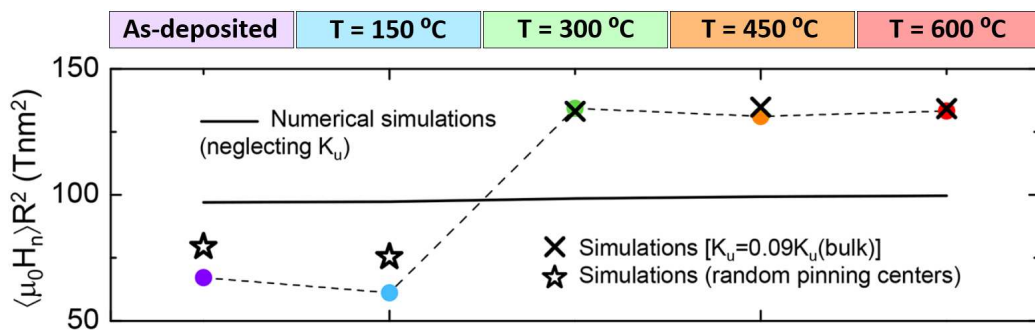
Figure 4.15. Experimentally determined (coloured dots) and numerically simulated (solid line) nucleation fields at 0 K multiplied by R^2 for the as-deposited nanowire and the ones annealed at 150 ℃, 300 ℃, 450 ℃ and 600 ℃.

Finally, as Table 4.2 displays, the total magnetic moment, μ_{NW}, and the Co purity of the nanowires can be estimated from Φ_{exp} (see Figure 4.13(b)). In order to attain those objectives, the values of Φ_{exp} are compared with the calculated flux, $\Phi_{theo} = |\phi_\mu|\mu_{NW}$, where ϕ_μ is the averaged coupling factor for each nanoSQUID across the nanowire volume. This factor is calculated knowing the position of the nanowire, its dimensions and those of the nanoSQUID. As a result, the μ_{NW} values and the Co purity, defined as $p = \mu_{NW}/V_{mag}\,B_{bulk}$, where V_{mag} is the magnetic volume of the nanowire, are obtained. Remarkably, p increases with increasing the annealing temperature in good agreement with the results extracted from STEM-EELS analysis shown in Figure 4.5. The results shown in the present subsection were obtained by Dr. María José Martínez-Pérez.

4.3 Annealing process on 3D iron nanowires

Most post-growth annealing processes are analysed in *ex situ* conditions, i.e., after the thermal treatment is actually performed; such is the case of the studies carried out on 3D FEBID Co in the previous section 4.2. *In situ* (i.e., in real time) evaluation of the chemical composition, local crystallinity and overall morphology is more challenging, and still rare, even though such studies would provide deeper insight in their fundamental nature. This improved understanding is the basis for further optimization of magnetic nanowires for application in sensing, memory and logic future applications. In this section, the live analysis of the annealing process of 3D FEBID Fe nanowires is tackled by *in situ* TEM [60]. In more detail, we focus on the formation and distribution of highly pure metallic Fe phases, including their crystallinity. These results are compared briefly with *ex situ* annealing performed on specimens that initially showed a higher Fe content.

4.3.1 Experimental details

The experimental setups and the most relevant parameters used in the fabrication, and the *in situ* and *ex situ* annealing and characterization of the 3D FEBID Fe nanowires will be described throughout this subsection.

4.3.1.1 *In situ* post-growth annealing

The sample for *in situ* TEM annealing (sample F) was fabricated in the commercial FEI Nova 200 Dual Beam system using $Fe_2(CO)_9$ precursor gas. The nanowires, with narrow diameter (~50 nm), high aspect ratio (>30) and an initial moderately-low Fe content (~40% at.), were grown directly on a heating chip (Wildfire S3 from DENSsolutions), shown in Figure 4.16(a), prepared to be loaded into a Wildfire TEM holder. As Figure 4.16(b) illustrates, the chip includes oval holes where the suspended nanostructures can be imaged through. The chip was tilted during the vertical growth of the nanowire, so that their projection falls into the hole once the chip recovers the horizontal position. All deposits were grown using an electron beam voltage of 30 kV, beam current of 21 pA, ΔP of 4×10^{-7} mbar and a single spot pattern scanned for 600 s.

The post-growth annealing in high vacuum was performed in the FEI Titan Cube G2 60-300 at the FELMI-ZFE (Graz). Figure 4.16(c) shows the temperature profile during the experiment, where individual annealing times are color-coded: 100 ℃ (12 min), 200 ℃ (12 min), 300 ℃ (12 min), 400 ℃ (56 min), 450 ℃ (36 min), 500 ℃ (44 min), 550 ℃ (14 min), 600 ℃ (47 min), 700 ℃ (26 min) and 800 ℃ (23 min).
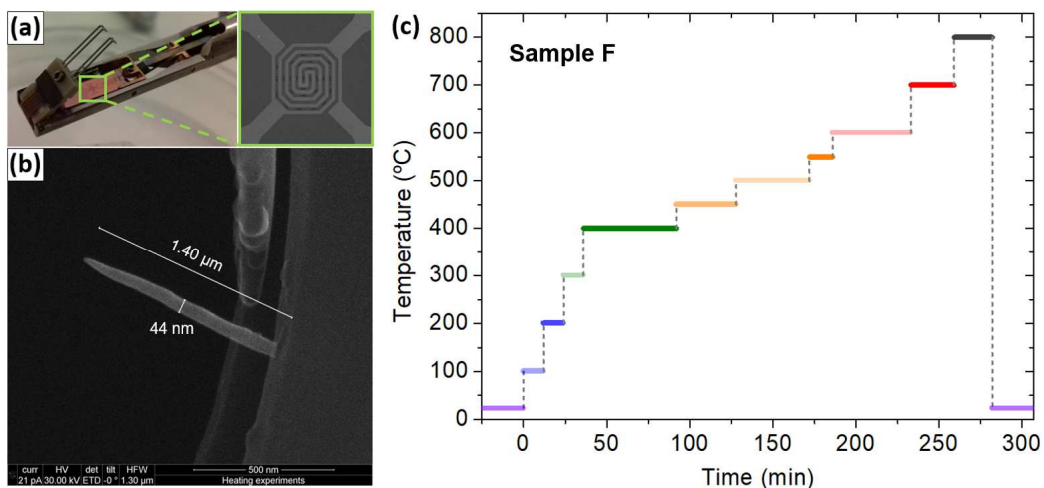
Figure 4.16. (a) Heating chip in the Wildfire TEM holder with (b) an Fe nanowire grown for *in situ* TEM annealing experiments. (c) Temperature profiles for the Fe nanowire studied.

STEM imaging in combination with EELS was performed at 300 kV using an X-FEG with monochromator, a C_S probe corrector (DCOR) which produces an electron probe below 0.7 Å in STEM, and a GIF Quantum. The STEM-EELS experiments were carried out with a 19.7 and 20.5 mrad convergence and collection semi-angles, respectively, energy dispersion of 0.5 eV/pixel with a resolution of 1.5 eV (FWHM of the zero-loss peak), GIF aperture of 5 mm, camera length of 58 mm, pixel time of 10 ms and a beam current of ~160 pA. ADF images were acquired with a Gatan ADF detector in the GIF with an inner detector angle of 38 mrad and an outer detector angle of 137 mrad. During the experiment, the microscope was operated by Dr. Georg Haberfehlner.

4.3.1.2 *Ex situ* post-growth annealing

The samples for *ex situ* annealing (samples G-K) were fabricated in the commercial Helios Nanolab 650 Dual Beam system using $Fe_2(CO)_9$ precursor gas. The nanowires, with narrow diameter (~50 nm), high aspect ratio (>50) and an initial moderately-high Fe content (~75% at.), were grown directly on five TEM Cu grids, shown in Figure 4.17(a,b). All deposits were grown using an electron beam voltage of 30 kV, beam current of 170 pA, ΔP of 4×10^{-7} mbar and a single spot pattern scanned for 105 s.

The post-growth annealing in high vacuum was performed in an SEM Quanta FEG 250 system at the INA (Zaragoza). The chamber was evacuated until the base pressure reduced below 3×10^{-6} mbar. According to Figure 4.17(c), a heating ramp of 50 ºC/min was set until reaching 150, 300, 450 and 600 ºC for samples H, I, J and K respectively, holding sample G at room temperature acting as the as-deposited reference. Then the sample was annealed for 25 minutes. The chamber pressure increased during the initial minutes before going down until the annealing treatment is finished (see Figure 4.18). After 25 minutes at the annealing temperature, the heater was switched off and the sample cooled down spontaneously to room temperature.
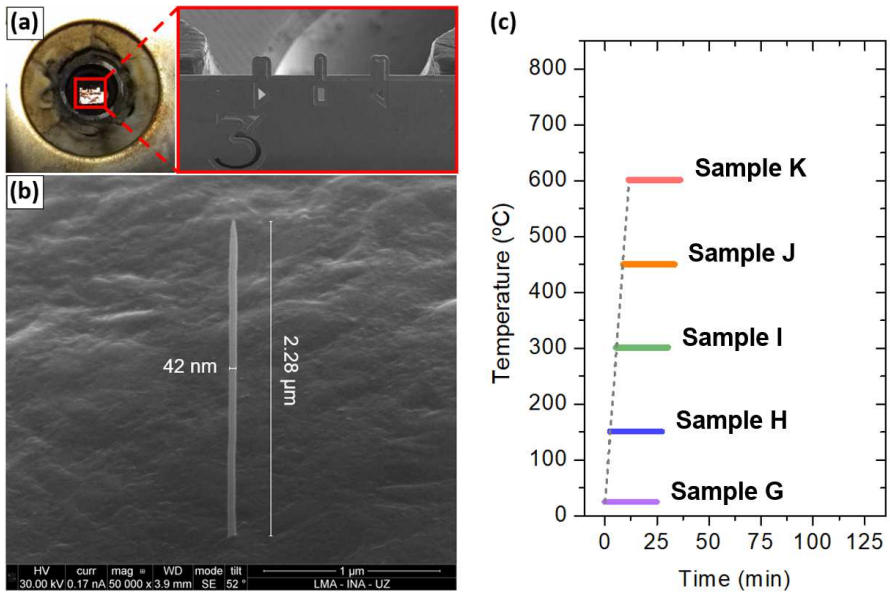
Figure 4.17. (a) TEM Cu grid mounted inside the heating stage with (b) an Fe nanowire grown for annealing experiments. (c) Annealing conditions for each of the Fe nanowires samples.
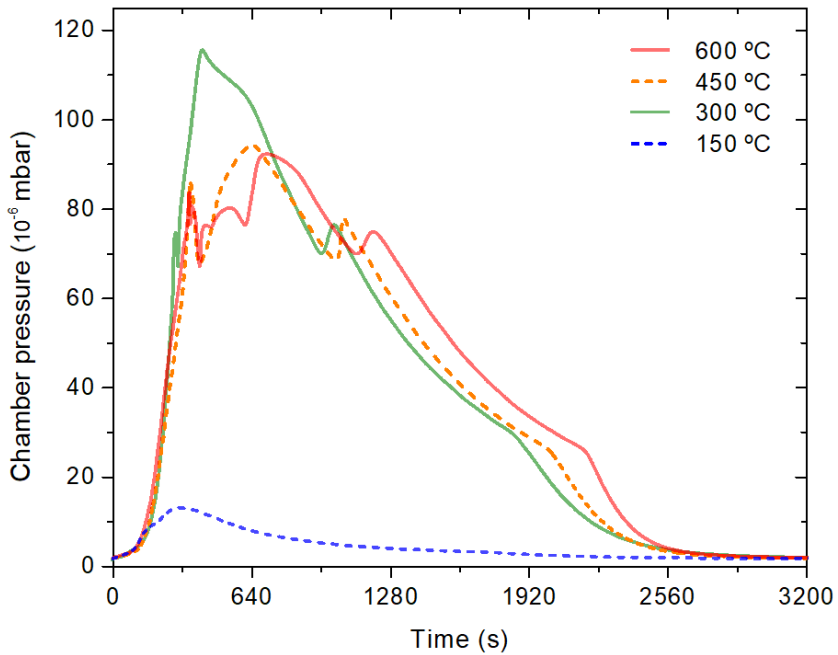
Figure 4.18. Chamber pressure evolution during the heating experiments inside the SEM.

HRTEM imaging was performed in a Titan Cube 60-300 system operated at 300 kV. The STEM-EELS experiments were carried out in a Titan Low Base 60-300 TEM operated at 300 kV, with a 25 mrad convergence semi-angle, an energy dispersion of 0.5 eV/pixel with a resolution of 1.5 eV, a GIF aperture of 2.5 mm, a camera length of 10 mm, a pixel time of 20 ms and an estimated beam current of 270 pA.

4.3.2 Morphology and composition of *in situ* annealed nanowires

ADF imaging and EELS compositional mapping in STEM mode have been used to trace *in situ* the morphological, structural and chemical changes of sample F with increasing annealing temperature. Figure 4.19 illustrates the general features observed upon heating by focusing the attention on a central region of the nanowire. The average diameter tends to decrease as the temperature raises. A 40% reduction is observed in certain regions, dropping down from ~50 nm at 24 °C to ~30 nm at 700 °C. This expected volume shrinkage is caused by the progressive reduction of C and O content, a mass loss due to the formation of volatile CO_x compounds as discussed in section 4.2 [61][62].
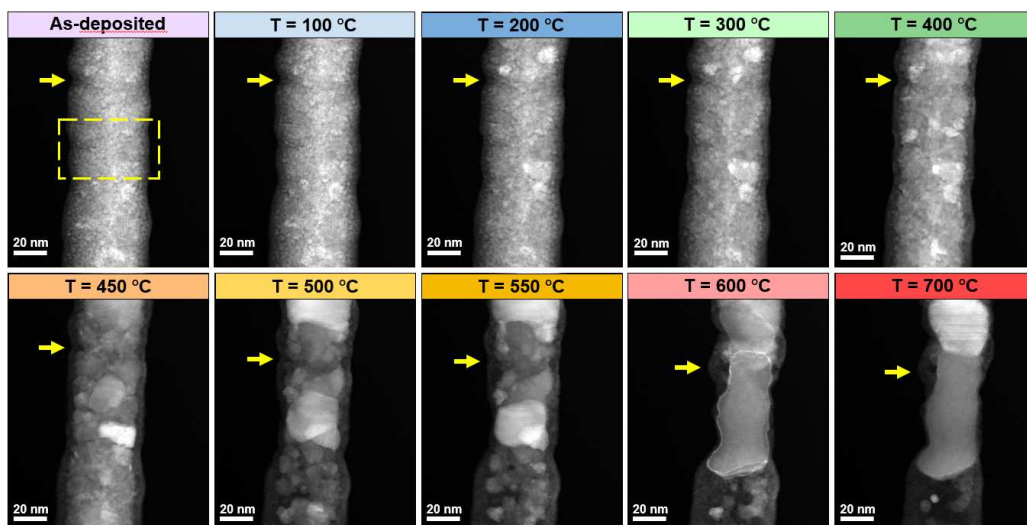
Figure 4.19. ADF-STEM images of the central section of an as-deposited Fe nanowire, sequentially annealed at 100 °C, 200 °C, 300 °C, 400 °C, 450 °C, 500 °C, 550 °C, 600 °C and 700 °C. Yellow arrows indicate the same point of the nanowire. The yellow dashed square indicates the area highlighted in Figure 4.20 for each temperature.

Regarding the microstructure, the as-deposited nanowire has a nanocrystalline structure which begins to change in the early stages of the experiment, as shown in greater detail in Figure 4.20. Firstly, from 24 ℃ to 300 ℃, only minor structural changes are observed. At 100 ℃ crystallites up to ~10 nm start to grow in specific regions, suggesting that a global homogeneous composition in the core is kept with the Fe starting to segregate from the rest of the components on specific areas. The low electron charge per unit of area (~0.42 nC/nm2) concentrated on the nanowire ensures that the driving force of the crystal emergence is provided by the heater temperature rise rather than by the irradiation-enhanced diffusion phenomenon [19][63]. When the sample is heated to 200 ℃, new isolated ordered arrangements of atoms oriented in different directions turn up at several areas, whilst maintaining the general structural shape of the nanowire. At 300 ℃ the number of high-purity Fe nanocrystals increases inside the core, giving rise to an overlap amongst them. In addition, general compositional changes happen, noticing a richer Fe central trace found along the long axis of the nanostructure (see Figure 4.21). Raising the temperature up to 400 ℃ favours the clustering of sizeable crystals, giving rise to an inhomogeneous distribution of Fe, which produces areas with remarkable higher metallic content. Indeed, a particularly active redistribution of the Fe, O and C can be noticed as a function of time, which is illustrated in Figure 4.21.
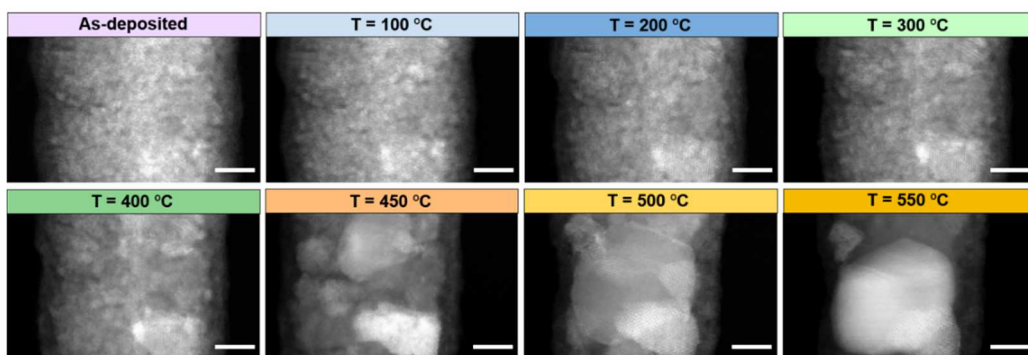
Figure 4.20. High-resolution ADF-STEM images of the area indicated with yellow dashed square in Figure 4.19 of an as-deposited Fe nanowire, sequentially annealed at 100 ℃, 200 ℃, 300 ℃, 400 ℃, 450 ℃, 500 ℃ and 550 ℃. Scale bars are 10 nm in all images.
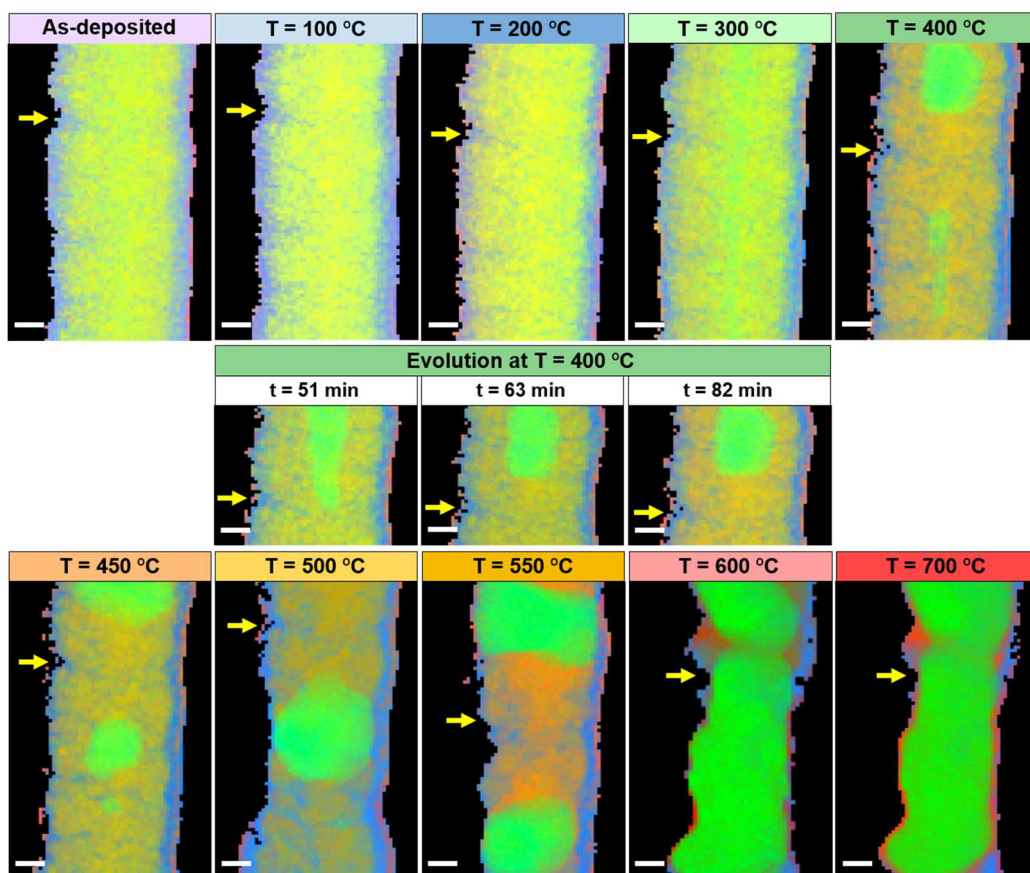
Figure 4.21. STEM-EELS chemical maps of an as-deposited Fe nanowire, sequentially annealed at 100 ºC, 200 ºC, 300 ºC, 400 ºC, 450 ºC, 500 ºC, 550 ºC, 600 ºC and 700 ºC, showing the spatial distribution of Fe, O, and C in green, red and blue, respectively. Yellow arrows indicate the same point of the nanowire. Scale bars are 10 nm.

At 450 ºC a sizeable growth of some Fe grains takes place, with crystals spreading all over the core thickness in certain regions. Figure 4.20 shows a clear change in the microstructure, virtually removing most of the remained amorphous material in Fe-rich parts. It is also noteworthy that, while Fe-rich areas appear inside the nanowire, other regions become C-rich and O-rich. Moreover, given that the initial Fe content was low (~40% at.), the complete purification throughout the whole nanostructure is not expected

to occur whilst keeping the total volume constant. At 500 ºC the diameter is not uniform anymore along the length of the nanostructure, considerably reducing its value below 45 nm in some sections. As illustrated in Figure 4.21, large Fe grains grow at the expense of surrounding smaller grains, to reach lateral sizes close to the nanowire width. At 550 ºC, the recrystallization of the Fe-rich regions is completed and have produced the expected large crystals of α-Fe with body-centered-cubic (*bcc*) structure. This correlates very well with the previous observation of the transformation of amorphous Fe:C:O as-grown nanocomposites into α-Fe single-crystals around this temperature [43].

As the component distribution does not change anymore as a function of time at 550 ºC, further temperature increase is required to stimulate further compositional dynamics. At 600 ºC, Fe crystal migration is powerfully promoted in some areas, with the grain front advancing with a mean speed of ~26 pm/s (see video in [46]). For the sake of comparison, Fe-C alloy nanoparticles were found to move inside a C nanopillar at 8 nm/s under comparable temperatures [64]. In the case of 3D Fe-FEBID nanowires, the diffusion suggests being subjected to the local morphology, the available metallic sources around the active grain front, and the possible crystal accommodation within the nanowire. The nanowire central section represented in Figure 4.21 shows a remarkable increase of the Fe content. However, despite not displaying the whole length of the nanostructure to have a better assessment of the fine compositional details, it is important to highlight that this local purification leads to the accumulation of C and O in other regions, as illustrated in Figures 4.19.

At 700 ºC, the thinnest regions have shrunk down to approximately 30 nm in diameter. At this point, it is likely that the growth of large α-Fe crystals is halted as the supply of small Fe particles nearby is depleted. The adopted configuration resembles the one obtained for the previous temperature stage and it can be assumed that the segregation between the components is finished. At 800 ºC, the nanowire suddenly bends at the upper part, suffering an important deformation and therefore losing the original pillar shape.

Hence, the large amount of C initially contained inside the structure not only hampers obtaining a homogeneously purified structure, but also leads to the collapse of the nanowire structure at high annealing temperatures.

To obtain quantitative information about the Fe, O and C relative compositions, STEM-EELS profiles were performed at each annealing temperature longitudinally (along the nanowires' axis, see Figure 4.22) and transversally (along its diameter, Figure 4.23). For the first one, the longitudinal profiles were acquired approximately in the same areas depicted in Figures 4.19 and 4.21, and obtained by integrating over the central ~12 nm. For the second one, the transversal profiles do not provide fair information about the overall composition, but allow studying the shell composition and obtaining numerical values of the relative contents of Fe, O and C in specific sections. Since there is an active displacement of the components depending on the temperature, it has been selected the regions which illustrate the general behaviour of the composition at the shell and the highest Fe percentage found throughout the nanowire for each annealing temperature.

Figure 4.22 indicates that the initial ~40% at. Fe, ~40% at. O and ~20% at. C is homogeneously distributed in the core from 24 °C to 300 °C. However, this considers the contribution coming from the shell because the whole thickness of the nanowire is integrated in the STEM-EELS data collection. As shown in Figure 4.23(a-d), in this temperature range, a ~7 nm shell composed by ~10% at. Fe, ~30% at. O and ~60% at. C represents nearly the 30% of the total width. Thus, it can be assumed that the real metallic content inside the core is much higher than the one displayed for the total volume.

Another relevant fact is the absence of the standard ~5 nm surface oxidation layer which typically covers magnetic FEBID nanostructures with higher metallic content [57]. Similarly to the *ex situ* annealed Co-FEBID nanowires, the formation of a C shell during the annealing of the original Fe nanowire prevents the natural oxidation of the metal species once the nanostructure is removed from the nanofabrication vacuum chamber. As a result, the O signal decreases from the core to the shell.
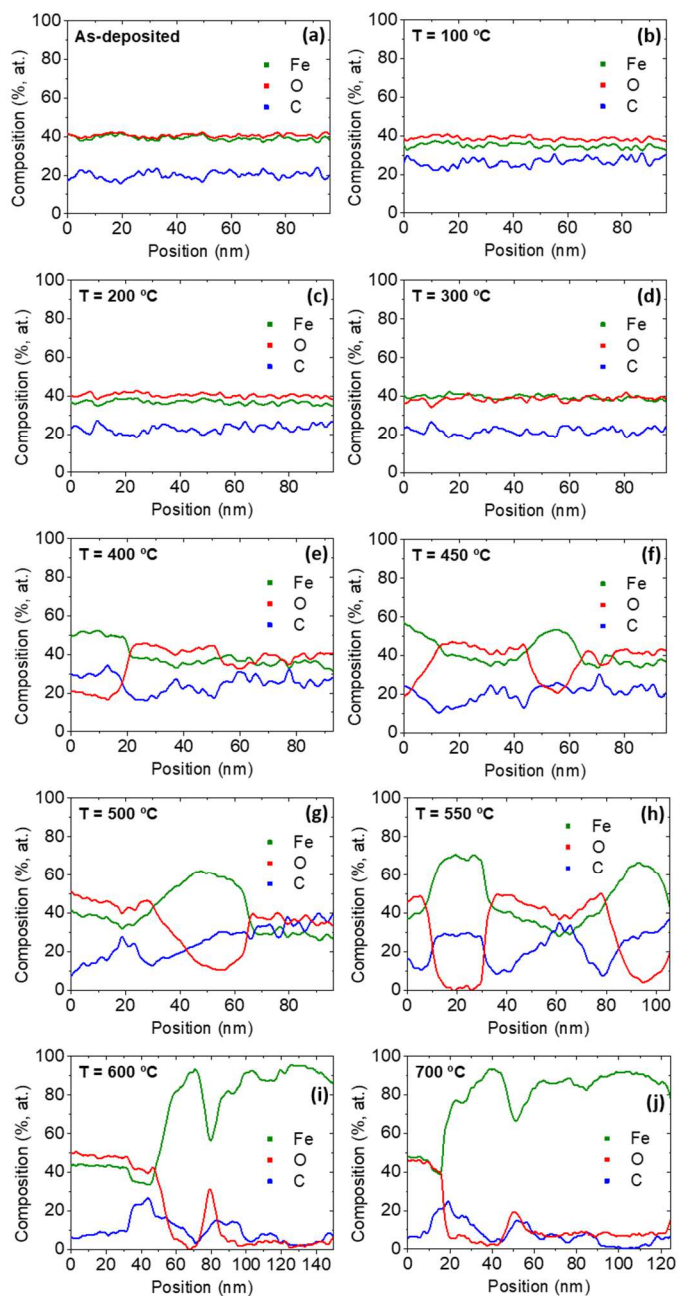
Figure 4.22. STEM-EELS longitudinal profiles of the relative composition of (a) an as-deposited Fe nanowire and the same nanostructure sequentially annealed at (b) 100 °C, (c) 200 °C, (d) 300 °C, (e) 400 °C, (f) 450 °C, (g) 500 °C, (h) 550 °C, (i) 600 °C and (j) 700 °C. The Fe, O and C relative compositions are represented in green, red and blue, respectively.
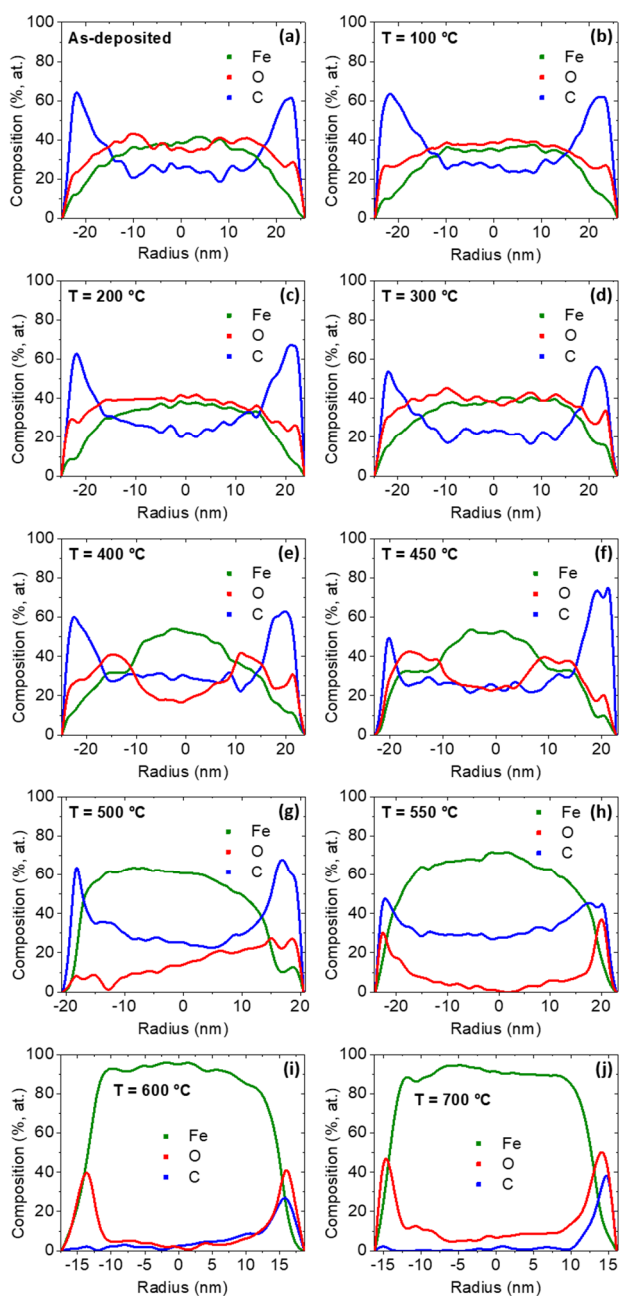
Figure 4.23. STEM-EELS transversal profiles of the relative composition of the highest-metallic areas for (a) an as-deposited Fe nanowire and the same nanostructure annealed at (b) 100 ℃, (c) 200 ℃, (d) 300 ℃, (e) 400 ℃, (f) 450 ℃, (g) 500 ℃, (h) 550 ℃, (i) 600 ℃ and (j) 700 ℃.

At 400 ºC and 450 ºC, a strong difference in the Fe contents along the length has been detected. According to Figure 4.22(e-f), the regions where a cluster of Fe appears improve the metallic composition up to 50-60% at., as well as the O signal decreases down to ~20% at. These data correlate appropriately with Figure 4.23(e-f). At 500 ºC, the Fe relative composition exceeds 60% at. in the areas with the highest metallic content, where the O is reduced below 20% at. At 550 ºC, the Fe content in those regions increase to around 70% at., whereas the C content at the shell starts to decrease and percentages below 50% at. are obtained for the first time. Simultaneously, the O signal decreases drastically in the central regions. At 600 ºC, looking at the transversal profile analysis shown in Figure 4.23(i), the C signal varies the tendency and decreases dramatically down to zero in some sections. Consequently, the Fe crystal has expanded all over the nanowire thickness, and the recrystallization and the purification are accomplished locally, approaching ~95% at. Fe. Besides, the O layer presented at the shell generally coincides with the Fe signal, demonstrating that the metallic material is eventually oxidized. Adding this to the overall reduction of the diameter, the ferromagnetic diameter shrinks to ~25 nm. Finally, at 700 ºC no significant changes can be noted with respect to the previous temperature.

In order to evaluate the degree of Fe purification with temperature, Figure 4.24(a) displays the radial dependence of the average Fe composition found in the highest-metallic area of the nanowire at each annealing temperature. The highest purification sections, which may vary their location from one temperature to another, show a clear increase of the Fe content as a function of the temperature, as illustrated in Figure 4.24(b). Simultaneously, the diameter evolution in these regions follows the opposite trend, attaining a remarkable small value (33 nm). Thus, sections of virtually pure Fe can be obtained by means of this annealing treatment from a low initial Fe content, but the full nanowire purification is not achieved.
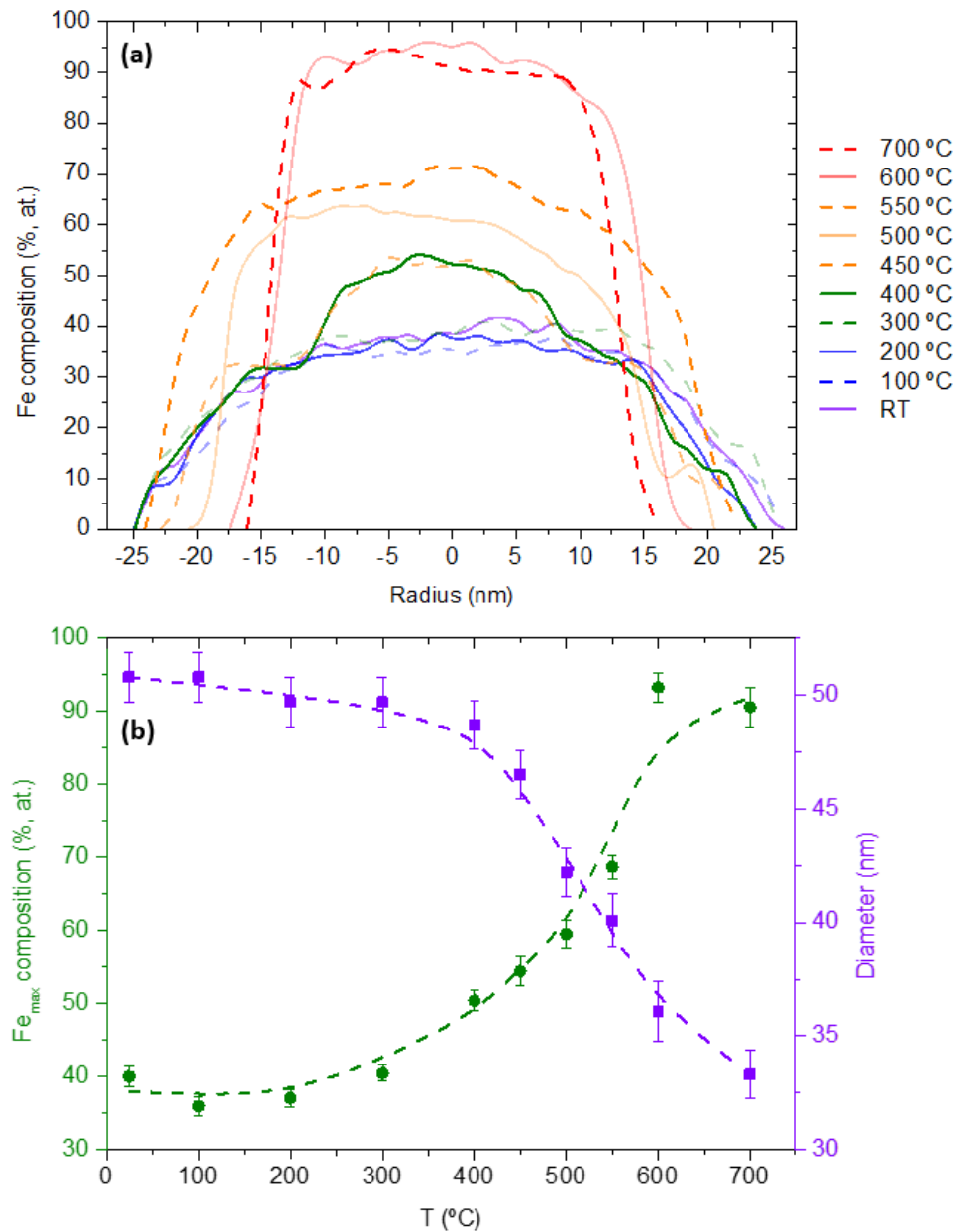
Figure 4.24. STEM-EELS transversal profiles of the average Fe relative composition in the areas with the highest metallic content of the Fe nanowire found at each temperature. (b) Maximum Fe relative composition (circle symbol) and average total diameter (square symbol) in the selected nanowire area shown in Figure 4.20 as a function of the annealing temperature.

In summary, Figure 4.25 shows a schematic illustration of the dimensional and organizational modifications of the components depending on the annealing temperature as obtained in the experiments. In brief, high-vacuum *in situ* annealing of 3D Fe-FEBID nanowires produces isolated purified (~95 at. % Fe) crystalline regions, reducing the diameter down to ~30 nm in specific areas, but retaining the general shape of the nanostructure.
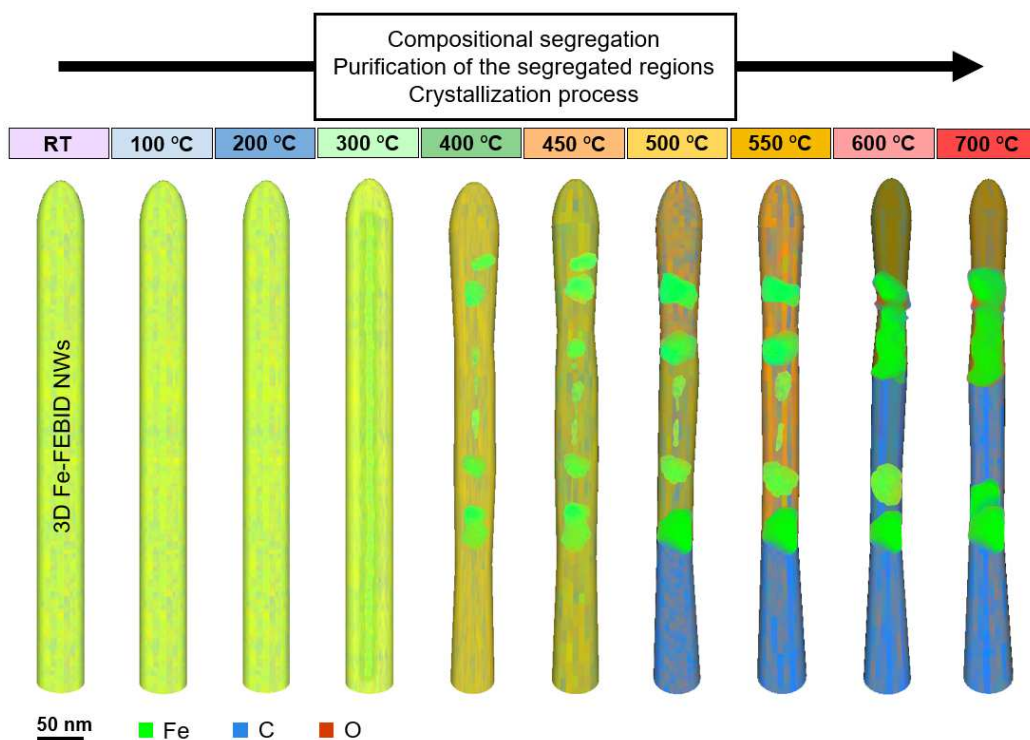
Figure 4.25. Sketch of the morphology, dimensions and composition distribution of an Fe nanowire as a function of the annealing temperature, as observed in the *in situ* TEM experiments. Fe, O and C are depicted in green, red and blue, respectively.

4.3.3 Morphology and composition of *ex situ* annealed nanowires

Morphological and chemical characterizations of samples G-K as a function of the annealing temperature have been carried out. Figure 4.26 illustrates the expected recrystallization of the as-grown nanocrystalline microstructure into Fe crystals in some

areas of the nanowires annealed at 300 ºC and above. However, as shown in Figure 4.27, despite the higher Fe initial content and the different temperature ranges, the chemical changes resemble the variations experimented by the *in situ* annealed Fe nanowire. The homogeneous composition of the core of the as-deposited nanowires starts to be segregated increasing the temperature and gives rise to clear independent regions in the 300 ºC-, 450 ºC- and 600 ºC-annealed nanowires.

For a more detailed study of the chemical composition, quantitative information about the Fe, O and C relative compositions was obtained performing longitudinal and transversal STEM-EELS profiles at each annealing temperature, represented in Figures 4.28 and 4.29, respectively. The first one reveals that in the as-deposited nanowires, the Fe content decreases as the tip is approached due to the higher contribution of the external oxidation layer, from the ~75% at. detected in the central area down to ~30% at. at the tip. At 150 ºC, the O distribution is approximately the same, whereas the Fe and C signals start to fluctuate, indicating a redistribution of these components. At 300 ºC and above, although the nanostructure is still Fe-rich, sharp separations can be identified between areas with Fe contents from ~55% at. to ~80% at.
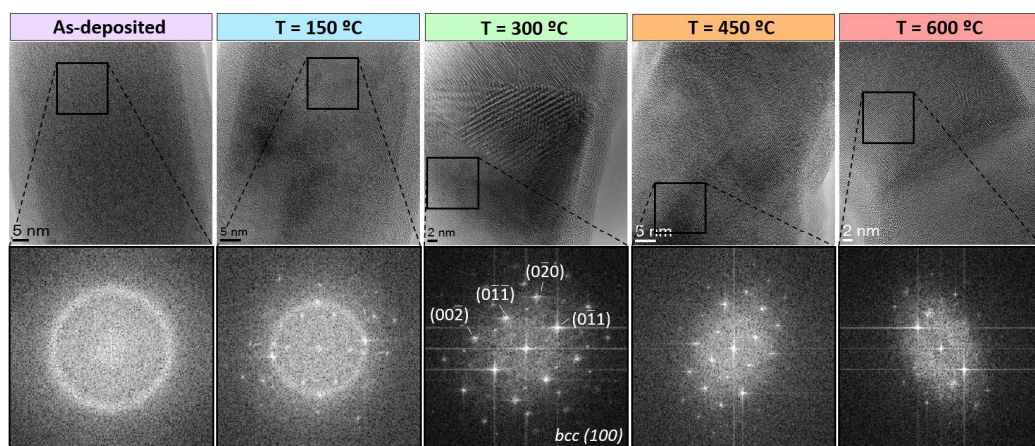
Figure 4.26. HRTEM images and their corresponding FFT of an as-deposited Fe nanowire and the ones annealed at 150, 300, 450 and 600 ºC.

186
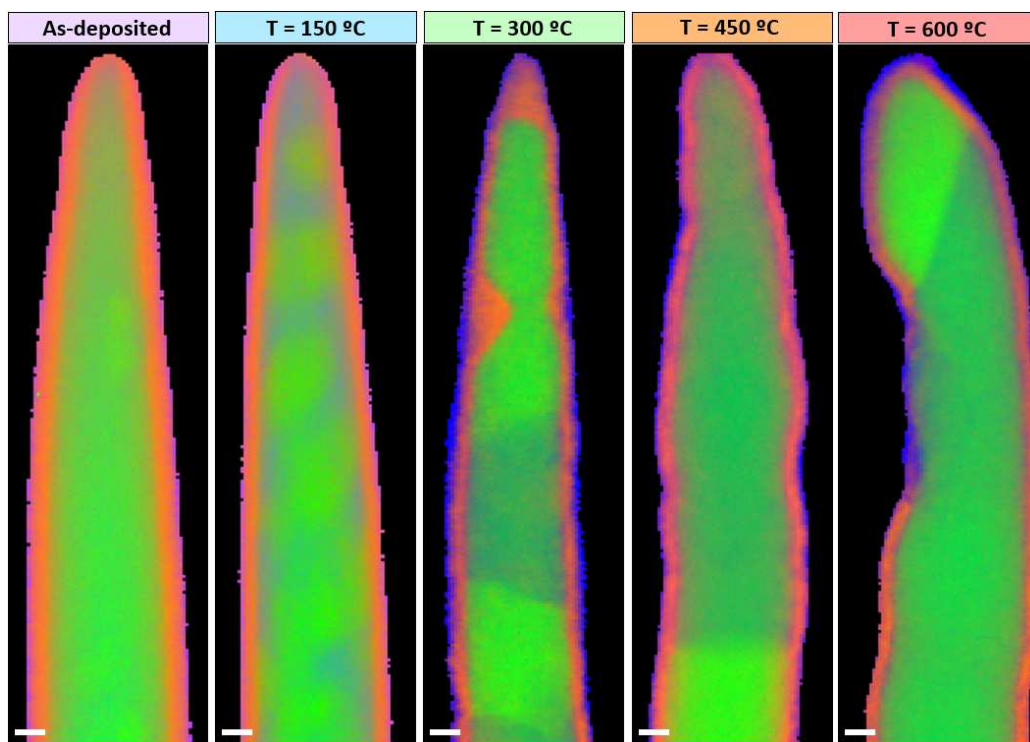
Figure 4.27. STEM-EELS chemical maps of an as-deposited Fe-FEBID nanowire with initial Fe content of 75% at. and the ones annealed at 150, 300, 450 and 600 ºC, showing the spatial distribution of Fe, O and C in green, red and blue, respectively. Scale bars are 10 nm.

To the contrary, the O signal distribution along the length of the nanowires remains nearly constant in all samples, evidencing the external oxidation layer. On the other hand, regarding the transversal profiles performed in the highest-metallic areas, the Fe composition is always in the 75-80% at. range. Thus, no remarkable improvement of the metallic material is achieved by this *ex situ* annealing treatment. In addition, the general architecture is preserved with increasing the annealing temperature, finding a constant diameter of ~50 nm. In fact, longer annealing times were tested (100 min at 150, 300, 450 and 600 ºC), obtaining deformations of the original nanowires shape.
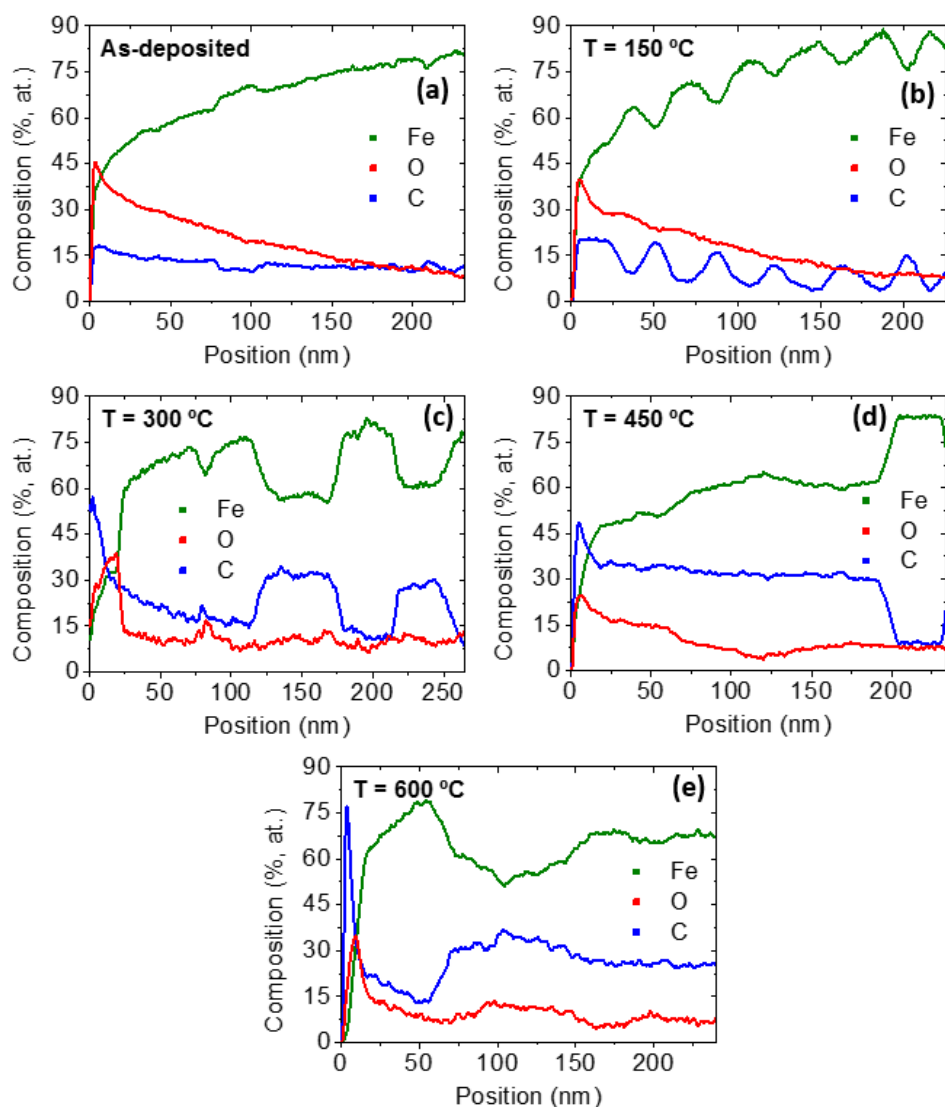
Figure 4.28. STEM-EELS longitudinal profiles of the relative composition of (a) an as-deposited Fe nanowire and the ones annealed at (b) 150, (c) 300, (d) 450 and (e) 600 °C. The Fe (in green), O (in red) and C (in blue) compositions are represented starting from the tip of each nanostructure.
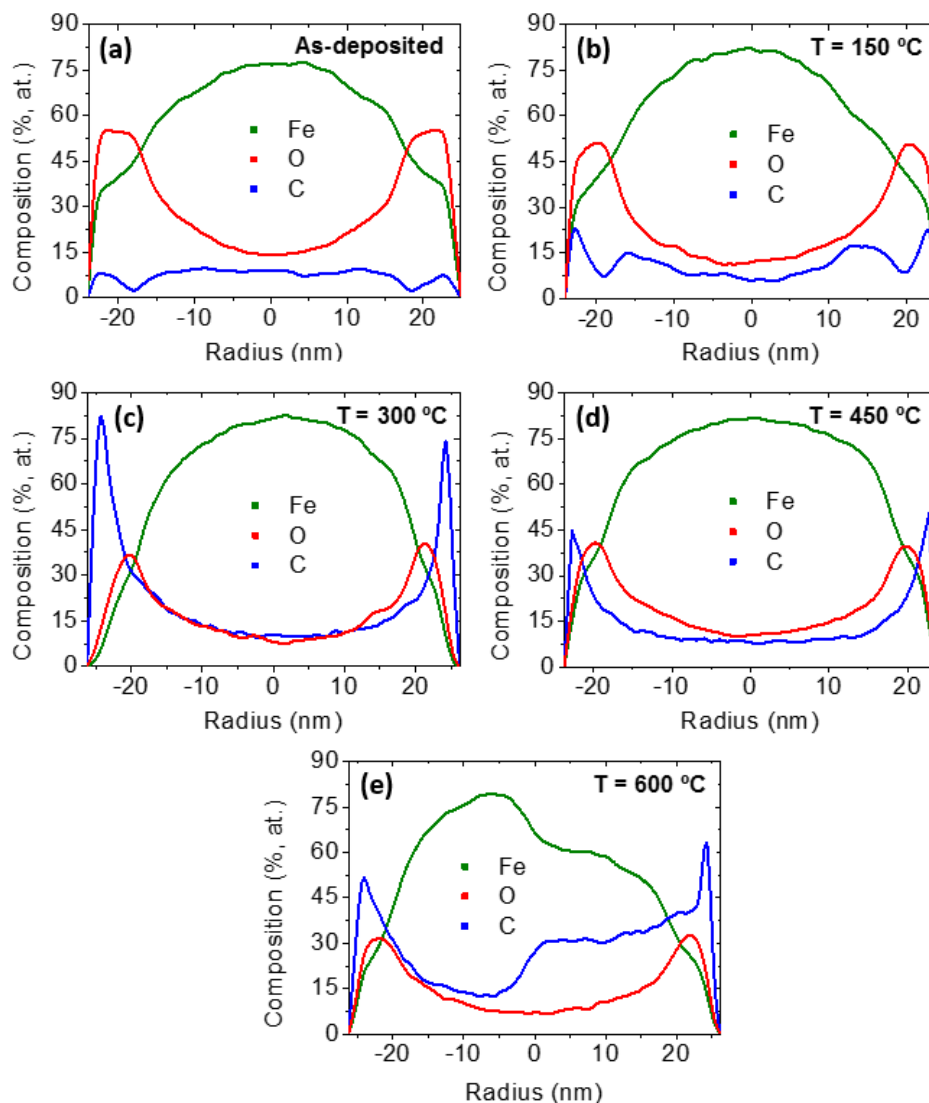
Figure 4.29. STEM-EELS transversal profiles of the relative composition of the highest-metallic areas for (a) an as-deposited Fe nanowire and the ones annealed at (b) 150, (c) 300, (d) 450 and (e) 600 °C. The Fe, O and C compositions are represented in green, red and blue respectively.

4.4 Conclusions

The purification of 3D Co- and Fe-FEBID nanowires has been addressed by *ex situ* and *in situ* annealing strategies, with the aim of studying the impact of the annealing in the microstructural, chemical and magnetic properties.

Firstly, in the case of the Co, purified and crystalline 3D nanowires of ~90 nm in diameter have been fabricated by *ex situ* post-growth high-vacuum annealing at 600 ºC. While increasing the metallic content of the nanowires up to 95% at., the thermal annealing process induces the recrystallization of the pseudo-amorphous as-deposited structure into bulk-like, *hcp* and *fcc* crystals with lateral sizes comparable to the nanowire diameter. Simultaneously, the net magnetization increases 80% with respect to as-grown values, up to 1.61 T, near bulk Co. In addition, a detailed study of their magnetic properties has been performed by nanoSQUID magnetometry. Experimental results point clearly to an enhanced Co content and an increased degree of crystallinity in the nanowires annealed at the highest temperatures. This gives rise to a high contribution of the effective magnetocrystalline anisotropy, revealed by the exceedingly large values for the switching magnetic fields.

Secondly, in the case of the Fe, *in situ* and *ex situ* post-growth annealing under high-vacuum conditions of ultrathin 3D Fe nanowires (~50 nm) has been performed. In the *in situ* and *ex situ* annealing of nanowires with low (~40% at.) and high (~75% at.) initial Fe content, respectively, the obtained nanoscale phase segregation will entail non-homogeneous physical properties in the nanowire. It differs from the result of a similar annealing processes conducted in 3D Co nanowires, which shows a homogeneous purification and recrystallization of the nanowires at 600 ºC. This indicates that probably a different mechanism is governing the purification process in both nanomaterials and/or, in this case, the amount of contaminants is higher than the one which can be removed by the thermal annealing, with profound implications on their functionality. The different morphologies obtained upon thermal annealing will have a significant impact on the

performance of nanodevices based on this material. In the case of applications requiring magnetic continuity, such as in magnetic domain-wall conduits [65], annealed Fe-FEBID nanowires would not be appropriate. However, in the case of magnetic sensing devices such as Hall sensors, the use of a nanomaterial with purified magnetic areas surrounded by non-magnetic areas could be beneficial [66]. Such annealed Fe-FEBID nanowires could be also of interest in magnetic tips used for MFM for two reasons: the enhancement of the spatial resolution due to the reduction of the nanowire diameter and the diminishment of their magnetic invasiveness, currently needed in the measurement of magnetic nanostructures such as skyrmions [67]. Another potential application of annealed Fe-FEBID nanostructures could reach the field of catalysis, given that the small metallic nanoparticles formed could act as catalytical centers for the growth of C nanotubes, as reported with Co-FEBID nanodots [68].

Especially, by the *in situ* approach, the morphological, compositional and crystallinity changes as a function of the temperature and time have been monitored in real time, shedding light on the nanoscale processes involved during the annealing. This work underlines the importance of *in situ* studies with nanoscale resolution for the optimization of nanomaterials and the understanding of their functionality. On an overall basis, this strategy provides the opportunity of choosing different annealing times at each temperature depending on the changes observed or required. Furthermore, the nanostructures can be tailored until the desired properties are achieved.

References

[1]   M. Huth, F. Porrati, C. Schwalb, M. Winhold, R. Sachser, M. Dukic, J. Adams and G. Fantner, "Focused electron beam induced deposition: A perspective", *Beilstein J. Nanotechnol.* **3**, 597 (2012).

[2]   A. Botman, J. J. L. Mulders and C. W. Hagen, "Creating pure nanostructures from electron-beam-induced deposition using purification techniques: a technology perspective", *Nanotechnology* **20**, 372001 (2009).

[3]   R. Winkler, B. B. Lewis, J. D. Fowlkes, P. D. Rack and H. Plank, "High-Fidelity

3D-Nanoprinting via Focused Electron Beams: Growth Fundamentals", *ACS Appl. Nano Mater.* **1**, 1014 (2018).

[4]   I. Utke, J. Michler, P. Gasser, C. Santschi, D. Laub, M. Cantoni, P. A. Buffat, C. Jiao and P. Hoffmann, "Cross Section Investigations of Compositions and Sub-Structures of Tips Obtained by Focused Electron Beam Induced Deposition", *Adv. Eng. Mater.* **7**, 323 (2005).

[5]   T. Lukasczyk, M. Schirmer, H. Steinrück and H. Marbach, "Electron-Beam-Induced Deposition in Ultrahigh Vacuum: Lithographic Fabrication of Clean Iron Nanostructures", *Small* **4**, 841 (2008).

[6]   L. Bernau, M. Gabureac, R. Erni and I. Utke, "Tunable Nanosynthesis of Composite Materials by Electron-Impact Reaction", *Angew. Chem. Int. Ed.* **49**, 8880 (2010).

[7]   R. Winkler, B. Geier and H. Plank, "Spatial chemistry evolution during focused electron beam-induced deposition: origins and workarounds", *Appl. Phys. A* **117**, 1675 (2014).

[8]   L. Serrano-Ramón, R. Córdoba, L. A. Rodríguez, C. Magén, E. Snoeck, C. Gatel, I. Serrano, M. R. Ibarra and J. M. De Teresa, "Ultrasmall functional ferromagnetic nanostructures grown by focused electron-beam-induced deposition", *ACS Nano* **5**, 7781 (2011).

[9]   T. Bret, I. Utke, A. Bachmann and P. Hoffmann, "In situ control of the focused-electron-beam-induced deposition process", *Appl. Phys. Lett.* **83**, 4005 (2003).

[10]   M. V. Puydinger Dos Santos, M. F. Velo, R. D. Domingos, Y. Zhang, X. Maeder, C. Guerra-Nuñez, J. P. Best, F. Béron, K. R. Pirota, S. Moshkalev, J. A. Diniz and I. Utke, "Annealing-Based Electrical Tuning of Cobalt-Carbon Deposits Grown by Focused-Electron-Beam-Induced Deposition", *ACS Appl. Mater. Interfaces* **8**, 32496 (2016).

[11]   M. Tanaka, M. Shimojo, M. Takeguchi, K. Mitsuishi and K. Furuya, "Formation of iron nano-dot arrays by electron beam-induced deposition using an ultrahigh vacuum transmission electron microscope", *J. Cryst. Growth* **275**, e2361 (2005).

[12]   K. Mitsuishi, M. Shimojo, M. Tanaka, M. Takeguchi and K. Furuya, "Resolution in new nanofabrication technique combining electron-beam-induced deposition and low-energy ion milling", *Jpn. J. Appl. Phys.* **44**, 5627 (2005).

[13]   M. Shimojo, M. Takeguchi, M. Tanaka, K. Mitsuishi and K. Furuya, "Electron beam-induced deposition using iron carbonyl and the effects of heat treatment on nanostructure", *Appl. Phys. A* **79**, 1869 (2004).

[14]   M. Takeguchi, M. Shimojo and K. Furuya, "Nanostructure Fabrication by Electron-Beam-Induced Deposition with Metal Carbonyl Precursor and Water

Vapor", *Jpn. J. Appl. Phys.* **46**, 6183 (2007).

[15]   H. Plank, J. H. Noh, J. D. Fowlkes, K. Lester, B. B. Lewis and P. D. Rack, "Electron-beam-assisted oxygen purification at low temperatures for electron-beam-induced Pt deposits: towards pure and high-fidelity nanostructures", *ACS Appl. Mater. Interfaces* **6**, 1018 (2014).

[16]   D. Belić, M. M. Shawrav, M. Gavagnin, M. Stöger-Pollach, H. D. Wanzenboeck and E. Bertagnolli, "Direct-Write Deposition and Focused-Electron-Beam-Induced Purification of Gold Nanostructures", *ACS Appl. Mater. Interfaces* **7**, 2467 (2015).

[17]   R. Córdoba, J. Sesé, J. M. De Teresa and M. R. Ibarra, "High-purity cobalt nanostructures grown by focused-electron-beam-induced deposition at low current", *Microelectron. Eng.* **87**, 1550 (2010).

[18]   J. J. L. Mulders, L. M. Belova and A. Riazanova, "Electron beam induced deposition at elevated temperatures: compositional changes and purity improvement", *Nanotechnology* **22**, 055302 (2011).

[19]   S. Frabboni, G. C. Gazzadi, L. Felisari and A. Spessot, "Fabrication by electron beam induced deposition and transmission electron microscopic characterization of sub-10-nm freestanding Pt nanowires", *Appl. Phys. Lett.* **88**, 213116 (2006).

[20]   H. Plank, G. Kothleitner, F. Hofer, S. G. Michelitsch, C. Gspan, A. Hohenau and J. Krenn, "Optimization of postgrowth electron-beam curing for focused electron-beam-induced Pt deposits", *J. Vac. Sci. Technol. B* **29**, 051801 (2011).

[21]   N. A. Roberts, J. D. Fowlkes, G. A. Magel and P. D. Rack, "Enhanced material purity and resolution via synchronized laser assisted electron beam induced deposition of platinum", *Nanoscale* **5**, 408 (2013).

[22]   N. A. Roberts, C. M. Gonzalez, J. D. Fowlkes and P. D. Rack, "Enhanced by-product desorption via laser assisted electron beam induced deposition of $W(CO)_6$ with improved conductivity and resolution", *Nanotechnology* **24**, 415301 (2013).

[23]   G. C. Gazzadi and S. Frabboni, "Structural transitions in electron beam deposited Co-carbonyl suspended nanowires at high electrical current densities", *Beilstein J. Nanotechnol.* **6**, 1298 (2015).

[24]   M. R. Henry, S. Kim and A. G. Fedorov, "High Purity Tungsten Nanostructures via Focused Electron Beam Induced Deposition with Carrier Gas Assisted Supersonic Jet Delivery of Organometallic Precursors", *J. Phys. Chem. C* **120**, 10584 (2016).

[25]   K. L. Klein, S. J. Randolph, J. D. Fowlkes, L. F. Allard, H. M. Meyer III, M. L. Simpson and P. D. Rack, "Single-crystal nanowires grown via electron-beam-induced deposition", *Nanotechnology* **19**, 345705 (2008).

[26]   S. Mehendale, J. J. L. Mulders and P. H. F. Trompenaars, "A new sequential EBID process for the creation of pure Pt structures from MeCpPtMe₃", *Nanotechnology* **24**, 145303 (2013).

[27]   O. V. Dobrovolskiy, M. Kompaniiets, R. Sachser, F. Porrati, C. Gspan, H. Plank and M. Huth, "Tunable magnetism on the lateral mesoscale by post-processing of Co/Pt heterostructures", *Beilstein J. Nanotechnol.* **6**, 1082 (2015).

[28]   E. Villamor, F. Casanova, P. H. F. Trompenaars and J. J. L. Mulders, "Embedded purification for electron beam induced Pt deposition using MeCpPtMe₃", *Nanotechnology* **26**, 095303 (2015).

[29]   K. Höflich, R. B. Yang, A. Berger, G. Leuchs and S. Christiansen, "The Direct Writing of Plasmonic Gold Nanostructures by Electron-Beam-Induced Deposition", *Adv. Mater.* **23**, 2657 (2011).

[30]   R. Winkler, F.-P. Schmidt, U. Haselmann, J. D. Fowlkes, B. B. Lewis, G. Kothleitner, P. D. Rack and H. Plank, "Direct-Write 3D Nanoprinting of Plasmonic Structures", *ACS Appl. Mater. Interfaces* **9**, 8233 (2017).

[31]   J. Pablo-Navarro, C. Magén and J. M. De Teresa, "Purified and Crystalline Three-Dimensional Electron-Beam-Induced Deposits: The Successful Case of Cobalt for High-Performance Magnetic Nanowires", *ACS Appl. Nano Mater.* **1**, 38 (2018).

[32]   M. V. Puydinger Dos Santos, A. Szkudlarek, A. Rydosz, C. Guerra-Nuñez, F. Béron, K. R. Pirota, S. Moshkalev, J. A. Diniz and I. Utke, "Comparative study of post-growth annealing of Cu(hfac)₂, Co₂(CO)₈ and Me₂Au(acac) metal precursors deposited by FEBID", *Beilstein J. Nanotechnol.* **9**, 91 (2018).

[33]   Y. M. Lau, P. C. Chee, J. T. L. Thong and V. Ng, "Properties and applications of cobalt-based material produced by electron-beam-induced deposition", *J. Vac. Sci. Technol. A* **20**, 1295 (2002).

[34]   R. R. Kunz and T. M. Mayer, "Catalytic growth rate enhancement of electron beam deposited iron films", *Appl. Phys. Lett.* **50**, 962 (1987).

[35]   A. Perentes, G. Sinicco, G. Boero, B. Dwir and P. Hoffmann, "Focused electron beam induced deposition of nickel", *J. Vac. Sci. Technol. B* **25**, 2228 (2007).

[36]   A. Fernández-Pacheco, J. M. De Teresa, R. Córdoba and M. R. Ibarra, "Magnetotransport properties of high-quality cobalt nanowires grown by focused-electron-beam-induced deposition", *J. Phys. D: Appl. Phys.* **42**, 055005 (2009).

[37]   R. Córdoba, N. Sharma, S. Kölling, P. M. Koenraad and B. Koopmans, "High-purity 3D nano-objects grown by focused-electron-beam induced deposition", *Nanotechnology* **27**, 355301 (2016).

[38]   J. M. De Teresa, A. Fernández-Pacheco, R. Córdoba, L. Serrano-Ramón, S.

Sangiao and M. R. Ibarra, "Review of magnetic nanostructures grown by focused electron beam induced deposition (FEBID)", *J. Phys. D: Appl. Phys.* **49**, 243003 (2016).

[39]   J. Pablo-Navarro, D. Sanz-Hernández, C. Magén, A. Fernández-Pacheco and J. M. De Teresa, "Tuning shape, composition and magnetization of 3D cobalt nanowires grown by focused electron beam induced deposition (FEBID)", *J. Phys. D: Appl. Phys.* **50**, 18LT01 (2017).

[40]   L. A. Rodríguez, L. Deen, R. Córdoba, C. Magén, E. Snoeck, B. Koopmans and J. M. De Teresa, "Influence of the shape and surface oxidation in the magnetization reversal of thin iron nanowires grown by focused electron beam induced deposition", *Beilstein J. Nanotechnol.* **6**, 1319 (2015).

[41]   S. Sangiao, C. Magén, D. Mofakhami, G. De Loubens and J. M. De Teresa, "Magnetic properties of optimized cobalt nanospheres grown by focused electron beam induced deposition (FEBID) on cantilever tips", *Beilstein J. Nanotechnol.* **8**, 2106 (2017).

[42]   E. Nikulina, O. Idigoras, J. M. Porro, P. Vavassori, A. Chuvilin and A. Berger, "Origin and control of magnetic exchange coupling in between focused electron beam deposited cobalt nanostructures", *Appl. Phys. Lett.* **103**, 123112 (2013).

[43]   M. Takeguchi, M. Shimojo and K. Furuya, "Fabrication of magnetic nanostructures using electron beam induced chemical vapour deposition", *Nanotechnology* **16**, 1321 (2005).

[44]   L. M. Belova, E. D. Dahlberg, A. Riazanova, J. J. L. Mulders, C. Christophersen and J. Eckert, "Rapid electron beam assisted patterning of pure cobalt at elevated temperatures via seeded growth", *Nanotechnology* **22**, 145305 (2011).

[45]   E. Begun, O. V. Dobrovolskiy, M. Kompaniiets, R. Sachser, C. Gspan, H. Plank, and M. Huth, "Post-growth purification of Co nanostructures prepared by focused electron beam induced deposition", *Nanotechnology* **26**, 075301 (2015).

[46]   J. Pablo-Navarro, R. Winkler, G. Haberfehlner, C. Magén, H. Plank, and J. M. De Teresa, "In situ real-time annealing of ultrathin vertical Fe nanowires grown by focused electron beam induced deposition", *Acta Mater.* **174**, 379 (2019).

[47]   M. J. Martínez-Pérez, J. Pablo-Navarro, B. Müller, R. Kleiner, C. Magén, D. Koelle, J. M. De Teresa and J. Sesé, "NanoSQUID Magnetometry on Individual As-grown and Annealed Co Nanowires at Variable Temperature", *Nano Lett.* **18**, 7674 (2018).

[48]   J. Pablo-Navarro, C. Magén and J. M. De Teresa, "Three-dimensional core-shell ferromagnetic nanowires grown by focused electron beam induced deposition", *Nanotechnology* **27**, 285302 (2016).

[49]   N. N. Greenwood and A. Earnshaw, "Chemistry of the Elements", *Butterworth-Heinemann* (1997).

[50]   W. Sucksmith and J. E. Thompson, "The Magnetic Anisotropy of Cobalt", *Proc. R. Soc. Lond. A* **225**, 362 (1954).

[51]   A. Fernández-Pacheco, L. Serrano-Ramón, J. M. Michalik, M. R. Ibarra, J. M. De Teresa, L. O'Brien, D. Petit, J. Lee and R. P. Cowburn, "Three dimensional magnetic nanowires grown by focused electron-beam induced deposition", *Sci. Rep.* **3**, 1492 (2013).

[52]   J. M. De Teresa, R. Córdoba, A. Fernández-Pacheco, O. Montero, P. Strichovanec and M. R. Ibarra, "Origin of the Difference in the Resistivity of As-Grown Focused-Ion- and Focused-Electron-Beam-Induced Pt Nanodeposits", *J. Nanomater.* **2009**, 936863 (2009).

[53]   E. C. Stoner and E. P. Wohlfarth, "A mechanism of magnetic hysteresis in heterogeneous alloys", *Trans. R. Soc. A* **240**, 599 (1948).

[54]   A. Hubert and R. Schäfer, "Magnetic Domains. The Analysis of Magnetic Nanostrucutres", *Springer* (1998).

[55]   P. M. Paulus, F. Luis, M. Kröll, G. Schmid and L. J. De Jongh, "Low-temperature study of the magnetization reversal and magnetic anisotropy of Fe, Ni, and Co nanowires", *J. Magn. Magn. Mater.* **224**, 180 (2001).

[56]   J. Stankiewicz, F. Luis, A. Camón, M. Kröll, J. Bartolomé and W. Blau, "Magnetization switching of Fe nanowires at very low temperatures", *J. Magn. Magn. Mater.* **272-276**, 1637 (2004).

[57]   J. Nogués, J. Sort, V. Langlais, V. Skumryev, S. Suriñach, J. S. Muñoz and M. D. Baró, "Exchange bias in nanostructures", *Phys. Rep.* **422**, 65 (2005).

[58]   L. He, C. Chen, N. Wang, W. Zhou and L. Guo, "Finite size effect on Néel temperature with Co_3O_4 nanoparticles", *J. Appl. Phys.* **102**, 103911 (2007).

[59]   D. Tripathy, A. O. Adeyeye, K. Chakrabarti and N. Singh, "Tuning the exchange bias in large area Co/CoO nanowire arrays", *J. Appl. Phys.* **107**, 09D705 (2010).

[60]   R. Straubinger, A. Beyer, T. Ochs, W. Stolz and K. Volz, "In Situ Thermal Annealing Transmission Electron Microscopy (TEM) Investigation of III/V Semiconductor Heterostructures Using a Setup for Safe Usage of Toxic and Pyrophoric Gases", *Microsc. Microanal.* **23**, 751 (2017).

[61]   B. Geier, C. Gspan, R. Winkler, R. Schmied, J. D. Fowlkes, H. Fitzek, S. Rauch, J. Rattenberger, P. D. Rack and H. Plank, "Rapid and Highly Compact Purification for Focused Electron Beam Induced Deposits: A Low Temperature Approach Using Electron Stimulated H_2O Reactions", *J. Phys. Chem. C* **118**, 14009 (2014).

[62]   R. Córdoba, R. Fernández-Pacheco, A. Fernández-Pacheco, A. Gloter, C. Magén, O. Stéphan, M. R. Ibarra and J. M. De Teresa, "Nanoscale chemical and structural study of Co-based FEBID structures by STEM-EELS and HRTEM", *Nanoscale Res. Lett.* **6**, 592 (2011).

[63]   B. Liu, T. Tahmasebi, K. Ong, H. Teo, Z. Mo, J. Lam, P. K. Tan, Y. Zhao, Z. Dong, D. Houssameddine, J. Wang, J. Xue and Z. Mai, "Electron radiation-induced material diffusion and nanocrystallization in nanostructured amorphous CoFeB thin film", *Acta Mater.* **161**, 221 (2018).

[64]   T. Ichihashi, J. Fujita, M. Ishida and Y. Ochiai, "In situ Observation of Carbon-Nanopillar Tubulization Caused by Liquidlike Iron Particles", *Phys. Rev, Lett.* **92**, 215702 (2004).

[65]   S. S. P. Parkin, M. Hayashi and L. Thomas, "Magnetic domain-wall racetrack memory", *Science* **320**, 190 (2008).

[66]   M. Gabureac, L. Bernau, I. Utke and G. Boero, "Granular Co-C nano-Hall sensors by focused-beam-induced deposition", *Nanotechnology* **21**, 115503 (2010).

[67]   E. Berganza, M. Jaafar, M. Goiriena-Goikoetxea, J. Pablo-Navarro, A. García-Arribas, K. Gusliyenko, C. Magén, J. M. De Teresa, O. Chubykalo-Fesenko and A. Asenjo, "Observation of hedgehog skyrmions in sub-100 nm soft magnetic nanodots", arXiv:1803.08768v1 [cond-mat.mes-hall] (2018).

[68]   M. H. Ervin and B. M. Nichols, "Electron beam induced deposition of cobalt for use as single- and multiwalled carbon nanotube growth catalyst", *J. Vac. Sci. Technol. B* **27**, 2982 (2009).

Chapter 5: Core-shell architectures

The combination of materials with different behavior to confer additional functional properties to nanostructures is an appealing challenge which has been barely explored by Focused Electron Beam Induced Deposition. The topics addressed throughout this chapter begin to deal with this matter by establishing two main targets: the avoidance of post-growth degradation of the ferromagnetic properties in 3D nanowires and the development of 3D ferromagnetic nanotubes. These particular objectives are tackled based on a core-shell architecture strategy, a first milestone of this nanolithography technique in the long-term objective of developing 3D multifunctional nanoscale heterostructures.

5.1 Three-dimensional ferromagnetic nanowires with a protective Pt-C shell

A novel nanofabrication approach has been developed to build 3D core-shell nanowires by FEBID. This consists of the nanofabrication of a vertical nanowire and a cylindrical coating, acting as core and shell, respectively. By selecting the appropriate materials, diverse functionalities can be obtained. In this section, in order to avoid the degradation of the ferromagnetic core due to oxidation, the attention will be focused on covering this inner part with a non-ferromagnetic shell. After describing the growth technical details, microstructural, chemical and magnetic characterization of the final nanostructures will be comprehensively analysed.

5.1.1 Introduction

FEBID has been remarkably successful in growing nanometer-scale objects and devices with complex 2D or 3D geometries [1][2][3][4][5][6][7][8][9][10]. Additionally, this nanolithography technique is nurtured from a growing catalogue of precursors that enable the deposition of an ever-growing number of materials and compounds, opening new possibilities given the great variety of available physical properties such as metallicity and magnetoresistance [11], insulating behavior [12], superconductivity [13], ferromagnetism and superparamagnetism [14][15], plasmonic behavior [16], etc. However, one of the challenges for FEBID technology is the fabrication of heterogeneous structures combining the properties of more than one material [17]. So far, limited attempts have been reported in this direction, such as the use of double-precursor deposition producing phase segregation [18], the growth of 2D multilayers with alternate deposition [19], the coverage of an array of nanopillars with a 2D layer [20] and the creation of magnetic-superconducting nanocontacts [21].

Interestingly, functional nanoscale devices are most often heterostructures composed of layers of different materials with the aim of adding multiple or new functionalities, improving the performance and/or protecting from oxidation or corrosion.

On the one hand, heterostructured materials combining different properties (ferromagnetic/non-magnetic, metallic/insulator, ferromagnetic/superconducting, ferromagnetic/plasmonic, etc.) present either multifunctionality or additional functional interface properties. Some examples of the latter are the emergence of a 2D high-mobility electron gas forming at the interface of two insulating films [22], or the appearance of ferromagnetism or superconductivity at the interface of two materials which do not exhibit such properties [23]. On the other hand, surface exposure to air can substantively degrade the properties of nano-objects. In the case of materials with a high surface-to-volume ratio, such as nanoparticles or nanowires, the surface exposed to ambient atmosphere represents a significant volume fraction of the whole object, showing different structural, magnetic and transport properties with respect to the inner volume. This is particularly true for ferromagnetic nanostructures such as Co and Fe objects, which exhibit natural surface oxidation layers of a few nanometers degrading or completely modifying their magnetic behavior [24][25].

Therefore, the fabrication of heterogeneous materials presents great potential across many research fields. Specifically, nanowires with core-shell design are functional nano-objects with applications in several areas operating as semiconductor-based elements for electronic devices [26] and photovoltaic applications [27], constituents of long-life lithium battery electrodes [28] and supercapacitors [29], efficient light absorbers in solar cells [30], etc. Nevertheless, in the field of magnetic nanowires, which are expected to underpin applications in magnetic memories, sensors, multiferroic devices, magnetoplasmonics, magnetic hyperthermia, etc., scarce successful investigations have been reported [31][32]. Based on this motivation and considering that the fabrication of these singular architectures remains nearly unexplored using FEBID, a first approach based on the sequential deposition of two different materials to produce 3D ferromagnetic core-shell nanowires by FEBID will be disclosed in this section.

In order to demonstrate the feasibility and versatility of FEBID to grow 3D core-shell nanowires, ferromagnetic cores made of either Co or Fe have been coated by Pt-C layers aiming to suppress the surface oxidation and maximize the magnetic response of the ferromagnetic core. The effectiveness of the Pt-C shell is demonstrated by TEM and EH characterization, which reveal the confinement of the oxidation in the Pt-C layer, protecting completely the magnetic core, and the subsequent increase of the average magnetic induction of the coated Co and Fe cores with respect to the uncoated ones. The successful application of FEBID to fabricate 3D core-shell magnetic nanowires not only opens a new path to engineer and modulate the physical properties of magnetic deposits, but also provides a general approach which can be applied using any pair of FEBID materials, significantly enlarging its interest.

5.1.2 Experimental details

The nanostructures were fabricated in the commercial Helios Nanolab 600 and 650 Dual Beam systems using $Co_2(CO)_8$, $Fe_2(CO)_9$ and $CH_3CpPt(CH_3)_3$ precursor gases. The substrates were TEM Cu grids to facilitate the subsequent characterization. The Co deposits were grown with an electron beam voltage of 5 kV, an electron beam current of 100 pA and a chamber growth pressure of 6×10^{-6} mbar (base pressure of $\sim 1 \times 10^{-6}$ mbar). In the Fe case, an electron beam voltage of 5 kV, an electron beam current of 86 pA and a chamber growth pressure of 3.3×10^{-6} mbar were set. Finally, Pt-C deposits were performed by selecting an electron beam voltage of 5 kV, an electron beam current of 100 pA and a chamber growth pressure of 1×10^{-5} mbar.

HRTEM imaging was carried out in the FEI Titan Cube 60-300 operated at 300 kV. STEM imaging and EELS chemical analyses were performed in the Titan Low Base 60-300 also operated at 300 kV. Both imaging and spectroscopic experiments were executed with a convergence semi-angle of 25 mrad. STEM-EELS spectrum imaging experiments

were carried out with an energy dispersion of 0.8 eV, an energy resolution of ~2 eV, a pixel time of 35 ms and an estimated beam current of ~250 pA.

EDS experiments were performed in the Helios 600 and 650 Dual Beam systems, using an electron beam voltage of 5 kV and an electron beam current of 800 pA.

The magnetization along the long axis of the nanowires was analyzed by Off-Axis EH in the FEI Titan Cube operated at 300 kV. The excitation of the biprism was varied between 180 V and 220 V, adjusting it according to the nanowires diameter. The fringe contrast of the holograms ranged from 20% to 25% and the acquisition time of the holograms was 5 s. The magnetic induction was calculated using the Equation A.3.

5.1.3 Core-shell fabrication approach

The starting point for the synthesis of the nanostructures is the growth of 3D Co and Fe nanowires by FEBID following the procedure described in previous chapters. The purpose of the research is the conservation of the as-deposited material features avoiding their natural deterioration. In accordance with this understanding, the appropriate growth parameter values have been chosen to obtain Co nanowires with a metallic content of ~80% at. and diameters of ~60-70 nm. In the case of the Fe, nanowires with a metallic purity of ~80% at. and diameters below 60 nm have been fabricated.

Since the original metallic content of Co and Fe nanowires is of the utmost importance and a straightforward comparison between them will be established, it is worthwhile to introduce a simple method in order to evaluate the degree of purity in these nanostructures, apart from the general chemical analyses. Overall inspection by SEM can serve as hints for suggesting the metallic content. For instance, the Co nanowires exhibit a smooth surface when having low metallic purity (approximately <70% at.), but sizable roughness can be noticed for higher metallic contents, with diameter variations on the order of 5 nm. Similarly, a comparable behavior is evinced in Fe nanowires for the highest metallic contents. Roughness is caused by the preferential growth of grains at the surface

of the nanowires. This effect is especially remarkable in the thinnest Fe nanowires, where the diameter variation can occasionally reach 30% of the average diameter. Thus, roughness can be used as an indirect qualitative indication of the metallic purity.

The basic steps of the procedure followed to fabricate the 3D core-shell nanowires are illustrated in Figure 5.1. Firstly, the Co or Fe core of the nanostructures was grown on the TEM Cu grid substrate mounted on the stage tilted 0 degrees. Once the fabrication of the ferromagnetic core is accomplished, the Pt-C coating was carried out. The stage is tilted 52 degrees respect to the horizontal axis, so the nanostructures are seen using the scanning electron beam with the same perspective as that in Figure 5.2.
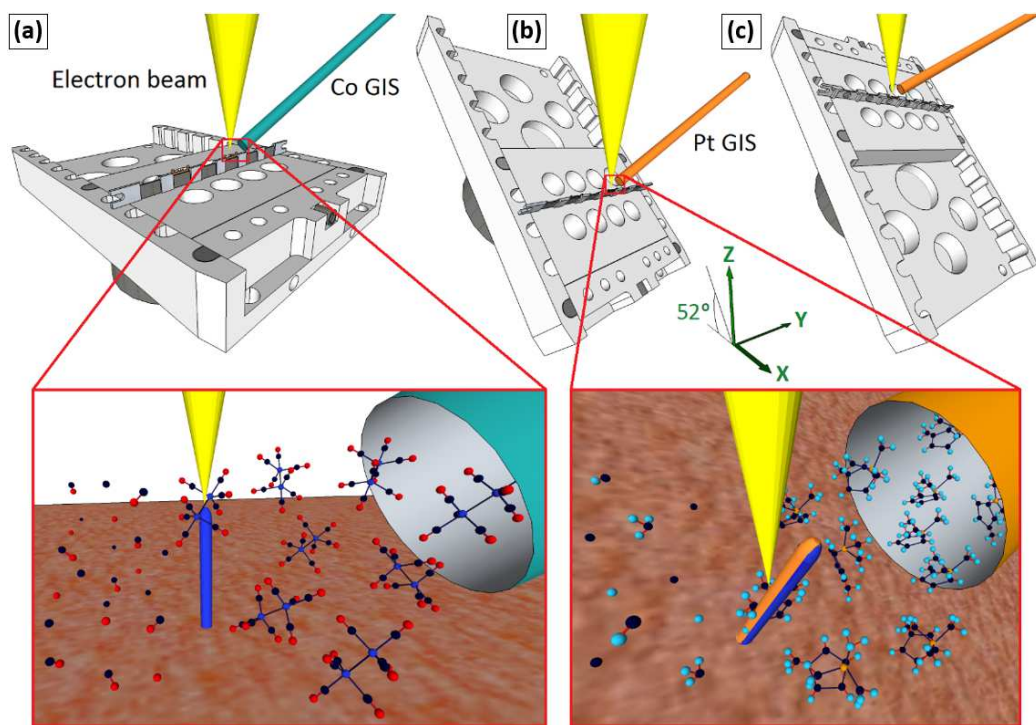
Figure 5.1. Diagram of the FEBID processes used to fabricate a core-shell Co@Pt nanowire. (a) Sketch of the ferromagnetic core growth, (b) the first Pt-C deposit on one nanowire side and (c) the stage position to perform an equivalent second Pt-C deposit on the opposite side.

Then a rectangular pattern with the same length and width as the core is set for Pt-C deposition. Finally, the stage is rotated 180 degrees and a new Pt-C deposit is performed in the same way, completing the whole coating. Even though only two opposite sides of the nanowire are patterned with Pt-C, the SE produced during the deposition induce a complete coverage of the non-oxidized ferromagnetic core. For experimental comparison, in all cases a second nanowire was grown immediately after, under the same experimental conditions, and left uncoated as a reference. Figure 5.2 shows SEM images of Co and Fe nanowires before and after the Pt-C coating.
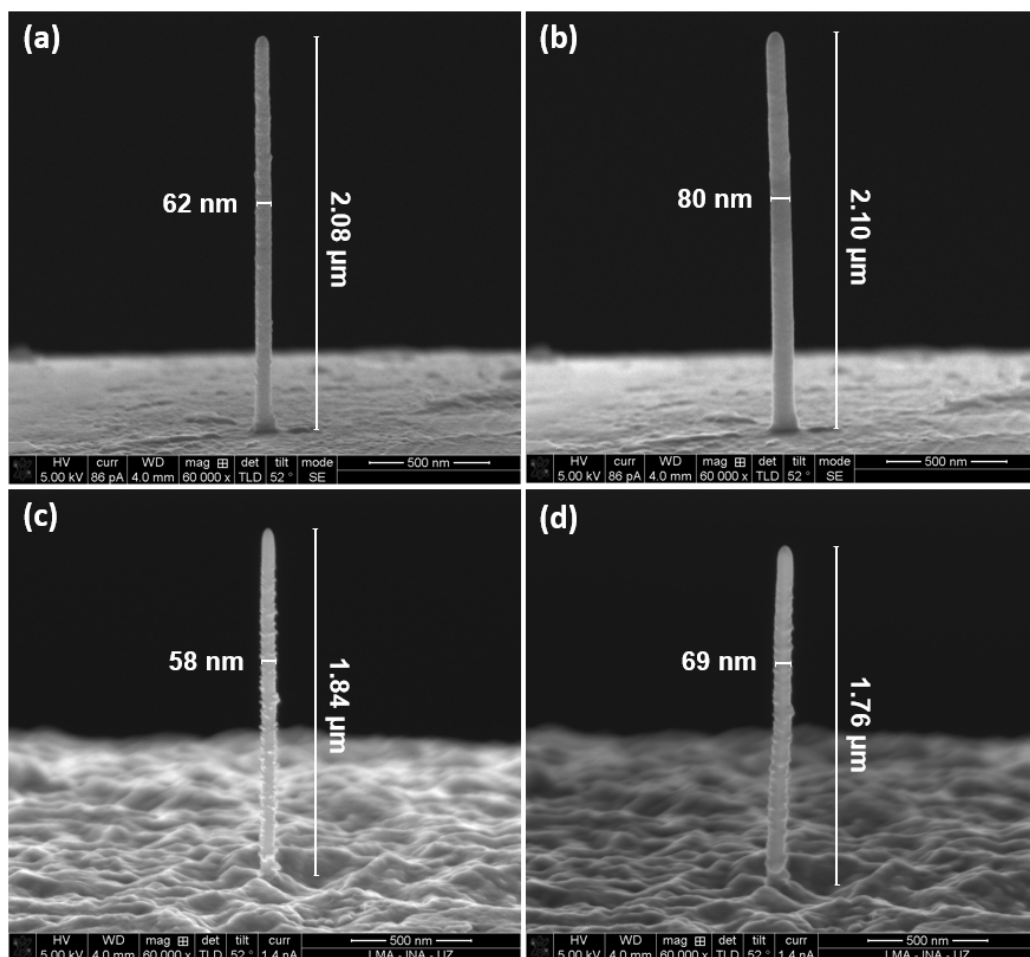
Figure 5.2. SEM images of (a) Co (b) Co@Pt, (c) Fe and (d) Fe@Pt nanowires.

First, this reveals that Co and Fe cores grow perfectly straight with uniform diameter. Afterwards, the Pt-C coating enlarges the diameter between 10-20 nm and smooths out the initial roughness of the Co and Fe cores, as noticed after careful inspection of the images. In addition, although an excellent preservation of the general shape can be appreciated, a slight deformation after the shell fabrication can be observed. This minor shape alteration is caused by local heating effect absorbed by the structure during the short Pt-C deposition time (~1-2 s) in each nanowire side.

In order to investigate the homogeneity of the Pt-C coverage as well as verifying the circular section of the nanowires, cross sectional slices perpendicular to the nanowire long axis were extracted in the form of TEM lamellae. Following the process shown in Figure 5.3, a very thin transversal cut was extracted from a Co@Pt nanowire with a core of 60 nm in diameter and a 10-nm-thick shell. In the standard procedure for lamella preparation, a protective Pt-C deposit covers the nanostructure under study to avoid beam damage during the ulterior thinning. Nonetheless, in this case the Pt-C deposition is not appropriate because it may be confused with the true shell of the Co@Pt nanowire.
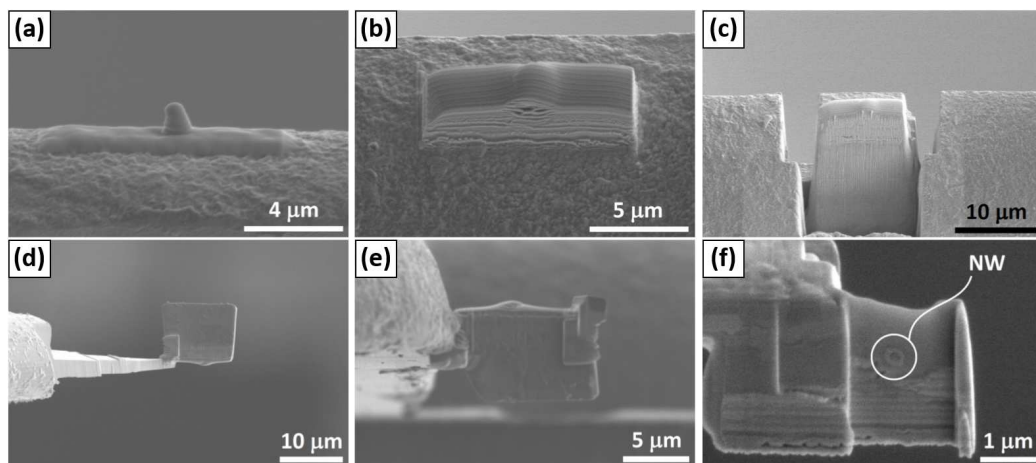
Figure 5.3. (a) Initial W-C and Pt-C depositions, (b) completed protective Pt-C deposition, (c) rough FIB milling of trenches around the object, (d) nanomanipulator tip holding the lamella after welding and cut-off, (e) lamella attached to a fresh TEM grid once detached from the tip, and (f) final thinning, where the nanowire slice can be observed.

Consequently, a first W-C deposit was grown by FEBID using $W(CO)_6$ precursor gas, followed by a second layer of the much faster Pt-C deposition. Then, the working chamber was opened and the TEM grid was placed in a flat position respect to the stage platform, so the nanowire long axis is perpendicular to the electron beam with the stage tilted 0 degrees. In addition, a new TEM grid was mounted inside the working chamber in the standard position. After locking the chamber, a milling process by FIB was carried out to create four trenches around the nanostructure. Then, the nanomanipulator tip was approached next to the edge of the lamella and welded to it by a Pt-C deposition using FEBID and FIBID. After that, the base part was cut and the structure lifted off the TEM grid, remaining fixed to the nanomanipulator. Then, the lamella was moved close to the fresh TEM grid, attaching it with a Pt-C deposit and cutting the welding between the tip and the nanomanipulator by FIB. The final lamella position allows the analysis of the specimen slice in the TEM microscope. The last step consisted of a final FIB thinning by gradually reducing the ion beam current to minimize damage. Eventually, a thickness of ~50 nm was obtained.

The cross section was analyzed by means of STEM-EELS chemical maps. Figure 5.4 illustrates the results obtained for the Co@Pt nanowire shown in Figure 5.2(b).
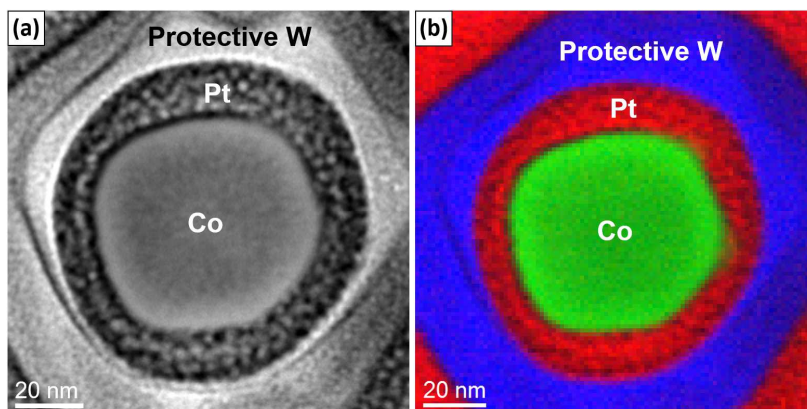
Figure 5.4. Cross section of the Co@Pt nanowire shown in Fig. 5.2(b). (a) HAADF-STEM image and (b) STEM-EELS chemical map of (a), where the integrated intensities of Co, Pt and W are depicted in green, red and blue, respectively.

It can be observed that the Co core section is approximately circular, while the Pt-C coating completely wraps the core with a 10-nm-thick shell, forming a protective layer. This proof certifies the first growth of a 3D cylindrical core-shell nanowire by FEBID via sequential deposition of the core and the shell targeted materials.

5.1.4 Structural and chemical characterization

HRTEM experiments were performed to describe in more detail the microstructure of the nanowires and confirm further the nature of the core-shell structure. Figure 5.5 illustrates the coated and uncoated Co and Fe nanowires.
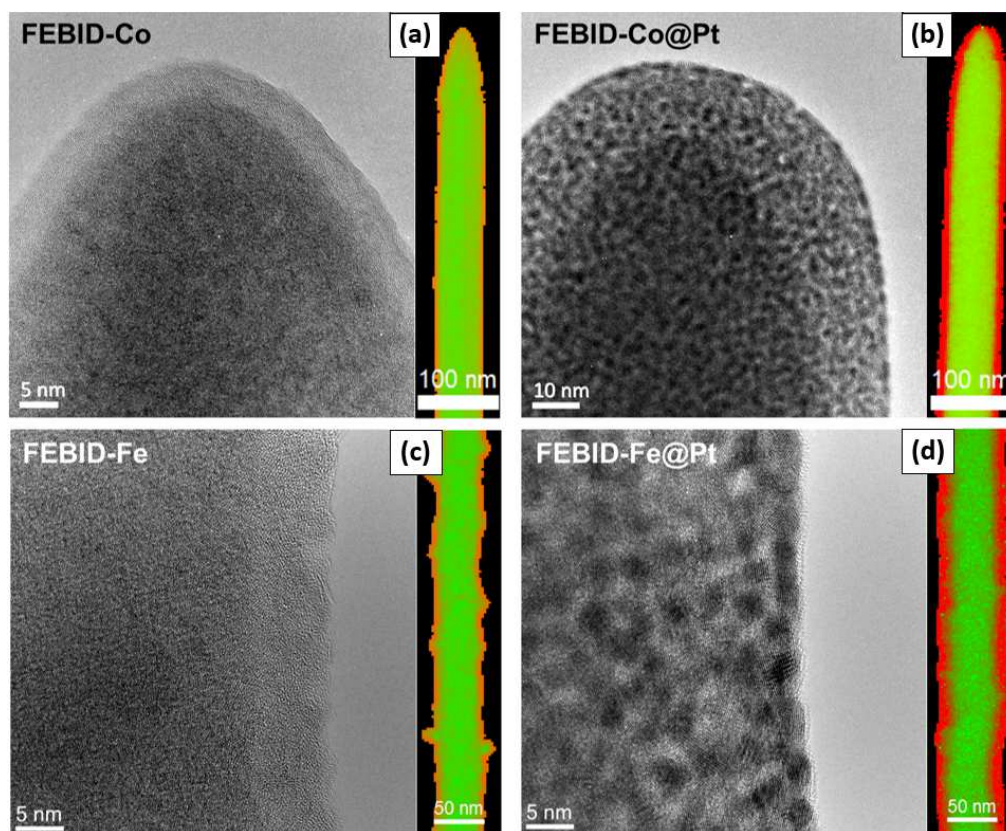
Figure 5.5. HRTEM images of the surface of (a) Co, (b) Co@Pt, (c) Fe and (d) Fe@Pt nanowires. Each image is accompanied by a STEM-EELS chemical map showing the spatial distribution of relative compositions of Co (Fe) and O in green and red, respectively.

In the case of the uncoated nanostructures, the expected nanocrystalline microstructure with no texture is present. This finding was already advanced in the previous chapter and reported for 2D materials with high metallic content [33]. Accordingly, the presence of nanocrystals of 2-3 nm is suggested, but here the large diameter in comparison with standard cross-sectional TEM specimens makes the nanocrystals difficult to observe. Interestingly, both uncoated Co and Fe nanowires exhibit a ~5-7 nm surface layer with brighter contrast, whose nanocrystalline nature is more easily observable with respect to the inside. This evidences the natural oxidation layer and is confirmed by the compositional analysis shown further on. In the case of the coated nanowires, the core contrast is a bit masked by the intense contribution of the Pt particles of the shell, which are less than 5 nm in diameter and embedded in the amorphous carbonaceous matrix covering isotropically the nanowire core.

Moreover, microstructural analyses of the uncoated and coated nanowires have been carried out by analyzing the FFT of different selected regions of HRTEM images. To clearly illustrate this, the results obtained for Co and Co@Pt nanowires are displayed in Figure 5.6. The FFTs of the Co core and the Co oxide shell regions in the uncoated nanowires, and those associated with the Pt-C shell area in the coated ones have been calculated.
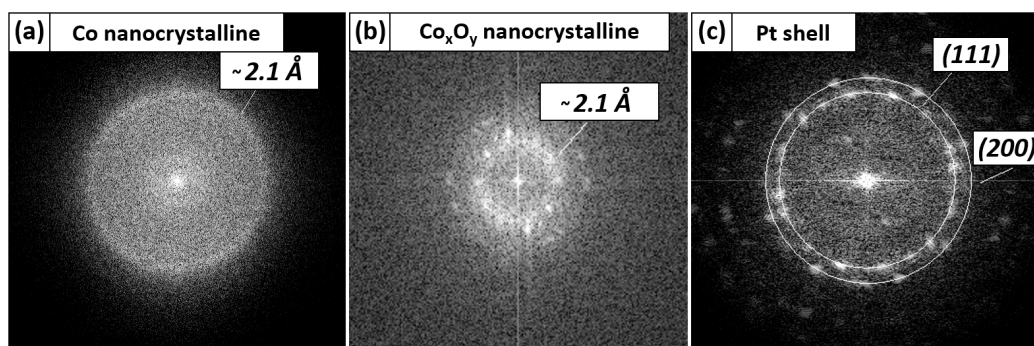
Figure 5.6. FFT of selected regions of the HRTEM images of Co and Co@Pt nanowires.

Figure 5.6(a,b) confirms the nanocrystalline nature of the core and the external surface oxidation layer, with typical reflections of Co and Co_xO_y at ~2.1 Å. Also, the Pt nanoparticles embedded in the carbonaceous matrix are evidenced by the sharp reflections in Figure 5.6(c).

Additionally, chemical mapping provides further insight about the core-shell architecture. Accompanying the correspondent HRTEM images, Figure 5.5 shows a comparison of the STEM-EELS chemical maps acquired in Co and Fe nanowires with the same core diameter. Firstly, these maps confirm that the surface layer observed in the uncoated nanowires indeed corresponds to an oxidation of the metallic Co or Fe material, represented by the orange-colored regions in the maps. These areas extend to approximately 5 nm, which corresponds nicely with the lighter-contrast surface observed in HRTEM images. A further proof of the connection between the high O content in the external regions and the natural surface oxidation upon exposure to ambient air is the fact that in the Fe case, with a significantly larger roughness than Co, the oxidation layer contours perfectly the irregularities of the surface, penetrating regularly about 4 nm into the nanowire.

In order to give a better account on the location of O in these nanostructures, Figure 5.7 plots STEM-EELS line profiles of the integrated intensities of Co (Fe), C and O. In this example, for the case of the Co it has been selected a thicker nanowire (~130 nm in diameter) to show that the core-shell architecture is also possible for thicker cores. Looking carefully at the edges of the coated nanowires, the O signal does not coincide anymore with the Co (Fe) signal, while there is a clear coincidence between the surface decaying metal signal and the O one when the nanowires are directly exposed to air. Thus, the growth of a thin (~10-20 nm) Pt-C layer fully protects the ferromagnetic core, avoiding its oxidation.
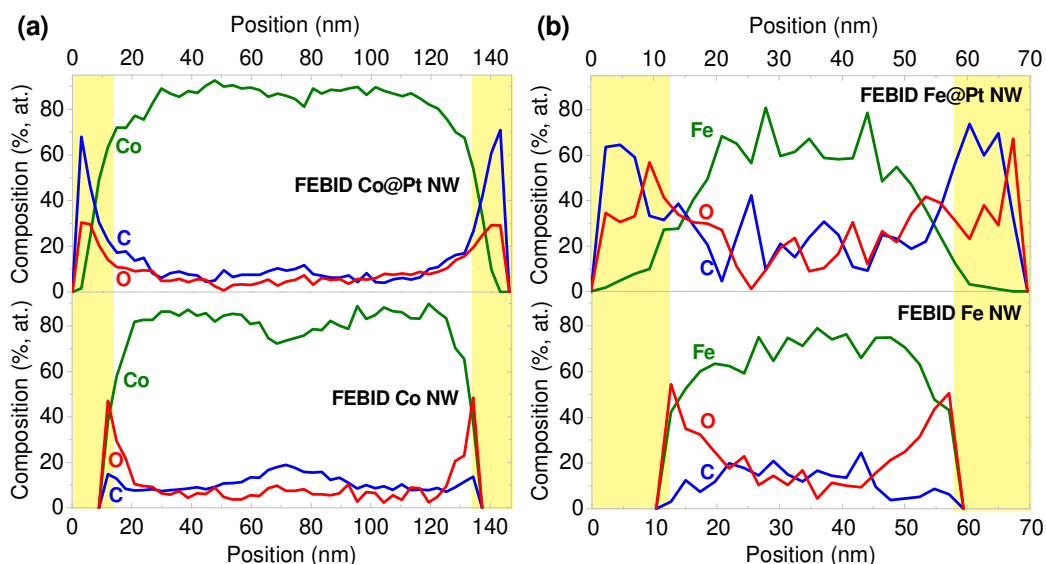
Figure 5.7. STEM-EELS chemical composition profiles comparing the position of the oxide layer in (a) Co and Co@Pt nanowires; and in (b) Fe and Fe@Pt nanowires. Yellow bands are guides to the eye showing the approximate position of the Pt-C shells in the coated nanowires (top panels) and the vacuum outside the nanostructure in the uncoated ones (bottom panels).

5.1.5 Magnetic characterization

The growth of a Pt coating also has a significant impact on the magnetic properties of the Co (Fe) nanowires. To check this, EH has been used to analyze quantitatively the magnetic induction of both Pt-C coated and naturally oxidized Co (Fe) nanowires [5][34].

Firstly, Figure 5.8(a-d) plots the magnetic flux lines distribution obtained for Co and Fe core-shell nanowires compared with the uncoated ones. The expected monodomain-type magnetization pointing along the long axis of the nanowire due to the high shape anisotropy of the nanostructure is shown. The maps have been extracted from central regions of the nanowires, far from the tip or any other major defect to help quantifying the average net magnetic induction, B, of the ferromagnetic volume. In order to establish a fair comparison, an important detail regarding B calculation must be clarified. In the case of coated nanowires, B must be obtained just taking the core diameter into account,

whilst in the case of uncoated nanowires, *B* should be obtained considering the total thickness of the nanostructure. Therefore, the oxidation layer will contribute to reduce *B* in the oxidized cores.

The comparison of this magnitude for both coated and uncoated nanowires in shown in Figure 5.8(e-f). It can be appreciated a systematic increase of *B* in the protected cores with respect to the naked ones, confirming that the oxidized shell is weakly or non-ferromagnetic.
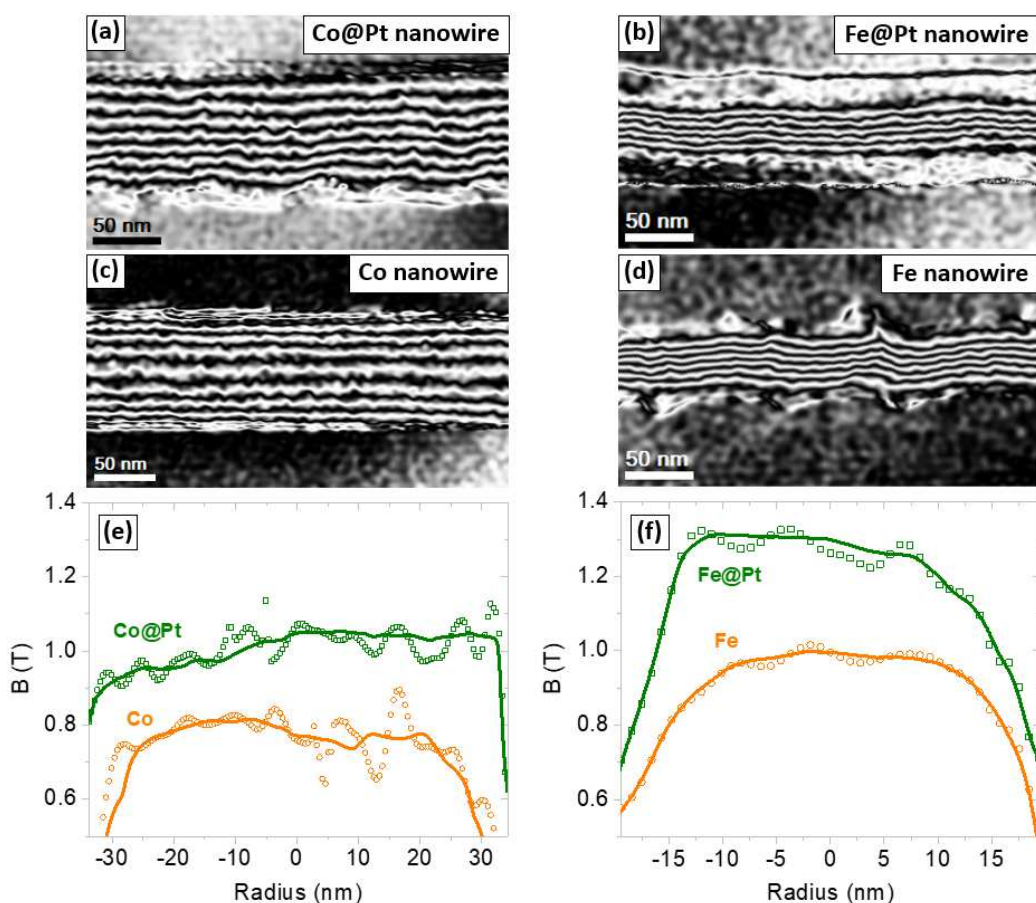
Figure 5.8. Magnetic flux lines distribution of (a) Co@Pt, (b) Fe@Pt, (c) Co and (d) Fe nanowires. Calculated *B* for the core-shell nanowires and their corresponding naked cores for (e) Co and (f) Fe measured across the nanowires width.

Whereas the *B* enhancement is moderate (~20%) in the ~70-nm-wide Co cores, it increases up to 35% for the Fe cores with ~35 nm in diameter. This is because the overall magnetic properties of thinner nanowires are more seriously affected by the surface oxidation than in thicker nanowires. Even though both magnetizations are still below the bulk values (1.76 T in bulk Co and 2.2 T in bulk Fe) due to the remaining ~20% at. of impurities of the Co and Fe cores, a remarkable *B* improvement has been obtained.

5.1.6 Discussion of the results and perspectives

Generally, this innovative synthetic FEBID strategy opens a new path for the fabrication of multifunctional nanostructures through the engineering of physical properties by tailored designed architectures based on a smart combination of materials, thicknesses and geometries [2][6][16]. More specifically, in the present matter the *B* enhancement could have a strong impact in magnetic devices, such as nanosensors, high-density magnetic memories or functionalized MFM tips, whose magnetic response can be highly disrupted by the degradation of the outer surface when it becomes a significant fraction of the volume. Also the transport properties can be affected, so additional characterization, such as magnetotransport measurements of individual nanowires could provide key information on the physical properties of the systems [35][36].

Furthermore, core-shell bimagnetic nanostructures could be grown, where basic magnetic properties such as coercivity or remanence can be fine-tuned by alternating two different magnetic materials or inserting non-magnetic spacing layers. Interestingly, some experiments were already performed in this regard, as illustrated in Figure 5.9. In this case, 3D core-shell Fe@Co nanowires have been grown after the oxidation of the Fe core on purpose to generate a non-magnetic gap in between Fe and Co. Indeed, a further refinement of the presented core-shell approach has been attempted by depositing the whole coating in one single step, from one of the sides of the core.
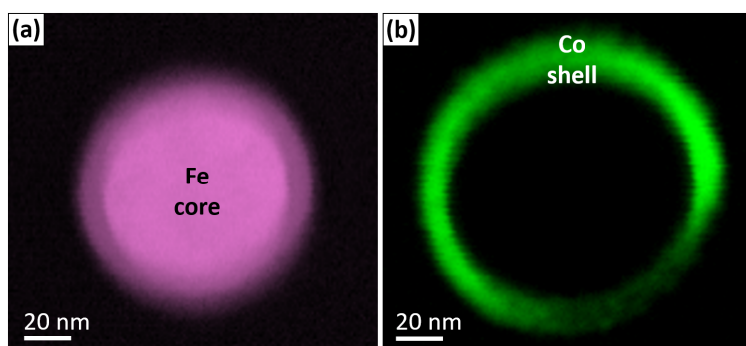
Figure 5.9. Cross section of an Fe@Co nanowire. STEM-EELS chemical maps of (a) the Fe core and (b) the Co shell, with integrated intensities of Fe in purple and Co in green.

This preliminary result also demonstrates the great potential of the SE in the precursor gas decomposition, since the entire circumference is generated. This suggests that the less covered region corresponds to the opposite scanned side, with the two lateral areas containing a higher Co content. However, the homogeneity and completeness of the shell is not totally satisfactory, so future experiments can be focused on improving the deposition parameters. Thus, so far, the double-shell deposition strategy is more effective, ensuring a great quality of the shell.

Other opportunities could arise from the optimization of the method presented in this work, such as the application of a continuous rotation of the core during shell deposition. This may also include the combination of FEBID with other synthesis or nanolithography techniques. For instance, atomic layer deposition of a wide variety of materials on FEBID-grown seeds could be used, which could produce new multifunctional structures enjoying the remarkable advantages of this deposition method. Furthermore, materials with different (even excluding) properties could be combined to explore novel phenomena or proximity effects at the nanoscale. Almost infinite combinations of materials and thicknesses could be explored, opening new prospects in the applicability of FEBID technique in the fabrication of functional nanodevices. For example, superconducting W-based FEBID nanowires [13] and ferromagnetic Co- or Fe-

FEBID ones could be integrated to produce superconducting-ferromagnetic core-shell nanostructures as playground for the investigation of the interplay between ferromagnetism and superconductivity in 3D confined nanostructures. In addition, the combination of noble metals (e.g., Au-FEBID) [12,13] and ferromagnetic FEBID materials to investigate magnetoplasmonic responses in nanoscaled core-shell devices could be challenged. Finally, exotic high-velocity magnetic domain walls could set in cylindrical ferromagnetic nanotubes grown around non-magnetic cores [36]. Indeed, this exciting possibility has been explored in this thesis, as described in the next section.

5.2 Three-dimensional cobalt nanotubes with a Pt-C core

The pioneering nanofabrication approach explained in the previous section to grow 3D core-shell nanowires by FEBID will be used to fabricate 3D ferromagnetic nanotubes by implementing minor adjustments. In this case, a non-magnetic core coated by a ferromagnetic shell gives rise to the magnetic tubular architecture. Additionally, an in-depth exploration of the magnetism of these nanostructures will be carried out by means of different magnetic characterization techniques.

5.2.1 Introduction

Magnetic nanotubes can provide many outstanding magnetic properties such as the stable ultrafast domain wall dynamics, reaching velocities higher than 1000 m/s under external magnetic fields of few mT [37]. Their architecture can induce transverse, vortex-like, Néel, Bloch or cross-tie domain walls [38][39][40][41][42], with different magnetization states and facilitating the motion of the domain walls under low current densities [43]. Besides, in comparison with magnetic nanostrips, where the domain wall elements become unstable when a threshold velocity is exceeded due to the precessional motion of the magnetization (Walker breakdown phenomenon) [44], this effect is not present in magnetic nanotubes, offering a long steady motion of the domain walls. These remarkable characteristics confer the nanotubes a strong potential to be used in a broad

variety of devices, from magnetic recording head to biomagnetic sensing [45][46][47]. Specifically, they are promising candidates for fast and low-power domain wall conduit used for storing and handling information. However, despite the advanced and ultimate magnetic properties of the nanotubes, their fabrication and characterization have not been comprehensively addressed because of the weak and poor reproducibility, governability and efficiency [48][49].

The magnetization dynamics in thin films and flat thin strips is very well known. Nevertheless, in the case of magnetic nanotubes, several theoretical predictions are still being investigated in order to fully understand their magnetic behavior [37][50][51][52]. These studies tried to comprehend the magnetization dynamics of Co, Ni and Fe nanotubes simulating and exploring the magnetic states and domain wall morphology and movement. Additionally, experimental investigations have been carried out in 3D nanotubes to tackle the magnetic properties by SQUID magnetometry [53][54] or sensitive cantilever magnetometry [55].

The growth of the functional magnetic nanotubes can be performed by several synthetic methods [56]: thermal decomposition with the precursor in templates for preparing Co structures [57], H reduction to synthesize FePt/Fe composite deposits [58], sol-gel approach for growing $CoFeO_4$ material [59], metal-organic chemical vapor deposition to produce NiO [60], atomic layer deposition for the growth of ordered Fe oxide nanotubes arrays [61], electro [62][63] and electroless deposition [64] for the fabrication of Fe, Co and Ni nanotubes, etc. During the fabrication, some inconveniences emerge from using these types of routes. For example, in the case of template processes, geometrical restrictions are evidenced, the use of masks constrains and hampers the growth procedures, and some impurities could also be present in the final products jeopardizing the proper operation of the magnetic nanostructures.

Moving forward in this challenging task, FEBID technique provides some advantages for the fabrication of 3D magnetic nanotubes. This deeply entrenched top-

down technique is capable to achieve lateral resolutions which have not been reported in literature yet for nanotubes, probably due to the challenge of combining different materials together. Following the strategy developed in the previous section for the growth of a protective coating onto 3D magnetic nanowires, henceforth the fabrication of 3D Co nanotubes by FEBID for the first time is presented, exploring their compositional and magnetic properties and pursuing a deeper understanding of the magnetic dynamics.

5.2.2 Experimental details

The nanostructures were fabricated in the commercial FEI Helios Nanolab 650 system using $CH_3CpPt(CH_3)_3$ and $Co_2(CO)_8$ precursor gases. The nanotubes were grown onto Si substrates and TEM Cu grids to simplify the characterization by MOKE magnetometry and TEM, respectively. The Pt-C core deposits were fabricated using an electron beam voltage of 30 kV, an electron beam current of 50 pA, a chamber growth pressure of 8×10^{-6} mbar (base pressure of $\sim 1 \times 10^{-6}$ mbar) and a single circle pattern scanned for 100 s. The Co shell deposits were grown using an electron beam voltage of 30 kV, an electron beam current of 100 pA and a chamber growth pressure of 3×10^{-6} mbar, scanning only once (one loop) from the top to the base of the core over two opposite sides for 35-110 s.

STEM and EELS were performed in the FEI Titan Low Base 60-300 operated at 300 kV. STEM-EELS experiments were carried out with a 25 mrad convergence semi-angle, an energy dispersion of 0.5 eV with a resolution of ~ 1.5 eV, a GIF aperture of 6 mm, a camera length of 10 mm, a pixel time of 10-25 ms and a beam current of ~ 270 pA.

EH experiments were carried out in the FEI Titan Cube 60-300 TEM, at 300 kV with a fringe contrast ranging from 20% to 25% and hologram acquisition time of 5 s, and in a Hitachi I2TEM at CEMES-CNRS in Toulouse, a high-end cold field emission-transmission electron microscope (FE-TEM) equipped with a spherical aberration

corrector reaching a spatial resolution of 0.5 nm in magnetic-field-free conditions. In this case, the holograms were recorded at 300 kV using a two-biprism setup, with a fringe contrast of ~20%, fringe spacing of 1.42 nm and a field of view of 492×492 nm^2. The hologram acquisition time was 480 s using a special acquisition procedure developed in CEMES, in which long exposures are feasible by correcting the sample and hologram drifts by the automatic compensation of calibrated beam deflectors.

The nanotubes devoted to MOKE experiments were felled totally flat on the substrate using a nanomanipulator, as shown in Figure 5.10. The measurements were performed at room temperature by applying an external magnetic field varying the angle respect to the long axis of the nanotube. The nanotube length guarantees a ferromagnetic volume enough to obtain a suitable signal-to-noise ratio.

The Object Oriented MicroMagnetic Framework (OOMMF) software was used for micromagnetic simulations. Unit cells of either $5 \times 1.5 \times 1.5$ nm^3 or $5 \times 3.6 \times 3.6$ nm^3, saturation magnetization $M_S = 1.4 \times 10^6$ A·m^{-1} and exchange constant $A = 3 \times 10^{-13}$ J/m were used, neglecting the magnetocrystalline anisotropy constant, K, due to the polycrystalline structure and small grain size of the samples. The magnetic fields were applied between -100 mT and +100 mT with a 10 mT step.
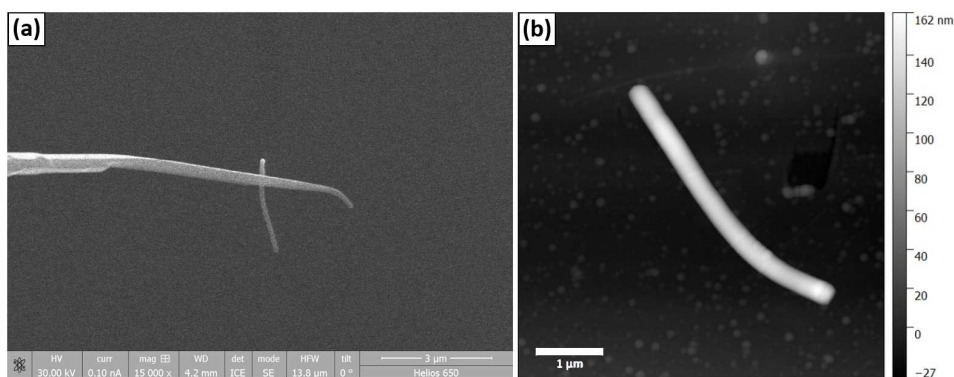
Figure 5.10. (a) SEM image of the process where the nanomanipulator is used to place the nanotubes totally flat on the substrate. (b) AFM image of a nanotube flat on the substrate.

5.2.3 Nanotubes fabrication strategy

Taking as a point of reference the approach developed for the fabrication of 3D core-shell nanowires by FEBID, Co ferromagnetic nanotubes have been grown by engineering 3D Pt@Co nanowires. Firstly, as shown in Figure 5.11(a), a vertical Pt-C core with small diameter (≤100 nm) and high aspect ratio (>30) is fabricated to serve as a template, by parking the electron beam in one single point with the stage in the horizontal position.
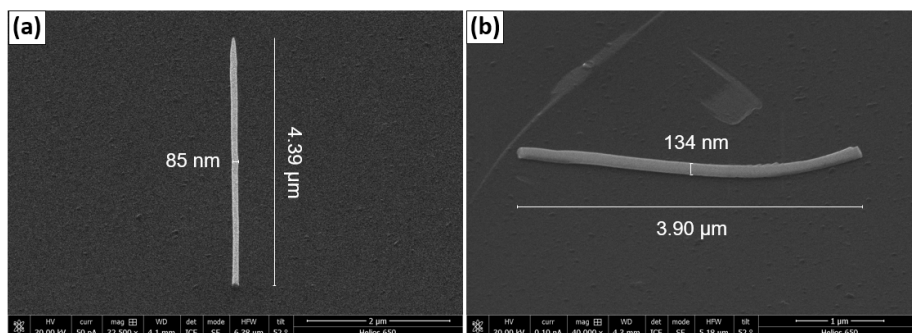
Figure 5.11. (a) 3D Pt-C nanowire acting as the core of the Co nanotube architecture. (b) Core-shell Pt@Co nanowire forming the Co nanotube and felled flat on the substrate.

Then, the stage is tilted allowing one nanowire side to be imaged by SEM as illustrated in Figure 5.11(a). The shell is built patterning, only once, two opposite sides of the nanowire from the top to the base setting a pattern adjusted to the nanowire shape. This constitutes a process refinement with respect to the previous method [65], where many swift scans, i.e., many loops from the top to the base of the nanowire, were carried out for shell fabrication in a short total deposition time (1-2 s).

The need for this refinement arises from the difficulties encountered with the different materials growth rates. Since the Pt-C deposition is much faster than the Co one under the same conditions, in this case longer times are required for the fabrication of a Co shell with similar thickness. This leads to a significant risk of deformation of the core, as larger amount of energy must be absorbed by the structure. After the first loops performed from the top to the base, the structure is not in the same position anymore

because it tends to bend. Consequently, subsequent loops are not performed on the nanostructure due to the impossibility of modifying the pattern position during the deposition. As a result, the solution was to execute the growth in one single loop from the top to the base in each side, reducing the scan speed to deposit a larger quantity of ferromagnetic material. For this purpose, just one prolonged scan must be performed on each side. In this way, the areas already scanned will suffer some deviation after the shell fabrication, but this is not of great importance anymore because no additional loops will be needed. Moreover, the most suitable method is to deposit the Co material while imaging at the same time, adjusting the beam position using beam shift if required.

Furthermore, both the core diameter and the shell thickness can be tuned controlling the growth parameters. High electron beam voltage and low current contribute to obtain small core diameters, and their length can be managed thanks to the total deposition time as the electron beam is always still in this step. In the case of the shell, the thickness could be incremented with increasing the dwell time parameter value. Typically, this parameter must be reduced in the base area, where a high number of precursor gas molecules arrive due to diffusion, to obtain a homogeneous thickness. Finally, Figure 5.11(b) shows the result after felling the nanotube on the substrate.

5.2.4 Structural and compositional results

In order to demonstrate if the ferromagnetic shell covers completely the non-magnetic core, transversal cross-sections of the nanotubes have been prepared. STEM imaging and STEM-EELS chemical mapping have been used to analyse morphological, dimensional and compositional properties of the 3D Co nanotubes. As shown in Figure 5.12(a), a Co shell of ~11 nm in width is fabricated. Although the metallic relative composition is ~70% at., the coating is not perfectly homogeneous and uniform. First, given the nature of the fabrication procedure, just the top end of the nanostructure is coated with magnetic material, which is not the case of the bottom end.
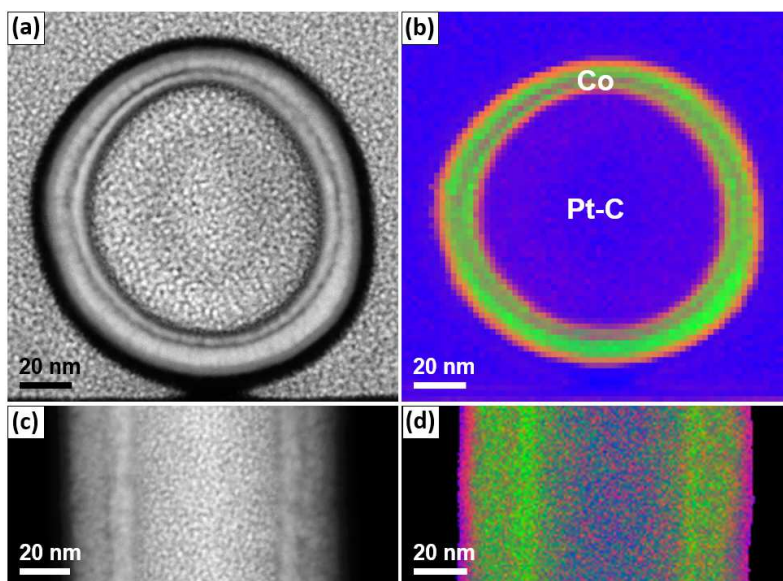
Figure 5.12. (a,c) STEM images of two Co nanotubes from the cross-sectional and lateral views with different inner and outer diameters and (b,d) their corresponding STEM-EELS chemical maps showing the spatial distribution of Co in green, C in blue and O in red.

Moreover, in Figure 5.12(b) an external surface oxidation layer which measures ~4 nm is identified, as reported in previous studies [24]. Also, an oxidation layer is appreciated in the surface of the core, since in this particular case the Pt-C core was exposed to ambient air before the Co coating, which is not the case of the nanotube showed in Figure 5.12(c,d).

On the other hand, two different outer Co layers can be clearly distinguished, being the result of the two-sided metallic depositions separated by a ~1 nm layer with less Co content, which can be noticed between the metallic layers. This occurs because the decomposition of the precursor gas molecules in the first nanometres of the deposit is not proper, so higher relative C contents may appear. As shown in Figure 5.12(c,d), these features can also be noticed in Co nanotubes with smaller core diameters and thicker Co coatings. Finally, in the wake of the results, despite one single Co deposition in any side

of the core can generate a fully covering, performing the deposits in two opposite sides guarantees and optimizes the cylindrical symmetry of the whole ferromagnetic shell.

5.2.5 Magnetic characterization

In order to evaluate theoretically the role played by this extremely thin apparent C-rich layer, micromagnetic simulations were performed. Firstly, it was assumed a core-shell Pt@Co nanowire with two ferromagnetic cylindrical shells (~5,25 nm in thickness) separated by a ~1,5-nm-wide non-ferromagnetic layer in the surroundings of a core with ~102 nm in diameter, imitating the architecture of the nanotube presented in Figure 5.12(a,b). As illustrated in Figure 5.13, in the simulated hysteresis loops a double switching event is observed, so the non-ferromagnetic layer promotes the decoupling between the two ferromagnetic shells. The outer shell would switch at ~15 mT whereas the coercivity, H_c, of the inner one would be ~65 mT.
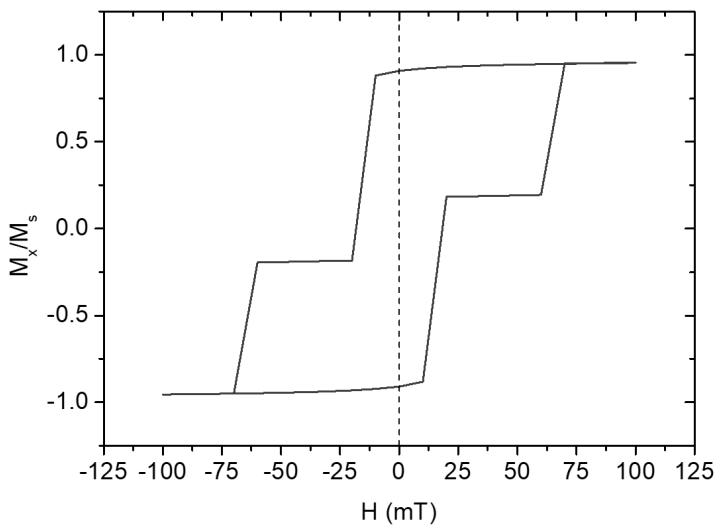
Figure 5.13. Simulated hysteresis loop of a nanotube with two ferromagnetic shells.

To strengthen this idea and verify these results, MOKE experiments were carried out. The goal is to measure the magnetic response (Kerr signal) as a function of the angle

of the applied external magnetic field, H, starting along the long axis direction of the nanotube, x, and modifying it up to 45 degrees respect to the initial position. The change of the angle has been achieved by applying in unison two perpendicular external magnetic fields, called H_x and H_y, and varying their modules separately. Whereas H_x is applied along the long axis of the nanotube, keeping constant its maximum module (32 mT) and always sweeping from +32 mT to -32 mT, H_y is applied in the perpendicular direction and changes the maximum module from 0 mT to 32 mT with a 2 mT step. This induces an associated effective modification of the H angle from 0 to 45 degrees. Indirectly, since H_y module changes gradually to vary the H angle, H module is also modified increasing its value from 32 mT at 0 degrees up to ~45.3 mT at 45 degrees. Despite this, those values are enough to ensure the saturation magnetization in every measurement. Different hysteresis loops have been acquired at each H angle, as illustrated in Figure 5.14.

Sharp magnetic switching fields were obtained, indicating their high structural quality and the absence of substantial pinning sites. On the one hand, contrary to expectations provided by the simulations, the decoupling between the two ferromagnetic shells is not observed, revealing the presence of only one single switching in the hysteresis loops. This proves that the low Co interlayer is not sufficient to induce the magnetic decoupling of the two Co deposition layers. As a result, this can be considered as a Co layer partially contaminated with C where the magnetic induction is reduced locally. On the other hand, H_c reduces its value ~2,5 mT increasing the angle from 0 to 45 degrees. Furthermore, H_c as a function of the H angle follows a linear trend, as shown in Figure 5.15.

In order to interpret this result, the magnetization reversal mechanism must be considered. Starting with the magnetization pointing along the long axis of the nanotube, two steps will be taken: the nucleation of a domain wall and the complete magnetization reversal.
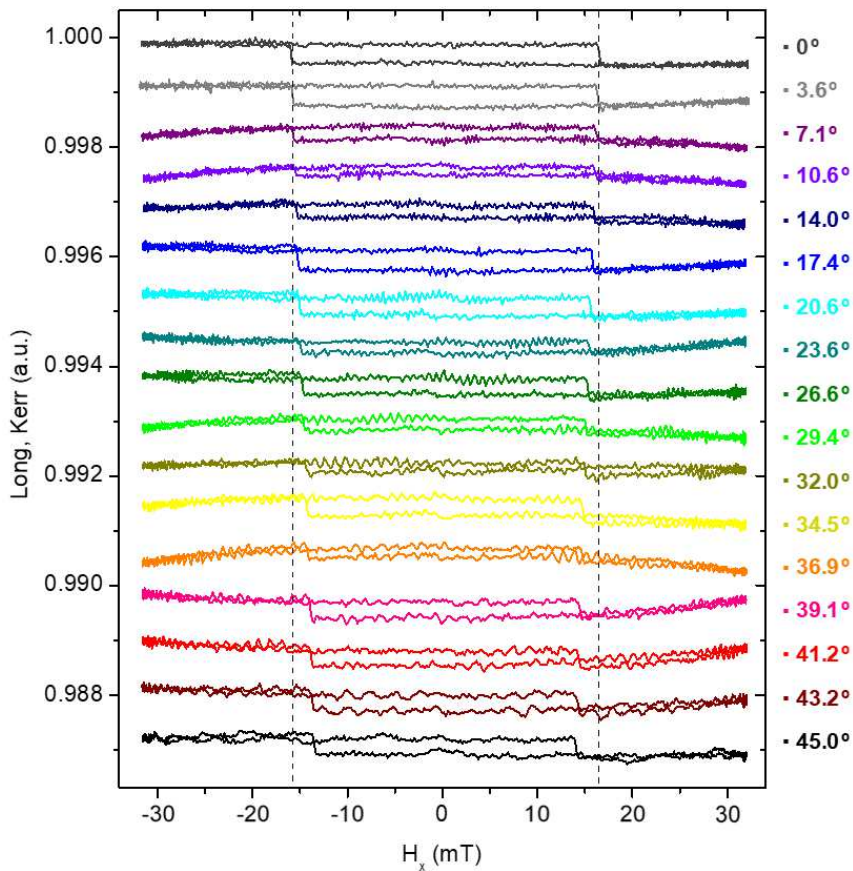
Figure 5.14. MOKE hysteresis loops representing the Kerr signal as a function of H_x depending on the H angle. Dashed lines are guides to the eye for comparing coercivity values.
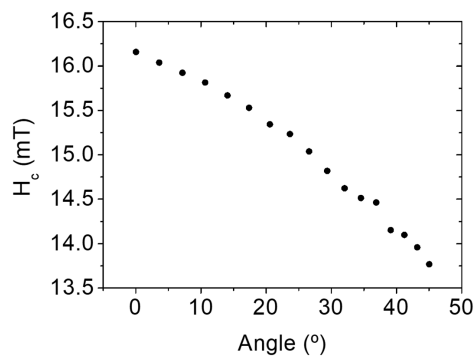
Figure 5.15. Coercivity as a function of the H angle where 0 degrees corresponds to the direction of the long axis of the nanotube with no H_y applied.

The nucleation of the domain wall might be favoured by increasing the H angle since the field will be pointing closer to some of the components direction of the domain wall. Although applying the external magnetic field along the long axis of the nanotube may be thought as an easier way to switch the magnetization direction, this hampers the domain wall nucleation, which is the first step for the magnetization reversal. As a result, the domain wall will be induced more easily at higher H angles.

Based on these results, new micromagnetic simulations were performed considering just one ferromagnetic layer around the non-ferromagnetic core. In this case, the inversion of the magnetic induction is produced in a single switching. A domain wall nucleates in one of the edges and propagates along the whole nanotube until coming to the opposite edge. The H_c obtained from the simulations was ~39 mT, a value much larger than the one obtained in the MOKE experiments where H_c of ~16 mT was found applying H along the long axis of the nanotube. The discrepancy between theoretical and experimental values should be mainly attributed to the temperature. The domain wall motion is a thermally activated process, so this switching field factor is crucial [66]. However, for sake of simplicity, whereas the simulations were carried out at 0 K, MOKE experiments were undertaken at room temperature. Nonetheless, a 60% increase of the switching field was observed in Co-FEBID nanowires between 300 K and 25 K [67]. Thus, a plausible result has been obtained, further considering that the nanotube is not perfectly straight and smooth, both the core and the shell may have not the same dimensions along the nanostructure length and different tip shapes can impact on H_c.

On the other hand, EH experiments revealed a clear change of the magnetic phase shift, φ_{MAG}, as a function of the width, which demonstrates that the shell is completely ferromagnetic, as illustrated in Figure 5.16. Also, there is a slightly higher slope in the external areas than in the centre region, which is in line with the Co volume present in the nanotube integrating across the total thickness. Finally, an average magnetic induction of ~0.9 T was obtained, in good correspondence with the metallic composition.
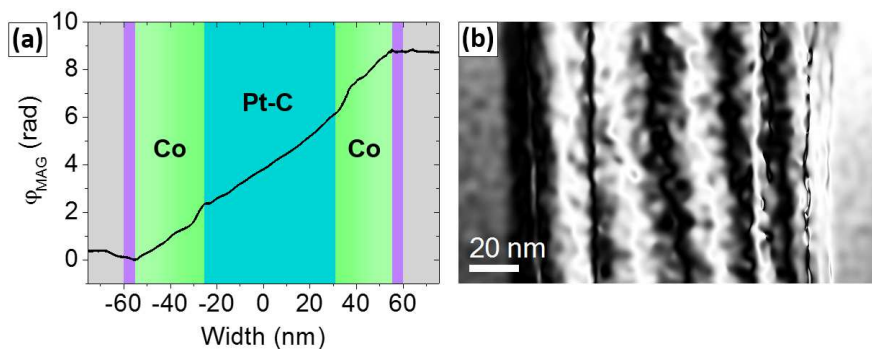
Figure 5.16. (a) Magnetic phase shift, φ_{MAG}, as a function of the width of the Co nanotube of Figure 5.12(d). (b) Magnetic flux lines distribution of the Co nanotube.

EH was also used for imaging a domain wall in a nanotube with a non-ferromagnetic core of ~70 nm in diameter and a Co shell of ~10 nm in thickness, as shown in Figure 5.17. The magnetization was first saturated in one direction of the nanotube. Then, a controlled magnetic field was applied in the opposite direction until a domain wall was nucleated in the middle of the nanostructure and tracked by Lorentz imaging. Figure 5.17(a) shows the SEM image of the nanotube used for this experiment with the domain wall pinning position indicated in the inset Lorentz image. A magnetic contrast discontinuity can be appreciated at the place where the domain wall sets. More clearly, φ_{MAG} and the magnetic flux lines are represented in Figure 5.17(b,d), where the position of the domain wall is evidenced by the stray fields leaking out of the nanostructure [68].

Trying to comprehend the magnetic characterization, the experimental results were correlated with micromagnetic simulations, as shown in Figure 5.17(c,e). The domain wall width could be estimated between 150 nm and 200 nm, and a magnetic induction of ~1.3 T is obtained in the rest areas of the nanostructure. This value is 74% that of the pure Co, which is in good agreement with the compositional results. The comparison between the experiment and theoretical simulations is performed by the experimental phase reconstruction and the simulation images. An accurate correspondence can be identified between the experiments and the theoretical simulations.
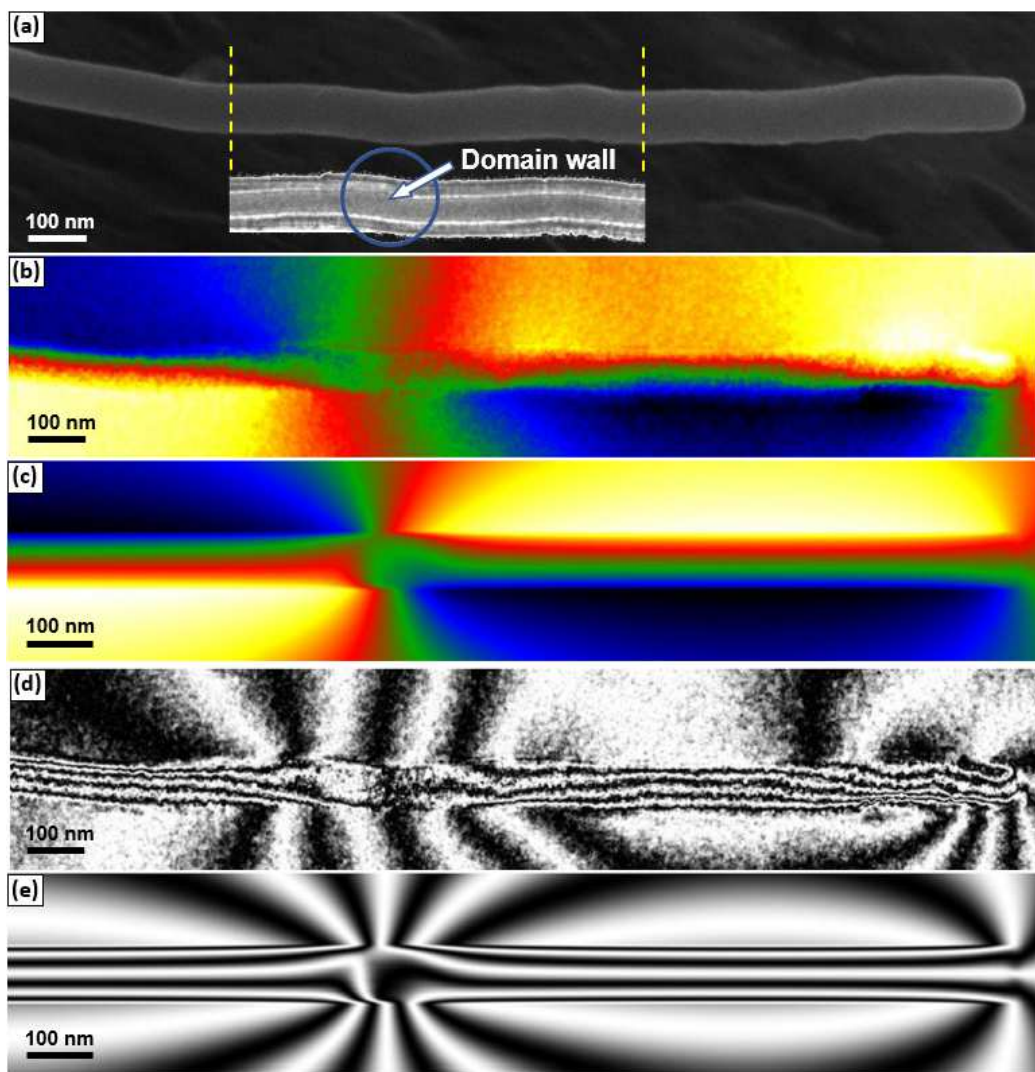
Figure 5.17. (a) SEM image of the Co nanotube used for a domain wall pinning, with the Lorentz image of the same section of the nanotube indicating the position of the domain wall. (b) Experimental magnetic phase shift and (d) magnetic flux lines distribution. (c) Micromagnetic simulations of the magnetic phase shift and (e) the magnetic flux lines.

Finally, the evaluation of the magnetization configuration in the domain wall region has been carried out. As Figure 5.18 displays, the magnetization is pointing in one direction in one of the sides of the nanotube and in the opposite direction in the other side

of the nanostructure, with a special configuration in the domain wall, which is composed by two opposite Néel walls separating two vortices, one of them pointing radially to the outside and the other to the inside of the nanotube. As a result, the magnetization circulates around the central axis in the Néel walls and leaks out of the nanostructure in the vortices.
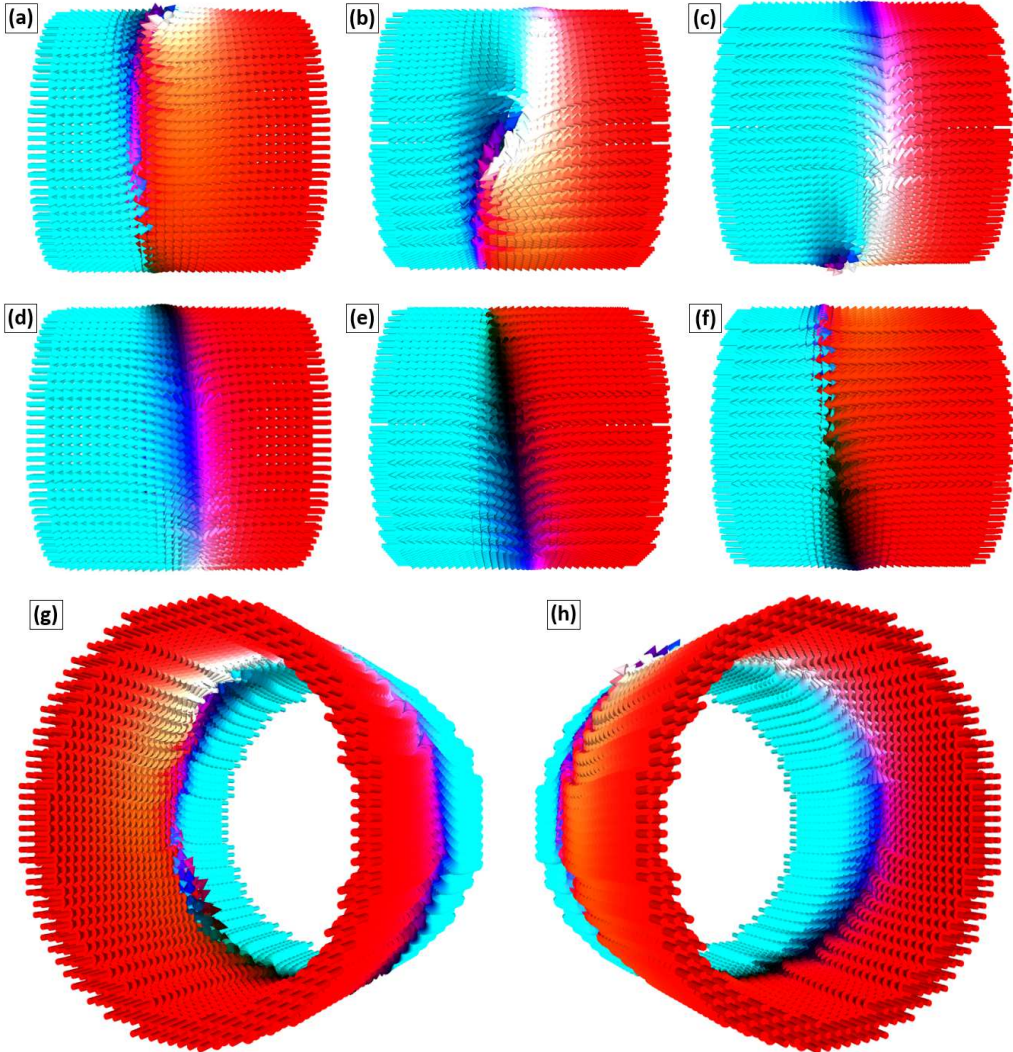
Figure 5.18. Simulation of the nanotube magnetic configuration after pinning a domain wall, with (a-f) enlarged views of the domain wall every 60 degrees of rotation. (g,k) 3D perspective view of the domain wall configuration.

5.3 Conclusions

Firstly, a procedure to create nanoscale heterostructured materials in the form of core-shell nanowires by FEBID technique has been developed. In particular, 3D nanowires with metallic ferromagnetic cores of Co or Fe have been grown and coated with a protective Pt-C shell aimed to minimize the degradation of magnetic properties caused by the natural surface oxidation of the core to a non-ferromagnetic material. A comparison between coated and uncoated nanowires has shown that, in the case of the core-shell configuration, the surface oxidation is suppressed from the ferromagnetic core and confined to the Pt-C layer, increasing the average magnetic induction of the core up to 35% in the case of the thinnest nanowires.

Secondly, 3D ferromagnetic nanotubes based on the same core-shell strategy have been grown for the first time. The heterostructured design is composed by a vertical Pt-C nanowire acting as a core and a Co coating forming the shell. To the best of our knowledge, the ~11-nm-thick shell is the lowest ferromagnetic thickness of a nanotube ever reported in literature. The magnetic characterization allowed detecting magnetic domain walls and estimating a remanent magnetic inductions between ~0.9 and 1.3 T. A maximum coercivity of ~16 mT is required to produce an abrupt magnetic switching governed by a domain wall formation and propagation. This is a critical point, because good domain wall motion can be reached applying small magnetic fields giving rise to a good performance of magnetic and logic devices. In addition, these findings were supported by micromagnetic simulations which helped to have a better understanding of the domain wall dynamics.

These results evidence that the proposed core-shell approach paves the way to the fabrication of 3D FEBID nanostructures based on the smart alternate deposition of two or more materials combining different physical properties or added functionalities. Furthermore, this procedure represents a novel strategy to produce new custom-designed heterostructures fabricated solely by FEBID or its combination with other methods.

References

[1]   K. Höflich, R. B. Yang, A. Berger, G. Leuchs and S. Christiansen, "The Direct Writing of Plasmonic Gold Nanostructures by Electron-Beam-Induced Deposition", *Adv. Mater.* **23**, 2657 (2011).

[2]   R. Winkler, A. Szkudlarek, J. D. Fowlkes, P. D. Rack, I. Utke and H. Plank, "Toward Ultraflat Surface Morphologies During Focused Electron Beam Induced Nanosynthesis: Disruption Origins and Compensation", *ACS Appl. Mater. Interfaces* **7**, 3289 (2015).

[3]   K. Mitsuishi, M. Shimojo, M. Tanaka, M. Takeguchi and K. Furuya, "Resolution in New Nanofabrication Technique Combining Electron-Beam-Induced Deposition and Low-Energy Ion Milling", *Jpn. J. Appl. Phys.* **44**, 5627 (2005).

[4]   A. G. Fedorov, S. Kim, M. Henry, D. Kulkarni and V. V. Tsukruk, "Focused-electron-beam-induced processing (FEBIP) for emerging applications in carbon nanoelectronics", *Appl. Phys. A* **117**, 1659 (2014).

[5]   L. Serrano-Ramón, R. Córdoba, L. A. Rodríguez, C. Magén, E. Snoeck, C. Gatel, I. Serrano, M. R. Ibarra and J. M. De Teresa, "Ultrasmall functional ferromagnetic nanostructures grown by focused electron-beam-induced deposition", *ACS Nano* **5**, 7781 (2011).

[6]   J. M. De Teresa and R. Córdoba, "Arrays of densely packed isolated nanowires by focused beam induced deposition plus Ar^+ milling", *ACS Nano* **8**, 3788 (2014).

[7]   G. Boero, I. Utke, T. Bret, N. Quack, M. Todorova, S. Mouaziz, P. Kejik, J. Brugger, R. S. Popovic and P. Hoffmann, "Submicrometer Hall devices fabricated by focused electron-beam-induced deposition", *Appl. Phys. Lett.* **86**, 042503 (2005).

[8]   A. Fernández-Pacheco, L. Serrano-Ramón, J. M. Michalik, M. R. Ibarra, J. M. De Teresa, L. O'Brien, D. Petit, J. Lee and R. P. Cowburn, "Three dimensional magnetic nanowires grown by focused electron-beam induced deposition", *Sci. Rep.* **3**, 1492 (2013).

[9]   L. Van Kouwen, A. Botman and C. W. Hagen, "Focused Electron-Beam-Induced Deposition of 3 nm Dots in a Scanning Electron Microscope", *Nano Lett.* **9**, 2149 (2009).

[10]   M. Gavagnin, H. D. Wanzenboeck, D. Belić and E. Bertagnolli, "Synthesis of individually tuned nanomagnets for Nanomagnet Logic by direct write focused electron beam induced deposition", *ACS Nano* **7**, 777 (2013).

[11]   M. Huth, F. Porrati, C. Schwalb, M. Winhold, R. Sachser, M. Dukic, J. Adams and G. Fantner, "Focused electron beam induced deposition: A perspective",

Beilstein J. Nanotechnol. **3**, 597 (2012).

[12] A. V. Riazanova, B. N. Costanzi, A. Aristov, Y. G. Rikers, V. Ström, J. J. L. Mulders, A. V. Kabashin, E. D. Dahlberg and L. M. Belova, "Gas-assisted electron-beam-induced nanopatterning of high-quality Si-based insulator", *Nanotechnology* **25**, 155301 (2014).

[13] S. Sengupta, C. Li, C. Baumier, A. Kasumov, S. Guéron, H. Bouchiat and F. Fortuna, "Superconducting nanowires by electron-beam-induced deposition", *Appl. Phys. Lett.* **106**, 042601 (2015).

[14] I. Utke, P. Hoffmann, R. Berger and L. Scandella, "High-resolution magnetic Co supertips grown by a focused electron beam", *Appl. Phys. Lett.* **80**, 4792 (2002).

[15] M. Gabureac, L. Bernau, I. Utke and G. Boero, "Granular Co-C nano-Hall sensors by focused-beam-induced deposition", *Nanotechnology* **21**, 115503 (2010).

[16] S. Graells, S. Aćimović, G. Volpe and R. Quidant, "Direct growth of optical antennas using e-beam-induced gold deposition", *Plasmonics* **5**, 135 (2010).

[17] L. Keller, M. K. I. Al Mamoori, J. Pieper, C. Gspan, I. Stockem, C. Schröder, S. Barth, R. Winkler, H. Plank, M. Pohlit, J. Müller and M. Huth, "Direct-write of free-form building blocks for artificial magnetic 3D lattices", *Sci. Rep.* **8**, 6160 (2018).

[18] M. J. Perez-Roldan, F. Tatti, P. Vavassori, A. Berger and A. Chuvilin, "Segregation of materials in double precursor electron-beam-induced-deposition: a route to functional magnetic nanostructures", *Nanotechnology* **26**, 375302 (2015).

[19] O. V. Dobrovolskiy, M. Kompaniiets, R. Sachser, F. Porrati, C. Gspan, H. Plank and M. Huth, "Tunable magnetism on the lateral mesoscale by post-processing of Co/Pt heterostructures", *Beilstein J. Nanotechnol.* **6**, 1082 (2015).

[20] F. Porrati, E. Begun, R. Sachser and M. Huth, "Spin-dependent transport between magnetic nanopillars through a nano-granular metal matrix", *J. Phys. D: Appl. Phys.* **47**, 495001 (2014).

[21] S. Sangiao, L. Morellón, M. R. Ibarra and J. M. De Teresa, "Ferromagnet-superconductor nanocontacts grown by focused electron/ion beam techniques for current-in-plane Andreev Reflection measurements", *Solid State Commun.* **151**, 37 (2011).

[22] N. Nakagawa, H. Y. Hwang and D. A. Muller, "Why some interfaces cannot be sharp", *Nat. Mater.* **5**, 204 (2006).

[23] M. Bibes, J. E. Villegas and A. Barthélémy, "Ultrathin oxide films and interfaces for electronics and spintronics", *Adv. Phys.* **60**, 5 (2011).

[24] L. A. Rodríguez, L. Deen, R. Córdoba, C. Magén, E. Snoeck, B. Koopmans and

J. M. De Teresa, "Influence of the shape and surface oxidation in the magnetization reversal of thin iron nanowires grown by focused electron beam induced deposition", *Beilstein J. Nanotechnol.* **6**, 1319 (2015).

[25]   J. Nogués, J. Sort, V. Langlais, V. Skumryev, S. Suriñach, J. S. Muñoz and M. D. Baró, "Exchange bias in nanostructures", *Phys. Rep.* **422**, 65 (2005).

[26]   L. J. Lauhon, M. S. Gudiksen, D. Wang and C. M. Lieber, "Epitaxial core-shell and core-multishell nanowire heterostructures", *Nature* **420**, 57 (2002).

[27]   J. Tang, Z. Huo, S. Brittman, H. Gao and P. Yang, "Solution-processed core-shell nanowires for efficient photovoltaic cells", *Nat. Nanotechnol.* **6**, 568 (2011).

[28]   L.-F. Cui, Y. Yang, C.-M. Hsu and Y. Cui, "Carbon-Silicon Core-Shell Nanowires as High Capacity Electrode for Lithium Ion Batteries", *Nano Lett.* **9**, 3370 (2009).

[29]   X. Lu, M. Yu, G. Wang, T. Zhai, S. Xie, Y. Ling, Y. Tong and Y. Li, "H-TiO$_2$@MnO$_2$//H-TiO$_2$@C Core-Shell Nanowires for High Performance and Flexible Asymmetric Supercapacitors", *Adv. Mater.* **25**, 267 (2013).

[30]   M. Law, L. E. Greene, A. Radenovic, T. Kuykendall, J. Liphardt and P. Yang, "ZnO-Al$_2$O$_3$ and ZnO-TiO$_2$ Core−Shell Nanowire Dye-Sensitized Solar Cells", *J. Phys. Chem. B* **110**, 22652 (2006).

[31]   Y. T. Chong, D. Görlitz, S. Martens, M. Y. E. Yau, S. Allende, J. Bachmann and K. Nielsch, "Multilayered core/shell nanowires displaying two distinct magnetic switching events", *Adv. Mater.* **22**, 2435 (2010).

[32]   D.-W. Shi, K. Javed, S. S. Ali, J.-Y. Chen, P.-S. Li, Y.-G. Zhao and X.-F. Han, "Exchange-biased hybrid ferromagnetic-multiferroic core-shell nanostructures", *Nanoscale* **6**, 7215 (2014).

[33]   R. Córdoba, R. Fernández-Pacheco, A. Fernández-Pacheco, A. Gloter, C. Magén, O. Stéphan, M. R. Ibarra and J. M. De Teresa, "Nanoscale chemical and structural study of Co-based FEBID structures by STEM-EELS and HRTEM", *Nanoscale Res. Lett.* **6**, 592 (2011).

[34]   D. Wolf, L. A. Rodriguez, A. Béché, E. Javon, L. Serrano, C. Magen, C. Gatel, A. Lubk, H. Lichte, S. Bals, G. Van Tendeloo, A. Fernández-Pacheco, J. M. De Teresa and E. Snoeck, "3D Magnetic Induction Maps of Nanoscale Materials Revealed by Electron Holographic Tomography", *Chem. Mater.* **27**, 6771 (2015).

[35]   J. Tang, C.-Y. Wang, W. Jiang, L.-T. Chang, Y. Fan, M. Chan, C. Wu, M.-H. Hung, P.-H. Liu, H.-J. Yang, H.-Y. Tuan, L.-J. Chen and K. L. Wang, "Electrical Probing of Magnetic Phase Transition and Domain Wall Motion in Single-Crystalline Mn$_5$Ge$_3$ Nanowire", *Nano Lett.* **12**, 6372 (2012).

[36]   G. Liu, Y.-C. Lin, L. Liao, L. Liu, Y. Chen, Y. Liu, N. O. Weiss, H. Zhou, Y.

Huang and X. Duan, "Domain Wall Motion in Synthetic Co$_2$Si Nanowires", *Nano Lett.* **12**, 1972 (2012).

[37]   M. Yan, C. Andreas, A. Kákay, F. García-Sánchez and R. Hertel, "Fast domain wall dynamics in magnetic nanotubes: Suppression of Walker breakdown and Cherenkov-like spin wave emission", *Appl. Phys. Lett.* **99**, 122505 (2011).

[38]   M. Staňo and O. Fruchart, "Magnetic Nanowires and Nanotubes", *Handbook of Magnetic Materials*, Edited by E. Brück (2018).

[39]   P. Landeros and A. S. Núñez, "Domain wall motion on magnetic nanotubes", *J. Appl. Phys.* **108**, 033917 (2010).

[40]   M. Staňo, S. Schaefer, A. Wartelle, M. Rioult, R. Belkhou, A. Sala, T. O. Menteş, A. Locatelli, L. Cagnon, B. Trapp, S. Bochmann, S. Y. Martin, E. Gautier, J.-C. Toussaint, W. Ensinger and O. Fruchart, "Flux-closure domains in high aspect ratio electroless-deposited CoNiB nanotubes", *SciPost Phys.* **5**, 038 (2018).

[41]   M. Zimmermann, T. N. G. Meier, F. Dirnberger, A. Kákay, M. Decker, S. Wintz, S. Finizio, E. Josten, J. Raabe, M. Kronseder, D. Bougeard, J. Lindner and C. H. Back, "Origin and Manipulation of Stable Vortex Ground States in Permalloy Nanotubes", *Nano Lett.* **18**, 2828 (2018).

[42]   A. Mehlin, B. Gross, M. Wyss, T. Schefer, G. Tütüncüoglu, F. Heimbach, A. Fontcuberta i Morral, D. Grundler and M. Poggio, "Observation of end-vortex nucleation in individual ferromagnetic nanotubes", *Phys. Rev. B* **97**, 134422 (2018).

[43]   R. Hertel, "Ultrafast domain wall dynamics in magnetic nanotubes and nanowires", *J. Phys.: Condens. Matter* **28**, 483002 (2016).

[44]   N. L. Schryer and L. R. Walker, "The motion of 180° domain walls in uniform dc magnetic fields", *J. Appl. Phys.* **45**, 5406 (1974).

[45]   J. Lee, D. Suess, T. Schrefl, K. H. Oh and J. Fidler, "Magnetic characteristics of ferromagnetic nanotube", *J. Magn. Magn. Mater.* **310**, 2445 (2007).

[46]   L. Krusin-Elbaum, D. M. Newns, H. Zeng, V. Derycke, J. Z. Sun and R. Sandstrom, "Room-temperature ferromagnetic nanotubes controlled by electron or hole doping", *Nature* **431**, 672 (2004).

[47]   S. J. Son, J. Reichel, B. He, M. Schuchman and S. B. Lee, "Magnetic Nanotubes for Magnetic-Field-Assisted Bioseparation, Biointeraction, and Drug Delivery", *J. Am. Chem. Soc.* **127**, 7316 (2005).

[48]   A. L. González, P. Landeros and A. S. Núñez, "Spin wave spectrum of magnetic nanotubes", *J. Magn. Magn. Mater.* **322**, 530 (2010).

[49]   D. Lee, R. E. Cohen and M. F. Rubner, "Heterostructured Magnetic Nanotubes", *Langmuir* **23**, 123 (2007).

[50]   R. Hertel, "Applications of Multi-scale Modeling to Spin Dynamics in Spintronics Devices", *Handbook of Materials Modeling. Applications: Current and Emerging Materials*, Edited by W. Andreoni and S. Yip, *Springer* (2019).

[51]   J. A. Otálora, J. A. López-López, A. S. Núñez and P. Landeros, "Domain wall manipulation in magnetic nanotubes induced by electric current pulses", *J. Phys.: Condens. Matter* **24**, 436007 (2012).

[52]   P. Landeros, S. Allende, J. Escrig, E. Salcedo and D. Altbir, "Reversal modes in magnetic nanotubes", *Appl. Phys. Lett.* **90**, 102501 (2007).

[53]   M. Daub, M. Knez, U. Goesele and K. Nielsch, "Ferromagnetic nanotubes by atomic layer deposition in anodic alumina membranes", *J. Appl. Phys.* **101**, 09J111 (2007).

[54]   D. Vasyukov, L. Ceccarelli, M. Wyss, B. Gross, A. Schwarb, A. Mehlin, N. Rossi, G. Tütüncüoglu, F. Heimbach, R. R. Zamani, A. Kovács, A. Fontcuberta i Morral, D. Grundler and M. Poggio, "Imaging Stray Magnetic Field of Individual Ferromagnetic Nanotubes", *Nano Lett.* **18**, 964 (2018).

[55]   D. P. Weber, D. Rüffer, A. Buchter, F. Xue, E. Russo-Averchi, R. Huber, P. Berberich, J. Arbiol, A. Fontcuberta i Morral, D. Grundler and M. Poggio, "Cantilever Magnetometry of Individual Ni Nanotubes", *Nano Lett.* **12**, 6139 (2012).

[56]   Y. Ye and B. Geng, "Magnetic Nanotubes: Synthesis, Properties, and Applications", *Crit. Rev. Solid State Mater. Sci.* **37**, 75 (2012).

[57]   K. Nielsch, F. J. Castaño, S. Matthias, W. Lee and C. A. Ross, "Synthesis of Cobalt/Polymer Multilayer Nanotubes", *Adv. Eng. Mater.* **7**, 217 (2005).

[58]   H. L. Su, S. L. Tang, N. J. Tang, R. L. Wang, M. Lu and Y. W. Du, "Chemical synthesis and magnetic properties of well-coupled FePt/Fe composite nanotubes", Nanotechnology **16**, 2124 (2005).

[59]   Y. Xu, J. Wei, J. Yao, J. Fu and D. Xue, "Synthesis of $CoFe_2O_4$ nanotube arrays through an improved sol-gel template approach", *Mater. Lett.* **62**, 1403 (2008).

[60]   G. Malandrino, L. M. S. Perdicaro, I. L. Fragalà, R. Lo Nigro, M. Losurdo and G. Bruno, "MOCVD Template Approach to the Fabrication of Free-Standing Nickel(II) Oxide Nanotube Arrays: Structural, Morphological, and Optical Properties Characterization", *J. Phys. Chem. C* **111**, 3211 (2007).

[61]   J. Bachmann, J. Jing, M. Knez, S. Barth, H. Shen, S. Mathur, U. Gösele and K. Nielsch, "Ordered Iron Oxide Nanotube Arrays of Controlled Geometry and Tunable Magnetism by Atomic Layer Deposition", *J. Am. Chem. Soc.* **129**, 9554 (2007).

[62] X. J. Xu, S. F. Yu, S. P. Lau, L. Li and B. C. Zhao, "Magnetic and Thermal Expansion Properties of Vertically Aligned Fe Nanotubes Fabricated by Electrochemical Method", *J. Phys. Chem. C* **112**, 4168 (2008).

[63] T. N. Narayanan, M. M. Shaijumon, P. M. Ajayan and M. R. Anantharaman, "Synthesis of High Coercivity Cobalt Nanotubes with Acetate Precursors and Elucidation of the Mechanism of Growth", *J. Phys. Chem. C* **112**, 14281 (2008).

[64] J. F. Rohan, D. P. Casey, B. M. Ahern, F. M. F. Rhen, S. Roy, D. Fleming and S. E. Lawrence, "Coaxial metal and magnetic alloy nanotubes in polycarbonate templates by electroless deposition", *Electrochem. Commun.* **10**, 1419 (2008).

[65] J. Pablo-Navarro, C. Magén and J. M. De Teresa, "Three-dimensional core-shell ferromagnetic nanowires grown by focused electron beam induced deposition", *Nanotechnology* **27**, 285302 (2016).

[66] A. Fernández-Pacheco, J. M. De Teresa, A. Szkudlarek, R. Córdoba, M. R. Ibarra, D. Petit, L. O'Brien, H. T. Zeng, E. R. Lewis, D. E. Read and R. P. Cowburn, "Magnetization reversal in individual cobalt micro- and nanowires grown by focused-electron-beam-induced-deposition", *Nanotechnology* **20**, 475704 (2009).

[67] A. Fernández-Pacheco, J. M. De Teresa, R. Córdoba and M. R. Ibarra, "Magnetotransport properties of high-quality cobalt nanowires grown by focused-electron-beam-induced deposition", *J. Phys. D: Appl. Phys.* **42**, 055005 (2009).

[68] N. Biziere, C. Gatel, R. Lassalle-Balier, M. C. Clochard, J. E. Wegrowe, and E. Snoeck, "Imaging the Fine Structure of a Magnetic Domain Wall in a Ni Nanocylinder", *Nano Lett.* **13**, 2053 (2013).

Chapter 6: Current and future applications based on FEBID

In this chapter, the potential of Focused Electron Beam Induced Deposition is brought forward by breakthrough applications. Special nanostructures based on this extraordinary nanolithography technique are put into operation in Magnetic Force Microscopy attesting to their promising and good quality performance. Specifically, a flagship model in the operability of 3D straight magnetic nanowires has been explored. Additionally, novel shape configurations were investigated towards the development of domain wall conduit applications in the near future.

6.1 Cobalt and iron Magnetic Force Microscopy tips

The implementation of 3D ferromagnetic nanostructures into a device is an arduous, but exciting task. Although basic research has been the common thread throughout this thesis, a practical application will be targeted in this chapter. The simplest 3D nanostructure, i.e., straight vertical nanowires, were used to functionalize AFM tips into MFM tips. Particularly, vertical Co and Fe nanowires have been grown, characterized magnetically, and tested in different environments to compare their operational performance with that of standard commercial MFM probes.

6.1.1 Introduction

Despite the fact that FEBID versatility allows the production of complex structures at the nanoscale [1][2][3], the applications which can emerge from this outstanding technique can be based in the most simple objects, such as vertical straight nanowires. Since the previous chapters have delved into the optimization for the growth of 3D ferromagnetic nanowires, it seems natural to start exploiting their potential before testing more sophisticated geometries. In this context, vertical Co and Fe nanowires will be used to functionalize AFM tips. This combination gives rise to novel MFM tips which could improve the performance of the standard magnetic tips. Given that MFM is one of the most used techniques both in research centres and companies for the characterization of magnetic properties at the nanoscale, further progress could have a significant impact in this field.

To enhance the operating performance of MFM, some of the main technical limitations should be contemplated. Firstly, the non-magnetic interactions between the tip and the sample must be eliminated, given that some spurious and undesired signals may reduce the quality of the measurements. This is closely related to the magnetic signal-to-noise ratio, which must be enough to ensure a suitable interpretation of the results. Moreover, on this basis, the characterization performed by MFM could be

improved by reducing the magnetic invasiveness. This concept is defined as the intensity of the magnetic interaction between the tip and the sample, being the control of this parameter essential. For instance, the magnetic configurations of small nanostructures can be adversely affected by the tip influence, altering the original magnetic state of the sample and compromising the reliability of MFM magnetic contrast.

Additionally, improving the lateral resolution obtained by the current MFM tips will lead to cutting-edge investigations, far beyond the present studies. Also, following this argumentative line, the incorporation of novel and refined MFM tips in enabling environments where the samples can be better explored (e.g., air/vacuum for metals or liquid media for biological specimens) could actively prompt the detection of new phenomena. Finally, the extraction of magnetic quantitative information is also one of the major challenges for the future MFM progress.

The growth of materials in the form of vertical nanowires by FEBID onto AFM probes have already been conducted during the last 20 years. Initially, supertips were produced by fabricating C nanowires onto AFM Si probes used as near field optical converters in photon scanning tunnelling microscopy [4]. On the other hand, proof-of-concept demonstrations were exhibited for the first time by growing high-aspect-ratio ferromagnetic Co nanowires and characterize them by analysing the tip performance in hard disks reference samples [5][6]. A few years later, the prevailing spatial magnetic resolution of ~40 nm was improved down to 10 nm by generating higher purity ferromagnetic Co-FEBID nanowires with thinner diameters [7]. Also, Fe-based deposits were grown on AFM tips correcting the angle formed with respect to the target sample, inducing an accurate and optimized MFM measurement of 3D nanomagnet logic arrays [8].

Although FEBID magnetic probes with potential application in MFM were used in the past, further efforts to optimize their performance are presented hereafter. In order to show that tailored FEBID tips are superior than standard MFM ones and can give rise to

the next generation of commercial MFM tips, dedicated nanofabrication and characterization experiments were performed for the sake of comparison. In particular, 3D Co and Fe nanowires have been grown on various types of tips and under different growth conditions. The tips have been tested in MFM experiments, in ambient conditions as well as in liquid environment, behaving appropriately in terms of mechanical stability, resolution and sensitivity [9].

6.1.2 Experimental details

The 3D Co and Fe nanowires were fabricated in the commercial Helios Nanolab 600 and 650 Dual Beam systems using $Co_2(CO)_8$ and $Fe_2(CO)_9$ precursor gases and electron beam voltage of 3-30 kV. The Co deposits were grown with an electron beam current of 50-100 pA and a chamber growth pressure of ~9×10^{-6} mbar (base pressure of ~1.4×10^{-6} mbar). In the Fe case, an electron beam current of 43-86 pA and a chamber growth pressure of ~6×10^{-6} mbar were used. Finally, some core-shell nanowires were fabricated by depositing Pt-C onto the Co (Fe) nanowires using $CH_3CpPt(CH_3)_3$ and setting an electron beam voltage of 5 kV, an electron beam current of 100 pA and a chamber growth pressure of 1×10^{-5} mbar.

TEM imaging was carried out in the FEI Titan Cube 60-300 operated at 300 kV. STEM imaging and EELS chemical analyses were performed in the Titan Low Base 60-300 also operated at 300 kV. Both imaging and spectroscopic experiments were carried out with a convergence semi-angle of 25 mrad. STEM-EELS experiments were performed with an energy dispersion of 0.8 eV, an energy resolution of ~1.5 eV, a pixel time of 10-20 ms and an estimated beam current of ~250 pA. Additionally, EDS spectroscopic experiments were carried out inside the Helios 600 and 650 Dual Beam systems, using an electron beam voltage of 5 kV and an electron beam current of 800 pA.

Off-Axis EH was performed for the local magnetic characterization in the Titan Cube operated at 300 kV. The excitation of the biprism was varied between 180 V and

220 V. The fringe contrast of the holograms ranged 20-25% and the acquisition time was 5 s. The magnetic induction was calculated using the Equation A.3.

The MFM experiments, characterization and interpretation of the results were performed by Dr. Agustina Asenjo and Dr. Miriam Jaafar, included in this chapter for consistency.

6.1.3 Growth optimization and tip characterization

The different geometries of the commercial tips —being pyramidal and cone-shaped the most typical ones— require a very sharp edge, i.e., a small radius of curvature in the apex. This ensures a good spatial resolution both in AFM and MFM measurements. Although the sensitivity and resolution are also limited by the mechanical properties of the cantilever and control electronics, in the MFM case the magnetic stray field is another key parameter to be discussed. In the present study, the target is to modify the final architecture of the probes by FEBID simultaneously customizing their magnetic behaviour. Particularly, the objective is to modulate not only the general aspect ratio but also the diameter and shape of the 3D ferromagnetic nanowires at the very end of the nanowire tip. As it will be explained, this possibility breaks new ground conferring novel behaviour to the central element of the functionalized MFM probes.

Firstly, considering that a proper adjustment of the electron beam astigmatism and focus is of the utmost importance, it is crucial to work with tips which favour an accurate aberration correction. For example, the *Nanoworld Arrow^{TM} EFM*, *Budget Sensors ElectriMulti75-G* and *Bruker* probes tested are suitable for this requirement, but this is not the case with *Olympus BioLever mini* due to a huge charging effect observed. For this reason, the nanofabrication process begins with the cantilever fitting on top of a conductor material, allowing charge dissipation and fixing the sample inside the working chamber. Typically, C adhesive tape was used underneath and over some edges of the cantilevers trying to solve or minimize this issue.
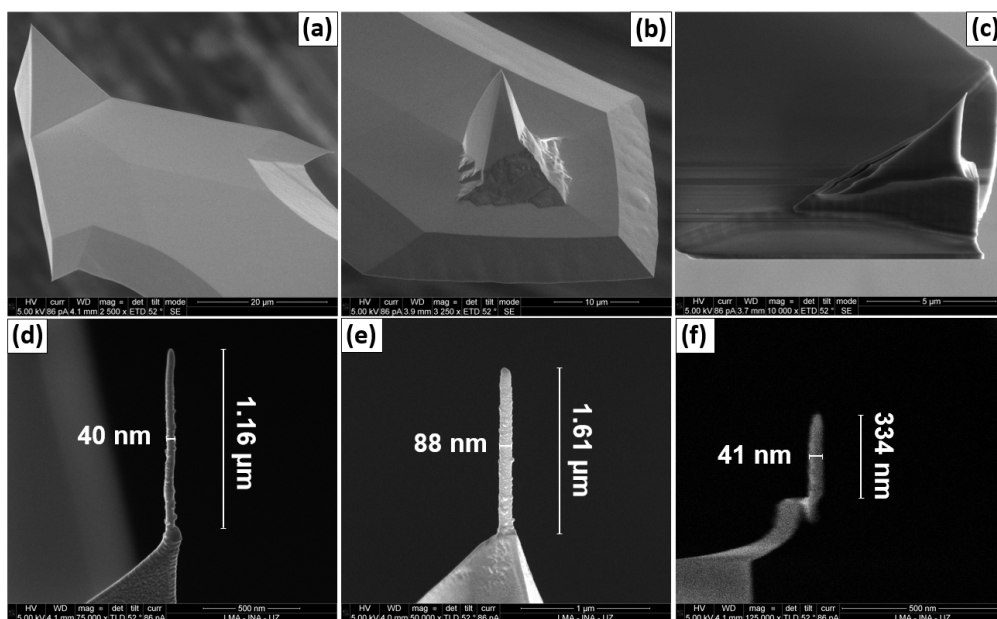
Figure 6.1. SEM images of (a) *Nanoworld Arrow^TM EFM*, (b) *Budget Sensors* and (c) *Olympus BioLever mini* AFM probes, with their corresponding (d,f) Fe and (e) Co nanowires.

Secondly, the small deposition surface compared to conventional substrates reduces the number of molecules available for decomposition. Under this situation, the GIS angle with respect to the horizontal axis becomes increasingly important as it determines the gas flow quantity [10]. Furthermore, the probe geometry also has a negative impact on the heat dissipation, promoting greater nanowire diameters due to temperature increase, especially working at low voltages (~3-5 kV). Nonetheless, this factor also helped to increase the metallic purity up to 80% at. both in Co and Fe material. As a result, depending on the growth parameters, sometimes a previous FIB cutting is required to facilitate the deposition, as shown in Figure 6.3(b).

Figure 6.1(d-f) illustrates 3D Co and Fe nanowires grown in different type of probes with diameters ranging from 40 to 90 nm fabricated at low voltages. Likewise, the control of the diameter and length is entirely possible mainly through the electron beam current and the deposition time, respectively (see Table 6.1).

In order to explore the tip-sample interaction, a comparison between FEBID and commercial tips has been established using CoPt multilayers as a reference sample. Whereas FEBID tips allow observing the original random domain configuration of the multilayers, the images obtained by the commercial tips are influenced by the high stray fields of the probe. The magnetic domains are preferentially pointing parallel to the magnetic field, revealing that their magnetization reversal was promoted by the tip.

Probe type	Sample	FEBID material	Deposition time (s)	Diameter (nm)	Length (µm)
Nanoworld Arrow™ *EFM*	1	Co	43	59	1.70
	2	Co	31	82	0.71
	3	Co	37	80	1.20
	4	Fe	48	51	0.85
	5	Fe	42	57	0.42
	6	Fe	52	48	0.64
	7	Fe	71	38	1.16
Budget Sensors ElectriMulti75-G	8	Co	43	88	1.61
	9	Co	34	65	1.31
	10	Fe	55	40	1.05
Olympus BioLever mini	11	Fe	52	41	0.33

Table 6.1. Data of 3D nanowires grown at 5 kV and 86 pA (Co) and 3 kV and 43 pA (Fe).
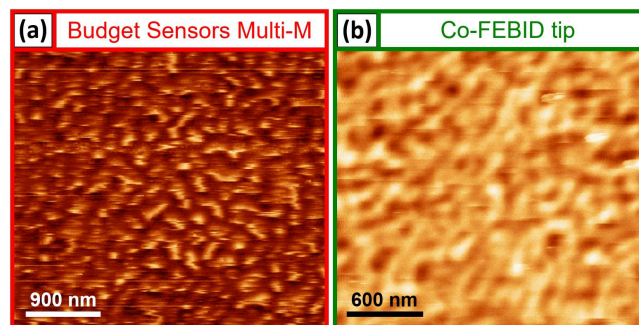
Figure 6.2. MFM images of a CoPt multilayer obtained by (a) the commercial *Budget Sensors Multi-M* probe with 50 nm of CoCr coating and (b) a Co-FEBID tip.

Applying the magnetic field parallel to the nanowire long axis, the high-coercive-field of the FEBID tips has been checked, reaching 55-60 mT, inhibiting the reversal magnetization of the tip caused by the sample field. In comparison, the commercial MFM tips showed experimental values of 20 mT (*Team Nanotec*) and 35 mT (*Budget Sensors*).

On the other hand, the sensitivity and image contrast have been compared using a high-density hard disk as a reference. Figure 6.3 shows similar performance for the three systems. However, it should be emphasized that the possible tuning of the magnetic properties of FEBID tips is an advantage to perform future quantitative studies.
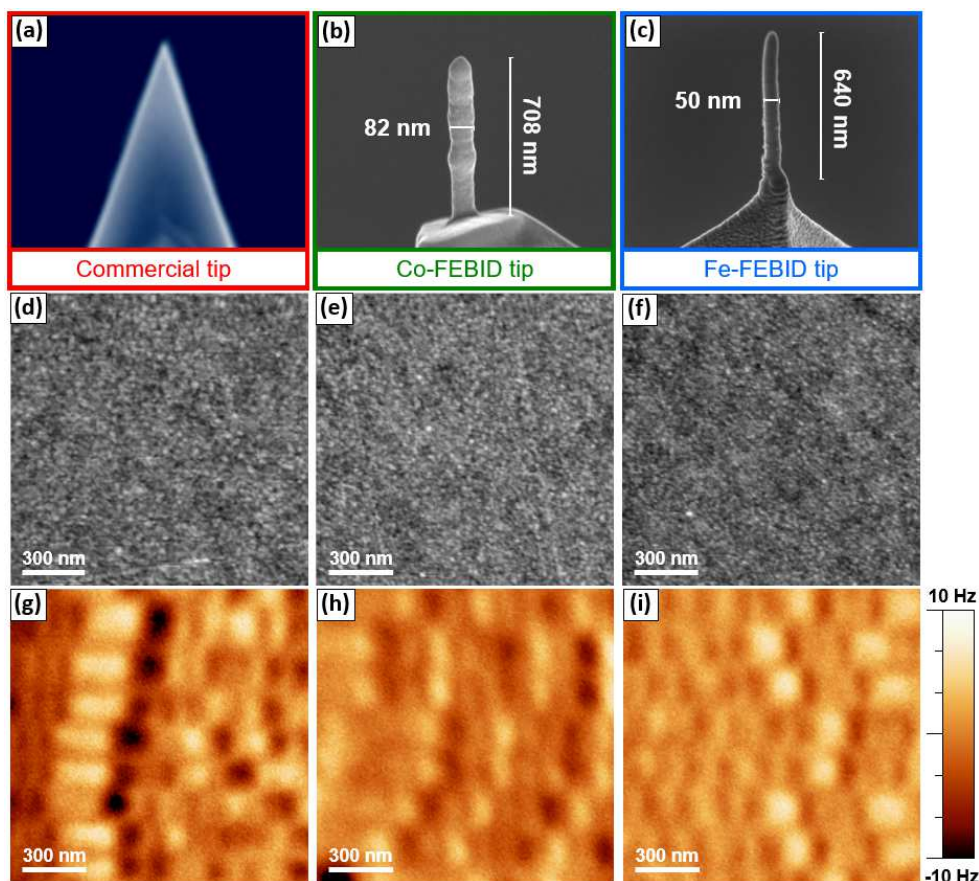
Figure 6.3. Images (a) a *Budget Sensors Multi-M* tip with 50 nm of CoCr coating, (b) Co-FEBID tip and (c) Fe-FEBID tip. (d,e,f) Topographic images obtained by the selected MFM probes and (g,h,i) their corresponding magnetic images, respectively.

Moreover, as illustrated in Figure 6.4(a), FEBID nanowires with different properties can be grown and implemented onto AFM probes, e.g., core-shell architectures and extremely thin diameters. One of the fundamental principles of image resolution is that the higher the voltage, the better the resolution of the image. This also works for the FEBID fabrication process, where the thinnest nanowires can be grown at the highest voltages. Besides, tuning this parameter, the shape of the nanowire tip end can be modulated. The upper nanowire part presents a blunt shape using 3-5 kV; however, it exhibits an extremely pointy end and a smaller general diameter setting 30 kV. These features can be appreciated in the thinnest ferromagnetic nanowire grown throughout this thesis (~22 nm in diameter) imaged in Figure 6.4(b) and, more precisely, in the replicable example of a nanowire grown at 30 kV in Figure 6.4(c). In this case, an overall diameter of around 35 nm and a ~7-8 nm-wide tip end are obtained with high reproducibility. This novel shape configuration is very useful to perform very high resolution MFM imaging as well as to obtain relatively low tip-sample interaction, minimizing the influence of the tip on the magnetic state of the sample structures [11].
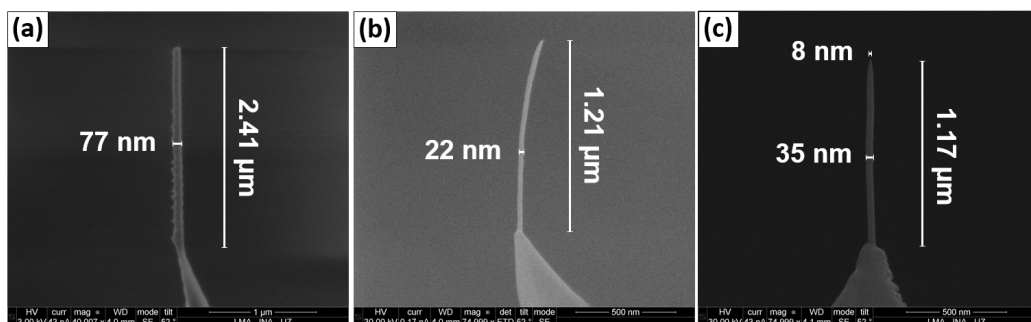
Figure 6.4. SEM images of (a) a core-shell Fe@Pt nanowire with a core diameter of 54 nm, (b) the thinnest Fe nanowire achieved and (c) an Fe nanowire exemplifying the possibility of fabricating an extremely sharp tip end with only 8 nm in diameter.

Since the best signal-to-noise ratio was obtained for Fe nanowires with ~35 nm in diameter, ~8-nm-sharp end and 80% at. Fe, this nanostructure was selected for the STEM-EELS chemical analyses.

As illustrated in Figure 6.5(a), the compositional profile along the length of the nanowire as a function of the distance to the tip end reveals that the Fe content is found to decrease as the tip end is approached. As expected, the higher contribution of the oxidation layer as the tip end is getting closer accounts for the Fe diminishment from >70% at. in the central region of the nanowire down to the half value at 3.5 nm from the tip, corresponding approximately with the thickness of the oxidation shell. The STEM-EELS chemical map is depicted in Figure 6.5(b) for a better comparison with the results extracted from TEM imaging and Off-Axis EH experiments.
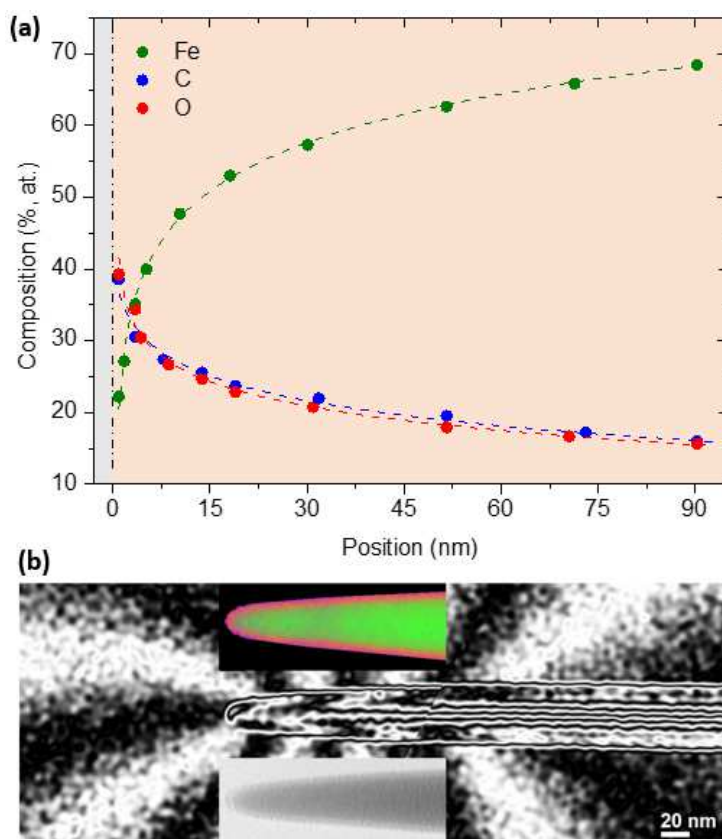
Figure 6.5. (a) STEM-EELS chemical profile of an Fe nanowire grown on top of an AFM probe. The vertical short dash dot line represents the nanowire apex edge. (b) Chemical map showing the relative composition of Fe, C and O contents in green, blue and red, respectively; magnetic flux lines representation illustrating the stray field distribution; and TEM image.

The magnetic characterization allows mapping not only the magnetic induction inside of the specimen (~1 T in the central region) but also the value of the magnetic stray field as a function of the distance to the tip end, which is particularly useful towards the development of quantitative MFM measurements [12]. The magnetic flux lines indicate that the saturation is high in the central part of the nanowire and decreases close to the tip, giving rise to smaller stray fields. Therefore, the tip shape has a significant impact on the magnetic stray fields generated in the surroundings of the nanowire tip.

In addition, different MFM experiments were carried out to explore the customization of the stray field by controlling accurately the nanowire tip dimensions. As shown in Figure 6.6, the standard commercial MFM probes usually present frequencies around 55 Hz, which can be used to calculate *B* when using a calibration sample. For comparison, two different FEBID nanowires with 1 µm in length and different diameter and shape tip ends were fabricated. The nanostructures with 50 nm in diameter and blunt shape showed frequencies of ~40 Hz, whereas the nanowires with diameter tip end of 7 nm and sharp shape exhibited ~15 Hz. This unveils that the tailoring of the nanowire geometry can be used to adjust the tip-sample interaction.

On the other hand, to provide rough magnetic quantitative information of the stray fields, micromagnetic simulations were performed. For a simplified data calculation, nanowires with a rectangular prism shape has been considered. Firstly, Figure 6.7 illustrates the magnetic induction along the long axis of the nanowire depending on the nanostructure aspect ratio, considering nanowires with 1 µm in length and diameters ranging from 50 nm to 95 nm, with $B = 1$ T in the central region of the nanostructure. An important difference in the magnetic signal can be appreciated in the estimated MFM working area —around 75 nm far away from the tip— reducing the magnetic induction 3.5 times when decreasing the diameter by half. Secondly, as shown in Figure 6.8, 50-nm-wide nanowires were explored varying the length between 300 nm and 1 µm. In this case, the impact of the nanowire's length is negligible in the MFM working area.
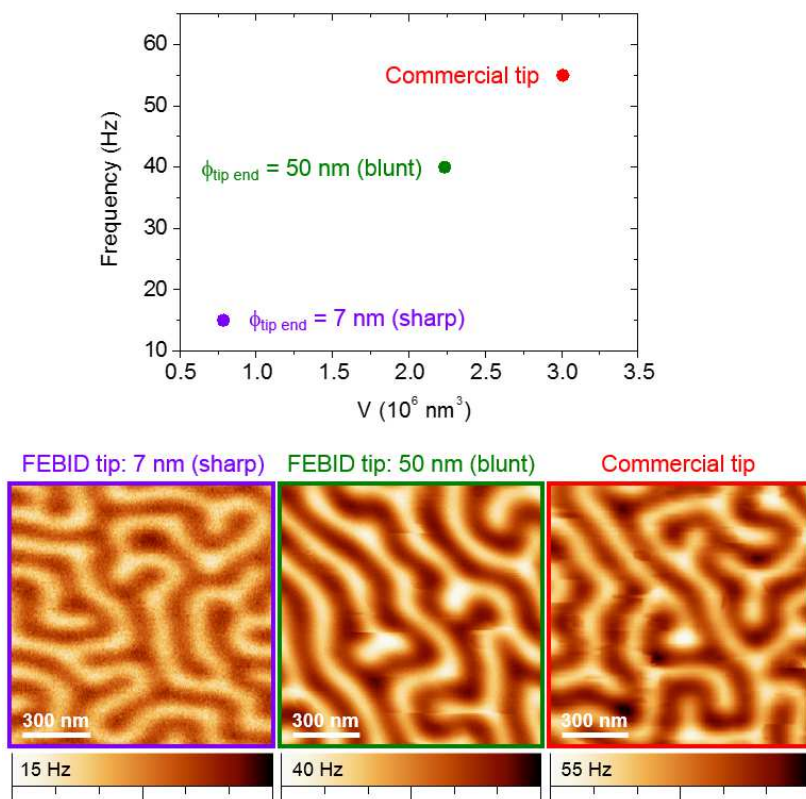
Figure 6.6. Measurement of the frequency, related to the stray field, and their corresponding MFM images of a tip fabricated with an Fe-FEBID nanowire with a sharp tip end of 7 nm (purple), with a blunt tip end of 50 nm (green), and a standard commercial MFM probe (red).

Finally, in Figure 6.9 a *B* modification on a nanowire with 750 nm in length and 50 nm in diameter is considered. The selected *B* values correspond to those obtained for the annealed Co nanowires represented in Figure 4.12. The results indicate that only slight differences can be noticed in the area where MFM usually operates.

Although the real shape and composition have not been modelled by means of this simple calculation, the results suggest that the nanowire length is not as relevant as the diameter in these values ranges. This allows the growth of shorter nanowires, which is an advantage concerning the fabrication time and their stability during the subsequent acquisition of the MFM images.
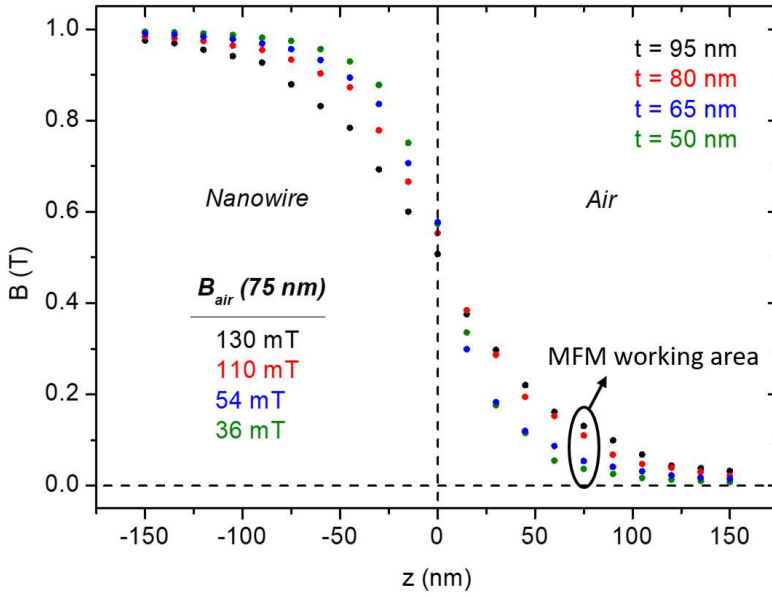
Figure 6.7. Magnetization as a function of the distance to the apex along the nanowire longitudinal axis direction for different diameter values. The QuickField software package was used.
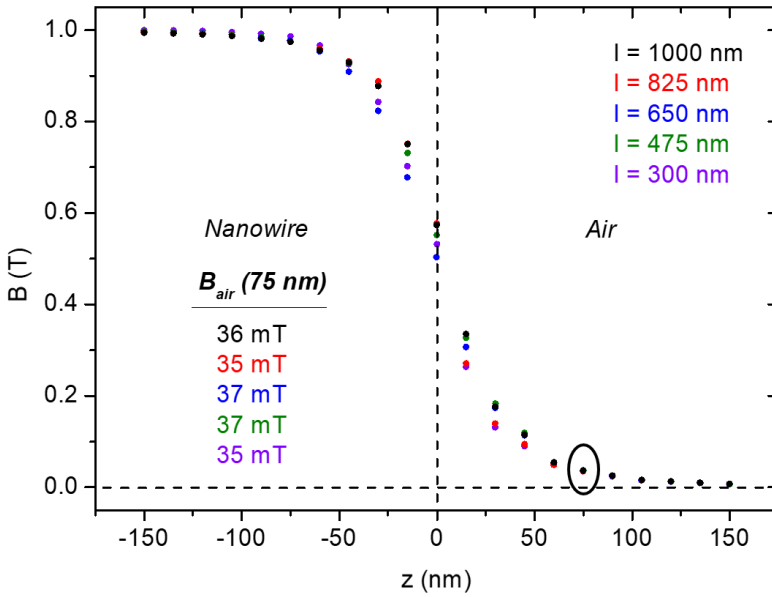
Figure 6.8. Magnetization as a function of the distance to the apex along the nanowire longitudinal axis direction for different length values.
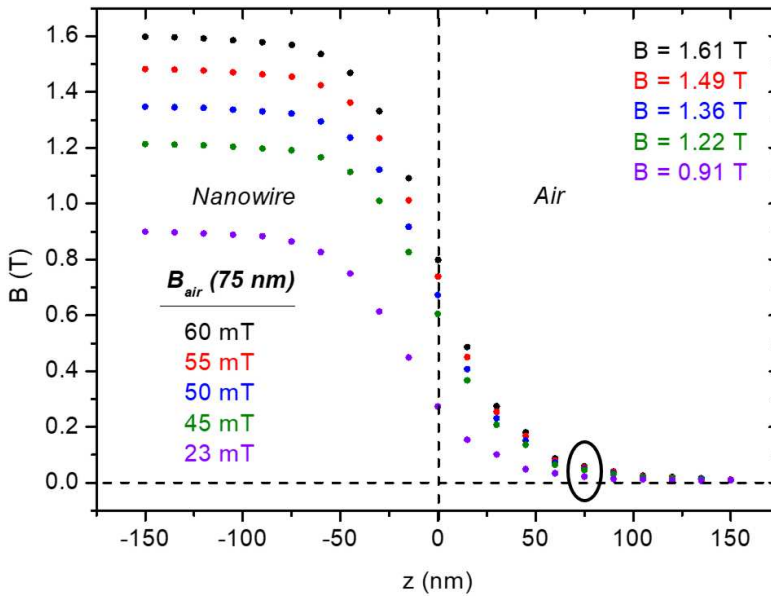
Figure 6.9. Magnetization as a function of the distance to the apex along the nanowire longitudinal axis direction for different B values in the central region of the nanostructure.

6.1.4 Biological sample detection

Many research lines rely on the investigation of samples which must remain in a liquid environment to be stabilized, e.g., culture media or dilutions. In these work environments, it is important to consider the sensitivity of the MFM technique, which is defined through the minimum change of the frequency shift, Δf. This magnitude, inversely proportional to the effective spring constant, K, is heavily dependent on Q, which is linked to the damping ratio and ultimately with the density of the media. The higher the density, the lower the Q. As a result, the signal-to-noise ratio is much worse in liquid media than in air conditions for the same cantilever. In order to improve the sensitivity, high resonance frequency and low K are required according to the Equation 2.22 [13], but a K decrease implies a noise increment, proportional to $(KQ)^{-1/2}$.

Diverse approaches have been followed trying to enhance the tips magnetic performance [14][15][16]. For instance, the fabrication of nano-objects located in the apex such as C nanotubes coated with magnetic material [17], the growth of magnetic nanowires [18] or the use of nanoscale magnets [19] are strategies to reduce the magnetic material of the probe and optimize the MFM signal. However, these procedures have not resulted in an improvement of the technique. In view of this, the development of new devices or refinements of the current systems [5][8] are required to provide a robust measurement method of magnetic samples, especially in liquids.

This subsection aims to establish an improved technology devoted to analysing biological samples (cells, tissues, proteins, virus, bacteria, nucleic acids, etc.) with magnetic traces, nanoparticles and nanowires which can act as contrast agents in nuclear magnetic resonance, nanostructures used in hyperthermia for cancer treatment and drug delivery, etc. Specifically, the magnetic properties which determine their effective implementation in biomedicine can be examined: magnetic domains configuration at remanence, magnetization reversal mechanism, stray fields, aggregate state of nanostructures in accordance with their size, level of material functionalization, etc. For that purpose, the technological challenge based on the observation and characterization of those magnetic samples can be addressed using Co- and Fe-FEBID tips.

Figure 6.10 and 6.11 shows the results obtained in air and liquid conditions for commercial and FEBID tips. Firstly, using the standard *Nanosensors PPP-MFMR* tip [20], a clear deterioration of the signal-to-noise ratio can be appreciated in water. Secondly, the commercial *Team Nanotec* tip was tested. Although a stable signal is obtained in the liquid medium, since the sensitivity improves but the noise gets worse, there is no improvement of the total signal-to-noise ratio.
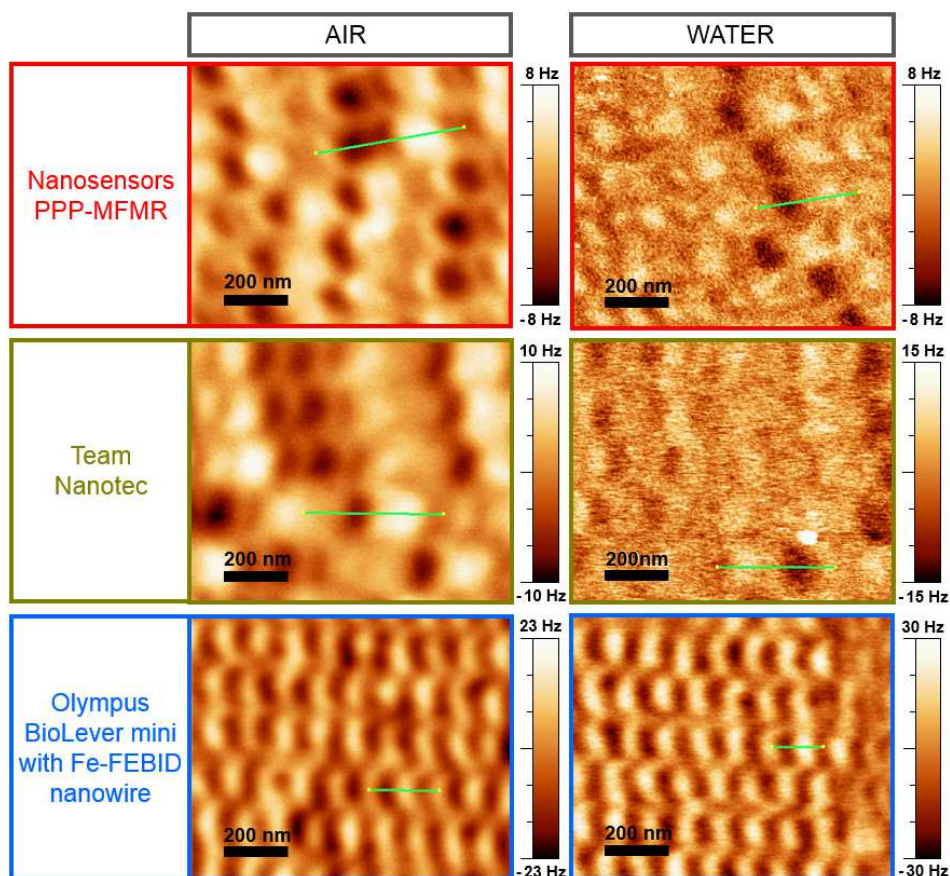
Figure 6.10. Comparison of the MFM images acquired in air and water environments for the commercial *Nanosensors PP-MFMR* and *Team Nanotec* tips, and for the functionalized *Olympus BioLever mini* with an Fe-FEBID nanowire.

Given the performance constraints of the commercial probes, experiments with FEBID functionalized tips were performed using dedicated cantilevers for working in liquid media. In particular, the *Olympus BioLever mini* AFM probe with a FEBID nanowire ensures very good performance, as shown in Figure 6.10 and 6.11, evidencing remarkable improvement of contrast with respect to the standard commercial MFM tips in liquid. In fact, the image quality and sensibility are approximately the same in both air and water. Also, this tip has shown an excellent performance after one year in storage.
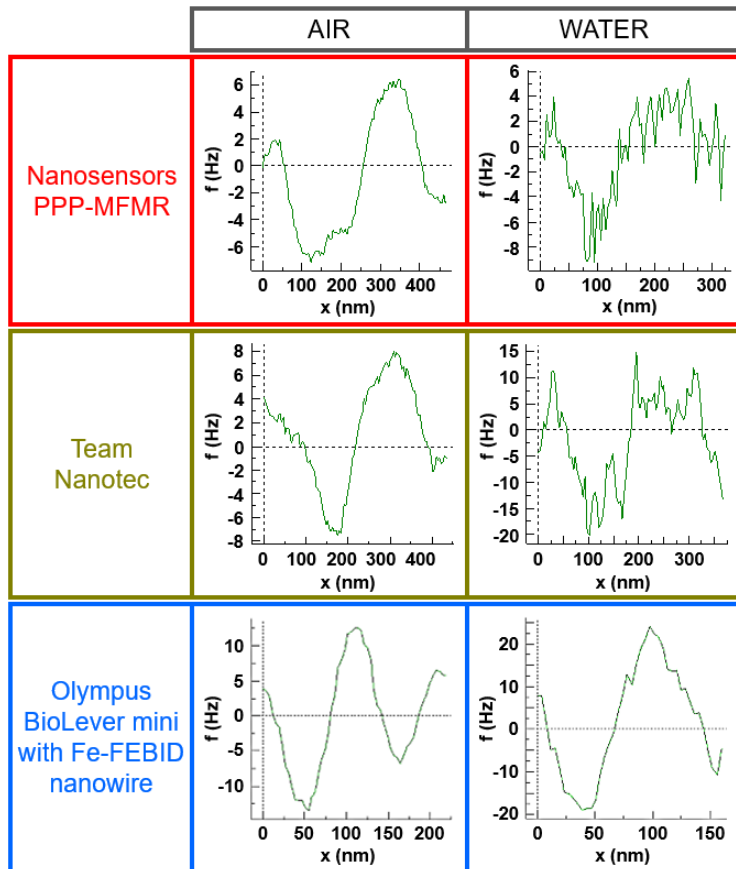
Figure 6.11. MFM signal profiles obtained from the green lines depicted in Figure 6.10 for each tip case.

The FEBID tips allow selecting the most appropriate cantilever to optimize the MFM acquisition, avoiding the lack of adhesion of the magnetic layer to the probe when working in liquid media, controlling the stray field and fabricating deposits with high magnetic induction, which is impossible using the typical sputtering or evaporation methods due to the cantilever geometry. Additionally, an increase of the signal-to-noise ratio can be accomplished by minimizing the van der Waals interaction thanks to a closer approach of the FEBID tip to the sample than the commercial ones. So far, there is no magnetic commercial probe which satisfies these requirements.

6.1.5 Magnetic skyrmions observation

The magnetic skyrmions are spin textures of nanometric scale which present outstanding potential properties for spintronic applications. These topologically-protected quasiparticles were predicted theoretically in the 1960s [21] and are typically stabilized in systems presenting Dzyaloshinskii-Moriya interaction (DMI) and uniaxial magnetic anisotropy [22][23][24][25]. The resulting Bloch and Néel skyrmions can be found in bulk non-centrosymmetric materials [26] or ultrathin films with strong spin-orbit coupling in the interface [27][28][29].

To date, the stabilization of either Bloch or Néel skyrmions was limited to systems with intrinsic magnetic anisotropy. However, an investigation conducted in collaboration with the group of Dr. Agustina Asenjo provides an evidence of the stabilization of Néel skyrmions in confined systems with neither DMI nor perpendicular magnetic anisotropy. In particular, the detection of the non-chiral magnetic Néel hedgehog skyrmions was performed at room temperature in soft magnetic sub-100 nm diameter polycrystalline nanodots made of permalloy where, however, either a vortex or a single domain state with IP magnetization was expected due to low magnetocrystalline anisotropy [30][31]. The permalloy nanodots have proven to serve as architectures to form metastable magnetic Néel skyrmions, consisting of rotating the out-of plane (OOP) magnetization component from the core to the boundaries by the spin curling in radial planes [32][33]. This has been demonstrated by analytical calculations, micromagnetic simulations and experiments based on applying external magnetic fields while performing MFM measurements [11].

Despite this remarkable result, the aim of this subsection is not to present a comprehensive study of the hedgehog skyrmions, but to introduce a novel potential in the performance of FEBID MFM tips. A great emphasis is to be given in the detection, observation and stabilization of the skyrmions configuration by the magnetic field arisen from these functionalized tips.

Whereas in permalloy nanodisks with 140 nm in diameter MFM images reveal dark (attractive interaction) or bright (repulsive interaction) contrast at the centre, corresponding to the magnetization parallel or antiparallel to the tip polarization; in sub-100 nm nanodots the contrast is always bright, evidencing an antiparallel tip-core configuration regardless of the MFM tip polarization, as illustrated in Figure 6.12(a). In a system with diameters below 30 nm, a non-skyrmionic behaviour is exhibited, establishing a radius boundary for the skyrmions stabilization.

On the other hand, as shown in Figure 6.13, under IP applied magnetic field the skyrmions core moves parallel or antiparallel to the field until reaching a critical value when the magnetization is completely aligned with the field direction. These experiments proved the existence of a radial IP magnetization component in the nanodots, discarding the vortex system and strongly demonstrating the Néel skyrmionic configuration. In addition, analytical calculations suggest that Néel skyrmions are highly metastable states which can be stabilized in permalloy nanodots in absence of external fields and destroyed by small perturbations. In order to evaluate the stabilization of this singular nanostructures considering the tip-sample interaction, MFM experiments with different types of probe have been carried out as a function of the IP applied magnetic field.
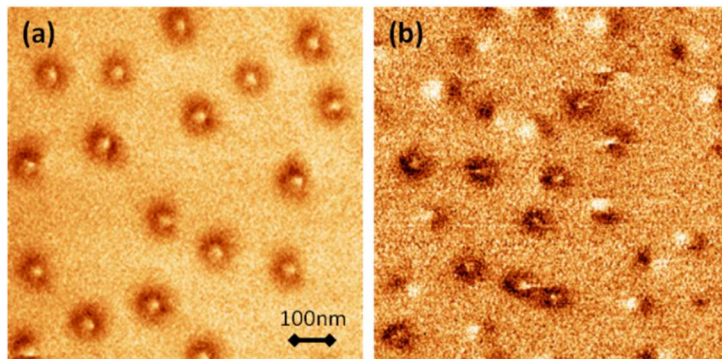
Figure 6.12. MFM images performed with an Fe-FEBID tip of (a) nanodots with 70 nm in diameter presenting 100% of skyrmion configuration and (b) nanodots with 30 nm in diameter presenting 22% of skyrmion configuration, the rest being single domain and other different configurations.

The experimental results are displayed in Figure 6.13, certifying that the stray field coming from the MFM tip contributes to the stabilization of the skyrmions [34]. The commercial *Nanosensors* probe presents the highest stray field, the Co-coated tip by sputtering offers an intermediate value and the Fe-FEBID nanowire tip exhibits the lowest one. As can be noted, the saturating field decreases as the stray field produced is reduced. As a result, the stray field of the tip enables the control of the skyrmion stability.

In the latter case, a nanowire of 1 µm in length, 30 nm in diameter and a very sharp apex with just 7 nm allows imaging the skyrmions with better resolution and under the lowest external tip invasiveness, maximizing the OOP/IP stray field ratio. Since the application of OOP stray fields serves to tune the stability of the skyrmions, FEBID nanolithography technique can modulate the stabilization providing the stray field customization. Therefore, the use of FEBID functionalized probes unveils a new ability to analyse magnetic skyrmions without perturbating their magnetic state and exploring their magnetization dynamics. Moreover, these tips are very useful to study magnetic textures which are very much sensitive to external perturbations.
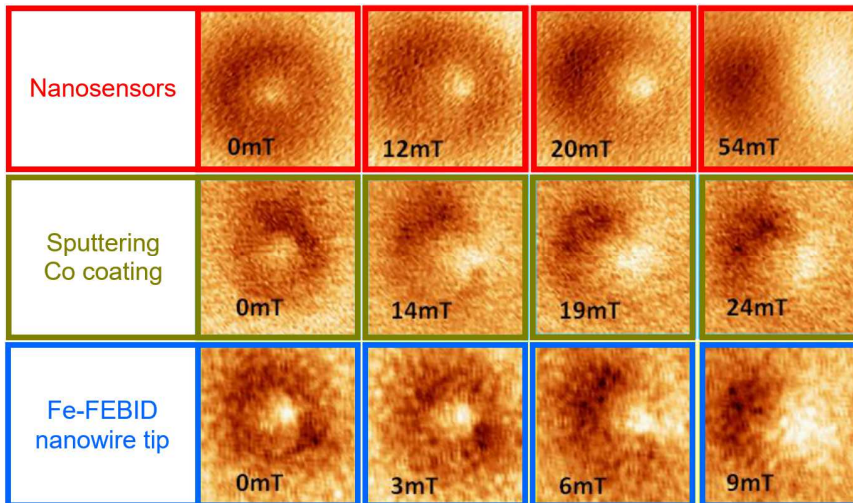
Figure 6.13. MFM images performed with a commercial *Nanosensors* probe, a Co-coated tip and an Fe-FEBID nanowire tip. The field sequences show different IP fields depending on the type of tip. All image sizes are 250×250 nm^2.

6.2 Engineered 3D cobalt nanowires

Shape customization by FEBID entails a great advantage for the fabrication of 3D samples with several features. Apart from the straight structural shape, this technical benefit enables a wide range of architectural configurations despite its difficulty. In this section, this asset will be further exploited to grow and investigate curved ferromagnetic FEBID nanostructures, pursuing the development of devices based on the domain wall motion such as high-density non-volatile memories.

6.2.1 Introduction

Although a large variety of shapes and materials can be produced by distinct techniques [35][36][37][38], the architecture of the nano-objects is usually restricted to straight cylindrical or tubular designs [39][40]. The possibility to fabricate 3D nanostructures with many different geometries by FEBID offers a great versatility in terms of shape, areal density and novel magnetic domain configurations [41]. Based on these fundaments and harnessing the polyvalence of this single-step nanolithography technology, engineered 3D Co and Co@Pt nanowires have been designed containing bent segments which can promote the formation of magnetic domain walls.

The strategy of curved nanostructures seems reasonable and well-adapted to the objective because the pinning of domain walls thanks to bending sections has already been reported in experimental [42] and theoretical [43] studies, where an increase in pinning situations was detected with the curvature and the angle of the bends [44][45]. The following study aims to grow 3D ferromagnetic nanowires with single or multiple very well-defined bends acting as pinning sites along the length of the nanostructure. The magnetic state will be characterized exploring the capability of such singular shapes to generate specific sites where magnetic domains pointing in different directions meet to form a domain wall. As shown in Figure 6.14, the purpose of this geometry is to trigger the presence of domain walls at remanence after saturating the sample with a magnetic

field applied parallel to the substrate and in the plane of the bends. Although this approach was tested in the past in many different systems, e.g., 2D cylindrical curved permalloy nanowires [46], its application in 3D nano-objects still constitutes a major challenge.

Regarding the detection of such magnetic configurations, no conventional magneto-optical and MFM methods are fully appropriate for 3D structures. For this reason, Off-Axis EH and X-ray magnetic circular dichroism in combination with photoemission electron microscopy (XMCD-PEEM) techniques have been selected [47][48][49][50]. In fact, although previous studies on 3D samples of diverse shapes were already reported using both techniques [51][52][53], shadow XCMD-PEEM had not been performed in vertical nanostructures with such high aspect ratio.
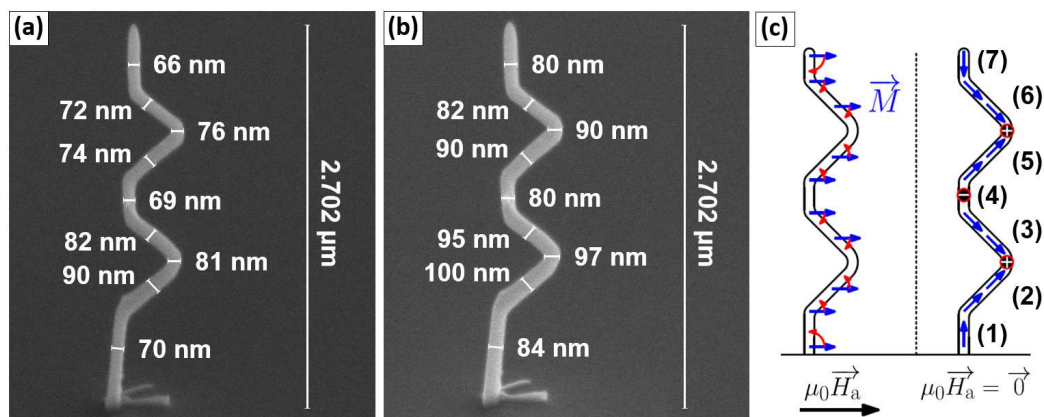
Figure 6.14. SEM images of a 3D Co@Pt nanowire (a) before and (b) after the Pt-C coating. (c) Scheme of the IP magnetic field application favouring the domain walls formation at remanence in the areas indicated by red-rimmed circles, where the alternating magnetic charge are denoted.

6.2.2 Experimental details

The nanostructures were grown in the commercial Helios Nanolab 650 Dual Beam system using $Co_2(CO)_8$ and $CH_3CpPt(CH_3)_3$ precursor gases. The substrates were TEM Cu grids and Si wafers. The Co nanowires were fabricated with a 5 kV electron beam voltage, a 100 pA electron beam current and a chamber growth pressure of 3.3×10^{-5}

mbar (base pressure of ~4.7 × 10^{-6} mbar). Although each segment of the nanowire could be fabricated separately tilting the stage at every stage, here the whole Co nanostructure was grown in one single deposition with the stage remaining in the horizontal position. The Co pattern is composed of 77 points separated 14 nm in a straight line parallel to the flat edge of the Co GIS, keeping constant the precursor molecules flux guaranteeing no shadowing effect [54]. As illustrated in Figure 6.14, the nanowire is formed by seven segments —numbered from bottom to top—, each one having its particular growth strategy. Vertical segments are obtained by scanning a single pattern point while the electron beam stands still. By contrast, bent segments are fabricated by scanning a sequence of 18 points while shifting the electron beam position. For a fixed total horizontal shift and dwell time during the sequence, the angle of the segment with respect to the substrate depends on the number of points. The higher that number, the shorter the distance between two subsequent points, and therefore the overlap between them will be higher and the angle with respect to the substrate will increase. Each bent segment corresponds to 18 pattern points with a scanning time of 97.2 ms. To form the ~90 degrees bends, the joint between the bent segments is fabricated by a single point scanned for 581.2 ms. Then, the bend is completed by reversing the electron beam shift direction.

The first segment was grown by depositing on the first point for 2903.8 ms. Then, the second and the third ones were fabricated scanning the sequence of 18 points for each one, as described above, taking into account that the points of the third one are exactly over those of the second segment but scanned in the reverse direction, thus forming the first bend of the nanostructure. The fourth segment was completed scanning a single point for 1549.1 ms. Then, the fifth and the sixth segments, as well as the joint between them were carried out just as the first bend. The top segment was fabricated scanning the last point during 2419.8 ms. On the other hand, following the same procedure, 3D Co nanowires with only one bend have also been fabricated.

For the Co@Pt nanowires, the Pt-C shell was grown immediately after the ferromagnetic core (~65%–70% at. Co) following the process described in Chapter 5 in order to avoid its oxidation [22]. An electron beam voltage of 5 kV and an electron beam current of 100 pA were used, with a chamber growth pressure of 2.4×10^{-5} mbar. In this case, a polygonal Pt-C pattern was set following the shape of the nanowire core viewed from the perspective shown in Figure 6.14(a). A Pt-C deposition of ~2 s in each side increases the diameter by ~13 nm, as seen in Figure 6.14(b).

In order to characterize magnetically the ferromagnetic nanowires, Off-Axis EH and XMCD-PEEM imaging experiments have been performed. In the first one, experiments were performed in the FEI Titan Cube, operated at 300 kV. The excitation of the biprism was adjusted according to the nanowires shape, with a fringe contrast ranging from 20% to 25% and an acquisition time of 5 s. The second technique was carried out in the XPEEM branch of the HERMES beamline (Synchrotron SOLEIL-France) [35] by the group of Dr. Olivier Fruchart.

6.2.3 Magnetic state characterization

Firstly, Off-Axis EH experiments were performed on single-bend 3D Co nanowires to check the pinning of domain walls at remanence in the bends after applying a magnetic field in the appropriate direction, i.e., in the plane of the bends and approximately perpendicular to the substrate surface. As illustrated in Figure 6.15, two almost identical nanostructures were used to explore the reproducibility of the experiment. The results show that two different domain walls were found in the first and second bends starting from the bottom, which is evidenced by the contrast change of the magnetic flux lines in the bend and the presence of stray fields in the surrounding vacuum. In fact, the two domain walls can be appreciated in the same places in each nanowire, guaranteeing the replicability of its formation.
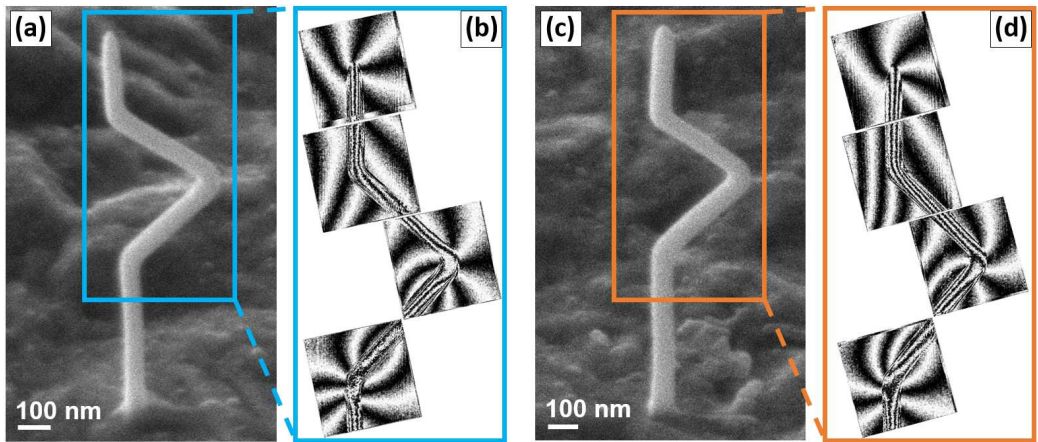
Figure 6.15. (a,c) SEM images of two different 3D Co nanowires and (b,d) their associated magnetic flux lines distribution.

In XMCD-PEEM experiments, the shadow of the nanostructure generated when the beam passes through the specimen provides information for recovering the magnetic configuration of the sample. On the one hand, the magnetic imaging with synchrotron soft X-rays is based on the magnetic circular dichroism, revealing the difference in resonant absorption of left and right circularly-polarized light and obtaining the projection of the magnetization. On the other hand, the collection of photoelectrons coming from the nanostructure during X-ray absorption allows imaging. Specifically, the image contrast, which is proportional to the cosine of the angle between the beam wave vector and the magnetization direction, is used for the reconstruction of the magnetic configuration.

As already suggested in Figure 6.14, after applying the magnetic field —parallel to the substrate and in the bends plane—, three domain walls are expected to be nucleated on double-bend 3D Co nanowires. Figure 6.16 shows the correlation between the shadow features and the magnetic state of the segments. Whereas the strong field emission at the nanowire tip leads to a reduction of the signal-to-noise ratio, the top segments (4, 5 and 7) are clearly identified in Figure 6.16(b), far away from the nanowire position. The lack

261

of contrast in segment 6 could be explained by the ~90 degrees beam incident angle with respect to this section. On the other hand, the faint dark domain at the top corresponds to segment 7, the dark domain to segment 5 and the bright one to segment 4. In addition, the homogeneous contrast of each area means that the magnetization is uniformly oriented inside them.

The opposite contrast presented in segments 4 and 5 demonstrates that the magnetic domains have different magnetization directions, reversing from one to the other. As a result, this proves that a domain wall was pinned in the transition region between them. It should be stressed that, thanks to the nanowire geometry and the precise control of the applied magnetic fields, the pinning and detection of domain walls have been possible.
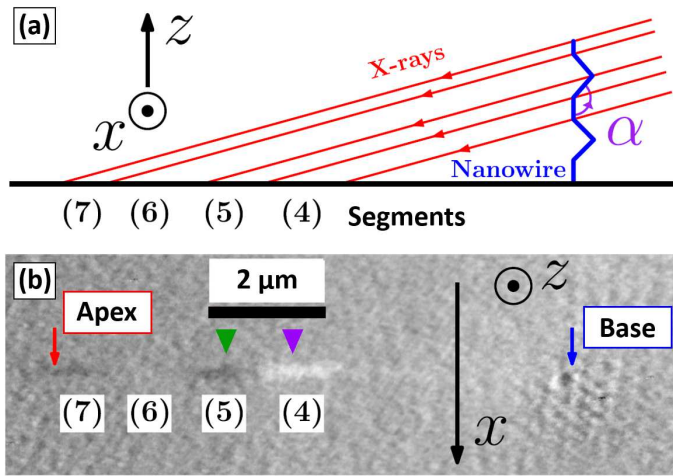
Figure 6.16. (a) Schematic representation of the X-ray beam passing through a nanowire with the lines crossing the segment junctions to determine the shadow sections of the top segments. (b) Shadow XMCD-PEEM image of the 3D Co@Pt nanowire shown in Figure 6.14, aligned vertically with (a).

6.3 Conclusions

Firstly, the flexibility of FEBID technology to select the nanowire diameter, length and composition has been found to be a fast, reproducible and reliable method for the fabrication of MFM probes. More specifically, the fabrication of the 3D Co and Fe nanowires has been performed onto different AFM cantilevers, giving rise to a system with optimized performance in terms of resolution, sensitivity and mechanical stability. Indeed, a resolution of ~15-20 nm has been recently demonstrated [55]. Also, the FEBID tips can be used in self-sensing cantilevers, which correlates the deflection of the cantilever with the electric resistance and cannot be coated because shortcut would be induced.

The customization of the stray field arisen from the tip by tuning the geometry of the ferromagnetic nanostructures offers a new degree of freedom, providing an alternative method to other functionalization techniques. It has been shown that narrow nanowires with very sharp tip end, leading to outstanding low stray fields, make the probes ideal to operate both in air and liquid media, bringing out new prospects for their application in biomagnetism. In addition, these functionalized FEBID tips behave perfectly for the measurement of magnetic nanostructures such as skyrmions. In fact, the detection and stabilization of Néel skyrmions in soft magnetic permalloy nanoparticles with no magnetic anisotropy has been carried out by using the local stray field coming from the MFM tips.

Finally, an accurate nanofabrication control by FEBID has allowed the growth of 3D ferromagnetic nanowires with bent sections as predefined sites for domain wall pinning. The magnetic characterization experiments confirmed the pinning of domain walls at these bends after the application of magnetic fields in a particular direction. As a result, this not only demonstrates the great versatility of the technique in terms of engineering capability, but also opens new possibilities to produce complex devices based on magnetization dynamics.

References

[1]   R. Winkler, A. Szkudlarek, J. D. Fowlkes, P. D. Rack, I. Utke and H. Plank, "Toward Ultraflat Surface Morphologies During Focused Electron Beam Induced Nanosynthesis: Disruption Origins and Compensation", *ACS Appl. Mater. Interfaces* **7**, 3289 (2015).

[2]   A. G. Fedorov, S. Kim, M. Henry, D. Kulkarni and V. V. Tsukruk, "Focused-electron-beam-induced processing (FEBIP) for emerging applications in carbon nanoelectronics", *Appl. Phys. A* **117**, 1659 (2014).

[3]   J. M. De Teresa and R. Córdoba, "Arrays of densely packed isolated nanowires by focused beam induced deposition plus Ar$^+$ milling", *ACS Nano* **8**, 3788 (2014).

[4]   M. Castagné, M. Benfedda, S. Lahimer, P. Falgayrettes and J. P. Fillard, "Near field optical behaviour of C supertips", *Ultramicroscopy* **76**, 187 (1999).

[5]   I. Utke, P. Hoffmann, R. Berger and L. Scandella, "High-resolution magnetic Co supertips grown by a focused electron beam", *Appl. Phys. Lett.* **80**, 4792 (2002).

[6]   Y. M. Lau, P. C. Chee, J. T. L. Thong and V. Ng, "Properties and applications of cobalt-based material produced by electron-beam-induced deposition", *J. Vac. Sci. Technol. A* **20**, 1295 (2002).

[7]   L. M. Belova, O. Hellwig, E. Dobisz and E. Dan Dahlberg, "Rapid preparation of electron beam induced deposition Co magnetic force microscopy tips with 10 nm spatial resolution", *Rev. Sci. Instrum.* **83**, 093711 (2012).

[8]   M. Gavagnin, H. D. Wanzenboeck, S. Wachter, M. M. Shawrav, A. Persson, K. Gunnarsson, P. Svedlindh, M. Stöger-Pollach and E. Bertagnolli, "Free-Standing Magnetic Nanopillars for 3D Nanomagnet Logic", *ACS Appl. Mater. Interfaces* **6**, 20254 (2014).

[9]   M. Jaafar, J. M. De Teresa, A. Asenjo, J. Pablo-Navarro, P. Ares, C. Magén and J. Gómez-Herrero, "System for an Atomic Force Microscope". Spanish patent *P201731292* (2017). International patent *PCT/ES2018/070709* (2018).

[10]   M. Toth, C. Lobo, V. Friedli, A. Szkudlarek and I. Utke, "Continuum models of focused electron beam induced processing," *Beilstein J. Nanotechnol.* **6**, 1518 (2015).

[11]   E. Berganza, M. Jaafar, M. Goiriena-Goikoetxea, J. Pablo-Navarro, A. García-Arribas, K. Gusliyenko, C. Magén, J. M. De Teresa, O. Chubykalo-Fesenko and A. Asenjo, "Observation of hedgehog skyrmions in sub-100 nm soft magnetic nanodots", arXiv:1803.08768v1 [cond-mat.mes-hall] (2018).

[12]   D. Wolf, L. A. Rodriguez, A. Béché, E. Javon, L. Serrano, C. Magen, C. Gatel, A. Lubk, H. Lichte, S. Bals, G. Van Tendeloo, A. Fernández-Pacheco, J. M. De

Teresa and E. Snoeck, "3D Magnetic Induction Maps of Nanoscale Materials Revealed by Electron Holographic Tomography", *Chem. Mater.* **19**, 6771 (2015).

[13] R. García and R. Pérez, "Dynamic atomic force microscopy methods", *Surf. Sci. Rep.* **47**, 197 (2002).

[14] Ó. Iglesias-Freire, M. Jaafar, E. Berganza, and A. Asenjo, "Customized MFM probes with high lateral resolution", *Beilstein J. Nanotechnol.* **7**, 1068 (2016).

[15] E. L. Román, L. Martínez, M. Díaz, Y. Huttel, "Modification of atomic force microscopy tips by deposition of nanoparticles with an aggregate source". Spanish patent *P201030712* (2010). International patent *PCT/ES2011/070319* (2011).

[16] N. Amos, R. Ikkawi, R. Haddon, D. Litvinov and S. Khizroev, "Controlling multidomain states to enable sub-10-nm magnetic force microscopy", *Appl. Phys. Lett.* **93**, 203116 (2008).

[17] H. Kuramochi, T. Uzumaki, M. Yasutake, A. Tanaka, H. Akinaga and H. Yokoyama, "A magnetic force microscope using CoFe-coated carbon nanotube probes", *Nanotechnology* **16**, 24 (2005).

[18] G. Yang, J. Tang, S. Kato, Q. Zhang, L. C. Qin, M. Woodson, J. Liu, J. W. Kim, P. T. Littlehei, C. Park and O. Zhou, "Magnetic nanowire based high resolution magnetic force microscope probes", *Appl. Phys. Lett.* **87**, 123507 (2005).

[19] H. Campanella, M. Jaafar, J. Llobet, J. Esteve, M. Vázquez, A. Asenjo, R. P. del Real and J. A. Plaza, "Nanomagnets with high shape anisotropy and strong crystalline anisotropy: perspectives on magnetic force microscopy", *Nanotechnology* **22**, 505301 (2011).

[20] P. Ares, M. Jaafar, A. Gil, J. Gómez-Herrero and A. Asenjo, "Magnetic Force Microscopy in Liquids", *Small* **11**, 4731 (2015).

[21] T. H. R. Skyrme, "A unified field theory of mesons and baryons", *Nucl. Phys.* **31**, 556 (1962).

[22] P.-J. Hsu, A. Kubetzka, A. Finco, N. Romming, K. Von Bergmann and R. Wiesendanger, "Electric-field-driven switching of individual magnetic skyrmions," *Nat. Nanotechnol.* **12**, 123 (2017).

[23] N. Romming, C. Hanneken, M. Menzel, J. E. Bickel, B. Wolter, K. Von Bergmann, A. Kubetzka, R. Wiesendanger, "Writing and Deleting Single Magnetic Skyrmions", *Science* **341**, 636 (2013).

[24] F. Büttner, C. Moutafis, M. Schneider, B. Krüger, C. M. Günther, J. Geilhufe, C. V. K. Schmising, J. Mohanty, B. Pfau, S. Schaffert, A. Bisig, M. Foerster, T. Schulz, C. A. F. Vaz, J. H. Franken, H. J. M. Swagten, M. Kläui and S. Eisebitt, "Dynamics and inertia of skyrmionic spin structures", *Nat. Phys.* **11**, 225 (2015).

[25] C. Jin, Z.-A. Li, A. Kovács, J. Caron, F. Zheng, F. N. Rybakov, N. S. Kisilev, H.

Du, S. Blügel, M. Tian, Y. Zhang, M. Farle and R. E. Dunin-Borkowski, "Control of morphology and formation of highly geometrically confined magnetic skyrmions", *Nat. Commun.* **8**, 15569 (2017).

[26]   A. Fert, V. Cros and J. Sampaio, "Skyrmions on the track", *Nat. Nanotechnol.* **8**, 152 (2013).

[27]   J. Sampaio, V. Cros, S. Rohart, A. Thiaville and A. Fert, "Nucleation, stability and current-induced motion of isolated magnetic skyrmions in nanostructures", *Nat. Nanotechnol.* **8**, 839 (2013).

[28]   O. Boulle, J. Vogel, H. Yang, S. Pizzini, D. D. S. Chaves, A. Locatelli, T. O. Menteş, A. Sala, L. D. Buda-Prejbeanu, O. Klein, M. Belmeguenai, Y. Roussigné, A. Stashkevich, S. M. Chérif, L. Aballe, M. Foerster, M. Chshiev, S. Auffret, I. M. Miron and G. Gaudin, "Room-temperature chiral magnetic skyrmions in ultrathin magnetic nanostructures", *Nat. Nanotechnol.* **11**, 449 (2016).

[29]   C. Moreau-Luchaire, C. Moutafis, N. Reyren, J. Sampaio, C. A. F. Vaz, N. Van Horne, K. Bouzehouane, K. Garcia, C. Deranlot, P. Warnicke, P. Wohlhüter, J.-M. George, M. Weigand, J. Raabe, V. Cros and A. Fert, "Additive interfacial chiral interaction in multilayers for stabilization of small individual skyrmions at room temperature", *Nat. Nanotechnol.* **11**, 444 (2016).

[30]   K. Y. Guslienko and V. Novosad, "Vortex state stability in soft magnetic cylindrical nanodots", *J. Appl. Phys.* **96**, 4451 (2014).

[31]   M. Goiriena-Goikoetxea, K. Y. Guslienko, M. Rouco, I. Orue, E. Berganza, M. Jaafar, A. Asenjo, M. L. Fernández-Gubieda, L. Fernández Barquín and A. García-Arribas, "Magnetization reversal in circular vortex dots of small radius", *Nanoscale* **9**, 11269 (2017).

[32]   I. Kézsmárki, S. Bordács, P. Milde, E. Neuber, L. M. Eng, J. S. White, H. M. Rønnow, C. D. Dewhurst, M. Mochizuki, K. Yanai, H. Nakamura, D. Ehlers, V. Tsurkan and A. Loidl, "Néel-type skyrmion lattice with confined orientation in the polar magnetic semiconductor GaV$_4$S$_8$", *Nat. Mater.* **14**, 1116 (2015).

[33]   S. D. Pollard, J. A. Garlow, J. Yu, Z. Wang, Y. Zhu, and H. Yang, "Observation of stable Néel skyrmions in cobalt/palladium multilayers with Lorentz transmission electron microscopy", *Nat. Commun.* **8**, 14761 (2017).

[34]   C. Wang, D. Xiao, X. Chen, Y. Zhou and Y. Liu, "Manipulating and trapping skyrmions by magnetic field gradients", *New J. Phys.* **19**, 083008 (2017).

[35]   Ó. Iglesias-Freire, C. Bran, E. Berganza, I. Mínguez-Bacho, C. Magén, M. Vázquez and A. Asenjo, "Spin configuration in isolated FeCoCu nanowires modulated in diameter", *Nanotechnology* **26**, 395702 (2015).

[36]   R. Lavín, C. Gallardo, J. L. Palma, J. Escrig and J. C. Denardin, "Angular dependence of the coercivity and remanence of ordered arrays of Co nanowires", *J. Magn. Magn. Mater.* **324**, 2360 (2012).

[37]   R. Streubel, J. Lee, D. Makarov, M.-Y. Im, D. Karnaushenko, L. Han, R. Schäfer, P. Fischer, S.-K. Kim and O. G. Schmidt, "Magnetic microstructure of rolled-up single-layer ferromagnetic nanomembranes", *Adv. Mater.* **26**, 316 (2014).

[38]   L. Mohaddes-Ardabili, H. Zheng, S. B. Ogale, B. Hannoyer, W. Tian, J. Wang, S. E. Lofland, S. R. Shinde, T. Zhao, Y. Jia, L. Salamanca-Riba, D. G. Schlom, M. Wuttig and R. Ramesh, "Self-assembled single-crystal ferromagnetic iron nanowires formed by decomposition", *Nat. Mater.* **3**, 533 (2004).

[39]   Y. Fukunaka, M. Motoyama, Y. Konishi and R. Ishii, "Producing Shape-Controlled Metal Nanowires and Nanotubes by an Electrochemical Method", *Electrochem. Solid-State Lett.* **9**, C62 (2006).

[40]   H.-M. Zhang, X.-L. Zhang, J.-J. Zhang, Z.-Y. Li and H.-Y. Sun, "Template-Based Electrodeposition Growth Mechanism of Metal Nanotubes", *J. Electrochem. Soc.* **160**, D41 (2013).

[41]   J. D. Fowlkes, R. Winkler, B. B. Lewis, A. Fernández-Pacheco, L. Skoric, D. Sanz-Hernández, M. G. Stanford, E. Mutunga, P. D. Rack and H. Plank, "High-Fidelity 3D-Nanoprinting via Focused Electron Beams: Computer-Aided Design (3BID)", *ACS Appl. Nano Mater.* **1**, 1028 (2018).

[42]   M. J. Benitez, M. A. Basith, R. J. Lamb, D. McGrouther, S. McFadzean, D. A. MacLaren, A. Hrabec, C. H. Marrows and S. McVitie, "Engineering Magnetic Domain-Wall Structure in Permalloy Nanowires", *Phys. Rev. Appl.* **3**, 034008 (2015).

[43]   K. V. Yershov, V. P. Kravchuk, D. D. Sheka and Y. Gaididei, "Curvature-induced domain wall pinning", *Phys. Rev. B* **92**, 104412 (2015).

[44]   S. Glathe and R. Mattheis, "Magnetic domain wall pinning by kinks in magnetic nanostripes", *Phys. Rev. B* **85**, 024405 (2012).

[45]   E. R. Lewis, D. Petit, L. Thevenard, A. V. Jausovec, L. O'Brien, D. E. Read and R. P. Cowburn, "Magnetic domain wall pinning by a curved conduit", *Appl. Phys. Lett.* **95**, 152505 (2009).

[46]   S. Da Col, S. Jamet, M. Staňo, B. Trapp, S. Le Denmat, L. Cagnon, J. C. Toussaint and O. Fruchart, "Nucleation, imaging, and motion of magnetic domain walls in cylindrical nanowires", *Appl. Phys. Lett.* **109**, 062406 (2016).

[47]   L. Serrano-Ramón, R. Córdoba, L. A. Rodríguez, C. Magén, E. Snoeck, C. Gatel, I. Serrano, M. R. Ibarra and J. M. De Teresa, "Ultrasmall functional ferromagnetic nanostructures grown by focused electron-beam-induced deposition", *ACS Nano*

5, 7781 (2011).

[48]   J. Kimling, F. Kronast, S. Martens, T. Böhnert, M. Martens, J. Herrero-Albillos, L. Tati-Bismaths, U. Merkt, K. Nielsch and G. Meier, "Photoemission electron microscopy of three-dimensional magnetization configurations in core-shell nanostructures", *Phys. Rev. B* **84**, 174406 (2011).

[49]   R. Streubel, V. P. Kravchuk, D. D. Sheka, D. Makarov, F. Kronast, O. G. Schmidt and Y. Gaididei, "Equilibrium magnetic states in individual hemispherical permalloy caps", *Appl. Phys. Lett.* **101**, 132419 (2012).

[50]   S. Jamet, S. Da Col, N. Rougemaille, A. Wartelle, A. Locatelli, T. O. Menteş, B. Santos Burgos, R. Afid, L. Cagnon, S. Bochmann, J. Bachmann, O. Fruchart and J. C. Toussaint, "Quantitative analysis of shadow x-ray magnetic circular dichroism photoemission electron microscopy", *Phys. Rev. B* **92**, 144428 (2015).

[51]   D. Shindo, "Electron Holography of Nanocrystalline Magnetic Materials", *Mater. Trans.* **44**, 2025 (2003).

[52]   R. Streubel, P. Fischer, F. Kronast, V. P. Kravchuk, D. D. Sheka, Y. Gaididei, O. G. Schmidt and D. Makarov, "Magnetism in curved geometries", *J. Phys. D: Appl. Phys.* **49**, 363001 (2016).

[53]   V. Rouco, R. Córdoba, J. M. De Teresa, L. A. Rodríguez, C. Navau, N. Del-Valle, G. Via, A. Sánchez, C. Monton, F. Kronast, X. Obradors, T. Puig and A. Palau, "Competition between Superconductor-Ferromagnetic stray magnetic fields in $YBa_2Cu_3O_{7-x}$ films pierced with Co nano-rods", *Sci. Rep.* **7**, 5663 (2017).

[54]   L. Keller and M. Huth, "Pattern generation for direct-write three-dimensional nanoscale structures via focused electron beam induced deposition", *Beilstein J. Nanotechnol.* **9**, 2581 (2018).

[55]   C. Schwalb, GETec Microscopy, *Private Communication* (2019).

Chapter 7: General conclusions and outlook

In this chapter, a global overview of the key results presented in this thesis and the main conclusions emanated from them are presented, together with the promising prospects for the future research on 3D FEBID magnetic nanostructures in the framework of Nanomagnetism.

Since the emergence of Nanotechnology and the multitude of applications derived from it, intensive efforts have been devoted to fabricating functional nanostructures. Specifically, magnetic nanostructured materials attract particularly keen interest because of their would-be implementation in key information and communications technologies, such as data storage, logic and sensing devices [1]. Accordingly, the development of novel nanofabrication techniques or the refinement of the existing methods is one of the essential cornerstones for the growth of advanced nano-objects, allowing the subsequent study of physical phenomena at nanometric scale [2].

In this light, Focused Electron Beam Induced Deposition (FEBID) arises as one of the most versatile nanofabrication technologies which could play a crucial role in the production of several types of architectures and materials in the nanoscale [3]. During the last decades, this single-step lithographic method has been widely used for the growth of two-dimensional deposits, creating magnetic nanostructures considered as promising candidates for the development of forthcoming spintronic applications. However, the increasing demand for high-density and low-power nanodevices naturally entails the expansion to three-dimensional (3D) deposits [4]. As a result, vertical magnetic nanostructures are currently a central topic in nanomagnetism. The functionality of these potential building blocks for 3D magnetic devices relies on the precise control of domain wall motion with spin-polarized currents or magnetic fields which, combined with the high areal density allowed by 3D architectures, is bound to boost their operational performance.

The overarching objective of this thesis involves the synthesis and characterization of 3D ferromagnetic nanowires, intending to shed light upon novel and advanced optimization processes which help to improve the operational behaviour of these nanostructures. The main achievements presented in this manuscript are described below.

7.1 Tailoring of 3D nanowires grown by FEBID

Firstly, the FEBID versatility has been exploited to adjust the thickness, composition and magnetic induction of 3D Co nanowires. In this regard, nanostructures with double-section diameters, different shapes and chemical contents have been investigated, providing insight on the linear and radial growth regimes. The interpretation of the results indicates that thermal and diffusion effects are ultimately responsible for these growth modes, helping in the progress towards future upgraded nanofabrication strategies. As a practical example, diameter changes or bent shapes are natural locations for magnetic domain-wall pinning with applications in magnetic storage and logics.

Standing by these arguments, simultaneous high metallic content (~80% at.), small diameters (<100 nm) and high magnetic induction (~1 T) have been obtained for nanowires grown under optimized conditions. These results are a forward step to the goal of driving FEBID towards a remarkably practical nanolithography technique to fabricate 3D functional nanostructures with unique lateral resolution. Along this line, Co and Fe nanowires with very sharp apex have been analysed and found to be ideal architectures for Magnetic Force Microscopy measurements.

Secondly, the difficulty of FEBID to fabricate nanostructures on insulating substrates due to severe charging effects has been overcome by using the ARchitectural Adjustment by Grid Overlay Nanotechnology (ARAGON) Chip, an electrically-biased patterned metal structure which enables charge evacuation during the growth of nano-objects. In addition, this novel approach has been proven to serve as a new knob for *in situ* modulation of the nanowire geometry, by dint of the application of spatially-dependent electric fields, acting as an electrostatic lens on the trajectories of the primary and secondary electrons. Therefore, the *in situ* modification of the applied voltage or the focus height offers a new route to create 3D functional complex nanostructures with tailored lateral dimensions. These findings have enabled not only a better understanding of the growth mechanisms by FEBID, but also hinting new approaches for the

implementation of the ARAGON-Chip. For instance, instead of patterning the holed metal plate onto the sample, the ARAGON-Chip could be redesigned to be inserted automatically in the vicinity of the substrate as an aperture in the Scanning Electron Microscopes, with different hole geometries to produce custom distributions of electric fields.

7.2 Annealing treatments to optimize nanowire properties

The crystallinity, composition and magnetic induction of 3D ferromagnetic Co and Fe nanowires differs greatly from the bulk materials mainly due to the presence of impurities coming from the incompletely dissociation of the precursor gas molecules. In order to remove these undesired byproducts, post-growth high-vacuum annealing processes have been performed.

In the case of Co, *ex situ* thermal annealing at 600 ºC has been found to produce purified and crystalline nanowires with diameters below 90 nm, a metallic content above 95% at., and a net magnetic induction up to 1.6 T, near the bulk Co. The combined effect of contaminants migration to the surface and recrystallization of the as-grown nanocrystalline structure gives rise to nanowires with physical properties close to bulk ones. Besides, given the relatively high metal content of the as-grown deposits (~70% at.), the changes in shape of the deposits after purification is minimal, facilitating their functional implementation in 3D devices.

In the case of Fe, real-time monitoring of the chemical purification and structural crystallization processes of ultra-narrow nanowires (<50 nm in diameter) has been carried out by *in situ* annealing in a Transmission Electron Microscope. The heating up to 700 ºC reveals local increases of the metallic content along the nanowire length concomitant with the growth of large Fe single crystals from initially pseudo-amorphous compounds with just ~40% at. of Fe. Besides, a reduction of the diameter down to ~30 nm has been achieved in the highest metallic regions. This evolution tracking has provided insight into

the nanoscale processes involved during the annealing treatment, serving as a future ideal method for determining the minimum requirements of purity and geometry for as-grown nanowires and the appropriate thermal conditions to be successfully annealed. Along this line of thought, future advances in the purification strategies could point towards exploring further crystallization upon longer and precise annealing times with the aim of routinely producing high-quality single-crystalline nanowires or the use of reactive atmosphere to etch the remaining contaminants at the surface [5]. The same route could be used to explore the possibility of annealing bimetallic or heterogeneous systems and the potential for temperature-induced alloying.

7.3 Dual purpose of the core-shell architectural approach

On the one hand, the natural surface oxidation of the ferromagnetic nanostructures to a non-ferromagnetic material (~5 nm in thickness) implies the degradation of the magnetic properties of 3D Co and Fe nanowires, which becomes critical at the smallest diameters. This negative impact can be palliated by growing a 10-20 nm-thick Pt-C protective shell, retaining the original net magnetic induction. This improvement with respect to the uncoated nanowires can reach 35% for the thinnest nanowires (<40 nm core diameters), when the surface oxidized layer greatly contributes to the total nanowire diameter. This strategy demonstrates that the operability of nanostructured objects often relies on the combination of more than one material, enhancing the performance of the device or conferring the desired functionality.

On the other hand, 3D ultra-thin Co nanotubes have also been synthesized on Pt-C templates adapting the core-shell approach to produce Pt@Co nanowires. Dimensional, compositional and magnetic characterization has proved the ferromagnetic behavior of the Co nanotubes and allowed studying their magnetization state and dynamics. The switching mechanism is governed by the domain-wall formation and propagation, having a strong and potential impact in the functionality of devices composed by these

nanostructures. In particular, ferromagnetic nanotubes are of tremendous interest for investigations of fast-propagating magnetic domain walls, which is a too-demanding requirement for the development of applications within Nanomagnetism.

References

[1]   S. S. P. Parkin, M. Hayashi and L. Thomas, "Magnetic domain-wall racetrack memory", *Science* **320**, 190 (2008).

[2]   M. Vázquez, "Magnetic Nano- and Microwires. Design, Synthesis, Properties and Applications", *Elsevier* (2015).

[3]   M. Huth, F. Porrati, C. Schwalb, M. Winhold, R. Sachser, M. Dukic, J. Adams and G. Fantner, "Focused electron beam induced deposition: A perspective", *Beilstein J. Nanotechnol.* **3**, 597 (2012).

[4]   A. Fernández-Pacheco, R. Streubel, O. Fruchart, R. Hertel, P. Fischer and R. P. Cowburn, "Three-dimensional nanomagnetism", *Nat. Commun.* **8**, 15756 (2017).

[5]   E. Begun, O. V Dobrovolskiy, M. Kompaniiets, R. Sachser, C. Gspan, H. Plank and M. Huth, "Post-growth purification of Co nanostructures prepared by focused electron beam induced deposition", *Nanotechnology* **26**, 075301 (2015).

Conclusiones generales y perspectivas

En este capítulo se presenta un resumen de los principales resultados obtenidos e incluidos en este documento. Asimismo, de forma global se recogen las conclusiones generales surgidas de esta tesis doctoral, acompañadas de unas perspectivas prometedoras y con gran potencial para futuras investigaciones con estructuras 3D fabricadas por deposición inducida por haz focalizado de electrones dentro del marco del Nanomagnetismo.

Desde el surgimiento de la Nanotecnología y de las múltiples aplicaciones derivadas de este campo, se han dedicado numerosos esfuerzos para la fabricación de nanoestructuras funcionales. Específicamente, los materiales magnéticos nanoestructurados atraen un gran interés por sus potenciales implementaciones en tecnologías de la información y la comunicación, tales como los dispositivos dedicados al almacenamiento, lógica y detección magnéticos [1]. En este sentido, el desarrollo de nuevas técnicas de nanofabricación o el perfeccionamiento de los métodos ya existentes es una de las piedras angulares para el crecimiento de nano-objetos avanzados, permitiendo el consiguiente estudio de los fenómenos físicos a escala nanométrica [2].

En este contexto, la deposición inducida por haz focalizado de electrones (FEBID) surge como una de las técnicas de nanofabricación más versátiles, la cual puede desarrollar un papel crucial en la producción de estructuras con diversas formas y materiales en la nanoescala [3]. Durante las últimas décadas, este método de nanolitografía se ha utilizado ampliamente para el crecimiento de depósitos en dos dimensiones, creando nanoestructuras magnéticas consideradas como candidatas potenciales para el desarrollo de los futuros dispositivos espintrónicos. Sin embargo, la creciente demanda para generar métodos de almacenamiento de información en nanodispositivos de alta densidad y con menor consumo de energía conlleva de forma natural a investigar depósitos en tres dimensiones (3D) [4]. Como resultado, las nanoestructuras magnéticas verticales se erigen actualmente como unos de los temas centrales dentro del Nanomagnetismo. La funcionalidad de estas piezas básicas para los futuros dispositivos magnéticos en 3D recae en la posibilidad de controlar de forma precisa el movimiento de las paredes de dominio, bajo la aplicación de corrientes de espín polarizadas o de campos magnéticos que, combinados con la mayor densidad de área ofrecida por las estructuras 3D, permite aumentar su rendimiento [2].

El objetivo principal de esta tesis doctoral integra la síntesis y caracterización de nanohilos ferromagnéticos en 3D, tratando de arrojar luz sobre nuevos y avanzados

procesos de optimización que ayuden a mejorar el comportamiento operacional de estas nanoestructuras. A continuación, se describen los principales resultados presentados en este documento.

7.1 Diseño de nanohilos 3D crecidos por FEBID

En primer lugar, la versatilidad de la técnica FEBID ha sido aprovechada para el ajuste del espesor, composición e inducción magnética de nanohilos de Co en 3D. En este sentido, se han investigado nanoestructuras de diámetro variable, con diferentes formas y contenido metálico, proporcionando un conocimiento y comprensión más profundos sobre los regímenes de crecimiento lineal y radial. La interpretación de los resultados indica que los efectos térmicos y de difusión son los responsables de los diferentes modos de crecimiento en último término, suponiendo un impulso para la mejora y actualización de las futuras estrategias de crecimiento mediante esta técnica. Como ejemplo práctico, cabe destacar que las regiones donde se modifica el diámetro son sitios naturales de anclaje para las paredes de dominio, con aplicaciones en almacenamiento y lógica magnéticos.

En base a estos argumentos, bajo condiciones optimizadas, se han obtenido nanohilos con alto contenido metálico (~80% at.), reducido diámetro (<100 nm) y altos valores de inducción magnética (~1 T). Estos resultados suponen un paso adelante para el objetivo de situar a la técnica FEBID como un método de litografía extraordinario para la fabricación de nanoestructuras funcionales en 3D con resoluciones laterales únicas. En esta línea, se ha comprobado que nanohilos de Co y Fe con puntas muy afiladas son estructuras ideales para medidas en Microscopía de Fuerza Magnética.

En segundo lugar, la dificultad de la técnica FEBID para la fabricación de nanoestructuras sobre sustratos aislantes debido a los severos efectos de carga, ha sido vencida mediante el uso del ARchitectural Adjustment by Grid Overlay Nanotechnology (ARAGON) Chip, es decir, un chip formado por una estructura metálica con forma de

cuadrícula que permite el crecimiento de depósitos de escala nanométrica, gracias a la disipación de carga eléctrica, y la modulación estructural de los mismos aplicando un voltaje eléctrico. Además, se ha demostrado que este método innovador sirve como parámetro de ajuste adicional para la modulación *in situ* de la geometría de nanohilos 3D, a consecuencia de la aplicación de campos eléctricos que actúan como una lente electrostática sobre las trayectorias de los electrones primarios y secundarios. Por tanto, la modificación *in situ* del voltaje aplicado o de la altura de foco ofrece nuevas rutas para la producción de nanoestructuras funcionales complejas en 3D con las dimensiones laterales deseadas. Estos hallazgos no sólo han permitido un mejor entendimiento de los mecanismos que gobiernan el crecimiento por FEBID, sino que también han motivado nuevas ideas de utilización basadas en el ARAGON-Chip. Por ejemplo, en lugar de litografiar la placa metálica con agujeros sobre la muestra, el ARAGON-Chip puede ser rediseñado para ser insertado automáticamente en una posición próxima al sustrato como una apertura en los microscopios electrónicos de barrido, y disponer de agujeros con diferentes geometrías para generar las distribuciones de campo eléctrico requeridas.

7.2 Tratamientos térmicos para optimizar propiedades de los nanohilos

La cristalinidad, composición e inducción magnética de nanohilos de Co y Fe en 3D difieren en gran medida de las características del material bulk, debido fundamentalmente a la presencia de impurezas provenientes de la disociación incompleta de las moléculas de gas precursor. Con el objetivo de eliminar estas especies contaminantes, se han llevado a cabo procesos de recocido en alto vacío tras los crecimientos de las estructuras.

En el caso del Co, se ha comprobado que recocidos térmicos *ex situ* a 600 °C originan nanohilos purificados y cristalinos con diámetros menores de 90 nm, contenidos de Co por encima del 95% at., e inducción magnética de hasta 1.6 T, cercana al valor del bulk. El impacto conjugado de la migración de los contaminantes hacia la superficie y la recristalización estructural da lugar a nanohilos con propiedades físicas similares a las

del bulk. Además, dado el contenido metálico relativamente alto de los depósitos originales (~70% at.), el cambio de forma en las nanoestructuras tras la purificación es mínimo, facilitando su incorporación funcional en dispositivos 3D.

En el caso del Fe, se ha realizado un seguimiento en tiempo real de los procesos de purificación y cristalización estructural en nanohilos ultra-estrechos (<50 nm de diámetro) por medio de tratamientos térmicos *in situ* en un microscopio de transmisión de electrones. El calentamiento hasta los 700 ºC ha revelado un incremento local del contenido metálico a lo largo de la longitud de los nanohilos, a consecuencia del crecimiento de grandes monocristales de Fe partiendo de un compuesto homogéneo y pseudo-amorfo con tan sólo un ~40% at. de Fe. Además, se ha conseguido una reducción del diámetro, llegando hasta los ~30 nm en las regiones con mayor contenido metálico. La exploración *in situ* de la evolución de las propiedades de los nanohilos ha promovido la comprensión a escala nanométrica de los procesos involucrados durante el proceso de recocido, brindando la posibilidad de servir como un método ideal para determinar los requisitos mínimos de pureza y geometría iniciales de los nanohilos y las condiciones de tratamiento térmico apropiadas para conseguir nanomateriales optimizados. En esta línea, los futuros avances en las estrategias de purificación podrían apuntar hacia la búsqueda de mayores niveles de cristalización bajo tiempos de recocido más largos y precisos, con el objetivo de fabricar nanohilos monocristalinos de alta calidad de forma rutinaria, o hacia el uso de atmósferas adecuadas para expulsar las especies contaminantes de la superficie [5]. Esta misma estrategia podría ser usada para explorar la posibilidad de recocer sistemas bimetálicos o heterogéneos, e investigar la potencial aleación inducida por el aumento de temperatura.

7.3 Doble finalidad del modelo estructural core-shell

Por un lado, se ha verificado que la oxidación natural en la superficie de nanoestructuras ferromagnéticas provoca la aparición de una capa de material no

ferromagnético (~5 nm de espesor), lo que implica la degradación de las propiedades magnéticas iniciales en nanohilos de Co y Fe en 3D, aspecto especialmente crítico para el caso de los nanohilos con diámetros más pequeños. Se ha comprobado que este impacto negativo puede ser eliminado mediante el crecimiento de una capa protectora de Pt-C de entre 10 y 20 nm de espesor, manteniendo la inducción magnética original de la estructura. Esta mejora con respecto a los nanohilos sin recubrimiento puede alcanzar el 35%, como ocurre para los nanohilos más estrechos con núcleos de menos de 40 nm donde la capa de oxidación externa contribuye en gran medida al diámetro total del nanohilo. Esta estrategia demuestra que, en ocasiones, la capacidad funcional de objetos nanoestructurados se basa en la combinación de más de un material, mejorando el rendimiento de los dispositivos en los que se encuentran integrados o confiriendo la operatividad deseada.

Por otro lado, también se han fabricado nanotubos de Co ultra-estrechos en 3D sobre pilares de Pt-C, adaptando el método core-shell para producir nanohilos de Pt@Co. La caracterización dimensional, composicional y magnética ha demostrado el comportamiento ferromagnético de los nanotubos de Co y ha permitido estudiar su estado y dinámica magnéticos. Además, se ha probado que el mecanismo de inversión de la magnetización está gobernado por un proceso de formación y propagación de paredes de dominio, teniendo un enorme impacto en la funcionalidad de dispositivos basados en estas nanoestructuras. En particular, los nanotubos ferromagnéticos despiertan gran atracción por la rápida propagación de paredes de dominio, que es uno de los requisitos más buscados en el desarrollo de aplicaciones dentro del Nanomagnetismo.

Referencias

[1]   S. S. P. Parkin, M. Hayashi and L. Thomas, "Magnetic domain-wall racetrack memory", *Science* **320**, 190 (2008).

[2]   M. Vázquez, "Magnetic Nano- and Microwires. Design, Synthesis, Properties and Applications", *Elsevier* (2015).

[3]   M. Huth, F. Porrati, C. Schwalb, M. Winhold, R. Sachser, M. Dukic, J. Adams and G. Fantner, "Focused electron beam induced deposition: A perspective", *Beilstein J. Nanotechnol.* **3**, 597 (2012).

[4]   A. Fernández-Pacheco, R. Streubel, O. Fruchart, R. Hertel, P. Fischer and R. P. Cowburn, "Three-dimensional nanomagnetism", *Nat. Commun.* **8**, 15756 (2017).

[5]   E. Begun, O. V Dobrovolskiy, M. Kompaniiets, R. Sachser, C. Gspan, H. Plank and M. Huth, "Post-growth purification of Co nanostructures prepared by focused electron beam induced deposition", *Nanotechnology* **26**, 075301 (2015).

Annex A: Electron Holography data processing

A.1 Data analysis

The procedure used to obtain qualitative and quantitative information of magnetic nanostructures, in this case nanowires and nanotubes, has been performed by using the Geometrical Phase Analysis (GPA) software [1][2]. The process is based on the extraction of the amplitude and the phase separately. Recalling Equation 2.2, from a general point of view the phase shift of an electron wave advancing along the z axis and passing through a specimen can be expressed as a linear combination:

$$\varphi(x, y) = \varphi_{MIP}(x, y) + \varphi_{MAG}(x, y) \qquad (A.1)$$

where φ_{MIP} and φ_{MAG} are the electrostatic and magnetic phase shift contributions, respectively [3]. Although different procedures can be followed to separate these contributions [4][5], the method proposed by Dunin-Borkowski has been used here [6]. It consists of recording two different holograms in remanence after saturating the magnetization of the sample in two opposite directions. For this purpose, the objective lens was excited to apply a magnetic field along the optical axis of the microscope with the nanostructure tilted an angle enough to guarantee that the magnetization points along its longitudinal axis. This technique is very useful in nanostructures with a strong magnetic shape anisotropy which tend to confine the magnetization in a certain direction. Therefore, the holograms are acquired for antiparallel configurations of the magnetic state of the nanowire with its long axis perpendicular to the z axis. Some examples are shown in Figure A.1. In addition, a reference hologram is recorded in the same conditions with no specimen in the field of view (free vacuum). This helps to remove the parasitic phase contributions which are not originated by the sample.
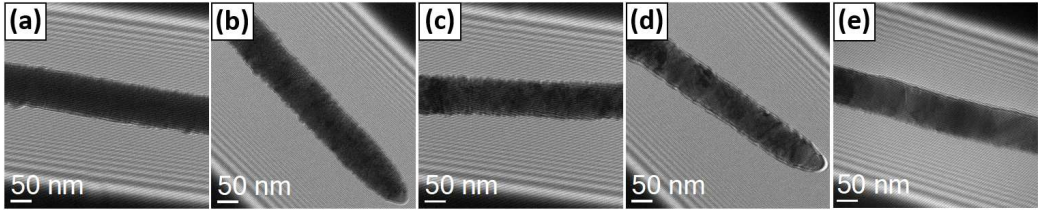
Figure A.1. Examples of electron holograms of different 3D Co nanowires: (a) as-deposited and annealed at (b) 150 ℃, (c) 300 ℃, (d) 450 ℃ and (e) 600 ℃.

Whereas both holograms include the same electrostatic phase shift contribution, the magnetic contribution changes its sign. After the addition and subtraction of the holograms, the two solutions obtained always cancelled one of the phase contributions giving rise to an image with two times the other one. As a result, the electrostatic and magnetic phase shift images can be plotted separately, as shown in Figure A.2.

The gradient of the phase shift can be calculated as:

$$\nabla\varphi(x,y) = \nabla\varphi_{MIP}(x,y) + \nabla\varphi_{MAG}(x,y) =$$

$$= C_E V_{MIP} t(x,y) - \frac{e}{\hbar} B_\perp(x,y) t(x,y) \tag{A.2}$$

where $C_E = \pi\gamma/\lambda U^*$ is a constant which depends on the energy of the incident electron beam with a value of $C_E = 6.53 \times 10^6$ rad·V^{-1}·m^{-1} at 300 kV, V_{MIP} is the mean inner potential and has a value of 26 V for pure Co [7] and 17.4 V for Fe [8], t is the magnetic thickness of the specimen, e is the electron charge, $\hbar$ is the reduced Planck constant, x and y are orthogonal equivalent directions in the plane of the sample and $B_\perp$ the magnetic induction component perpendicular to one of the in-plane components and the electron beam direction, z.
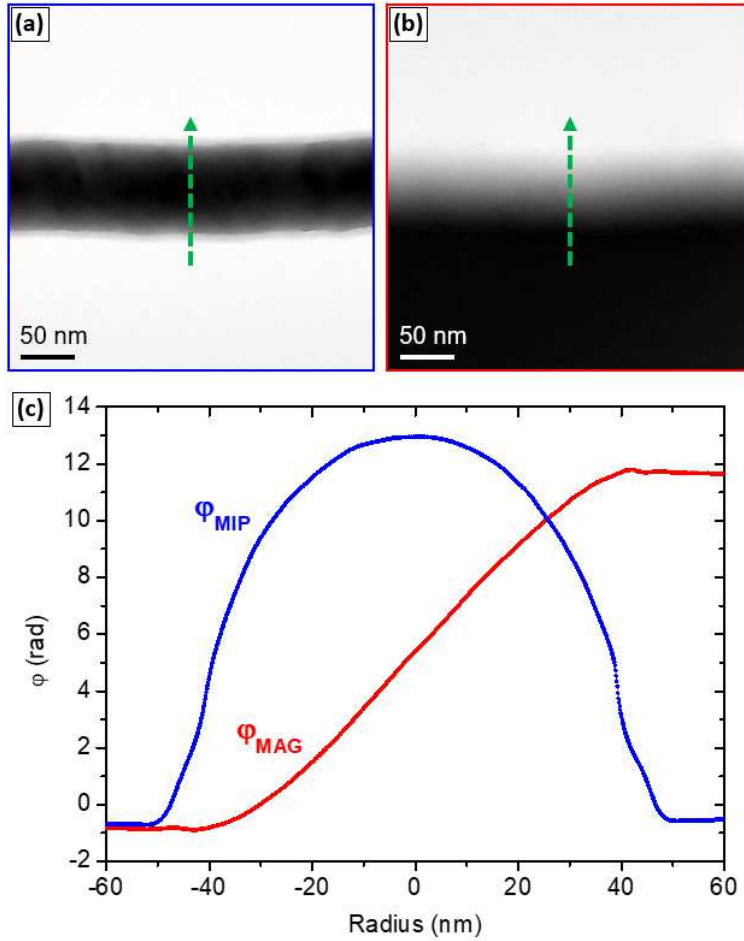
Figure A.2. (a) Electrostatic and (b) magnetic phase shift images extracted from a 3D Co nanowire. (c) Profiles of both types of phase shifts along the green arrows averaged across a length of 58 nm.

Since the nanostructures are not usually composed by a pure material, V_{MIP} value does not correspond to that of the bulk. Thus, considering the first term of the right-hand side of Equation A.2, the electrostatic phase shift image can be used to calculate V_{MIP}, knowing C_E value and the nanowire thickness, assuming that the nano-object is cylindrical and chemically homogeneous. Then, attending to the second term of the right-hand side of Equation A.2, the magnetic induction can be calculated by straightforward

mathematical operations using the gradient of the magnetic phase shift image considering one of the two equivalent directions, *x* and *y*. For instance, in the case of the *x* axis:

$$|B_\perp(x,y)| = \frac{\hbar}{e \cdot t} \frac{\partial \varphi_{MAG}(x,y)}{\partial y} \tag{A.3}$$

Figure A.2 simultaneously demonstrates the cylindrical shape of the nanostructure (φ_{MIP} profile) and shows the change of the φ_{MAG} which proves the ferromagnetic behavior of the nanowire. Indeed, the steeper the slope, the higher the magnetic induction.

Finally, the magnetic flux representation can be illustrated normalizing the magnetic phase contribution to the maximum thickness for a better comparison and calculating the cosine of *n* times the magnetic phase shift.
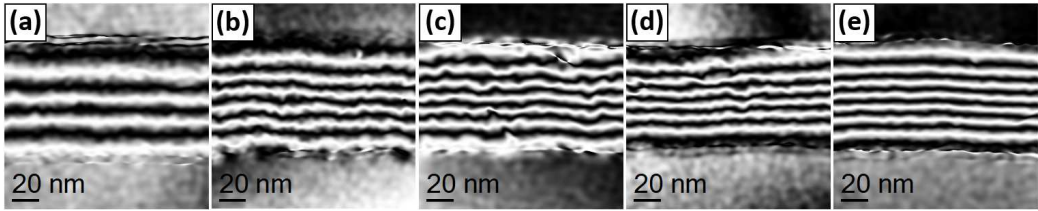

Figure A.3. Magnetic induction flux representations of different 3D Co nanowires: (a) as-deposited and annealed at (b) 150 ℃, (c) 300 ℃, (d) 450 ℃ and (e) 600 ℃.

References

[1]   M. J. Hÿtch, E. Snoeck and R. Kilaas, "Quantitative measurement of displacement and strain fields from HREM micrographs", *Ultramicroscopy* **74**, 131 (1998).

[2]   L. A. Rodríguez, C. Magén, E. Snoeck, C. Gatel, L. Marín, L. Serrano-Ramón, J. L. Prieto, M. Muñoz, P. A. Algarabel, L. Morellon, J. M. De Teresa and M. R. Ibarra, "Quantitative in situ magnetization reversal studies in Lorentz microscopy and electron holography", *Ultramicroscopy* **134**, 144 (2013).

[3]   H. Lichte and M. Lehmann, "Electron holography-basics and applications", *Rep. Prog. Phys.* **71**, 016102 (2008).

[4]   A. Tonomura, T. Matsuda, J. Endo, T. Arii and K. Mihama, "Holographic interference electron microscopy for determining specimen magnetic structure and thickness distribution", *Phys. Rev. B* **34**, 3397 (1986).

[5]   J. C. Loudon, N. D. Mathur and P. A. Midgley, "Charge-ordered ferromagnetic phase in $La_{0.5}Ca_{0.5}MnO_3$," *Nature* **420**, 797 (2002).

[6]   R. E. Dunin-Borkowski, M. R. McCartney, B. Kardynal and D. J. Smith, "Magnetic interactions within patterned cobalt nanostructures using off-axis electron holography", *J. Appl. Phys.* **84**, 374 (1998).

[7]   M. De Graef, N. T. Nuhfer, and M. R. McCartney, "Phase contrast of spherical magnetic particles", *J. Microsc.* **194**, 84 (1999).

[8]   T. Fujita, M. Chen, X. Wang, B. Xu, K. Inoke and K. Yamamoto, "Electron holography of single-crystal iron nanorods encapsulated in carbon nanotubes", *J. Appl. Phys.*, **101**, 014323 (2007).

Annex B: Mechanical properties of 3D cobalt nanowires

B.1 Introduction

Nanowires have also a high interest because of their potential applications in electro-mechanical devices [1][2]. Although the mechanical characterization of these nanostructures is not straightforward, it is critically important to understand their performance behaviour and determine their mechanical properties. For this purpose, the fabrication and characterization of suspended 3D Co nanowires grown by FEBID have been carried out.

Several approaches are used for the mechanical analysis such as AFM nanoindentation [3], contact resonance AFM [4], AFM bending [5], *in situ* SEM resonance [6] and tension [7] or *in situ* TEM resonance [8] and tension [9]. Here, the three-point bending method by AFM is proposed [10][11], consisting of the bending of a double-clamped suspended nanostructure. On this basis, horizontally-suspended double-clamped Co nanowires have been synthesized with diameters between ~55 and ~75 nm and a suspended length of 1.2 µm. Then, the Young modulus and the yield strength have been investigated.

B.2 Experimental details

The nanowires were fabricated in the commercial Helios Nanolab 650 Dual Beam system using $Co_2(CO)_8$ as precursor gas. The substrate consists of arrays of micro-trenches between Si pads separated 1.2 µm, patterned by optical photolithography and reactive ion etching. The suspended nanowires were grown acting as a bridge between the pads, as shown in Figure B.1.

The deposits were fabricated with an electron beam voltage of 5 kV, an electron beam current of 100 pA and a chamber growth pressure of ~2.3×10^{-5} mbar (base pressure of ~1.5×10^{-6} mbar). The pattern was formed by an array of 120 points, separated 15 nm between each other, connecting two Si pads. The electron beam scanned only once from one edge to the other with a dwell time of 1 µs. To compensate the natural inclination of the nanowire with respect to the horizonal axis due to the overlap of the points sequence, the substrate was tilted ~35-45 degrees with respect to the horizontal axis to make the connection possible. EDS experiments after the natural oxidation of the nanostructures revealed chemical compositions of ~53% at. Co, ~20% at. C and ~27% at. O.

The mechanical characterization of the nanowires was performed using a Dimension ICON AFM from Bruker. The bending tests were carried out applying a force in the midpoint of the nanowire and measuring its displacement. The spring constants of the cantilevers were 3 and 20 N·m^{-1}, with a tip approaching speed from 100 to 500 nm·s^{-1}.
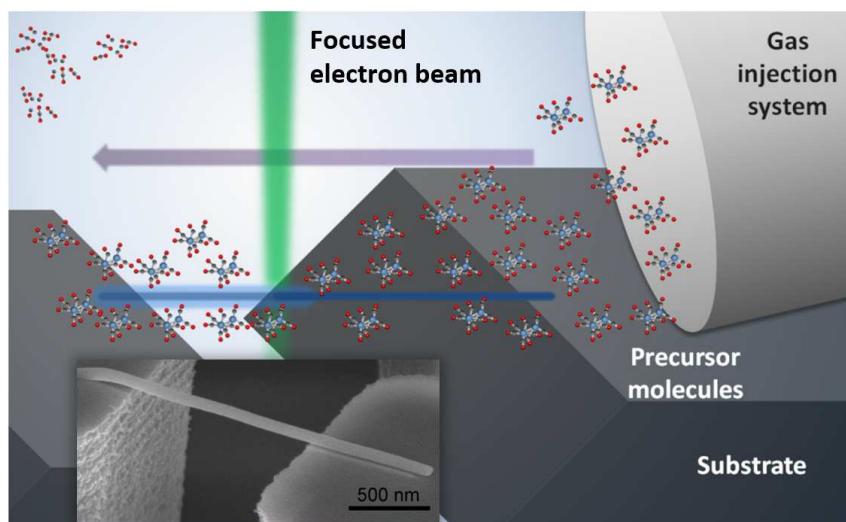

Figure B.1. Schematic diagram illustrating the FEBID process for the fabrication of 3D horizontally-suspended Co nanowires. Noting that during the process the stage was tilted ~35-45 degrees with respect to the horizontal position. The inset shows an SEM image of a 3D Co nanowire.

B.3 Results and discussion

The bending experiment was performed with an AFM tip at the midpoint of the nanowire, undertaking a load-unload process to obtain the relationship between the applied force and the displacement of the central part of the nanostructure. Figure B.2(a) shows the typical curve acquired below the fracture load point. The overlap between the load and unload data reveals the absence of hysteresis. In addition, AFM and SEM inspections performed after these bending experiments did not indicate any failure of the clamping sites.

To determine the Young modulus, E, and the yield strength, σ_y, the three-point bending method was carried out until the nanowires fracture. Figure B.2(b) plots the mechanical behaviour for a Co nanowire, where a linear trend with pure elastic behaviour can be identified in the small deflection range and tends to grow when increasing deflections [12] before the fracture, evidenced by a decrease of the applied force.

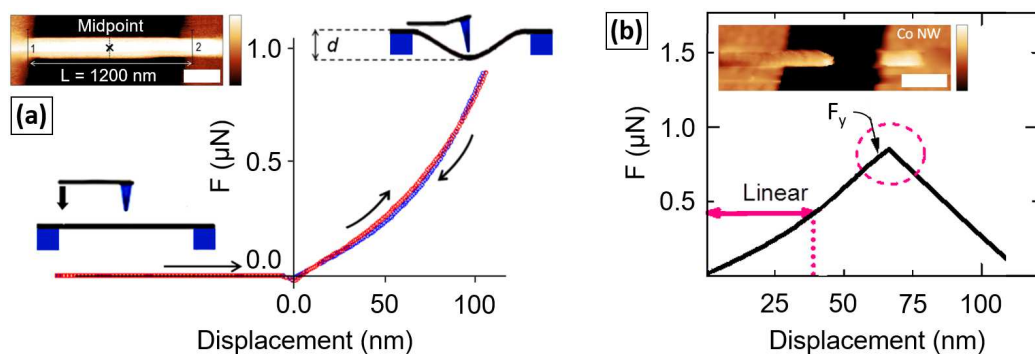Figure B.2. (a) AFM image of a 3D Co nanowire, representing the bending force as a function of the displacement, where the load (red) and unload (blue) curves are shown. (b) Plot of the bending experiment where the linear region and the fracture are highlighted. The inset shows an AFM image of the Co nanowire after the fracture. Undefined colour scale range and scale bars in all images are 100 and 200 nm, respectively.

Firstly, from the linear region, considering the apparent elastic constant, k_w, i.e., the slope of the experimental curves, E can be calculated according to the following equation, corresponding to a double-clamped nanowire with diameter, D, and suspended length, L [13][14]:

$$E = \frac{k_w L^3}{3\pi D^4} \tag{B.1}$$

where k_w is calculated from the linear fit of the bending curves.

The experimental value of E ranges from (58 ± 5) GPa to (209 ± 24) GPa for nanowires between ~55 nm and ~75 nm in diameter, noticing a slight association of the higher E values with the smaller diameters. Thus, these result shows that the E values for the narrower nanowires are very close to the bulk one (~209 GPa), and the values obtained for the wider nanowires are comparable to the ones reported for polycrystalline Co oxide nanowires [10].

Secondly, the subsequent non-linear behaviour is comparable to that reported for double-clamped Si [14], Au [15] and ZnO [16]. When the displacement begins to not be comparable to the nanowire radius, the axial tension due to stretching dominates over the radial one and the curve departs from the linear behaviour.

Thirdly, the applied force reduction evidences the nanowire's plastic deformation and, finally, the fracture. Along this line, the yield strength, σ_y, defined as the stress at which the material starts to be deformed plastically, can be estimated using the following expression [15]:

$$\sigma_y = \frac{4F_y L}{\pi D^3} \tag{B.2}$$

where F_y is the yield force, corresponding to the maximum load immediately before the fracture. An average σ_y of (6.1 ± 2.3) GPa was found, not far from the theoretical one ($\sigma_y \sim 0.1E$) [17], but significantly greater than the bulk Co value ($\sigma_y \sim 345$-485 MPa).

The fracture occurs typically by the emergence of fissures originated at defects [18]. Since the probability of producing a fissure decreases with reducing the material size [15], nanostructures are expected to undergo higher stress than bulk materials. Therefore, the higher σ_y values obtained for nanowires can be explained by the limited number of defects. Additionally, differences in the microstructure and composition of the Co nanowires fabricated by FEBID with respect to the bulk can also contribute towards improving σ_y, e.g., noticing that the small grain sizes present in the nano-objects hampers the formation of defects.

Similar results have been obtained by us on the mechanical properties of suspended W-C nanowires grown by FIBID and investigated using the same experimental technique [19].

B.4 Conclusions

A novel nanofabrication method for the growth of horizontally-suspended 3D Co nanowires by FEBID has been presented. The mechanical characterization performed by the three-point bending method shows good mechanical performance of the nanostructures with Young modulus values comparable to the bulk material ones, and exhibiting a yield strength 15 times higher than the bulk one. The small lateral resolution and the microstructure of these 3D nanostructures confers the nanowires outstanding mechanical properties which provide robustness, potentially constituting the basis for the design of future advanced nano-mechanical devices.

References

[1]   X. L. Feng, R. He, P. Yang and M. L. Roukes, "Very High Frequency Silicon Nanowire Electromechanical Resonators", *Nano Lett.* **7**, 1953 (2007).

[2]   P. Vavassori, M. Pancaldi, M. J. Perez-Roldan, A. Chuvilin and A. Berger, "Remote Magnetomechanical Nanoactuation", *Small* **12**, 1013 (2016).

[3]   X. Li, H. Gao, C. J. Murphy and K. K. Caswell, "Nanoindentation of Silver Nanowires", *Nano Lett.* **3**, 1495 (2003).

[4]   G. Stan, C. V. Ciobanu, P. M. Parthangal and R. F. Cook, "Diameter-dependent radial and tangential elastic moduli of ZnO nanowires", *Nano Lett.* **7**, 3691 (2007).

[5]   E. W. Wong, P. E. Sheehan and C. M. Lieber, "Nanobeam Mechanics: Elasticity, Strength, and Toughness of Nanorods and Nanotubes", *Science* **277**, 1971 (1997).

[6]   C. Q. Chen, Y. Shi, Y. S. Zhang, J. Zhu and Y. J. Yan, "Size dependence of Young's modulus in ZnO nanowires", *Phys. Rev. Lett.* **96**, 075505 (2006).

[7]   M.-R. He, Y. Shi, W. Zhou, J. W. Chen, Y. J. Yan and J. Zhu, "Diameter dependence of modulus in zinc oxide nanowires and the effect of loading mode: In situ experiments and universal core-shell approach", *Appl. Phys. Lett.* **95**, 091912 (2009).

[8]   P. Poncharal, Z. L. Wang, D. Ugarte and W. A. de Heer, "Electrostatic deflections and electromechanical resonances of carbon nanotubes", *Science* **283**, 1513 (1999).

[9]   M.-F. Yu, O. Lourie, M. J. Dyer, K. Moloni, T. F. Kelly and R. S. Ruoff, "Strength and Breaking Mechanism of Multiwalled Carbon Nanotubes Under Tensile Load", *Science* **287**, 637 (2000).

[10]   B. Varghese, Y. Zhang, L. Dai, V. B. C. Tan, C. T. Lim, and C.-H. Sow, "Structure-Mechanical Property of Individual Cobalt Oxide Nanowires", *Nano Lett.* **8**, 3226 (2008).

[11]   P. Zhou, C. Wu and X. Li, "Three-point bending Young's modulus of nanowires", *Meas. Sci. Technol.* **19**, 115703 (2008).

[12]   L. D. Landau and E. M. Lifshitz, "Theory of Elasticity", *Pergamon Press* (1970).

[13]   A. Heidelberg, L. T. Ngo, B. Wu, M. A. Phillips, S. Sharma, T. I. Kamins, J. E. Sader and J. J. Boland, "A generalized description of the elastic properties of nanowires", *Nano Lett.* **6**, 1101 (2006).

[14]   Y.-J. Kim, K. Son, I.-C. Choi, I.-S. Choi, W. I. Park and J.-I. Jang, "Exploring nanomechanical behavior of silicon nanowires: AFM bending versus nanoindentation", *Adv. Funct. Mater.* **21**, 279 (2011).

[15]   B. Wu, A. Heidelberg and J. J. Boland, "Mechanical properties of ultrahigh-strength gold nanowires", *Nat. Mater.* **4**, 525 (2005).

[16]   B. Wen, J. E. Sader and J. J. Boland, "Mechanical Properties of ZnO Nanowires", *Phys. Rev. Lett.* **101**, 175502 (2008).

[17]   N. H. MacMillan, "The theoretical strength of solids", *J. Mater. Sci.* **7**, 239 (1972).

[18]   B. Chen, J. Wang, Q. Gao, Y. Chen, X. Liao, C. Lu, H. H. Tan, Y.-W. Mai, J. Zou, S. P. Ringer, H. Gao and C. Jagadish, "Strengthening Brittle Semiconductor

Nanowires through Stacking Faults: Insights from in Situ Mechanical Testing",
Nano Lett. **13**, 4369 (2013).

[19]   R. Córdoba, M. Lorenzoni, J. Pablo-Navarro, C. Magén, F. Pérez-Murano and J.
M. De Teresa, "Suspended tungsten-based nanowires with enhanced mechanical
properties grown by focused ion beam induced deposition", *Nanotechnology* **28**,
445301 (2017).

Publications

This doctoral thesis has been the source of 8 articles already published in peer-reviewed international journals that belong to the Science Citation Index, and 1 international licensed patent. In addition, there is 1 article under review process (published in arXiv repository) and 2 articles in preparation.

- Articles:

[1]   J. Pablo-Navarro, C. Magén and J. M. De Teresa, "Three-dimensional core-shell ferromagnetic nanowires grown by focused electron beam induced deposition", *Nanotechnology* **27**, 285302 (2016).

[2]   J. Pablo-Navarro, D. Sanz-Hernández, C. Magén, A. Fernández-Pacheco and J. M. De Teresa, "Tuning shape, composition and magnetization of three-dimensional cobalt nanowires grown by Focused Electron Beam Induced Deposition (FEBID)", *Journal of Physics D: Applied Physics* **50**, 18LT01 (2017).

[3]   R. Córdoba, M. Lorenzoni, J. Pablo-Navarro, C. Magén, F. Pérez-Murano and J. M. De Teresa, "Suspended tunsgten-based nanowires with enhanced mechanical properties grown by focused ion beam induced deposition", *Nanotechnology* **28**, 445301 (2017).

[4]   A. Wartelle, J. Pablo-Navarro, M. Staňo, S. Bochmann, S. Pairis, M. Rioult, C. Thirion, R. Belkhou, J. M. De Teresa, C. Magén and O. Fruchart, "Transmission XMCD-PEEM imaging of an engineered vertical FEBID cobalt nanowire with a domain wall", *Nanotechnology* **29**, 045704 (2018).

[5]   J. Pablo-Navarro, C. Magén and J. M. De Teresa, "Purified and crystalline three-dimensional electron-beam-induced deposits: the successful case of cobalt", *ACS Applied Nano Materials* **1**, 38 (2018).

[6]   M. J. Martínez-Pérez, <u>J. Pablo-Navarro</u>, B. Müller, R. Kleiner, C. Magén, D. Koelle, J. M. De Teresa and J. Sesé, "NanoSQUID Magnetometry on Individual As-grown and Annealed Co Nanowires at Variable Temperature", *Nano Letters* **18**, 7674 (2018).

[7]   <u>J. Pablo-Navarro</u>, R. Winkler, G. Haberfehlner, C. Magén, H. Plank and J. M. De Teresa, "*In situ* real time annealing of ultrathin vertical Fe nanowires grown by focused electron beam induced deposition", *Acta Materialia* **174**, 379 (2019).

[8]   <u>J. Pablo-Navarro</u>, S. Sangiao, C. Magén and J. M. De Teresa, "Diameter modulation of 3D nanostructures in Focused Electron Beam Induced Deposition using local electric fields and beam defocus", *Nanotechnology* (2019).

[9]   E. Berganza, M. Jaafar, M. Goiriena-Goikoetxea, <u>J. Pablo-Navarro</u>, J. A. Fernández-Roldán, A. García-Arribas, K. Gusliyenko, C. Magén, J. M. De Teresa, O. Chubykalo-Fesenko and A. Asenjo. "Obersvation of hedgehog skyrmions in sub-100 nm soft magnetic nanodots", arXiv:1803.08768v1 [cond-mat.mes-hall] (2018) and *submitted*.

[10]   <u>J. Pablo-Navarro</u>, I.-M. Andersen, L. A. Rodríguez, D. Sanz-Hernández, A. Fernández-Pacheco, C. Gatel, E. Snoeck, J. M. de Teresa and C. Magén. "Exploring ferromagnetism in 3D Co nanotubes grown by focused electron beam induced deposition", *manuscript in preparation*.

[11]   H. Mattiat, N. Rossi, B. Gross, <u>J. Pablo-Navarro</u>, C. Magén and J. M. de Teresa. "Nanowire magnetic force sensors fabricated by focused electron beam induced deposition", *manuscript in preparation*.

- Patents:

[1]   M. Jaafar, J. M. De Teresa, A. Asenjo, <u>J. Pablo-Navarro</u>, P. Ares, C. Magén and J. Gómez-Herrero, "System for an Atomic Force Microscope". Owning body: CSIC, Universidad de Zaragoza, Universidad Autónoma de Madrid, Fundación Agencia Aragonesa para la investigación y el desarrollo. Spanish reference: *OEPM P201731292* (2017). International reference: *PCT/ES2018/070709* (2018).